Mechanics and durability of surface treated structural foamed concrete

by

Algurnon Steve van Rooyen

Dissertation presented for the degree of Doctor of Philosophy in Engineering in the Faculty of Engineering at Stellenbosch University

Supervisor: Prof Gideon P.A.G. van Zijl

March 2020

Declaration – Plagiarism

1. Plagiarism is the use of ideas, material and other intellectual property of another's work and to present it as my own
2. I agree that plagiarism is a punishable offence because it constitutes theft
3. I also understand that direct translations are plagiarism
4. Accordingly all quotations and contributions from any source whatsoever (including internet) have been cited fully. I understand that the reproduction of text without quotation marks (even when the source is cited) is plagiarism.
5. I declare that the work contained in this dissertation, except where otherwise stated, is my original work and that I have not previously (in its entirety or in part) submitted it for obtaining a qualification

Algurnon Steve van Rooyen

Abstract

Lightweight foamed concrete (LWFC) has been around for a few decades and has mostly been used in non-structural applications such as void filling, soil stabilisation, and backfill. Historically, LWFC has been characterised as a material with low mechanical properties (compressive- and tensile strength) which has prevented the material from being considered for structural applications. However, advances in technologies lead to better mechanical properties for LWFC. Better mechanical properties coupled with good thermal performance is what makes LWFC an attractive alternative to normal weight concrete (NWC). Jones and McCarthy (2005) published a study investigating the potential of foamed concrete (FC) as a structural material. Jones and McCarthy found that FC can indeed be used for structural application based on its compressive strength but should not directly replace NWC concrete. Based on the history of LWFC and its promising future a study was launched at Stellenbosch into the mechanics and durability properties of LWFC. The mechanics portion includes the characterisation of the mechanical properties such as compressive- and tensile splitting strength, elastic modulus, specific fracture energy and bond behaviour of deformed steel in reinforced lightweight foamed concrete (R/LWFC). The durability aspect includes the study of carbonation and chloride-induced corrosion of R/LWFC and the enhancement of these properties using surface treatment agents.

In this research the compressive- and splitting tensile strength of LWFC was tested in accordance with the South African National Standards, the specific fracture energy was measured using the wedge splitting test, and, the bond between deformed steel reinforcement and LWFC is characterised using the conventional pull-out (PO) test and the modified beam-end (BE) test methods. Tests were conducted on LWFC specimens with densities of 1200 kg/m^3 - 1600 kg/m^3. The application of steel reinforced LWFC with density 1400 kg/m^3 in a prefabricated structural walling system is successfully demonstrated in laboratory experiments.

The results of the compressive strength tests showed that LWFC with density of 1400 kg/m^3 and above can be designed to produce strengths considered structural. The tensile splitting strength of LWFC holds similar proportionality of roughly 10 % of the compressive strength. The specific fracture energy of LWFC is relatively low compared with NWC, of which the relative brittle nature of LWFC is testimony. Significant improvement is accomplished by adding low volume of synthetic fibre. The results of the PO test yielded design bond values greater than that obtained from the BE tests for LWFC. The design bond values of LWFC are considerably lower than that of NWC and is highly influence by the specific fracture energy and tensile strength of the concrete. A model for predicting the design bond stress of LWFC was set-up using the principle of equilibrium and performed with the more appropriate BE test results. Evaluation of the predictive model shows relative agreement between the predicted results and the actual results. Based on the results of the model LWFC with density of 1200 kg/m^3 exhibits poor bond behaviour, suggesting only higher densities, 1400 kg/m^3 and above, should be considered for reinforcement and structural use.

The resistance to carbonation penetration and carbonation-induced corrosion was tested on a single density (1400 kg/m^3) of LWFC. The evolution of the carbonation front over time was monitored on freshly cut cube specimens sprayed with phenolphthalein and singly reinforced rectangular specimens were prepared for corrosion assessment using the half-cell potential method. Additionally, the enhancement of LWFC with two surface treatment agents (integral hydrophobic agent and a non-integral hydrophobic agent) was also tested. All LWFC specimens were exposed to a carbonation rich environment of 0.13% CO_2 concentration.

The results of the carbonation penetration test show that LWFC carbonates at a high rate due to the porous nature of the concrete. The use of surface treatment significantly reduces the rate of carbonation rate of LWFC. This is evident in the result at the end of the experiment whereby a near 50% reduction was achieved by using non-integral surface treatment. The results of the corrosion potential indicated that little to no corrosion took place over the study period.

The durability of LWFC against chloride penetration and chloride-induced corrosion was tested in three separate series. For Series 1 singly Y12 reinforced rectangular specimens of dimension 460x100x100 mm with cover depth 24 mm and a 6 mm stainless steel counter-electrode were prepared for cyclic ponding and corrosion assessment using the coulostatic method. For this series the enhancement of LWFC durability was promoted using two surface treatments, non-integral "hydrophobic" agent and integral "pore-blocker", respectively.

The results of chloride profiling using XRF showed deep penetration of chlorides in the untreated concrete and cracked regions (cracks caused by restraint drying shrinkage) passed the reinforcement level. Surface treatment significantly reduced the penetration depth of chlorides in cracked and uncracked regions with the non-integral treatment performing the best. Reduced corrosion rates were observed in treated specimens.

For Series 2 unreinforced and singly reinforced rectangular specimens of dimension 500x100x100 mm and 460x100x100 mm made with concrete cover of 20 mm and 35 mm were prepared for chloride penetration testing and corrosion assessment respectively. For this series the enhancement of LWFC durability against was done similarly to that of Series 1. Specimens were prepared using a single density (1600 kg/m^3) of LWFC with different ash to cement ratios, 0, 1, and, 2, respectively. Chloride penetration testing was done on freshly cut specimens sprayed with a solution of 0.3 M $AgNO_3$.

The results of the chloride penetration tests showed an increase in chloride penetration depth with an increase in ash to cement ratio and increase over time. The use of surface treatment agents proved effective with a decrease of over 80% achieve for the chloride penetration depth for the worst performing specimen at the end of the experiment. The corrosion assessment specimens underwent severe cracking before the start of testing. This complicated the assessment of the efficiency of surface treatment agents in preventing corrosion or reducing the corrosion rates for Series 2.

For Series 3 corrosion assessment of singly reinforced rectangular specimens of dimension 660x150x150 mm with cover depth 69 mm produced with 1200 kg/m^3, 1400 kg/m^3, and, 1600 kg/m^3 was performed over a period of 21 weeks. Similar to Series 3 the efficacy of surface treatment was also evaluated. Untreated specimens generally have the highest corrosion rates, with the non-integral treated specimens generally experiencing the lowest corrosion rates.

LWFC can be reinforced with steel for structural application. However, the material has a relatively low elastic modulus which will result in greater deflections for structural elements and will initiate cracking earlier during loading compared to NWC. The design of structural elements for R/LWFC may be governed by SLS.

Acknowledgements

I wish to express my thanks and gratitude to all who have played a role in my life and work.

To my mom and sister, Astrid “Astrido” van Rooyen and Nicole Fortune thank you for your love and support. We have had great conversations, now we can live again.

To Prof Gideon van Zijl, honestly you are the one who has set me on this journey. Without your encouragement, this project would never have happened. Thank you for guidance I have learnt a lot and will continue to learn from you. You are without a doubt my role model.

To my students, JP de Villiers (Petri), MS Mubatapasango (Marlinto), AR Zvinokona (Admire), TPA Dunn (Trevor) thank you for your hard work. It has been a great pleasure guiding you through your studies. Your work has contributed tremendously to my research. Thank you Jasmin Grafe.

Thank you to Aurecon, The Concrete Institute (TCI), and the National Research Foundation (NRF) for your financial support.

Thank you to PPC, Mapei, Larfarge, Ulula and Ash Resource for their kind donations of materials.

Finally, to Grasshopper, I will never forget the significant impact you have made in my life – To infinity and beyond!

Contents

Table of Figures

List of Tables

List of symbols and abbreviations

A – Contact area [mm^2]

a – Steel rib width [mm]

A_{bar} – Cross-sectional area of the rebar [mm^2]

A_b – Representative rib contact area on which v_b acts [mm^2]

A_c – Area of crack plane [mm^2]

A_s – Representative shear contact area on which v_s acts [mm^2]

a/c – ash to cement ratio w.r.t. weight

b – Outer steel bar diameter [mm]

BE – Beam-end

c – steel rib centre spacing [mm[

cm – The smaller length between the bottom cover and half the clear spacing between the bars [mm]

c_M – The larger length between the bottom cover and half the clear spacing between the bars [mm]

c_{clear} – The clear distance between the ribs of the steel reinforcement [mm]

d – Outer rib spacing of the steel rebar [mm]

E_c – Elastic modulus of the concrete [GPa]

E_s – Elastic modulus of the steel [GPa]

e – Rib spacing [mm]

F – Force [N]

F_h – Horizontal crack opening force [N]

F_v – Vertically applied force [N]

f – Rib inclination in degrees

f_{cu} – Mean concrete cube compressive strength [MPa]

f_{ct} – Mean concrete split cylinder tensile strength [MPa]

f_{ctd} – Characteristic design tensile strength [MPa]

f_r – Relative rib area [mm^2]

f_t – Mean cube tensile splitting strength [MPa]

G_f – Specific fracture energy [N/m]

GFR – Glass fibre reinforcement

h – Rib height [mm]

ILWC – Infra Lightweight Concrete

jd – Lever arm of the embedded rebar within a structural member [mm]

k – Cementing efficiency factor

L – Debonded length [mm]

l_c – Characteristic length [mm]

l_d – Development length [mm]

l_e – Embedment length [mm]

LWAC – Lightweight Aggregate Concrete

LWFC – Lightweight Foam Concrete

LVDT – Linear Variable Displacement Tranducer

NWC – Normal weight concrete

OPC – Ordinary Portland Cement

PC – Portland Cement

PF-LWFC – Polystyrene Foam Lightweight Concrete

PO – Pull-out

RD_a – Relative density of fly-ash

RD_c – Relative density of cement

RD_f – Relative density of foam

S – Embedded rebar slip [mm]

S_d – Design free-end bar slip (taken as 0.1mm) [mm]

S_f – Free-end bar slip [mm]

S_l – Loaded-end bar slip [mm]

S_{PR} – Projected area of the ribs of the steel reinforcement bar [mm^2]

S_1 – First characteristic slip value [mm]

S_2 – Second characteristic slip value [mm]

S_3 – Third characteristic slip value [mm]

T – Tensile force in a reinforcing steel bar [N]

T_b – Bond force in reinforcing steel bar [N]

T_d – Bond force in reinforcing steel bar at the design point [N]

V – Shear force over the cross-section [N]

V_f – Volume of foam [l]

v_a – Adhesion stress between the concrete and steel reinforcement [MPa]

v_b – Bearing stress at the steel rib concrete interface [MPa]

v_s – Shear stress at the bond interface [MPa]

w_p – Pull-out failure weight factor

w_s – Splitting failure weight factor

W/C – Effective water to cement ratio

w/c – Water to cement ratio

w/a – Water to ash ratio

x – Distance along the embedded rebar [mm]

x_c – Cement content in LWFC [kg/m^3]

Greek symbols

α – Regression constant of bond slip model

α_b – Binder ratio

α_{ct} – Coefficient for the long term effects on tensile strength

β – Bond stress ratio

δ_b – Bar elongation / shortening [mm]

ε – The strain in reinforcement [-]

ε_{sy} – The yield strain of reinforcement [-]

ε_0 – Strain corresponding to 33% of the ultimate strain

ε_1 – Strain corresponding to 40% of the ultimate strain

φ – Steel reinforcing nominal bar diameter [mm]

γ_c – Partial safety factor of concrete

η_1 - Bond condition factor

η_2 – Bar size factor

μ - Ratio of the design bond stresses obtained from the beam-end tests to the pull-out tests

μ_{12} – Factor for simulating change in ratio μ observed for beam-end testing of Y12 bars

μ_{20} - Factor for simulating change in ratio μ observed for beam-end testing of Y20 bars

ρ – Casting density of LWFC [kg/m^3]

ρ_{dry} – Oven dry density [kg/m^3]

ρ_{LWAC} – Density of LWAC [kg/m^3]

ρ_t – Target density of LWFC [kg/m^3]

σ_b – Bond stress of embedded bar [MPa]

σ_{bavg} – Average uniform bond stress across the embedded length [MPa]

σ_{bmax} – Peak bond stress [MPa]

σ_d – Design bond stress [MPa]

σ_f – The residual bond capacity [MPa]

σ_s – Tensile stress in the embedded reinforcement [MPa]

σ_0 – Stress corresponding to 33% of the ultimate strength [MPa]

σ_1 – Stress corresponding to 40% of the ultimate strength [MPa]

Chapter 1 - **Introduction**

The chapter provides a brief overview of the details for the study undertaken on foamed concrete. The motivation and problem statement are discussed along with the scope and limitation of the study. Lastly a layout of the dissertation is presented

1.1. Background / Motivation

Foamed concrete (FC) is a type of lightweight concrete that consists only of cement, filler, water and 20 % air or more by volume. FC has several advantages over normal weight concrete (NWC). These advantages, as discussed by various authors (Kearsley and Wainwright (2002), Narayanan and Ramamurthy (2000), Nambiar and Ramamurthy (2008)), include reduced weight, lower coefficient of thermal conductivity, better flow ability and the fact that it can be designed to contain high percentages of industrial waste (i.e. fly ash and ground granulated blastfurnace slag). FC can be designed to have in a density range of 400 to 1600 kg/m^3, is self-levelling, requires little to no vibration, and can incorporate up to 75% waste material in its mix design. However, as pointed out by Panesar (2013), due to the high percentage of air in the concrete, several disadvantages may arise, including low strength and elastic modulus, and of particular concern, durability. Another disadvantage is high shrinkage (Nambiar and Ramamurthy (2009)). These disadvantages are preventing the use of cast in-situ FC for structural application. Normally FC has low compressive strength values (1 to 10 MPa (Neville (1998)). Jones and McCarthy (2005) argued that unless FC can be designed to achieve compressive strength values greater than 25 MPa that concrete mix designers are unlikely to give FC any serious attention. Jones and McCarthy therefore attempted to address some of the durability issues and early age engineering properties of FC and concluded that FC is indeed a viable alternative to NWC but should not just be used to replace it based on strength.

Despite research being conducted on FC, the concrete is still not being used regularly in construction as an alternative to NWC. This is due to the fact that designers are not familiar with FC. Also, limited studies are available on FC durability. Durability of concrete, against chemical attacks such as chloride ingress and carbonation, is affected by the transport properties of the concrete. Various tests have been proposed and used to characterise the transport properties of concrete. Tests to determine the depth of carbonation can also be done. Carbonation is a special type of chemical attack in the sense that it reduces the pH levels of the concrete and in-turn promotes the corrosion of steel reinforcement in the concrete. If the concrete is not reinforced carbonation is not a concern.

Nambiar and Ramamurthy (2007) investigated the water sorptivity of FC and found that the water sorptivity decreases with a decrease in density. The results therefore suggest that FC with lower densities will be more durable than with higher FC densities. However while investigating the effect of synthetic and protein foaming agents on FC, Panesar (2013) found that for the same concrete density the synthetic

foaming agents gave a higher water sorptivity than natural protein based foaming agent. This result suggests that synthetic foaming agents produce connected air voids in FC. Jones and McCarthy (2005) performed accelerated durability tests on FC beams subjected and found that the depth of carbonation after 14 weeks was 23 mm, this suggests that if steel reinforcement were placed below 23 mm inside the concrete then steel corrosion would have initiated.

Two approaches, indirect and direct, exist to address durability in concrete. In the indirect approach the restrictions are placed on the cement content, water cement ratio and cover depth of the concrete to ensure durability and in the direct method the transport properties such as permeability is specified by the engineer and the designer designs a suitable mix to meet the durability criteria. Under the direct approach one can also alter the surface properties of the concrete. This can be done with the aid of surface treatment agents (STAs).

Surface treatment agents (STAs) are chemicals that alter the surface of the concrete. These agents can be classified into three groups based on their method of action (Medeiros and Helene (2009), Johansson-Selander et al. (2010)). The first group's method of action is coating, whereby the concrete is coated with paint or an impermeable membrane is used. In the second group the mode of action is to block the pores "pore blockers" in the concrete. For example, Sandrolini et al (2013) use ethyl silicate for surface treatment in concrete. Ethyl silicate reacts with some of the products of the concrete and produces C-H-S (calcium silicate hydrate) which densifies and improves the strength of the surface. In the third group the agents penetrate the cement matrix and line the pores. The agent is hydrophobic and therefore repels water preventing penetration. In this group silane based chemicals are normally used as water repellent agents (Franzoni et al (2013), Dai et al (2010)). These chemicals can therefore be used to improve the durability by preventing or delaying fluid penetration which leads to initiation of corrosion.

In summary, FC is a highly porous concrete which makes the concrete susceptible to fluid ingress. STAs are a group of chemicals used to alter the surface of concrete. It is therefore proposed to investigate the use of surface treatment agents, namely pore blockers and pore-liners to enhance the durability of FC.

1.2. Problem statement

FC by design contains high volume percentages of air in its fresh and hardened state. These high volume percentages of air are what predominantly control the properties of LWFC. In large part FC has been used for non-structural applications, due to its low mechanical strength, whereby it is not necessary to consider nor determine the mechanical properties (compressive and tensile strength, elastic modulus, bond behaviour) or durability properties (chloride and carbonation resistance) that lead to structural failure. However the utilisation of advances in foaming materials (foaming agents forming well-dispersed smaller voids) and high volume percentages of industrial waste as mix constituents have led to higher mechanical strength and subsequently renewed interest in the structural properties of FC. Therefore in order to advance FC as a durable structural material the mechanical and durability properties have to be investigated and characterised.

1.3 Aims and Objectives

The aim of the research project is to advance R/LWFC as a durable structural material. The objectives are to (i) determine and characterise the mechanical properties (compressive-, tensile strength, elastic modulus, and fracture energy), (ii) address the lack of information on key design information by determining and characterising the bond properties of FC, and, (iii) address the lack of information on durability of FC by determining the resistance of FC against carbonation- and chloride-induced corrosion. A comprehensive laboratory investigation is designed and executed by the author, complemented by research students his supervision, to achieve these objectives.

1.4 Scope and limitation

The scope of the dissertation is limited to the mechanical and durability properties of FC designed with target densities between 1200 and 1600 kg/m^3. Literature presented in Chapter 2 shows in this range LWFC can achieve high (> 25 MPa) compressive strengths sufficient for structural application depending on the materials used in the mix design. For the mechanical properties of FC, namely compressive and tensile strength testing, verification of trends existing in the current body of literature is confirmed. Structural bond between reinforcing steel is determined using pull out tests and the modified ASTM beam end tests methods identified from the literature as suitable and identified as key missing design information needed for structural advancement of LWFC. The durability testing is geared towards corrosion monitoring caused by accelerated tests to fit within the timescales of this research. This is limited to accelerated chloride and carbon dioxide penetration, chloride- and carbonation-induced corrosion respectively. A suitable corrosion mitigating strategy, i.e. the use of STAs, was identified from literature and is implemented to enhance the durability properties of FC is restricted to a two products based on their method of action.

1.5 Dissertation layout

The layout of the dissertation is influenced by the motivation of the study. A thorough understanding of the mechanical and durability properties of FC is what is sought after. The dissertation is therefore structured in such a way to relay the relevant knowledge to the reader for the document to make sense. In the introductory chapter, Chapter 1, the background and motivation of the study is given along with the scope and limitation. Chapter 2 presents the literature survey on the main topics covered in the dissertation. The chapter contains a brief overview of FC followed by the background theory of mechanical bond between concrete and steel. This is followed by information on durability properties and corrosion assessment. The relevant theories of corrosion assessment are also presented. Chapter 3 is dedicated to the methodology of the research. Included in Chapter 3 is a detailed account of the experimental design and the tests conducted. Chapter 4 and Chapter 5 provides the results using appropriate data representation techniques. The dissertation then concludes with Chapter 6 which provides the conclusions and recommendations based on the research presented in the preceding chapters. Appendices A to C present detailed, complete sets of results of the X-ray nano-CT tests

reported in Section 5.2.2 and 5.3.2, restrained shrinkage cracking in steel-reinforced LWFC specimens as reported in Section 5.3.5, and corrosion potential and corrosion rate readings reported in Sections 5.3.6.1 and 5.3.6.2.

1.6 References

Dai, JG et al.(2010). Water repellent surface impregnation for extension of service life of reinforced concrete structures in marine environments: The role of cracks. Cement and Concrete Composites. Vol. 32(2). pp. 101-109.

Franzoni, E., Pigino, B. and Pistolesi, C. (2013). Ethyl silicate for surface protection of concrete: Performance in comparison with other inorganic surface treatments. Cement and Concrete Composites. 44. pp. 69-76.

Johansson-Selander, A., Janz, M., Slifwerbrand, J., and Trägárdh. (2010). Penetration profiles of water repellent agents in concrete as a function of time – Determined with FTIR-Spectroscopy. International Journal Nordic Concrete Research. Vol 41(1), pp. 51-61.

Jones, M.R. and McCarthy, A. (2005). Preliminary views on the potential of foamed concrete as a structural material. Magazine of Concrete Research 57.1, pp. 21-31.

Kearsley, E.P. and Wainwright, P.J. (2002). Ash content for optimum strength of foamed concrete. Cement and Concrete Research 31. pp. 241-246.

Medeiros, M.H.F. and Helene, P. (2009). Surface treatment of reinforced concrete in marine environments: Influence on chloride diffusion coefficient and capillary water absorption. Construction and Building Materials. 23(3). pp. 1476-1484.

Nambiar, E.K.K. and Ramamurthy, K. (2009). Shrinkage behaviour of foam concrete. Journal of Materials in Civil Engineering. 21(11). pp. 631-636

Nambiar, E.K.K. and Ramamurthy, K. (2008). Fresh state characteristics of foam concrete. Journal of Advanced Concrete Technology. 20(2). pp. 111-117.

Narayanan, N. and Ramamurthy, K. (2000). Structure and properties of aerated concrete: A review. Cement and Concrete Composites. Vol. 22(5), pp. 321-329.

Neville, A.M. (1988). Properties of Concrete. 4th Edition. Longman Scientific and Technical, Harlow.

Panesar, D.K. (2013). Cellular concrete properties and the effect of synthetic and protein foaming agents. Construction and Building Materials. 44. pp. 575-584.

Sandrolini, F. et al. (2012). Ethyl silicate for surface treatment of concrete - Part 1: Pozzolanic effect of ethyl silicate. Cement and Concrete Composites. 34(3). pp. 306-312.

Chapter 2 – **Literature Review**

The chapter begins with a brief overview of foam concrete. The mix design principles are discussed along with the mechanical and durability properties of the concrete. Background information of bond behaviour in reinforced concrete and durability assessment is also presented.

2.1. Introduction

Lightweight foam concrete (LWFC), created by the inclusion of air via foam and the exclusion of coarse aggregate in the traditional concrete mix, has been around for decades. The material has a superior thermal performance relative to its normal weight counterpart is what makes it an attractive alternative. Despite other benefits such as low self-weight, low raw material usage, and being environmentally friendly, the material's usage has been restricted to non-structural applications which include backfill, sound and thermal insulation and void filling. This restriction could be attributed to the low mechanical properties and elastic modulus at inception of LWFC. Regardless, over the decades advances in foaming technology and inclusion of waste and nano-materials have brought about better mechanical properties which opens up different avenues of investigation for the material. These enhanced mechanical properties have shifted the focus of the material's application from non-structural to structural. However, to fully realise the structural application potential of LWFC a few key issues such as bond between the concrete and reinforcing steel have to be investigated alongside durability concerns such as carbonation and chloride induced corrosion reinforced in LWFC. In the following sections, the state-of-the-art of FC is complemented by knowledge of the mechanics and durability of concrete, lightweight aerated concrete and lightweight aggregate concrete from literature. This information borrowed from other cement-based composites, is consider to form a relevant basis for the design of an experimental programme to characterise the mechanics and durability of structural foamed concrete.

2.2. Lightweight Foam Concrete (LWFC)

2.2.1 Mix design and formulation of LWFC

Various approaches to the mix design of foam concrete (FC) have been presented. Perhaps one of the most notable mix design formulations is that presented by Kearsley and Mostert (2005). This mix design formulation builds on the principles of foam stability and conservation of mass. For foam stability in the fresh state of the concrete mix the water demand of the mix must be satisfied. Stated differently the water in the mix must be sufficient so that water is not drawn from the foam resulting in foam destabilisation. Kearsley and Mostert noted this and developed an approach to determine the water demand of the mix constituents using an adapted version of the ASTM turntable for hydraulic cements (ASTM C230/C230M-14). Nambiar and Ramamurthy (2006) had a similar observation, however, they added water to the base mix slurry followed by foam until no visual breakdown of the foam was

observed. Assuming no chemical interaction between the base mix and the foam, these two approaches are more or less the same. In this section the base mix is discussed.

2.2.1.1 Base mix

The base mix of LWFC consists of water, cement and filler. Generally, fly ash (graded or ungraded) is the preferred choice of filler because it is a waste product that can be used in large volume quantities, contributes to the long-term strength development (Kearsley and Wainwright (2001)), and decreases the drying shrinkage (Bing et al. (2012), Jones and McCarthy (2005)). Other fillers include sand (Kunhanandan Nambiar and Ramamurthy (2006)) and stone (Panesar (2013)). Regardless of the composition of the base mix the main obstacle in designing LWFC is the determination of the water demand of the mix to achieve foam stability. The composition of the base mix is what determines the water demand, foam stability and to some degree the compressive strength of LWFC.

The water demand of the mix is the total amount of water needed in the mix to produce a density ratio of 1. The density ratio is defined as the ratio of design target density and the casting density. The design target density is the theoretical density of the mix constituents and the casting density is the density of LWFC in the fresh or plastic state. Kearsley and Mostert (2005) used the ASTM hydraulic turntable test on cement paste and cement fly ash paste base mixes to determine the water demand of each mix constituent. They found that base mixes that achieved spreadability values in the range of 220 to 250 mm produced stable FC. This result indicates that there is a set range of acceptable water to constituent ratios required to produce FC. Figure 2.1 depicts the water demand for cement and fly-ash.

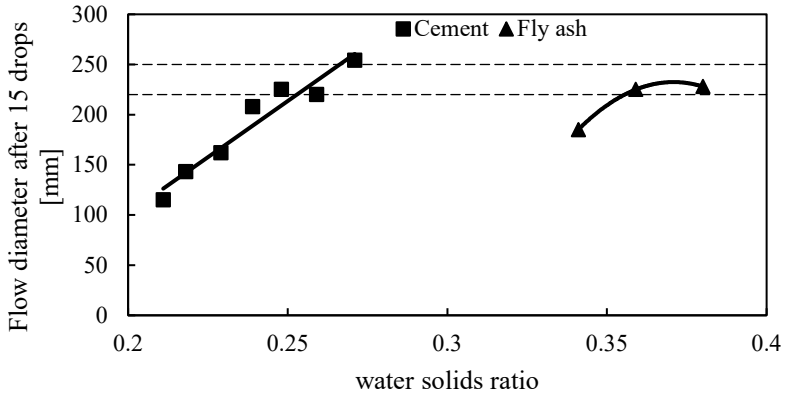

Figure 2.1: Flow diameter after 15 drops versus water a solids ratio (reproduced from Kearsley and Mostert (2005))

Nambiar and Ramamurthy (2006) made a similar observation about the water demand of the base mix. They investigated the influence of filler type (fine and coarse sand and fly ash) on the properties of FC. This included the effect of the consistency of the mix, design density, density ratio and the strength of the concrete. They found that the water solids ratio varied with the composition of the base mix and marginally increased with a decrease in design density, illustrated in Figure 2.2a. This marginal increase in the water solids ratio reinforces the idea that a band of water solids ratio exist for which stable FC

can be produce. A reason for this is that for the same base mix composition the surface area to water ratio required to "wet" the mix constituents remains the same regardless of the volume of the mix. Figure 2.2b and Figure 2.2c illustrates the plot of density ratio versus water solids ratio for 1000 and 1500 kg/m^3 design density mixes, respectively. The results indicate that there exist only a particular water solids ratio that corresponds to a density ratio of 1 for the various mix compositions shown.

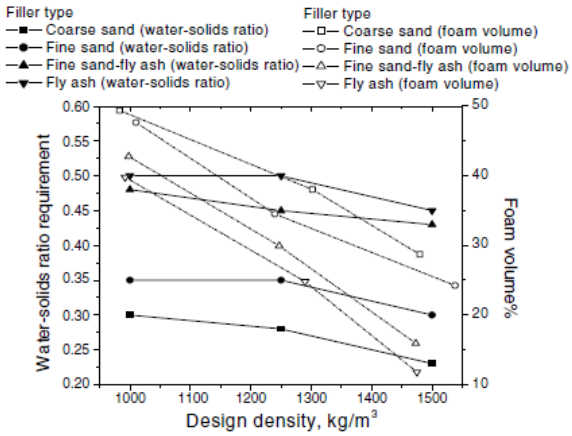

(a)

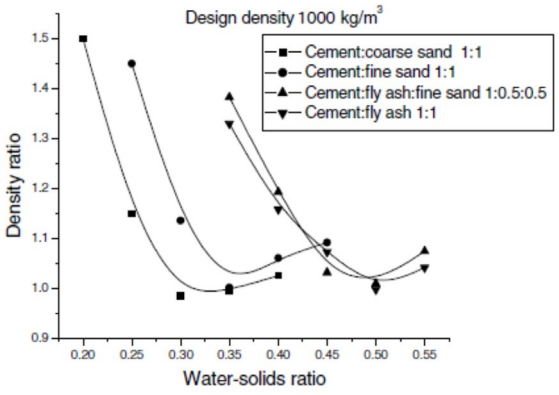

(b)

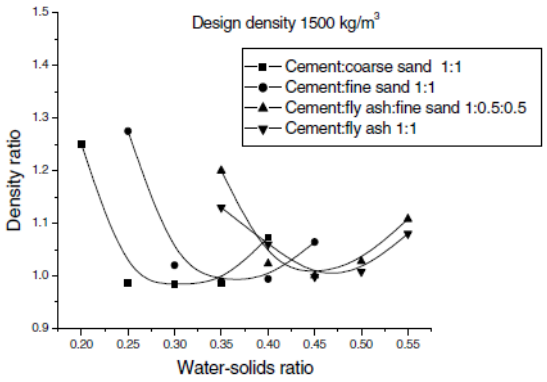

(c)

Figure 2.2: (a) Consistency requirement of water solids ratio, (b) density ratio versus water solids ratio for design density of 1000 kg/m^3 , and (c) desity ratio versus water solids ratio for design density of 1500 kg/m^3 (Nambiar and Ramamurthy (2006))

2.2.1.2. Mix design equations

The mix design equations of FC can be expressed as two equations, namely Equations 2.1 and 2.2 and can be found in Kearsley and Mostert (2005). Equation 2.1 mathematically describes the total mass of the mix constituents whereas Equation 2.2 describes the total volume of the mass constituents. Setting Equation 2.2 equal to 1000 litres lets Equation 2.1 also represent the density of the concrete mix design.

$$m_{tot} = \rho_m = x + x\left(\frac{w}{c}\right) + x\left(\frac{a}{c}\right) + x\left(\frac{a}{c}\right)\left(\frac{w}{a}\right) + RD_f V_f \qquad (2.1)$$

$$V_{tot} = 1000 = \left(\frac{x}{\mathrm{RD}_c}\right) + x\left(\frac{w}{c}\right) + \left(\frac{x\left(\frac{w}{c}\right)}{\mathrm{RD}_a}\right) + x\left(\frac{a}{c}\right)\left(\frac{w}{a}\right) + V_f \quad (2.2)$$

where

m_{tot} is the mass of the mix constituents,

ρ_m is the density of the mix,

V_{tot} is the volume of the mix,

m_{tot} is the mass of the cement,

$\frac{w}{c}$ and $\frac{a}{c}$ is the water cement ratio and fly ash cement ratio,

$\frac{w}{a}$ is the fly ash cement ratio,

V_f is the volume of foam,

RD_c, RD_a, and RD_f, is the relative density of the cement, ash, and foam.

The factor $\frac{a}{c}$ refers to the fly ash cement ratio chosen by the mix designer and $\frac{w}{c}$ and $\frac{w}{a}$ is the water cement ratio and water fly ash ratio determined using the hydraulic turntable test based on foam stability principles.

2.2.2 Mechanical properties of FC

2.2.2.1 Compressive strength (f_{cu}) of FC

One of the criteria used to classify a concrete mix as acceptable is compressive strength. For NWC this is almost entirely controlled by the $\frac{w}{c}$ ratio provided that the concrete is fully compacted. This relationship was proposed by Abrams in the early 1900s which is as stated by numerous researchers as a special case of Ferets' law. Ferets' law, Equation 2.3, states that the compressive strength of the concrete is inversely proportional to the square of the ratio of cement volume to the cement, water and air volume in the concrete mix.

$$f_{cu} = K\left[\frac{c}{c+w+a}\right]^2 \quad (2.3)$$

Where f_{cu} is the compressive strength; K is a constant and c, w and a is the volume of the cement, water and air.

In addition to the mix proportions the type of cement also contributes to the strength of the concrete. For instance, for the same water cement ratio, a higher grade of cement would produce a higher compressive strength. In the case of air, the higher the air content of the concrete mix the lower the compressive strength. Studies have shown that the inclusion of air at low percentages (2-5%) improve the workability and durability (freeze-thaw cycles) of concrete but can significantly decrease the compressive strength. The very definition of FC calls for the inclusion of a large volume percentage (10

– 70% Panesar (2010), 20% or more van Rooyen et al 2013)) of air introduced as foam into the concrete. The inclusion of air reduces the density, making it lightweight, and also increases the porosity of the concrete. The compressive strength of FC is a function of density and hence the porosity of the concrete. Hoff (1972), Equation 2.5, used Balshins' model, shown in Equation 2.4, to predict the compressive strength of neat LWFC based on the theoretical porosity. An extension of this model, shown in Equation 2.6, was later presented by Kunhanandan Nambiar and Ramamurthy (2008b) which made provision for the addition of sand.

$$f_{cu} = \sigma_o(1-n)^b \quad \text{Balshin} \quad (2.4)$$

$$f_{cu} = \sigma_o\left[\frac{\rho_m}{\left(1+\frac{w}{c}\right)}\right]^b \left[\frac{1+0.2RD_c}{\gamma_w RD_c}\right]^b \quad \text{Hoff} \quad (2.5)$$

$$f_{cu} = \sigma_o\left[\frac{\rho_m}{\left(1+\frac{w}{s}\right)}\right]^b \left[\frac{1+0.2RD_c+s_v}{(1+s_v)\gamma_w RD_c}\right]^b \quad \text{Nambiar and Ramamurthy} \quad (2.6)$$

where; σ_o is the strength at zero porosity, n is the porosity of the concrete, b is a constant, $\frac{w}{s}$ is the water solids ratio, and γ_w is the unit weight of water.

Currently, for the strength prediction of FC there exist only one model that incorporates the time parameter. That is the model proposed by Kearsley (1999). The following section presents a review of the model.

2.2.2.1.1 Compressive strength prediction model by Kearsley

In an investigation into the influence of high volume replacement of cement with ungraded and graded fly ash in FC by Kearsley (1999) a model for predicting the compressive strength of FC with target casting density between 1000 and 1500 kg/m^3 was derived. In the investigation Kearsley kept the water binder ratio constant at 0.30, with fly ash (FA) replacement ($\frac{a}{c}$) 0, 1, 2 or 3, and tested the compressive strength for the various densities (1000, 1250, 1500 kg/m^3, and, full density) at ages of 7, 28, 56, 90, 180, 270 and 365 days. The tests were performed on 100 mm cube specimens made of (CEM I 42.5R) PPC, PPC/FA (graded – pfa), or, PPC/FA (ungraded – pozz-fill) and were sealed up until the day of testing. Figure 2.3a,b show the results of the compressive strength evolution over time of the pastes (full density) alongside the fitted function (Equations 2.7 – 2.10). Figure 2.3c-f show the results of the compressive strength evolution over time of the 1500 and 1000 kg/m^3 concrete mixes alongside the fitted functions using Equations 2.10 and 2.14.

$$\frac{W}{C}\left(\frac{w}{c};k;\frac{a}{c}\right) = \frac{w}{c}\left[\frac{1}{\left(1+k\left(\frac{a}{c}\right)\right)}\right] \quad (2.7)$$

$$k\left(t;\frac{a}{c}\right) = \left(0.457 + \frac{0.00315t}{\left(\frac{a}{c}+1\right)}\right)^2 \tag{2.8}$$

$$f_c\left(t;\frac{W}{C}\right) = 88.04 + 6.569ln(t) - 130.5\frac{W}{C} \tag{2.9}$$

$$f_{cu} = 1.172 f_c \alpha_b^{3.7} \tag{2.10}$$

Where $\frac{W}{C}$ as the effective water cement ratio (based on the work by Smith (1967)),

$\frac{w}{c}$ as the actual water cement ratio,

k as the cementing efficiency (0.21 at 7 days, 0.55-1.11 between 7-365 days, 1.1 after 365 days),

t as the time elapsed since casting,

α_b as the binder ratio,

f_c as the cube compressive strength.

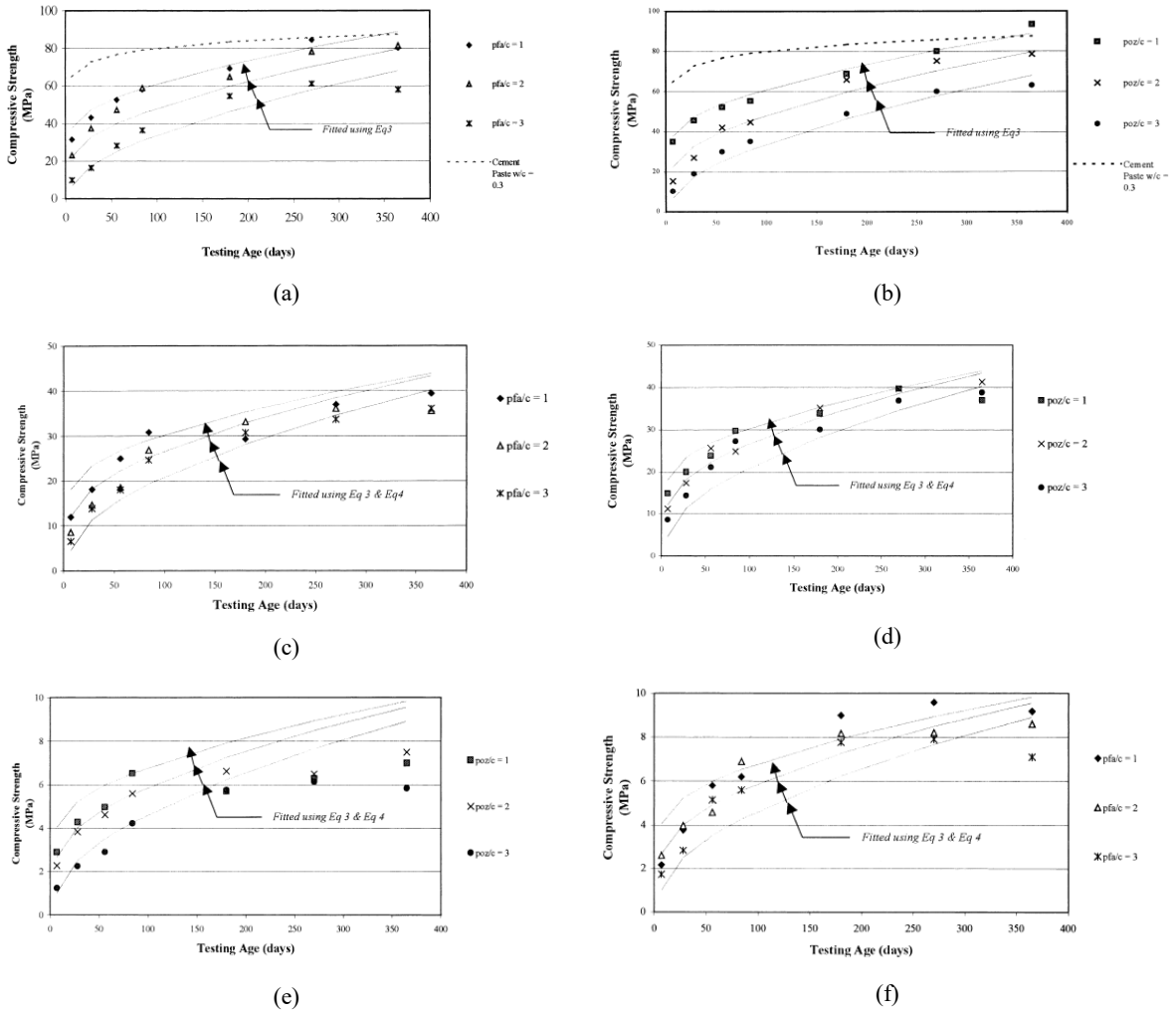

Figure 2.3: Compressive strength as a function of time (a) paste pozz-fill mixes, (b) paste pfa mixes, (c) 1500 kg/m^3 pozz-fill mixes, (d) 1500 kg/m^3 pfa mixes, (e) 1000 kg/m^3 pozz-fill mixes, and (f) 1000 kg/m^3 pfa mixes (Kearsley and Wainwright (2001))

Equation 2.14 can be used to predict the strength of FC up to a year as proposed by Kearsley (1999). The model fits the data with an R^2 value of 96.3% therefore indicating a high degree of confidence in the predicted values. Analysing the compressive strength results and the predicted results from the model it can be shown that the 1 year compressive strength of FC may be double that of the 28 day strength. There is also a steeper gradient present for long-term strength development of FC with FA replacement (ungraded and graded) compared to the plain cement mixes. Also, it can be concluded from the trend in the data that the strengths of mixes made with FA surpass that of just the plain cement mixes, it therefore appears to be beneficial to replace cement with FA in FC. The results of ungraded and graded FA have insignificant differences and therefore cost can be saved by using ungraded FA.

2.2.2.1.2 Compressive strength model by Kearsley based on porosity

Kearsley and Wainwright (2002) used the relationship developed by Balshin for porosity-strength considerations to present a model for FC based on porosity. Balshin proposed that the strength of concrete can be captured by a multiplicative model using an absolute zero porosity parameter multiplied by the unit volume of the material; see Equation 2.4 reproduced here for convenience as Equation 2.11. The theoretical porosity, n, can be estimated using Equation 2.12. Substituting Equation 2.12 into Equation 2.11 leads to the extended model form by Hoff, Equation 2.5 repeated here as Equation 2.13 for convenience. Whereas the original relationship proposed by Balshin only made provision for water and cement, the extended form can be used for all mix constituents.

$$f_{cu} = \sigma_o(1-n)^b \tag{2.11}$$

$$n = 1-(1+0.2\rho_c) \tag{2.12}$$

$$n = \frac{1-(\rho_m)(1+0.2\rho_c)}{\gamma_w \rho_c (1+k)}$$

$$f_{cu} = \sigma_o \left[\frac{\rho_m}{\left(1+\frac{w}{c}\right)}\right]^b \left[\frac{1+0.2RD_c}{\gamma_w RD_c}\right]^b \tag{2.13}$$

Kearsley and Wainwright (2002) used the results of a previous study (Kearsley (1999)) and performed a linear regression analysis to determine the constant σ_o and power b. Kearsley and Wainwright obtained a value of 321 MPa for σ_o and 3.6 for b. However, they used the matured 1 year porosity of the concrete whereas previous models have made use of the 28 day porosity and assume it stayed constant. For FC based on the values of the compressive strength it is safe to assume that the porosity is a function of time and not constant. A solution is found by presenting the σ_o as a function of time, based on the result of a previous study also conducted by Kearsley and Wainwright (2001b). The final model based on porosity as proposed by Kearsley and Wainwright (2002) is given as Equation 2.14.

$$f_c = 39.6[ln(t)]^{1.174}(1-p)^{3.6} \quad (2.14)$$

The model proposed by Kearsley and Wainwright (2002) fits the data shown in Figure 2.4 with an R^2 value of 89.6 % and a correlation coefficient of 0.946 which indicates a strong relationship between the variables. Figure 2.4 shows a plot of the measured compressive strength versus the predicted strength as obtained from the model.

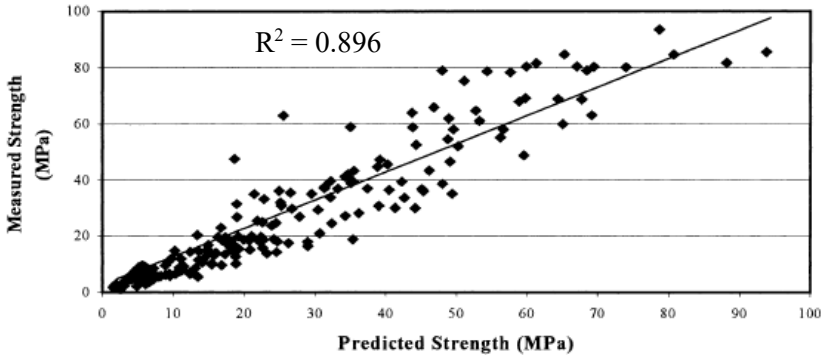

Figure 2.4: Measured strength versus the predicted strength from Equation 2.14 (Kearsley and Wainwright (2002))

2.2.2.2 Tensile strength (f_t) of foam concrete

Jones and McCarthy (2005) published values of the split tensile strength of FC based on split cylinder tensile strength tests performed in accordance with BS EN 12390-6. Figure 2.5 shows the results obtained by the Jones and McCarthy as a function of the 28 day compressive strength plotted alongside relationships found in literature of NWC by Oluokun (1991) and lightweight aggregate concrete (LWAC) by Federation Internationale de la Precontraine (1983).

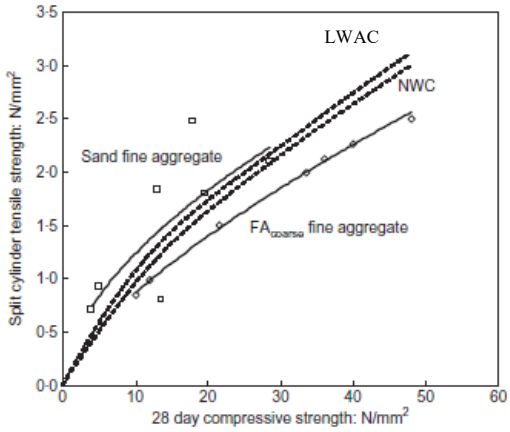

Figure 2.5: Split cylinder tensile strength (f_{ct}) versus corresponding 28 day compressive strength (f_{cu}) of FC, NW[a] and LWAC[b] concretes. (adapted from Jones and McCarthy (2005))
a $f_{ct} = 0.2(fcu)^{0.70}$ by Oluokun (1991)
b $f_{ct} = 0.23(fcu)^{0.67}$ by FIP (1983)

From Figure 2.5 it can be seen that it is possible to produce FC with higher tensile strength values than that of NWC[a] and LWAC[b] for the same corresponding compressive strength. FC produced with sand

obtained higher tensile split strengths than those produced with fly ash. Jones and McCarthy attributed this to the improved shear capacity between the sand and the paste.

2.2.2.3 Elastic modulus (E_c) of foam concrete

In the same study, mentioned earlier, Jones and McCarthy (2005) determined the static modulus of elasticity of FC (E) as set out in BS 1881-121. The results are shown in Figure 2.6a, alongside the NWC (BS 8110) and LWC (BS 8110) equivalent found in literature, as a function of the 28 day compressive strength. Figure 2.6b displays the same results obtained by Jones and McCarthy compared to Addis and Owens (2009) for FC, NWC and LWC calculated from the equations found in BS EN 1992-1-1 (2004).

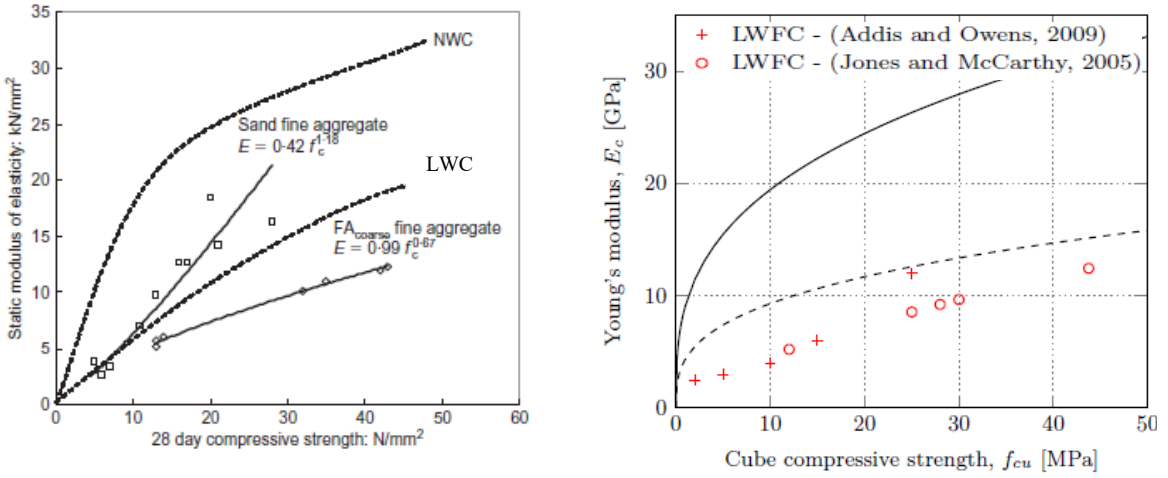

(a) (b)

Figure 2.6: Elastic modulus (E) as a function of 28 day compressive strength for FC, NW and LW concrete (values for NW and LW concretes calculated from equations in BS 8110) (a) Jones and McCarthy (2005), and (b) de Villiers (2015)
a $E = 9.1(f_{cu})^{0.33}$ by BS 8110
b $E = 1.7x10^{-6}(\rho_{dry})^2(f_{cu})^{0.33}$ by BS 8110

From Figure 2.6a,b it can be seen that the elastic modulus (E) of LWAC and FC is lower than the equivalent NWC counterpart. In the case of FC produced with fine sand aggregate, E values may be higher than the corresponding LWAC equivalent. FC produced with fly ash showed the lowest E values. It should be noted that materials with low E values such as LWC have been implemented in building codes (see Chapter 11 of BS EN 1992-1-1 (2004)). Based on this it is possible that FC can one day be used safe and effectively as an alternative material to NWC. However, Jones and McCarthy (2005) concluded from their study that FC cannot just be substituted for NWC based on strength equivalency. Substituting FC based on strength for NWC may lead to serviceability issues due to its lower tensile splitting strength and E.

2.2.2.4 The effect of fibre reinforcement in foam concrete

The addition of fibres in concrete has been around now for several decades. The advantages of fibre addition includes the rheology improvements, tensile strength improvement and crack control. A few of the disadvantages are loss of workability and compressive strength. Kearsley and Mostert (2003) studied

the influence of synthetic fibres in FC on crack formation and impact resistance. They found that the 12 mm polypropylene (PP) fibres positively influenced the post-crack behaviour of LWFC. The PP in the study did not significantly reduce the compressive strength and elastic modulus and did not affect the porosity or sorptivity of FC.

Jones and McCarthy (2005) added PP fibres (19.2 mm) in FC and found that an addition of 0.5% PP fibres (w.r.t. volume), for FC density of 1400 kg/m^3, increased the compressive strength by 52% compared to the reference FC. In the study the compressive, flexural and elasticity modulus were improved by fibre addition. The addition of this type of fibres did however lead to the decrease in workability of LWFC. A suggestion from Jones and McCarthy is to restrict the fibre content to less than 0.5%.

El Zareef and Schlaich (2008) tested the bond behaviour of various types of reinforcement in lightweight concrete (LWC). They made concrete beams with reinforcing steel (RS) and glass fibre reinforcement (GFR). For the various concrete mixes the addition of PP fibres was kept constant at 1 kg/m^3, however, the fibre lengths (6, 12, and, 20 mm) were varied for the investigation. El Zareef and Schlaich reported increases in the tensile strength of the concrete 10%, 23%, and 30% with the increase in PP fibre lengths in relation to the control mix. However, a decrease of 56%, 43%, and 41% respectively was reported in the compressive strength of the concrete with an increase in fibre length. El Zareef and Schlaich suggest that the decrease in compressive is a result of the early micro cracks formed in the concrete matrix triggered by to the inclusion of fibres. Comparing the result of Jones and McCarthy (2005) and El Zareef and Schlaich (2008) a conclusion can be drawn that the use of long PP may result in more desirable properties for LWC.

Byun et al. (n.d.) launched a study into developing structural FC using polymere foam agent and reported on the effect of fibre inclusion. They used 19 mm and 30 mm vinylon fibres and recorded an increase of 97% and 104% in the tensile strength of the concrete. Also, an increase of 30% in the flexural strength of the concrete was reported for the addition of 30 mm vynylon fibres. A drawback of the study is that the authors did not report on the quantity of fibres included in the mix.

2.2.3 Microstructure and durability properties of FC

In this section a definition of the microstructure is given, followed by a brief overview of its evolution. The parameters influencing the microstructure is also discussed and its relation to strength and durability of the concrete.

2.2.3.1 Definition of microstructure

According to Mehta and Monteiro (2006) the microstructure is the type, size, shape, and distribution of phases in a solid constitute. A cross-section of the solid constitute would readily reveal large elements of the microstructure, generally referred to as the macrostructure and is visible with the naked eye. However, finer elements approximate smaller than 200 µm can only be viewed with the aid of a microscope. Therefore, the microstructure is the microscopically magnified portion of the

macrostructure. For concrete, the macrostructure consists out of the cement paste, interfacial transition zone (ITZ), coarse aggregate (normally stone) and entrapped or entrained air. The microstructure consists of the hydrated and anhydrous phases of cement particles, and air voids formed due to cement hydration or entrainment. It has been accepted in literature that the properties of the concrete, mechanical and durability, are largely dependent and attributed to the microstructure.

2.2.3.2 Evolution, origin of voids, and parameters influencing the microstructure

The basic dry materials required for concrete is cement, sand and aggregate. When the dry materials is mixed with water, concrete is formed, and almost immediately cement hydration starts taking place. During this process anhydrous cement particles, typically in the range of 1 to 50 μm, hydrate and begin to form needle shaped crystals called ettringite. A few hours into the hydration process calcium silicate hydrate (C-S-H) and calcium hydroxide (CH) crystals begins to form and starts occupying the space left behind by the dissolving cement particles and water. This process will continue in the presence of sufficient water.

In the microstructure of the well hydrated cement paste the typical phases and their respective volumes are as follows (1) C-S-H about 50 to 60%, (2) CH between 20 and 25%, (3) ettringite between 15 to 20%, and, (4) unhydrated clinker (Mehta and Montero (2006)). The final component of the microstructure is voids. The presence of voids in the microstructure is due to the space between the C-S-H, interlayer space, unfilled space left behind by hydration, capillary pores, and entrapment or entrainment of air. Generally, depending on their size, voids can be classified as micro pores, meso pores, and macro pores. Micro pores are up to 2 nm and includes interlayer space, meso pores range from 2 to 50 nm and includes capillary pores and macro pores are greater than 50 nm and includes entrained and entrapped air. Table 2.1 lists the classification of voids based on their size and provides an indication of its influences on the properties of concrete (Aligizaki (2006)).

The microstructure of concrete changes over time due to the continued chemical reactions within. For instance, the hydration of cement may not be complete and may occur on and off due to the presence of water. It is well known that large particles of cement may take years or even decades to fully hydrate. Thus, the microstructure will continue to evolve as a result of the continued hydration of larger cement particles. Powers (1978) demonstrated through simple calculations and assumptions that the capillary voids in the microstructure is dependent on the water cement ratio and the age of hydration. Assuming full hydration of cement particles Powers showed that the amount of capillary voids increases with an increase in water cement ratio. Also, assuming different degrees of hydration at different ages of hydration, Powers showed that the amount of capillary voids decreases with an increase in the age of hydration. Therefore, the parameters identified as affecting the microstructure of concrete are water cement ratio, age of hydration, cement content, water content, relative humidity and temperature.

Table 2.1: Classification of pore sizes (reproduced from Aligizaki (2006))

IUPAC		Mehta (1986)		Mindness et al. (2002)					
Name	Diameter	Pore type	Size range	Name			Diameter	Role of water	Paste properties
Micropores	Up to 2nm	Inter-particle space between C-S-H sheets	1nm to 3nm	Micropores "inter layer"	Gel pores		Up to 0.5nm	Structural water involved in bonding	Shrinkage, creep at all RH
				Micropores			0.5nm to 2.5nm	Strongly absorbed water; no menisci form	Shrinkage, creep at all RH
Mesopores	2nm to 50nm			Small (gel) capillaries		Capillary pores	2.5nm to 10nm	Strong surface tension forces generated	Shrinkage between 50% and 80% RH
		Capillary pores (low w/c)	10nm to 50nm	Medium capillaries	Hollow shell pores		10nm to 50nm	Moderated surface tension forces generated	Strength, permeability, shrinkage at high RH > 80%
Macropores	> 50nm	Capillary pores (high w/c)	3µm to 5µm	Large capillaries			50nm to 10µm	Behaves as bulk water	Strength, permeability
		Entrained voids	50µm to 1mm	Entrained air			0.1mm to 1mm		Strength

2.2.3.3 Microstructural parameters and durability properties of FC

The presence of voids in concrete is unavoidable and in most cases unwanted. In Table 2.1 the influence of voids on the properties of concrete are listed. Micropores are small and is listed as affecting the shrinkage and creep of concrete. Mesopores affect the strength, permeability and shrinkage of concrete. Macropores affect the strength and permeability of concrete. Clearly, based on the research conducted the influence of voids should be interpreted alongside the void size distribution for complete understanding. In this section influence of voids on the durability properties of FC are discussed.

2.2.3.3.1 Microstructural parameter of FC

Depending on composition and density FC contains a large percentage of air voids compared to NC. In NC the voids present in the microstructure are gel and capillary voids and for FC there is the additionally entrained air voids. In order to characterise the microstructure of FC two parameters namely air void diameter size and air void spacing may be used. The air void size distribution of FC maybe determined using microscopic images or other techniques such as scanning electron microscopy (SEM), mercury intrusion porosimetry (MIP), and, computed tomography (CT). The air void spacing may be determined using the distance formula, given as Equation 2.15. A 2D visualisation of the air void spacing is shown in Figure 2.7.

$$S_{1,2} = \sqrt{(x_1 - x_2)^2 + (y_1 - y_2)^2} - R_1 - R_2 \tag{2.15}$$

where $S_{1,2}$ is the minimum direct distance between air-voids, and,

x and y are the coordinates of the centroid of the respective air voids.

R_1 and R_2 are the radii of the respective air-voids

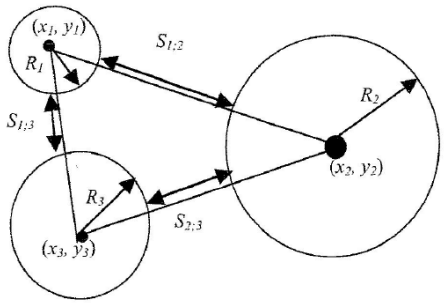

Figure 2.7: Spacing of air-voids (reproduced from Visagie and Kearsley (2000))

Visagie and Kearsley (2000) used microscopic images of FC samples with dry densities between 500 and 1250 kg/m^3 to characterise the microstructure of FC. Visagie and Kearsley obtained the air void diameter size distribution of the FC samples by assuming all voids on the images are perfect spheres and obtained the 10 and 50 % oversized air void diameter (D_{10} and D_{50}) corresponding to the oversize of 10 and 50%, Figure 2.8a,b. Visagie and Kearsley found that the cumulative function for the air void diameter was best described by an exponential fit. Similar calculations were used to determine the 50 and 90 % oversize air void spacing (S_{10} and S_{90}), Figure 2.8c,d.

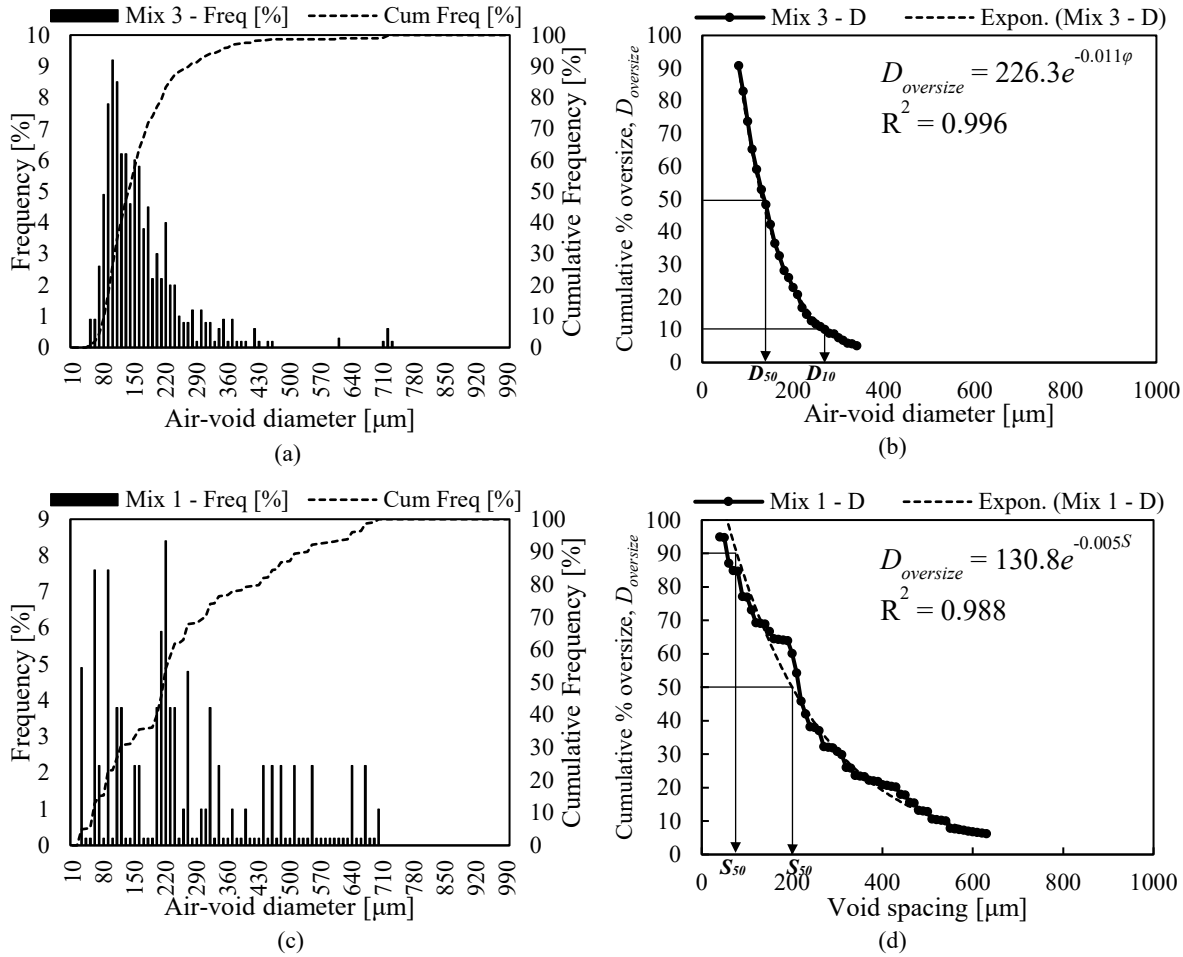

Figure 2.8: Air void (a) diameter size (D) distribution, (b) diameter versus cumulative function (indicating D_{10} and D_{50}), (c) spacing (S) distribution, and, (d) spacing versus cumulative function (indicating S_{50} and S_{90}) (reproduced from Visagie and Kearsley (2000))

Figure 2.9 shows a plot of the air void diameter parameters, and the air void spacing parameters versus the 28 day dry density of FC. The results show that there is a decrease in the air void diameter parameters with an increase in dry density. However, there is no clear trend for FC with dry densities greater than 1000 kg/m^3. For the air void spacing parameters an increase with an increase in dry density observed with clear trend. The results show that lower density FC has larger air voids with smaller distances between air voids compared to higher density FC

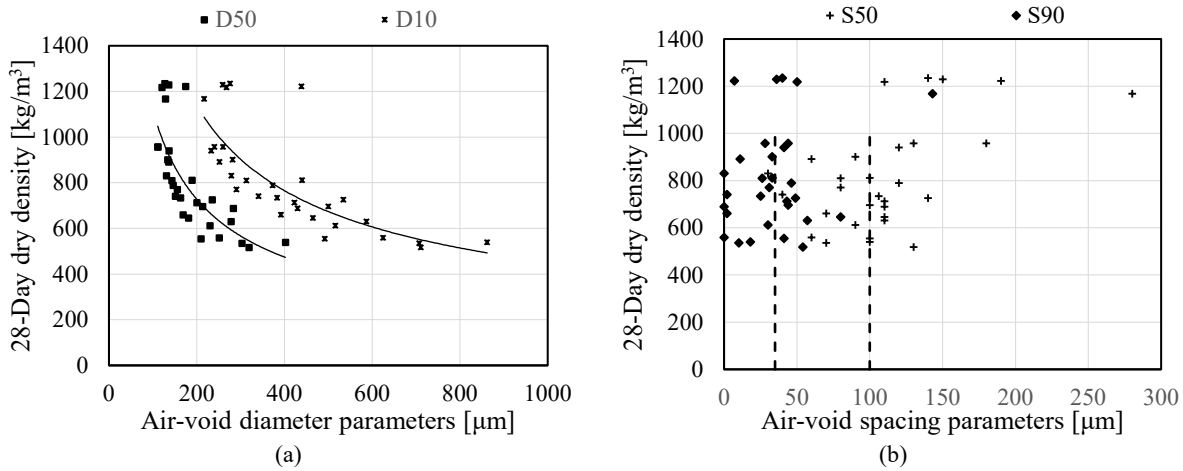

Figure 2.9: Air void (a) diameter parameters, and, (b) spacing parameters versus 28 day dry density of FC (reproduced from Visagie and Kearsley (2000))

Visagie and Kearsley also reported on the influences of the air void parameters on the 28 day compressive strength of FC, shown in Figure 2.10. The results show that the 28 day compressive strength decreases with an increase in the air void diameter parameters for FC specimens with densities lower than 1000 kg/m^3. Visagie and Kearsley also noted that no relationship could be found between the air void spacing parameters and the 28 day compressive strength. Visagie and Kearsley concluded that the compressive strength of FC in the range of 500 and 1000 kg/m^3 is influenced by the air void diameter and therefore could be optimised for a given density for improved compressive strength.

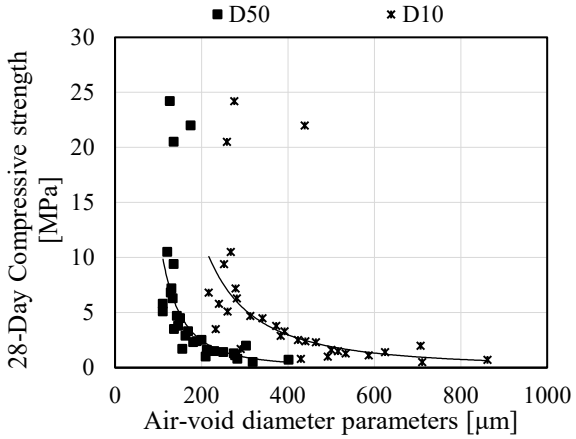

Figure 2.10: Air void diameter parameters versus 28 day compressive strength (reproduced from Visagie and Kearsley (2000)

2.2.3.3.2 Porosity, water absorption, and, water vapour permeability of FC

Porosity is described as the total volume of voids, normally expressed as a percentage, present in a material. For FC the porosity is the sum of the volume of voids in the cement paste and the volume of entrapped and entrained (foam) air (Kearsley and Wainwright (2001), Nambiar and Ramamurthy (2007), Hilal et al. (2014)). Kearsley and Wainwright (2001) used the vacuum saturation apparatus to determine the porosity of FC with target densities of 1000, 1250 and 1500 kg/m^3 made with either cement or cement and graded or ungraded fly ash. Kearsley and Wainwright found that the porosity increases as a result of a decrease in dry density and that the porosity is largely independent of the type and content of fly ash, or the inclusion of foam, shown in Figure 2.11. Hilal et al. (2014) used three different methods, namely (1) MIP - Mercury Intrusion Porosimetry, (2) vacuum saturation method, and, (3) apparent method to determine the porosity of FC with target densities of 1300, 1600 and 1900 kg/m^3. Hilal et al. also found that the porosity increases with a decrease in density and that the vacuum saturation apparatus yielded the largest porosity followed by MIP method, see Table 2.2. The reason for the lower porosity values obtained from the MIP method compared to the vacuum saturated method could be explained by the limitation of the MIP test. The MIP cannot measure pore diameters greater than 400 µm.

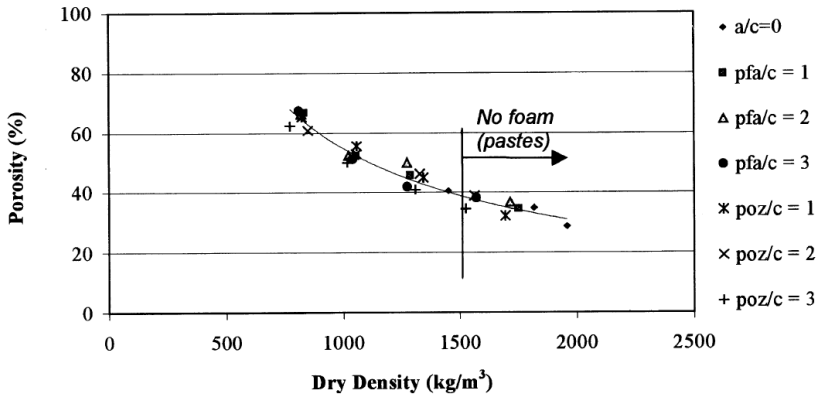

Figure 2.11: Porosity versus dry density (reproduced from Kearsley and Wainwright (2001))

Table 2.2: Measured porosity results (reproduced from Hilal et al.(2014)

Mix	Measured density	Dry density	Foam Content	Porosity [%]		
	[kg/m^3]	[kg/m^3]	[% of Vol.]	Apparent	Vacuum	MIP
FC3	1305	1130	42.4	17.77	51.63	44.84
FC6	1610	1460	29.5	20.23	40.76	36.36
FC9	1890	1785	16.6	20.65	28.73	28.01

In the same study Kearsley and Wainwright also determined the water absorption and water vapour permeability. Kearsley and Wainwright found that when expressing the water absorption as a percentage increase of oven dry density a near linear relationship is found as shown in Figure 2.12a. Interpreting the results from Figure 2.12a leads to the conclusion that lower densities absorb more water than higher densities and therefore higher densities of FC are more durable. However, expressing the water absorption results for FC as a percentage increase of oven dry density is misleading. Alternatively, expressing the results as the increase in mass per unit volume as given in Figure 2.12b shows that the lower densities absorb only marginally more. There are slight differences between the results of the mixes made with fly ash. However, it should be noted that the mix made with only cement and a water cement ratio of 0.6 recorded the highest value for water absorption. Nambiar and Ramamurthy (2007) also determined the water absorption of FC with different aggregate (cement-sand-fly ash) replacement ratios and at different ages (<7, 28, 90 days). Nambiar and Ramamurthy found that the water absorption is greater in cement-fly ash mixes than cement-sand mixes even though the difference is marginal as shown in Figure 2.12c and d. Nambiar and Ramamurthy attributed the marginal difference in water absorption between cement-sand and cement-fly ash mixes to the increased water demand and lower specific gravity of fly ash mixes. FC mixes made with fly ash require more water but less foam to achieve the same density and leads to a higher volume of paste and therefore higher water absorption. Figure 2.12e and f show the water absorption up to 7 days. Reviewing Figure 2.12c-f show that there is an initial increase in the water absorption up to 7 days which is followed by little to no increase up to 90 days.

Figure 2.13a shows a plot of the water vapour permeability as a function of dry density for FC obtained by Kearsley and Wainwright. The water vapour permeability increases with a decrease in dry density. However, it should be noted, water vapour permeability results for FC dry densities greater than 1250 kg/m^3 are approximately the same as the cement paste with water cement ratio of 0.6. Kearsley and Wainwright argue that for this case FC is not necessarily more permeable than the cement paste. The influence of fly ash cement ratio is shown in Figure 2.13b. The results indicate that the water vapour permeability increases with an increase in fly ash cement ratio. This effect is more prominent in lower densities. This result differs from that of the water absorption whereby little to no differences was observed between mixes containing cement only and those containing fly ash. Kearsley and Wainwright postulate that this difference suggest that the transfer mechanism for water vapour permeability is different to that of water absorption. Kearsley and Wainwright argue that the water vapour permeability test may better represent the in service condition of concrete than the water absorption test.

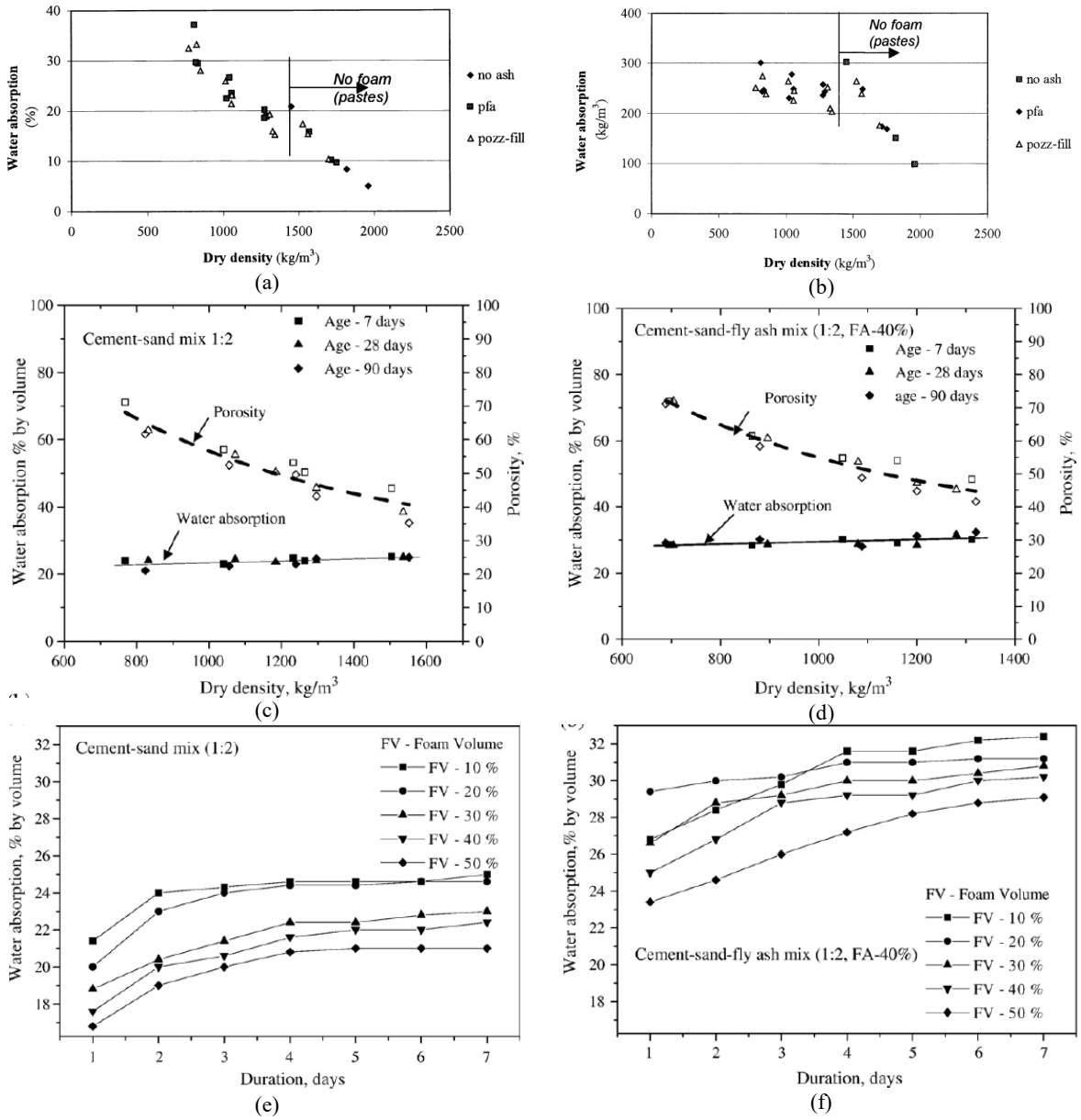

Figure 2.12: Water absorption of FC (a) percentage increase of oven dry mass, and, (b) mass increase per unit volume (reproduced from Kearsley and Wainwright (2001), (c) cement-sand mix, and, (d) cement-sand-fly ash mix (e) cement-sand mix versus duration, and (f) cement-sand-fly ash versus duration (reproduced from Nambiar and Ramamurthy (2007)

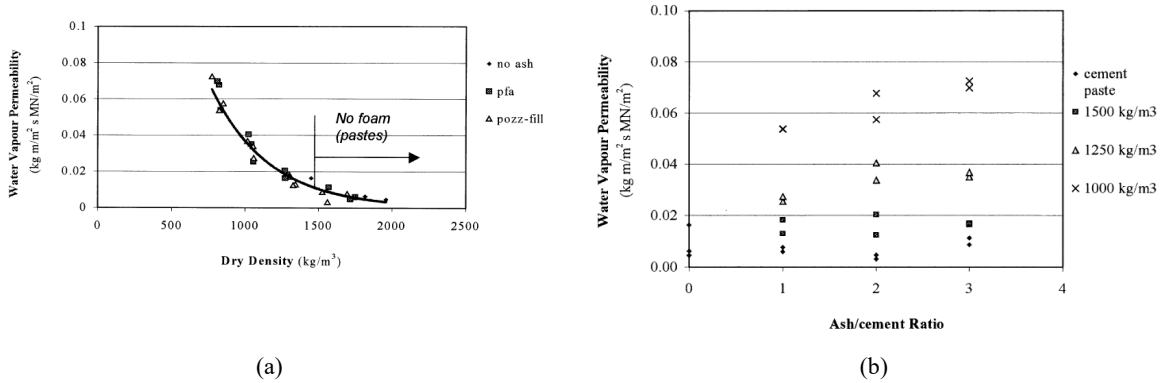

Figure 2.13: Water vapour permeability (a) function of dry density, and, (b) indicating the influence of ash cement ratio (Kearsley and Wainwright (2001))

2.3 Bond Behaviour

2.3.1 Bond definition and theoretical bond

Simply put, bond can be defined as the chemical and mechanical interaction between two materials. The chemical interaction encompasses the adherence ability and the mechanical interaction deals with the force transmission ability. The strength of the interaction, and thus the bond capacity, between the two materials is governed by the bond interface. Figure 2.14 depicts a concrete pull-out (PO) test specimen during testing (left) and the distributions of the bar slip (S(x)), tensile stresses developed in the bar ($\sigma_s(x)$), and the bond stresses ($\sigma_b(x)$) to the right as a result of the loading.

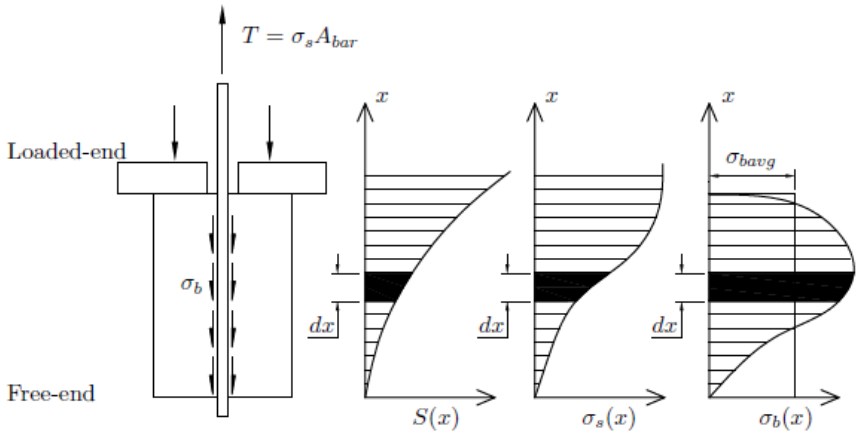

Figure 2.14: Concrete PO test specimen during testing (left) and the distributions of the bar slip (S(x)), tensile stresses developed in the bar ($\sigma_s(x)$), and the bond stresses ($\sigma_b(x)$) to the right as a result of the loading (reproduced from Penelis and Penelis (2014))

Slip is defined as the relative displacement of one material relative to the other. In Figure 2.14 the slip is measured vertically, along the length of the embedded steel bar, starts at zero from the free-end and reaches a maximum at the loaded end. This slip distribution arises as a result of the elastic elongation of the embedded steel bar subjected to tensile stresses and the partial delamination starting from the loaded-end. Since the bar force is transmitted to the surrounding concrete through interfacial shear no bond stresses can exist below the free-end. Therefore, the axial stress distribution also starts at zero from the free-end and develops along the length of the embedded bar. According Penelis and Penelis (2014) the exact distribution of the bond stress is not known and the assumption of a constant bond stress, σ_{bavg}, is acceptable for short embedment lengths.

Figure 2.15 depicts the free body diagram of the differential element, length dx, shown in Figure 2.14. T is the axial tensile force in the bar, A_{bar} is the cross sectional area of the bar, and φ the diameter of the bar.

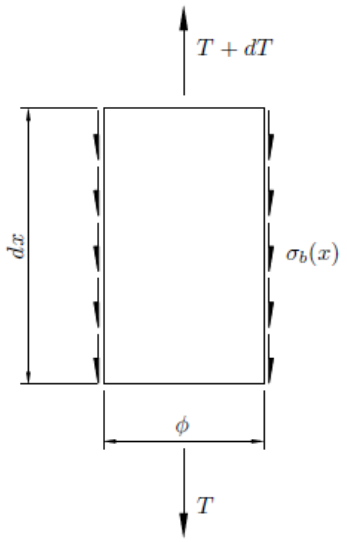

Figure 2.15: Free body diagram of the differential element of length dx (reproduced from Penelis and Penelis (2014))

Taking the sum of the forces in the vertical direction to satisfy equilibrium of the differential element produces Equation 2.16. Rearranging Equation 2.16 yields Equation 2.17

$$d\sigma_s\left(\frac{\pi\varphi^{\,2}}{4}\right) = (\varphi\,\pi\sigma_b)dx \tag{2.16}$$

$$d\sigma_s = \left(\frac{4\sigma_b}{\varphi}\right)dx \tag{2.17}$$

where σ_s is the axial tensile stress in the embedded steel bar,
φ is the nominal diameter of the embedded steel bar,
σ_b is the bond stress along the steel bar,
dx is the length of the differential element.

Equation 2.17 basically states that any change in the axial stress results in the development of bond stress at bond interface. As a result, tensile stresses cannot develop without the force transfer mechanisms present in bond behaviour. The force transfer mechanism in bond can be classified as either chemical or mechanical. The first mechanism is the chemical adhesion between the cement paste and embedded steel reinforcement. The chemical adhesion typically has a bond value in the range of 0.5 and 1.0 MPa. Once the chemical adhesion has been overcome, the embedded steel bar starts to experience slip at the free-end, which activates the frictional mechanism. The frictional bond experienced at the interface transfers the force via shear stress and increases due to confinement and the transverse pressures. The bond stress continues to increase due to mechanical interlock caused by the wedging of concrete between the steel ribs. The continued rise in bond stress leads to two possible scenarios. In the first scenario, the force developed in the embedded steel rod is enough to pull it free from the concrete. In this scenario the specimen has failed by PO failure. In the second scenario the tensile stresses arising

in the surrounding concrete exceed its tensile strength, causing splitting parallel to the steel bar. The specimen is said to have failed in splitting failure. It should be noted that the mechanical locking mechanism that contributes to bond development is influenced by confinement, internal cracks and steel geometry. When conducting bond experiments all three mechanism may be activated. A bond-slip curve is presented in Figure 2.16. The bond stress used in the design of reinforced concrete is not the peak bond value, but rather the bond at a specific free-end slip, known as the design slip (S_d). According to Leonhardt (1977) this approach is found throughout literature and can originally be found in German lectures of reinforced concrete design.

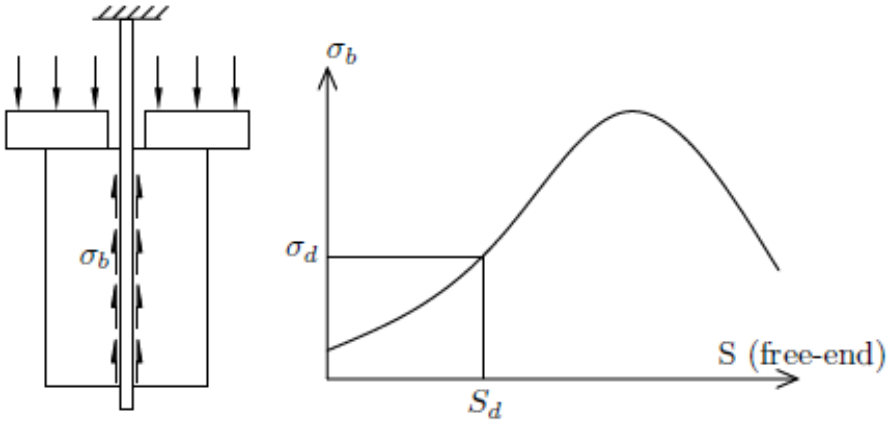

Figure 2.16: PO test set-up (left) and illustration of a typical bond-slip curve (reproduced from Penelis and Penelis (2014))

2.3.2 Experimental determination of bond

The experimental determination of bond stress can be done by conducting either the standard PO test or beam-end (BE) test. In order to characterise bond under various conditions, testing parameters may include (1) mechanical properties of the surrounding concrete, (2) embedment length, (3) confinement (active- secondary reinforcement or passive-cover depth), (4) concrete cover depth, (5) lateral pressure, (6) bar diameter and spacing, (7) bar rib factor, or relative protruding area of the bar rib, etc. When testing for bond it is important that all the factors mentioned previously be considered as they may have a profound effect on the bond results.

2.3.2.1 Bond in lightweight concrete (LWC)

The properties of concrete are strongly dependent on its composition. Replacing any of its mix constituent's yields changes. Therefore, although a fair amount of research has been conducted on the characterisation of the material properties of concrete, studies on recently developed concretes are still lacking. LWC is produced by adding air into the concrete to reduce it weight. The large amount of entrained air in FC may significantly alter the bond development and failure mechanisms.

In 2013 Farghal Maree and Hilal Riad (2014) launched a study to experimentally and analytically determine the bond properties of polystyrene foam lightweight concrete (PFLWC). PFLWC is produced by the partial replacement of normal weight aggregate by polystyrene. The incorporation of polystyrene leads to an approximate weight reduction between 15 and 20% of the NWC counterpart. The

experimental determination of the bond comprised of testing standard PO and BE specimens and comparing the results with the NWC counterpart.

For the standard PO test Farghal Maree and Hilal Riad varied the type of concrete (PFLWC and NWC), the nominal bar diameter (12 mm, 16 mm, and 22 mm) and the embedment length (3 and 4 times the bar diameters). Farghal Maree and Hilal Riad reported that most of the specimens failed in splitting failure mode. This is as a result of the low tensile splitting strength of the PFLWC and is common for LWC as reported in literature (Sancak et al.(2011), Dae-Ji et al.(2014))

In order to compare different bond results of different concrete mixes Farghal Maree and Hilal Riad introduced the bond stress ratio, β, given in Equation 2.18. In Equation 2.18 the bond stress ratio is calculated by dividing the design bond (σ_b) by the square-root of the compressive strength (f_{cu}) of the concrete. It should be noted that care should be taken when using this normalisation as it may be considered representative for NWC but not for LWC.

$$\beta = \frac{\sigma_b}{\sqrt{f_{cu}}} \tag{2.18}$$

Figure 2.17 shows a plot reproduce from Farghal Maree and Hilal Riad of the bond stress ratio versus nominal bar diameter. Farghal Maree and Hilal Riad obtained the design bond stress at a slip of 0.1 mm from the bond stress-slip curve and used Equation 2.18 to obtain the bond stress ratios. It is common practice to take the design bond stress at a slip of 0.1 mm (Sung-Nam et al. (2008)). This is attributed to the fact that slip is the primary mechanism of crack growth according to Leonhardt (1977) and that several codes including the ACI (ACI 318-11 (2011)), Eurocode 2 (BS EN 1992-1-1 (2004)) and SANS (SABS 0100-01 (2000)), specify an allowable maximum crack width in the range of 0.1 to 0.4 mm for RC.

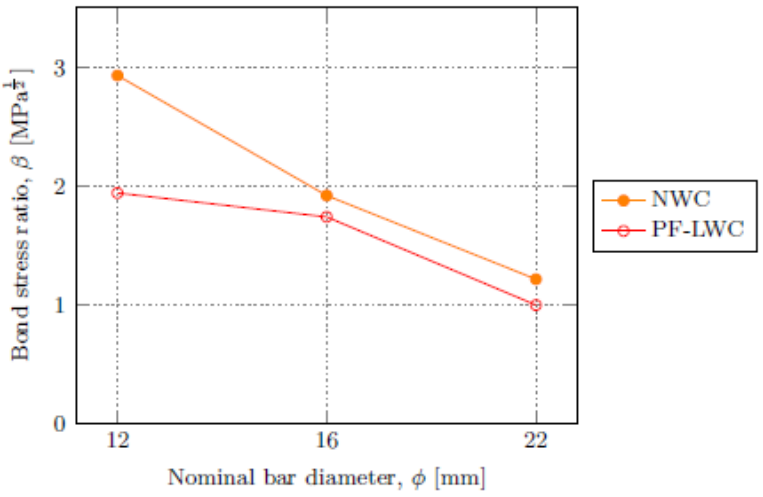

Figure 2.17: Bond stress ratio versus nominal bar diameter as obtained from the PO test (reproduced from Farghal Maree and Hilal Riad (2014))

From Figure 2.17 it can be seen that the bond stress ratios, consequently the design bond stress, of PFLWC is lower than that of the equivalent NWC. The largest difference is observed for the smallest nominal bar diameter of 12 mm and is significantly less for 16 mm and 22 mm nominal bar diameter. The bond stress ratio also shows a decrease with an increase in nominal bar size. This is attributed to the decrease in passive confinement (cover depth) which increase the likelihood of the specimens failing in splitting failure that yields a much lower design bond capacity.

Farghal Maree and Hilal Riad also reported on the effect of the embedment length (l_e) on the average bond stress ($\sigma_{b,avg}$). See Table 2.3 for a summary of the average bond stress values for different embedment lengths (3φ and 4φ) in PFLWC. The results in Table 2.3 show a decrease in average bond stress with an increase in embedment length. Also, the same behaviour is observed for the increase in nominal bar size. This is a result of an increase in the likelihood of the specimens failing in splitting failure that yields a much lower design bond capacity. Another possible reason is that the shear stress distribution is not uniform. This will always lead to a lower average bond stress, by dividing the associated bar force with the larger bar surface.

Table 2.3: Average bond stress and bond stress ratio values obtained from the PO tests conducted on PFLWC (reproduced from Farghal Maree and Hilal Riad (2014))

φ	l_e	$\sigma_{b,avg}$ [MPa]	Failure
12	3φ	26.85	Pull-out
	4φ	22.01	
16	3φ	19.31	Splitting
	4φ	15.67	

The effect of confinement (active –secondary reinforcement) on the bond was also investigated in the study by Farghal Maree and Hilal Riad (2014). Table 2.4 summarizes the results as obtained from the BE tests for PFLWC and NWC. The results in Table 2.4 shows that the bond stress ratio values increased with the provision of confinement for all cases tested. As observed in the PO test results a similar observation that the increase in nominal bar diameter size leads to a decrease bond stress value are reported for the BE tests.

Table 2.4: Bond stress ratios calculated from the BE tests results conducted on PFLWC and NWC (reproduced from Farghal Maree and Hilal Riad (2014))

	Confined				Unconfined			
	PFLWC		NWC		PFLWC		NWC	
φ	12	16	12	16	12	16	12	16
β	1.64	0.94	1.81	1.41	1.49	0.82	1.73	1.40

El Zareef and Schlaich (2008) conducted a study to illuminate the effects of confinement on bond behaviour. El Zareef and Schlaich tested two stirrups, steel and glass-fibre stirrups, with three different

side-lengths, 60, 90, and 120 mm respectively. El Zareef and Schlaich found no significant change for both steel and glass-fibres stirrups of size 90 and 120 mm. A 3% and 37% increase was observed for steel and glass-fibre stirrups of 60 mm side-lengths and a reduction of 57% and 95% in slip values for the maximum bond stress.

Figure 2.18 shows the influence of transverse pressure on bond strength and failure mode. Transverse pressure is a result of confinement. The confinement can either be classified as active or passive. Larger concrete cover depths tend to yield larger bond stress value, El Zareef and Schlaich (2008) and Model Code (2010), as a result of the increased crack path for the internal crack. An initial increase in confinement may only result in an increase in bond strength but with further increases the failure mode may change from splitting failure to PO failure. Additional increases in confinement thereafter may not be beneficial to the bond strength. It should be noted that for design purposes PO failure should be ensured by providing adequate active confinement due to the higher bond strength and typically more gradual and safe failure mechanism of PO.

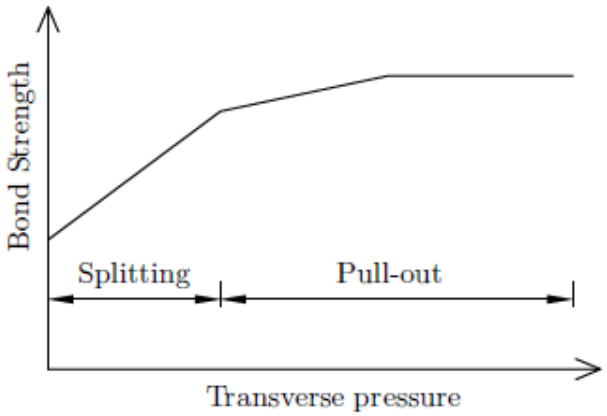

Figure 2.18: The influence of transverse pressure on the bond strength and failure mode (Model Code (2010))

El Zareef and Schlaich also studied the effects of incorporating polypropylene fibres of 6 and 20 mm length into the concrete mix design. Figure 2.5 provides a summary of the results obtained from the PO tests. It was found that the incorporation of 0.1% by volume PP fibres in the mix lead to a reduction in the compressive strength, Section 2.2.2.4, that was offset with an increase in tensile strength. El Zareef and Schlaich found an increase of 2.4% and 25.3% in the maximum bond stress with 6 mm and 20 mm pp fibre incorporation. The incorporation of PP also lead to the maximum bond stress occurring at lower slip values.

Table 2.5: Increase in maximum bond stress of LWC due to incorporation of PP fibres (adapted from El Zareef and Schlaich (2008))

Fibre length	***Steel***
6 mm	2.4%
20 mm	25.3%

2.3.2.2 Bond in lightweight aggregate concrete (LWAC)

A study investigating the bond strength in artificial LWAC of deformed steel reinforcement was published by Dae-Jin et al. (2014). Dae-Jin et al. performed PO tests to determine the bond strength of four types of concrete, three LWAC and one NWC. Additionally, three different diameter sizes (12 mm, 16 mm, and 19 mm) and four embedment lengths (40 mm, 80 mm, 120 mm, and 150 mm) were used. During the PO tests, the free-end slip and loaded-end slip of the embedded reinforcing steel bar was recorded. The elongation (δ_{bar}) of the embedded bar is given in Equation 2.19 and can be calculated as the difference of the loaded-end slip (S_l) and free-end slip (S_f).

$$\delta_{bar} = S_l - S_f \tag{2.19}$$

where

$$\delta_{bar} = \frac{TL}{E_s A_{bar}}$$

where T is the force in the bar

L is the debonded length of the bar

E_s is the elastic modulus of the steel

A_{bar} is the cross-sectional area of the bar.

In the study specimens either failed in yielding of the embedded reinforced steel bar, tensile splitting failure or PO failure. By observing the load-slip curves the various failure modes can easily be identified. PO failure is characterised by an ascending bond strength, to a maximum peak bond stress, with an increase in slip. After the peak load is reached the load decreases and remains constant as the slip increases. The PO failure behaviour can be explained in five stages (1) micro-slip (2) internal cracking (3) PO (4) descending and (5) residual. In the first stage, micro-slip, small loads are recorded with virtually no slip at the free-end of the embedded steel bar. The second stage, internal cracking, is characterised by the onset of free-end slip. This occurs when the load is sufficient to overcome the chemical adhesion between the materials. In the third stage, PO, the load increases to a peak as a result of the internal crushing of concrete between the ribs of the embedded steel bar. Once the peak load has been reach the fourth stage, descending, is entered. In the fifth stage, residual, the main mechanism contributing to the bond is friction. In this stage a residual load of approximately 10 – 20 % of the peak load is maintained.

Splitting failure is similar to the PO failure behaviour except after internal cracking a peak load is reached and is followed by a sudden loss of resistance. This is as a result of the local tensile stresses in the material interface overcoming the concrete tensile stress capacity causing cracks that propagate concrete-steel interface to the surface of the concrete resulting in splitting. The loss of resistance causes the force in the embedded steel bar to drop to zero and subsequently zero bond stress is attained.

Figure 2.19a,b shows the failure modes observed in the tests. As can be in seen in Figure 2.19a,b splitting failure is the dominant failure mode for LWAC which according to Dae-Jin et al. (2014) is attributed to the low tensile splitting failure of the concrete. PO failure occurred more often in NWC than in LWAC and increased with a reduction in bar diameter and embedment length.

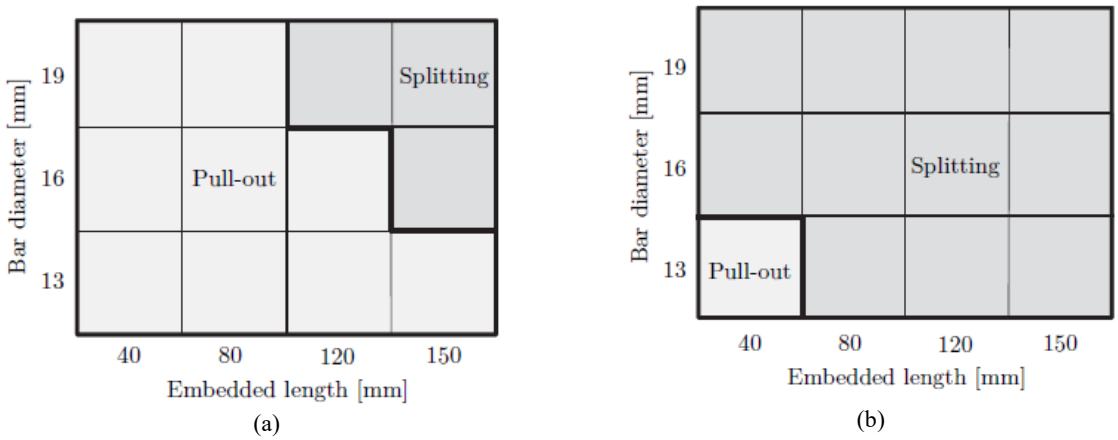

Figure 2.19: Failure modes observed in (a) NWC and (b) LWC (Dae-Jin et al. (2014))

From the results of their study Dae-Jin et al. concluded the following; (1) bar diameter has a minor influence on bond strength, (2) the bond strength is inversely proportional to the embedment length, and, (3) the bond strength is directly proportional to the compressive strength of the concrete.

Finally Dae-Jin et al. compared their results for bond strength against those published in literature for NWC, see Table 2.6. Dae-Jin et al. found that the results for LWAC did not correlate well with those calculated from the existing models for NWC and concluded that a simple substitution does not suffice.

Table 2.6: Bond equations found in literature

From literature:		
Orangun et al. (1977)	$\frac{\sigma_b}{\sqrt{f_{cu}}} = 0.1 + 0.25\left(\frac{c_m}{\varphi}\right) + 4.15\left(\frac{\varphi}{l_e}\right)$	(2.20)
ACI committee 408 (1992)	$\sigma_b = 20.23\frac{\sqrt{f_{cu}}}{\varphi}$	(2.21)
Zuo and Darwin (2000)	$\left(\frac{T_b}{f_{cu}}\right)^{1/4} = [1.44 l_e (c_m + 0.5) + 56.3 A_{bar}]\left(0.1\frac{c_M}{c_m} + 0.9\right)$	(2.22)
Study of Dae-Jin et al. (2014)		
Dae-Jin et al. (2014)	$\frac{\sigma_b}{\sqrt{f_{cu}}} = \frac{37.5}{\sqrt[4]{\varphi + l_e}} - 9.4$	(2.23)

where c_m smallest (clear bottom cover, half clear spacing between bars),

c_M largest (clear bottom cover, half clear spacing between bars),

T_b as the ultimate bond force.

2.3.3 Models for Bond determination

2.3.3.1 Model Code 2010

Figure 2.20 shows an illustration of the bond development in between reinforcing steel and concrete as presented in Model Code (2010). An analytic model is proposed to estimates the bond-slip as a piece-wise defined function of the relative displacement (S), given as Equation 2.24. When Equation 2.24 expresses the bond-slip relation illustrated in Figure 2.20.

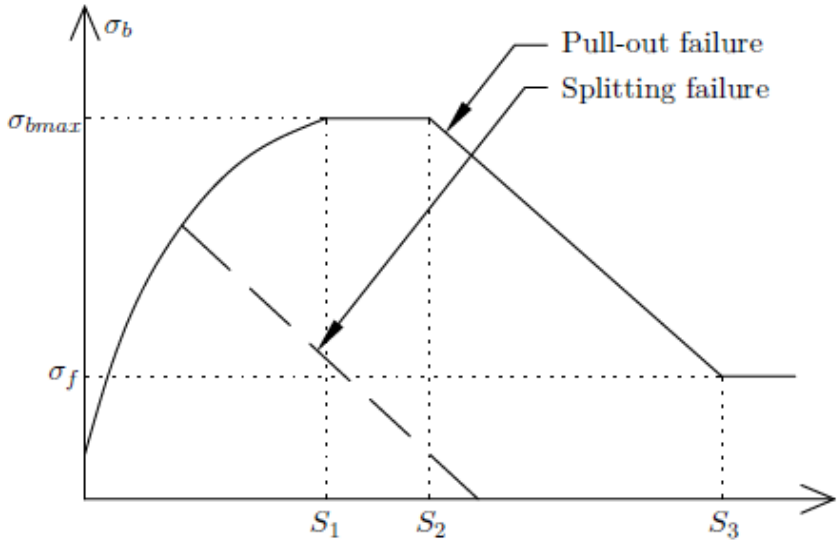

Figure 2.20: Illustration of the bond-slip relation (bond-slip curve) (reproduced from Model Code (2010))

$$\sigma_b = \begin{cases} \sigma_{bmax}\left(\frac{S}{S_1}\right)^{\alpha} & \text{for } 0 \le S \le S_1 \\ \sigma_{bmax} & \text{for } S_1 \le S \le S_2 \\ \sigma_{bmax} - \frac{\sigma_{bmax} - (\sigma_{bmax} - \sigma_f)(S - S_1)}{S_3 - S_2} & \text{for } S_2 \le S \le S_3 \\ \sigma_f & \text{for } S_3 \le S \end{cases} \quad (2.24)$$

where σ_b is the bond stress,

σ_{bmax} is the peak bond stress

σ_f is the residual bond stress

S_1, S_2, and S_3 characteristic slip values

Typical values for the variables given in Equation 2.24 can be found in Table 2.7.

Table 2.7: Bond-slip model parameters for the different failure modes, bond conditions and confinement regimes (reproduced from Model Code (2010))

	Pull-out failure		**Splitting failure**			
	$\varepsilon_s < \varepsilon_{s,y}$		$\varepsilon_s < \varepsilon_{s,y}$			
	Good bond cond.	**other bond cond.**	**Good bond cond.**		**other bond cond.**	
			Unconfined	**Confined**	**Unconfined**	**Confined**
σ_b	$2.5\sqrt{f_{cu}}$	$1.5\sqrt{f_{cu}}$	$7(f_{cu}/25)^{0.25}$	$8(f_{cu}/25)^{0.25}$	$5(f_{cu}/25)^{0.25}$	$5.5(f_{cu}/25)^{0.25}$
S_1	1.0	1.8	$S(\sigma_{bmax})$	$S(\sigma_{bmax})$	$S(\sigma_{bmax})$	$S(\sigma_{bmax})$
S_2	2.0	3.6	S_1	S_1	S_1	S_1
S_3	c_{clear}	c_{clear}	$1.2S_1$	$0.5c_{clear}$	$1.2S_1$	c_{clear}
α	0.4	0.4	0.4	0.4	0.4	0.4
σ_f	$0.4\sigma_{bmax}$	$0.4\sigma_{bmax}$	0	$0.4\sigma_{bmax}$	0	$0.4\sigma_{bmax}$
with c_{clear} the clear distance between ribs of steel reinforcement						
with ε_s and $\varepsilon_{s,y}$ being the reinforcement strain and yield strain respectively						
with α the regression constant used for empirical data fit						
with σ_f the residual bond capacity as a result of confinement steel						

2.3.3.2 Proposed bond models for LWC

The study conducted by Farghal Maree and Hilal Riad (2014), lead to the development of an analytical model for the bond-slip relationship. Farghal Maree and Hilal Riad studied the equations of the CEB-FIP 1990 model code (recently updated as Model Code 2010) and concluded that the equations do not take into account the increase in bond stress and decrease in slip as a result of the use of steel reinforcing bars with relatively large rib areas. Therefore Farghal Maree and Hilal Riad proposed modifications to the equations found in CEB-FIP 1990 which takes into account the effects of nominal bar diameter and concrete types. The modifications, obtained from fitted curves of their results, are presented in Table 2.8.

Table 2.8: Proposed modifications to CEB-FIP 1990 equations (reproduced from Farghal Maree and Hilal Riad (2014))

Parameter	**NWC**	**PFLWC**
S_1	$0.11e^{0.054\varphi}$	$0.11\text{x}1.1e^{0.054\varphi}$
S_2	$0.11e^{0.054\varphi}$	$0.11\text{x}1.1e^{0.054\varphi}$
S_3	1	1
α	0.4	0.55
σ_{bmax}	$10.4\varphi^{-0.35}\sqrt{f_{cu}}$	$10.4\text{x}1.1\varphi^{-0.35}\sqrt{f_{cu}}$
σ_f	$0.15\ \sigma_{bmax}$	$0.15\ \sigma_{bmax}$

2.3.4 Design bond formulations

2.3.4.1 NWC and LWAC (BS EN 1992-1-1, 2004)

BS EN 1992-1-1 (2004) provides Equation 2.25 for determining the design bond stress for NWC. In this equation there is a direct proportionality between the design bond stress and the concrete's characteristic tensile strength.

$$\sigma_b = 2.25\eta_1\eta_1 f_{ctd} \tag{2.25}$$

where η_1 is the bond condition factor taken as 1 for good bond conditions and 0.7 otherwise

η_2 is the bar size factor equal to 1.0 for $\varphi \leq 32$ mm and $\left(\frac{132-\varphi}{100}\right)$ for $\varphi \geq 32$ mm

f_{ctd} is the design tensile strength calculated using Equation 2.26,

$$f_{ctd} = \alpha_{ct}\left(\frac{f_{ctk,0.05}}{\gamma_c}\right) \tag{2.26}$$

Given $f_{ctk,0.05}$ as the 5% fractile value of the characteristic tensile strength, provided in tables or National Annex

α_{ct} as a coefficient taking account of long term effects on the tensile strength, recommended as 1.0, provided in tables or National Annex

γ_c as the partial safety factor for concrete equal to 1.5

BS EN 1992-1-1 (2004) provides a supplementary clause that caters to the design criteria of LWAC. The supplementary clause provides an alternative equation, given as Equation 2.27, to calculate the characteristic tensile strength (f_{lctd}) of LWAC.

$$f_{lctd} = \left(\frac{f_{lctk,0.05}}{\gamma_c}\right) \tag{2.27}$$

where

$$f_{lctk,0.05} = f_{ctk,0.05}\left(0.4 + \frac{0.6\rho_{LWAC}}{2200}\right)$$

and ρ_{LWAC} is the density provided in Table 11.1 in BS EN 1992-1-1 (2004) for LWAC density classes.

2.3.4.2 NWC and LWAC (BS 8110-1, 1997)

BS 8110-1 (1997) makes use of Equation 2.28 to determine the bond stress (σ_b) for different NWC compressive strengths. The method makes use of the bond stress ratios (β), given in Table 2.9, and concrete compressive strength (f_{cu}) to determine the bond stress. According to Robberts and Marshall (2010) the deformed bar found in South Africa conforms to a type 2 deformed bar. The equation presented for NWC can also be applied to LWAC by making use of a supplementary clause given in B8110-2 (1985). For LWAC the bond stress is calculated using Equation 2.28 and applying a multiplication factor of 0.8. This approach is identical to the one provided in the South African standards (SABS 0100-1 (2000)).

$$\sigma_b = \sqrt{f_{cu}} \tag{2.28}$$

Table 2.9: Bond stress ratios for various bar types and loading states (reproduced from BS 8110-1 (1997))

Bar type	Bars in Tension	Bars in Compression
Type 1: deformed	0.40	0.50
Type 2: deformed	0.50	0.63

2.4 Durability Assessment

Durability as defined by the ACI committee 201 (1977) is the ability of Portland cement concrete to withstand weathering action, chemical attack, abrasion, or any other process of deterioration. Therefore a durable concrete will retain its original form, quality, resistance and serviceability when exposed to its environment. These causes rarely act alone as one normally leads to the other making it difficult to categorise. For example, chemical reactions between the aggregate and the cement matrix give rise to expansive products which cause physical deterioration. Nevertheless Mehta and Monteiro (2006) grouped the physical causes into two categories (a) surface wear or loss of mass due to abrasion, erosion and cavitation; and (b) cracking due to normal temperature and humidity gradients, crystallisation of salts in pores, structural loading and exposure to temperature extremes such as freezing or fire. For the chemical group the Mehta and Monteiro used three groups (1) hydrolysis of the cement paste components by soft water; and (2) cation exchange between aggressive fluids and the cement paste; and (3) reactions leading to formation of expansive products. The following sections briefly reports only on the two forms of chemical attacks, carbonation and chloride attack, investigated in this research.

2.4.1 Carbonation in concrete

2.4.1.1 Introduction to the process of carbonation in concrete

Carbonation, in concrete, is a process whereby carbon dioxide (CO_2) from the environment reacts with the concrete. The CO_2 reacts with the pore solution to form carbonic acid (H_2CO_3) (Domone and Illston (2015), Taylor (1990)), as presented in Equation 2.29. In turn, the carbonic acid formed in the pore solution reacts with the calcium hydroxide ($Ca(OH)_2$) present to form calcium carbonate ($CaCO_3$) and water as shown in Equation 2.30. It should be noted that the calcium carbonate formed exists either

as (1) calcite, (2) aragonite, or (3) vaterite. The resultant state of calcium carbonate formed is dependent on the temperature and pressure and has a larger molecular volume than its predecessors. The formation of calcite results in a 12 % increase in molecular volume whilst a 3 % and 12 % is observed for aragonite and vaterite. At room temperature and atmospheric pressure calcite is formed. During carbonation the hardened cement paste is densified as a result of the larger molecular volume of calcium carbonate formed, see Equations 2.29 and 2.30. Additionally, Borges et al. (2009) reported that upon depletion of the calcium hydroxide the carbon dioxide then starts to react with the calcium-silicate-hydrate.

$$CO_2 + H_2O \rightarrow H_2CO_3 \quad (2.29)$$

$$H_2CO_3 + Ca(OH)_2 \rightarrow CaCO_3 + 2H_2O \quad (2.30)$$

The consumption of calcium hydroxide leads to a decrease in the pH of the concrete and in the presence of sufficient oxygen corrosion may take place. The effect of pH level on the corrosion rate is illustrated in Figure 2.21. Other factors affecting the rate of carbonation and corrosion include the water cement ratio, binder content, cover, RH and curing conditions.

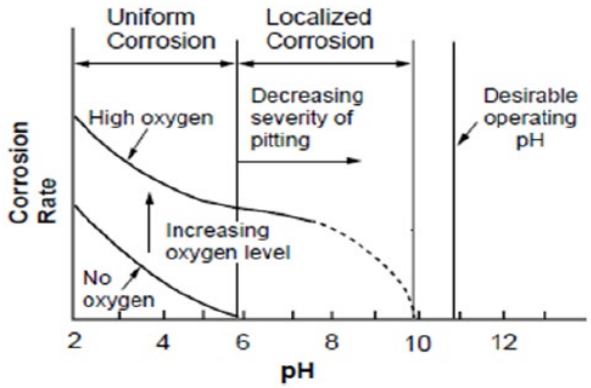

Figure 2.21: Depiction of the effect of pH level on corrosion rate (reproduced from Roberge (1999))

2.4.1.2 Parameters influencing carbonation in concrete

2.4.1.2.1 Mix constituents (proportioning) influencing carbonation of concrete

The mix constituents influencing carbonation include the water cement ratio, supplementary cementitious material, binder content, and initial water content. Fattuhi (1986) studied the effects of the mix constituents and initial water curing period on carbonation of concrete. Fattuhi used rectangular prisms, 50x50x285 mm, made with three different water cement ratios of 0.4, 0.6 and 0.7, respectively. After demoulding, the rectangular specimens were either water cured for a period of either 1, 3, 7, 21, or 28 days. After the initial water curing period the rectangular prisms were surface dried and placed in a carbonation chamber with constant CO_2 supply. To monitor the depth of carbonation, slices were cut from the rectangular prisms and sprayed with phenolphthalein. Fattuhi found that there is a significant increase in carbonation depth with an increase in the water cement ratio and a considerable decrease with an increase in the initial water curing period.

Leemann and Loser (2019) investigated carbonation resistance of concrete containing recycled aggregate (RA), moisture state of the aggregates prior to mixing and cement type for accelerated and natural carbonation exposure conditions. In the study they chose two different replacement levels of natural aggregate (NA), 25 or 50 % w.r.t. weight, and three different blended cement types, CEM II/A, CEM II/B, or CEM III/B, respectively. The state of the RA was either dry or saturated prior to mixing. Leemann and Loser used the carbonation coefficient, calculated as the regression of the carbonation depth as a function of the square root of time, for accelerated exposure (K_{ACC}) and natural exposure (K_{NA}) against the 28 day compressive strength to express their results. The results are plotted in Figure 2.22a,b.

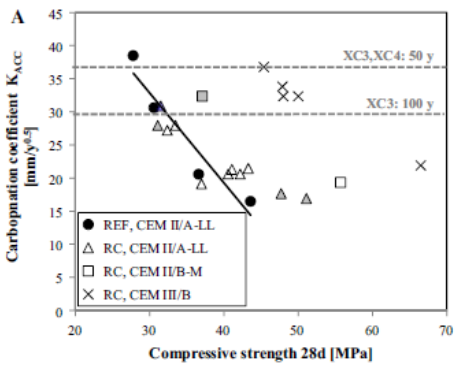

Figure 2.22: (a) Carbonation coefficient K_{AAC} as a function of compressive strength at 28 days (Leeman and Loser (2019))

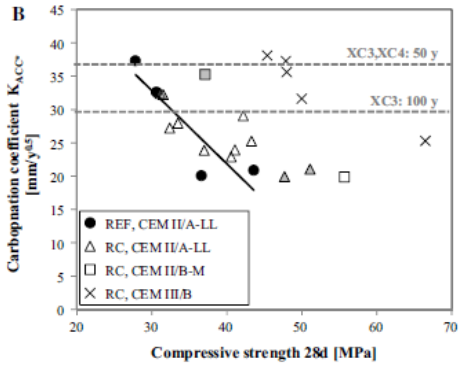

Figure 2.22: (b) Carbonation coefficient K_{AAC*} (local effects taken into account) as a function of compressive strength at 28 days (Leeman and Loser (2019))

From Figure 2.22a,b Leemann and Loser found little difference in the accelerated carbonation coefficient (K_{AAC}) between the recycled aggregate concrete (RAC), irrespective of the replacement level, and the reference mix made with the same cement type (CEM II/A-LL). A slight increase in K_{AAC} was found in the two RAC mixes produced with the CEM II/B-LL cement type compared to the CEM II/A-LL. The two RAC mixes made with CEM III/B showed a significant increase in the K_{AAC} compare to CEM II/A-LL. Leemann and Loser attributed the increase in K_{AAC} to the decrease in the clinker content between the cement types and the decrease in the CO_2 buffer capacity. Also, when accounting for the condition (already carbonated regions) of the RA used, the K_{AAC} increased by a mean value of 10%, see Figure 2.22b. No difference was found between saturated and unsaturated RA.

Leemann and Loser also investigated the relationship between accelerated carbonation and natural (sheltered and unsheltered) carbonation. Leemann and Loser plotted the results of the unsheltered and sheltered natural carbonation coefficients, $K_{N,S}$ and $K_{N,US}$, as a function of the accelerated carbonation coefficient K_{ACC} as shown in Figure 2.23a,b. The results as seen in Figure 2.23a,b indicate that there is little correlation between accelerated carbonation and natural carbonation.

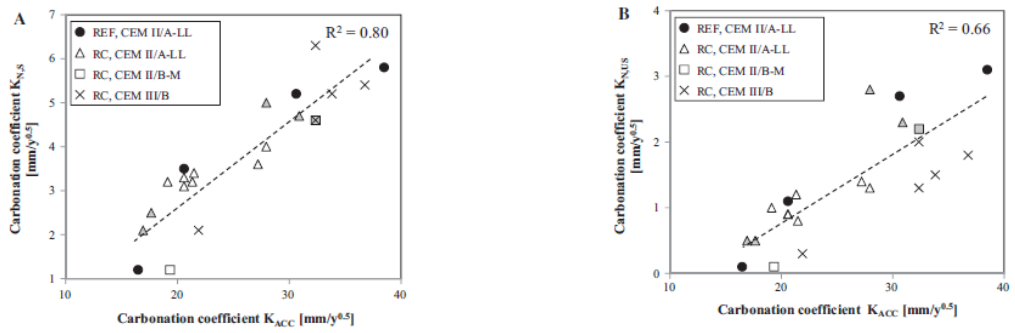

(a) (b)

Figure 2.23: Carbonation coefficient (a) $K_{N,S}$ and (b) $K_{N,US}$ as a function of carbonation coefficient K_{AAC} (Leeman and Loser (2019))

Shah and Bishnoi (2018) studied the carbonation resistance of concrete samples made with cements containing supplementary cementitious materials (SCMs) exposed to natural and accelerated conditions. In the study Shah and Bishnoi prepared samples using as a reference control blend OPC (U-unblended/unary), OPC and fly ash (B1-blended 1/binary 1), OPC and slag (B2-blended 2/binary 2), OPC, calcined clay and limestone (T1-ternary 1 and T2-ternary 2), and OPC, slag and fly ash (T3-ternary 3). Shah and Bishnoi found that the carbonation depth increases with increased exposure time for all samples, as shown in Figure 2.24a,b. Using the relationship between carbonation depth and time Shah and Bishnoi performed a linear regression analysis to obtain the carbonation coefficients listed in Table 2.10. Shah and Bishnoi generally found good relationships as indicated with the high R-squared values, ranging from 0,9438 to 0,9851 for 3% CO_2 accelerated exposure conditions and 0,9639 to 0,9969 for sheltered natural exposure conditions, except for the U1 sample set exposed to sheltered natural conditions with a R-squared value of 0,7913. Analysing the carbonation coefficients shows that substituting the cement with SCMs leads to a decrease in the carbonation resistance of the concrete. Shah and Bishnoi attributed the decrease in the carbonation resistance to the reduction in the clinker content of the samples. The samples made from B1, which has 30 % less clinker than the reference U1, showed a better carbonation resistance than samples made from B2, T1, T2 and T3 which have 50% less clinker than U1. The clinker content is listed alongside the carbonation coefficients in Table 2.10. Interestingly the type of SCM also plays a role in the carbonation resistance. Samples made from slag had a higher carbonation resistance than samples made with fly ash for the same clinker replacement level. Shah and Bishnoi attributed this phenomenon to the hydration process of slag and fly ash. The hydration of slag leads to the production of $Ca(OH)_2$ whereas the hydration of fly ash leads to the consumption of $Ca(OH)_2$. This production of $Ca(OH)_2$ compensates for the loss of alkalinity due to carbonation and therefore has a dilution effect. Similar observations were made from the T1 and T2 samples which have a higher resistance than the T3 samples.

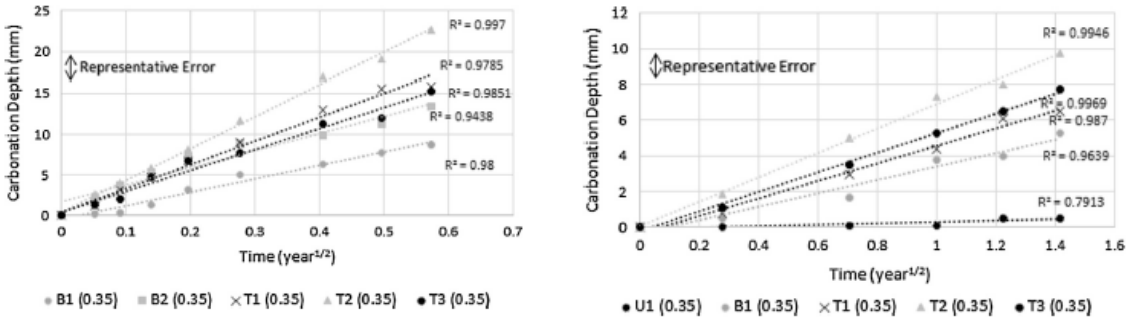

(a) (b)

Figure 2.24: Carbonation depth as a function of the square root of exposure time (a) w/c = 0,35; RH = 60%; T = 27°C; 3% CO_2 environment (b) w/c = 0,35; natural sheltered CO_2 conditions (Leeman and Loser (2019))

Table 2.10: Carbonation coefficient of samples exposed to different conditions (mm/year$^{1/2}$) (reproduced from Leeman and Loser (2019))

	1% CO_2	3% CO_2	Natural sheltered	Clinker factor
U1 (0,35)	0,61	0,90	0,47	0,97
B1 (0,35)	11,83	17,03	4,19	0,67
B2 (0,35)	-	19,29	-	0,50
T1 (0,35)	19,14	28,58	5,26	0,50
T2 (0,35)	30,07	38,42	6,76	0,50
T3 (0,35)	18,77	25,08	5,79	0,50
U1 (0,45)	15,14	19,45	-	0,97
B1 (0,45)	23,15	34,83	6,53	0,67
T1 (0,45)	28,58	42,01	7,73	0,50
T2 (0,45)	45,11	59,49	10,80	0,50
T3 (0,45)	31,15	36,09	-	0,50

2.4.1.2.2 Effect of environmental conditions and transport properties on carbonation

The internal and external environmental conditions of concrete and transport properties affect the carbonation rate. The internal and external environmental conditions include the moisture content of the concrete pores, and, temperature, relative humidity (RH) and CO_2 concentration. The dominant transport mechanism in carbonation is diffusion and thus the permeability of the concrete also influences the carbonation process.

The effect of the internal environment of the concrete, moisture content, and the external environmental RH on carbonation is shown in Figure 2.25. As observed by numerous research (Böhni (2005), Utgenannt (2004), Shah and Bishnoi (2018)) the rate of carbonation is dependent on the moisture content of the concrete, which can be related to the RH. At low RH the concrete loses moisture to the environment and therefore the concrete pores are dry. CO_2 from the environment can thus not dissolve in the solution and therefore carbonation does not take place. At the opposite end, high RH, the concrete pores are water-fill and CO_2 cannot diffuse into the concrete and therefore little to no carbonation takes

place. The rate of carbonation is therefore at a maximum when the concrete pores are partially fill at a moderate RH. Utgenannt (2004) suggests that the maximum rate of carbonation occurs at 70% RH.

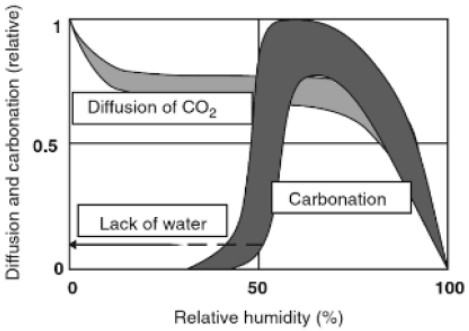

Figure 2.25: The relative CO_2 diffusion and carbonation rate versus RH (reproduced from Böhni (2005))

In the study by Shah and Bishnoi (2018), they tested samples at 27°C exposed to 3% CO_2 at 40%, 50% and 60% humidity and samples at 45°C exposed to 3% CO_2 and 60% humidity, shown in Figure 2.26a,b. For these samples Shah and Bishnoi observed a linear relationship between the carbonation coefficients and the RH. In the study the samples exposed to 40% relative humidity had the highest carbonation coefficients and subsequently carbonation penetration depth. The carbonation coefficients, see Figure 2.26a, decreased as the relative humidity increased. Shah and Bishnoi attributed this to the phenomenon mentioned previously about the pore water level of the concrete. The effect of temperature on carbonation is illustrated in Figure 2.26b. Samples exposed to 45°C have higher carbonation coefficients than the same samples exposed to 27°C. The likely explanation for this is that a higher rate of drying occurs thereby increasing the diffusion of carbon dioxide into the concrete. Shah and Bishnoi did however state that the difference in carbonation coefficients is marginal. Shah and Bishnoi believe that the higher carbonation diffusion rate is offset by the decrease in solubility of carbon dioxide and calcium hydroxide which therefore only leads to minor increases in the rate of carbonation.

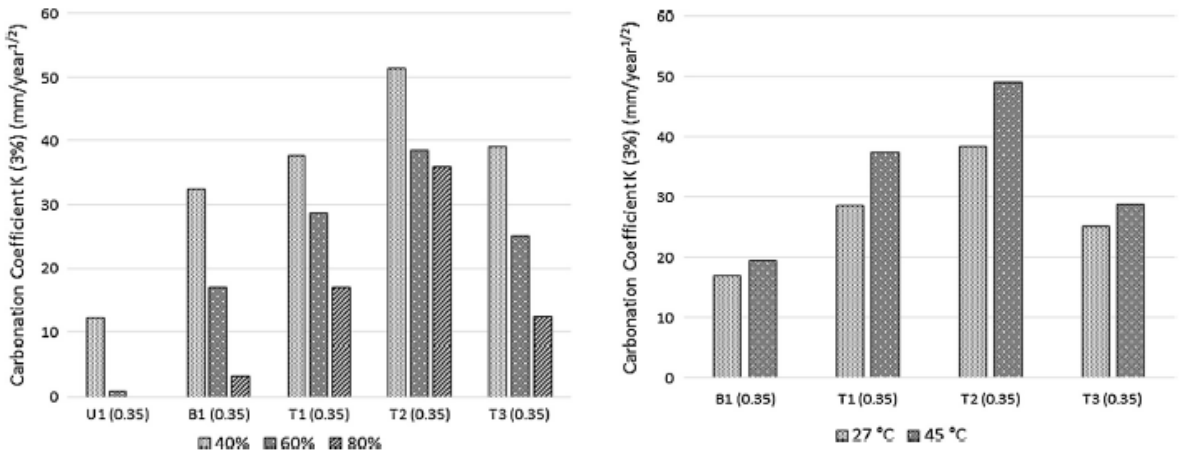

Figure 2.26: Carbonation coefficient of (a) samples (w/c = 0,35) exposed to different relative humidity (b) samples exposed to 27°C and 45°C temperature at 60 % relative humidity (reproduced from Shah and Bishnoi (2018))

2.4.1.3 Models predicting carbonation depth (penetration) in concrete

Carbonation in concrete is a process that occurs over a long period of time. It is therefore worthwhile to be able to estimate the extent of carbonation as it is directly related to the service life of RCS. Hence, several attempts founded in different principles have been made to estimate the carbonation depth in concrete. In this section, two models namely (1) a mathematical model, and, (2) a reaction rate model are discussed. It should be noted that some of these models have taken on the form of an empirical model that is based on the relationship between the carbonation depth and time, see Equation 2.31. A discussion is presented followed by the shortcomings of each approach.

$$x = k\sqrt{t} \tag{2.31}$$

where x is the carbonation depth

k is the carbonation coefficient,

t is the elapsed time

2.4.1.3.1 Modelling carbonation in concrete

The mathematical model for carbonation is based on the diffusion of CO_2 and its chemical reaction with the calcium hydroxide present in the concrete. An illustration of the diffusion process and the parameters of the mathematical model is shown in Figure 2.27 on a differential element of length dx.

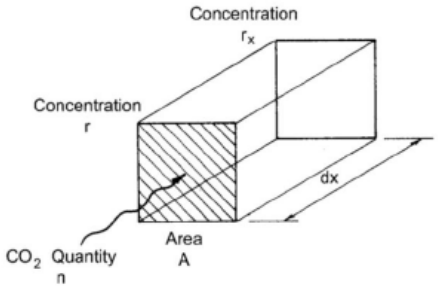

Figure 2.27: Diffusion process and the parameters used for the mathematical model (reproduced from Richardson (2004))

where n is the mass of CO_2 diffusing through an area, A, into the element,

A is the highlighted area,

r is the CO_2 concentration at the surface,

r_x is the CO_2 concentration at depth x.

The mass of CO_2 diffusing into the differential element can mathematically be described using Equation 2.32 and the quantity of CO_2 used in the chemical reaction with calcium hydroxide is given as Equation 2.33. Assuming that the entire amount of CO_2 diffusing inward is used in the carbonation process and that the quantity present at the carbonation front, or the boundary separating the carbonated and uncarbonated regions of concrete, is negligible Equations 2.32 and 2.33 can be equated, simplified and integrated to produce Equation 2.34.

$$dn = DA\left(\frac{r - r_x}{dx}\right)dt \tag{2.32}$$

$$dn = CAdx \tag{2.33}$$

where D as the carbonation diffusion constant,

C as the amount of alkaline material in a unit volume,

t as the time.

$$x = \frac{\sqrt{2Drt}}{C} \tag{2.34}$$

In Equation 2.34 the carbonation depth, x, can be calculated by substituting the values of the carbonation diffusion constant, D, the carbonation concentration, r, and the amount of alkaline material C. The carbonation diffusion coefficient can be determined from experiments under steady state conditions. Whilst the carbon dioxide concentration is normally known and the amount of alkaline material can be determined based on the mix proportions.

Reviewing literature, it is clear that the mathematic model does not take all parameters influencing the carbonation process in concrete into account. For instance, the model lacks a parameter taking the RH into account. Also, the evolution of the microstructure due to carbonation is not accounted for. This ignores key contributing factors such as (1) the effect of pore water level or pore saturation, and, (2) dissolution of CO_2 in concrete. A temperature term is also not present and it should be noted that the carbonation diffusion constant changes over time.

2.4.1.3.2 Reaction rate model for carbonation in concrete

Papadokis (2000) set up a reaction rate carbonation model by using mass balance and applying it to the mix constituents, see Equation 2.35.

$$\frac{C}{\rho_C} + \frac{P}{\rho_P} + \frac{A}{\rho_A} + \frac{W}{\rho_W} + \frac{D}{\rho_D} + \varepsilon_{AIR} = 1 \tag{2.35}$$

where C, A, *W*, and, D is the cement, aggregate, water and, admixture content

ρ_C, ρ_P, ρ_A, ρ_W, and, ρ_D is the density of respective materials, and,

ε_{air} is the volume of air (entrapped or entrained)

According to Papadakis under “complete” hydration and pozzolanic action the cement, $Ca(OH)_2$ (CH), $C_3S_2H_3$ (CSH) and the total porosity of the carbonated concrete, ε_c, can be calculated from Equations 2.36-2.38.

Silica Fume (SF) – Portland cement concrete (SF < 0.18C)

$$CH = 029C - 1.62SF \tag{2.36a}$$

$$CSH = 0.57C + 2.49SF \tag{2.36b}$$

$$\varepsilon_c = \frac{W - 0.267C - 0.0278SF}{1000} \tag{2.36c}$$

Fly ash (low calcium) – Portland cement concrete (FL < 0.23C)

$$CH = 0.3C - 1.3FL \tag{2.37a}$$

$$CSH = 0.57C + 1.25FL \tag{2.37b}$$

$$\varepsilon_c = \frac{W - 0.268C - 0.177FL}{1000} \tag{2.37c}$$

Fly ash (high calcium) – Portland cement concrete (FH < 0.58C)

$$CH = 0.3C - 1.3FH \tag{2.38a}$$

$$CSH = 0.57C + 0.79FH \tag{2.38b}$$

$$\varepsilon_c = \frac{W - 0.267C - 0.203FL}{1000} \tag{2.38c}$$

The reaction rate model set up by Papadakis et al. (1992) takes into account physiochemical processes during carbonation in concrete. These processes include the gaseous diffusion of CO_2 in the concrete pores, the dissolution of solid CH in the pore solution of the CO_2 in the aqueous film of the pores, the dissolution of CH and the reaction with CO_2, and, the reaction between the CO_2 and the CSH and some of the unhydrated phase of cement. From these processes a mathematical model yields a set of complex nonlinear system of differential equations in space and time. The system can be solved by using simplified assumption that lead to the formation of the carbonation front. For a one dimensional geometry, the analytical expression presented in Equation 2.39 can be used to estimate the evolution of the carbonation front, x_c, over time.

$$x_c = \sqrt{\frac{2D_{eCo2}\left(\frac{CO_2}{100}\right)t}{0.33CH + 0.214CSH}} \tag{2.39}$$

where,

$$D_{e,cos}=D_{e,co2} = A\left(\frac{2C}{\frac{c}{\rho_c}+\frac{p}{\rho_p}+\frac{w}{\rho_w}}\right)^a\left(1-\frac{RH}{100}\right)^b \tag{2.40}$$

For 0.5 < W/C < 0.8

A = 1.64 x 10-6, a = 1.8, and b = 2.2

For 0.38 < W/(C+kP) < 0.58

A = 6.1 x 10-6, a = 3, and b = 2.2

	SF	FL	FH
k =	2	0.5	1

2.4.2 Chloride ingress in concrete

Chloride ingress and associated corrosion deterioration of reinforcing bars embedded in concrete counts under the most prevalent forms of deterioration in RC structures. The outcome of such an attack is the initiation of reinforcement corrosion. The mechanism of destroying the passivity by the high alkaline (high pH) holds similarities to that of carbonation. However, in this case the corroding area is typically localised to a small area. This significantly decreases the service life of RC structures because of what is known as pitting corrosion. In the following sections the process that leads to chloride induced corrosion is discussed. The sections begin with a brief overview of the sources of cracks in concrete, followed by chloride penetration in concrete. The effect of the mix constituents is also touched and the section finally ends off with models predicting the time to corrosion initiation due to chloride penetration.

2.4.2.1 Chloride ingress (penetration) and chloride-induced corrosion in reinforced concrete

The introduction of chlorides into reinforced concrete leads to the inevitable loss of service life through chloride-induced corrosion of the steel reinforcement. The mechanism of corrosion initiation, destruction of the passivity layer by lowering the pH at the steel, is thought to be similar to that of carbonation. Carbonation is usually a slow process, over several years or decades. Chloride ingress into uncracked concrete is typically also gradual, requiring several years to reach reinforcing steel in sufficient quantities to cause corrosion initiation. However, cracks in concrete are pathways along which environment chlorides penetrate at relatively high rates. This mechanism of chloride penetration into concrete dramatically shortens the service life of RC structures, especially if the crack penetrates to the reinforcement level. Once at the reinforcement level, chlorides reduce the resistance of the passivity layer by lowering the pH of the concrete. At this point, when the chloride concentration reaches a critical level (chloride threshold), chloride-induced corrosion of the reinforcing steel may initiate. Equations 2.40 to 2.42 present the chemical processes that occur at the concrete steel interface once chloride reaches the reinforcement.

$$Fe^{2+} + 2Cl^{-} \rightarrow FeCl_2 \tag{2.41}$$

$$FeCl_2+ + 2H_2O \rightarrow Fe(OH)_2 + HCl \tag{2.42}$$

$$FeOCl + H_2O \rightarrow FeCl_2 + Cl^{-} \tag{2.43}$$

It should be noted that chloride-induced corrosion deterioration may have more severe consequences than carbonation-induced corrosion. Carbonation typically causes uniform corrosion over the length of the reinforcement, whilst chlorides tend to cause localised corrosion (pitting). Localised corrosion is characterised by a small anodic region and a large cathodic region which has been linked to high levels of corrosion rates. This phenomenon can be explain by the chemical reactions in Equations 2.41 to 2.43. The small region (pitting area) of reinforcement exposed by the crack is attacked by chlorides thus forming ferric chloride, $FeCl_2$, which in-turn reacts with water to form hydrochloric acid, HCl. The formation of $FeCl_2$ and HCl leads to the reduction in the pH of the pitting area which may expand to

adjacent regions due to oxychloride formed, FeOCl, which sets free chlorides in a hydrolysis reaction. As mentioned earlier, chloride-induced corrosion will only initiate once a critical level of chloride concentration is reached. According to Nilsson et al. (1996) the critical level of chloride concentration is a dependent on binder type, concrete cover, temperature, relative humidity and the electrical potential of the reinforcement. Typical values found in literature are tabulated in Table 2.11.

Table 2.11: Typical values of the critical chloride level as found in literature

Reference	Binder type	Critical chloride level (% mass w.r.t. binder)
Trejo et al. (2003)	OPC[a]	0.02 – 0.24
Scott (2004)	Various binders-	0.08 – 0.53
Lambert et al. (1991)	OPC[a] and SRPC[b]	1.0 – 3.0
Alonso et al. (2000)	OPC[a]	1.24 -3.08

[a] Ordinary Portland Cement
[b] Sulphate Resistant Portland Cement

2.4.2.2 Parameters influencing chloride-induced corrosion in concrete

2.4.2.2.1 Types of cracks in concrete

Cracks, in reinforced concrete, serve the major role of providing direct pathways for chlorides to penetrate to the reinforcement level. Figure 2.28 shows some of the causes of cracks.

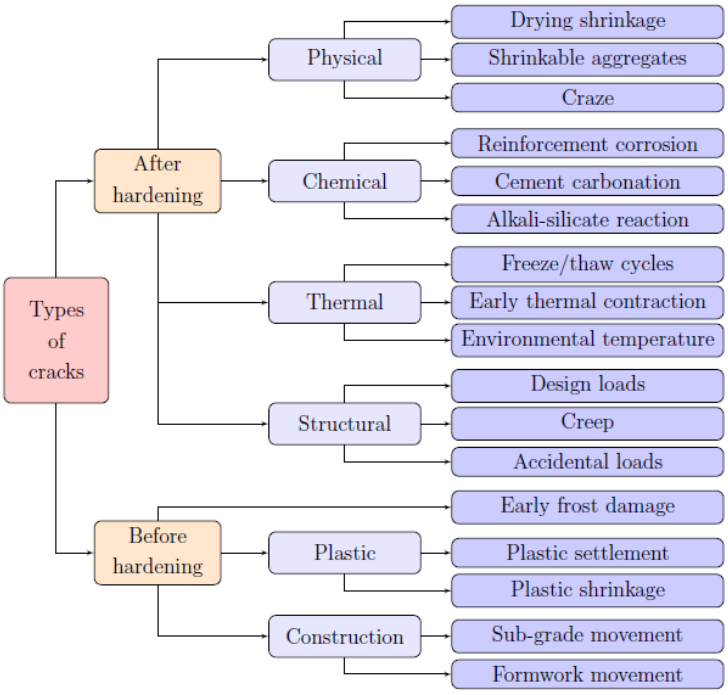

Figure 2.28: Cause of cracks in reinforced concrete structures (reproduced from Bezuidenhout (2017))

In general the causes of cracks can be grouped into two categories, namely (1) fresh state / before hardening, and (2) hardened state, as shown in Figure 2.28. A few of these causes are discussed in this section.

In the fresh state of concrete, cracks may arise due to plastic shrinkage, environmental temperature and due construction errors such formwork movement. In areas like South Africa, where concrete in its fresh state is rarely exposed to freeze thaw, common causes of early age cracks are as a result of poor construction techniques, plastic settlement and plastic shrinkage. Combrinck (2016) investigated cracking of plastic concrete in slab-like elements. Combrinck listed the causes of plastic concrete cracking as differential settlement and evaporation of the free pore water. The differential settlement leads to plastic settlement cracking and the evaporation of the free pore water leads to plastic shrinkage cracks. Boshoff and Combrinck (2013) also proposed a so called "severity model" based on the volume of water evaporating from the concrete to predict and describe the severity of plastic shrinkage cracks with a value called the Plastic Shrinkage Severity value (PShC Severity value). Figure 2.29 depicts the results of the experiment used to set up the model. From Figure 2.29 it can be seen that as a result of the evaporation rate exceeding the bleeding rate there is a build-up of capillary pressure which drops after the formation of a crack. The crack continues to grow with the increase in the evaporation but tends to stabilise after the final set. In the same study Boshoff and Combrinck also found that the addition of fibres decreases the PShC Severity value, see Figure 2.29a and Figure 2.29b.

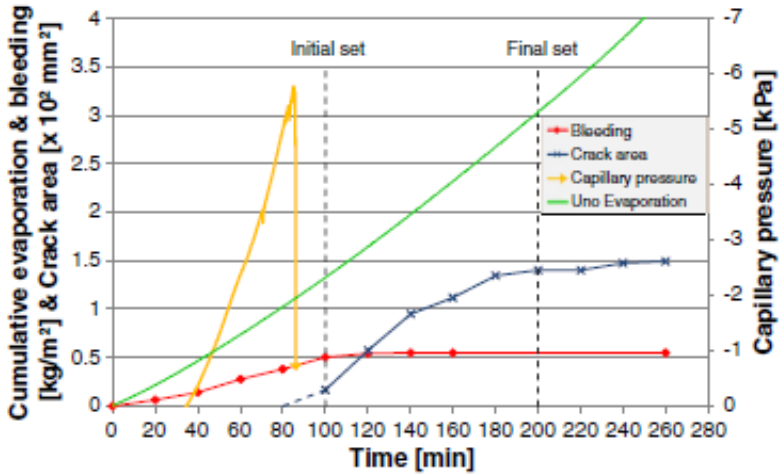

Figure 2.29: Result of a typical plastic shrinkage cracking test (Boshoff and Combrinck (2013))

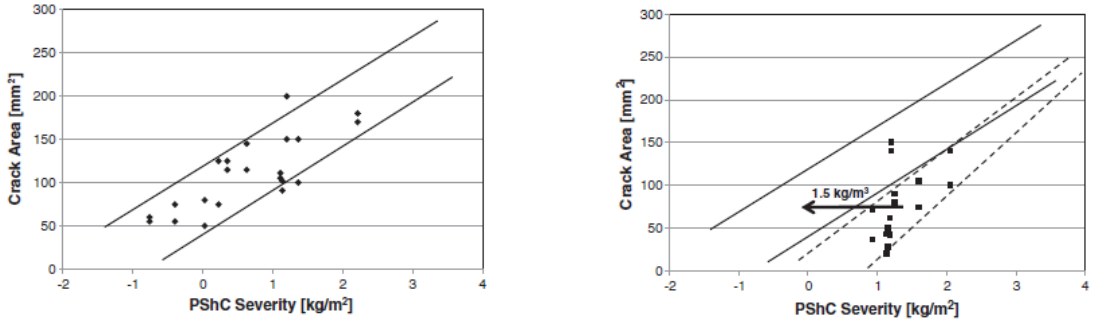

(b) (c)

Figure 2.30:Severity value as a function of the measured crack area (b) no fibres and (c) effect of 0.1% fibre volume on the PShC Severity. Dashed lines indicating fibres, solid lines indicating no fibres (Boshoff and Combrinck (2013))

In the hardened state the causes of cracks are categorised as (1) physical, (2) chemical, (3) thermal, and, (4) structural. The physical mechanism include shrinkable aggregates and drying shrinkage of the paste. Under chemical, processes that lead to volumetric change are included such as reinforcement corrosion and alkali-silicate reaction that cause expansion, and cement carbonation that leads to shrinkage. Another thermal crack mechanism is prevalent in frosty regions, namely freeze / thaw, thermal expansion due to the heat of hydration of the concrete, and direct sun exposure. Structural causes of cracks are, amongst others, self-weight and imposed loads on the structure, occupancy, wind or seismic, as well as accidental loads.

2.4.2.2.2 The influence of cracks in concrete on chloride-induced corrosion

Cracks in concrete are undesirable for aesthetic and durability purposes. They are not only an "eye-sore" but influence the processes in concrete. In this section the influence of the properties of cracks such as orientation, width and spacing on chloride-induced corrosion are discussed.

Crack orientation

Cracks in concrete may orientate themselves along the length of the reinforcement, longitudinal cracks, perpendicular to the reinforcement, transverse cracks, or at an angle in the case of shear structural cracks. The mechanism involved in forming the crack is what governs the orientation. For example, transverse cracks are most likely to occur in beams as a result of flexural behaviour. However, longitudinal cracks may arise in beams due to differential settlement of the concrete in its plastic state, or tensile splitting cracking in regions of high bond stress between reinforcing steel and the surrounding concrete. In chloride-induced corrosion, cracks allow chlorides, oxygen and water easy penetration into the concrete. For transverse cracks, the cathodic region is initially limited to the reinforcement area exposed by the intersecting crack. When a crack forms longitudinally along the length of the reinforcement, the area exposed is large relative to transverse cracks. An argument can therefore be made that longitudinal cracks may result in more severe corrosion due to the larger area exposed. This reasoning is in line with Bezuidenhout (2017).

Crack width

In concrete the crack width in most cases refers to the surface crack width. This parameter is consider important in the corrosion process (Paul (2015), Bezuidenhout (2017), Otieno et al. (2010)). However, the crack width should be coupled with the depth of the concrete cover. A crack of a certain width and cover depth (say 0.1 mm width and 15 mm concrete cover depth) would not have the same effect as one with the same width and double the concrete cover depth (30 mm concrete cover depth). Pettersson et al. (1996) studied the effect of cracks on reinforcement corrosion of high performance concrete in a maritime environment. In the study the corrosion rates of specimens with crack widths smaller than 0.4 mm were affected by a change in concrete cover depth (15 mm to 30 mm). The results of specimens with large crack widths, exceeding 0.4 mm, showed no significant changes in the corrosion rate obtained from specimens of different cover depths.

Otieno et al. (2010) studied chloride-induced corrosion of steel in cracked concrete. In the study Otieno et al. kept the water binder ratio, cement composition constant and varied the crack width. The results obtained, after week 26 to 31 of accelerated chloride-induced corrosion, in the study showed that an increase in the crack width leads to an increase in the average corrosion rate. It should be noted that after 31 weeks of the study, uncracked specimens were still experiencing passive corrosion rates (values lower than 0.1 µA/cm^2) and that self-healing was prevented in the pre-cracked specimens by reloading the specimens twice within the study period. Figure 2.31 shows the results of the corrosion rates.

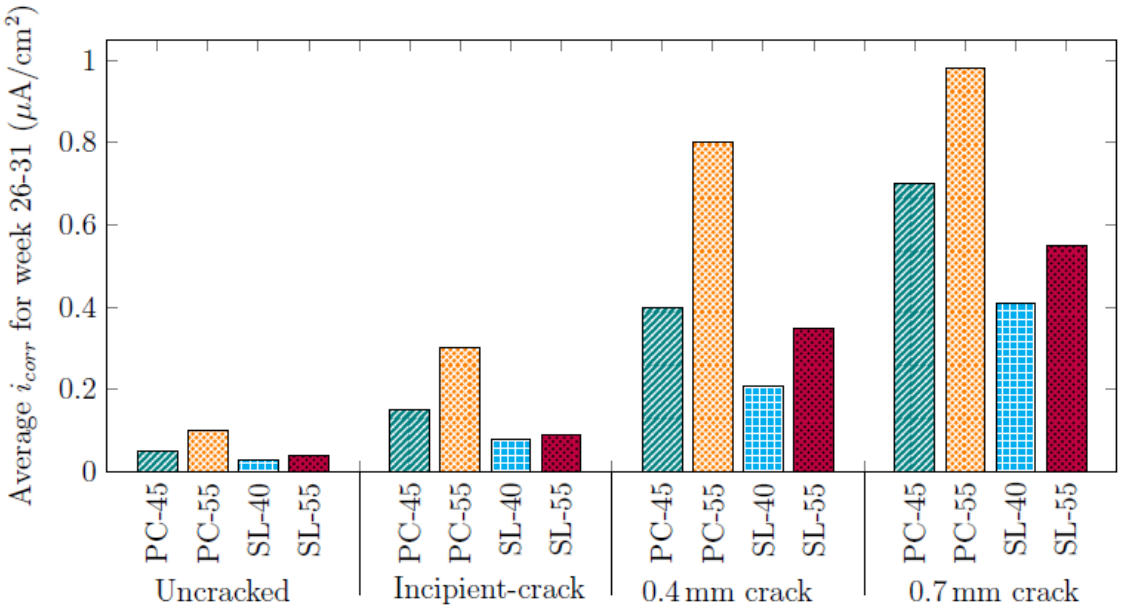

Figure 2.31: Results of week 26-31 showing corrosion rates (reproduced from Otieno et al.(2010))

It should be noted that there is agreement in the literature that crack widths do influence the corrosion rate of steel in reinforced concrete as indicated by researchers (Schieβ et al. (1997), François et al. (2006), Pacheco Farias (2015)). See Table 2.12 for allowable crack widths as listed in the various national and internal standards.

Table 2.12: Allowable crack widths (w_{cr}) of reinforced concrete structures exposed to chloride environments

Standard	w_{cr} [mm]
ACI 224 (1994)	0.15
NEN 6720 (1995)	0.2
Eurocode 2 (2004)	0.3
SANS 10100-1 (2000)	0.3
BS 8110 (1997)	0.3
FIB/Model code (2010)	0.3

Crack spacing (frequency / density)

Crack density as defined by Bezuidenhout (2017) is the number of transverse cracks penetrating to the reinforcement per unit length. It has been shown in the literature that crack density and crack spacing play a role in the corrosion rate (Paul (2015), Bezuidenhout (2017) and Ahmed and Mihashi (2010)).

Arya and Ofori-Darko (1996) investigated the influence of crack spacing on reinforcement corrosion in concrete using beam specimens of 1360 mm in length exposed to chloride. The beam specimens were reinforced with two steel bars and a central stainless steel rod acting as a counter-electrode. In order to test the crack frequency (*f*) parameter, specimens were made with 0, 1, 4, 8, 12, 16 and 20 cracks. This corresponds to the crack spacings (S_c) of 680, 272, 150, 105, 80 and 65 mm. Other parameters such as crack depth, concrete cover, water binder ratio and total crack width were kept constant for all specimens at 40 mm, 42 mm, 0.65 and 2.4 mm. Figure 2.32a shows the test setup and Figure 2.32b shows the result obtained from the tests.

The results obtained by Arya and Ofori-Darko show that generally there is an increase in mass loss with an increase in crack frequency. Interpreting these results using crack spacing indicates that the mass loss increases with a decrease in crack spacing. However, it should be noted that in the study the they found that the results of the beam specimen with a crack frequency of 20 (Sc = 65 mm) yielded a lower cumulative mass loss than that of the beam specimens with crack frequency 16, 12, and 8 (80 mm, 105 mm, and 150 mm). This is ascribed to crack healing, as the 20 cracks in the beam had fine widths of 0.12 mm (2.4 mm/20).

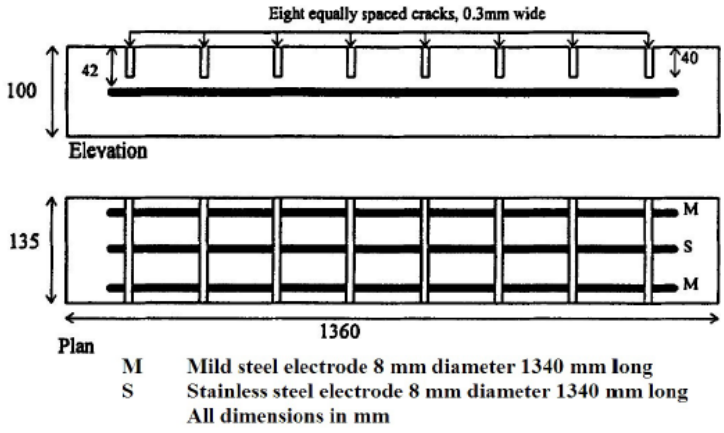

(a)

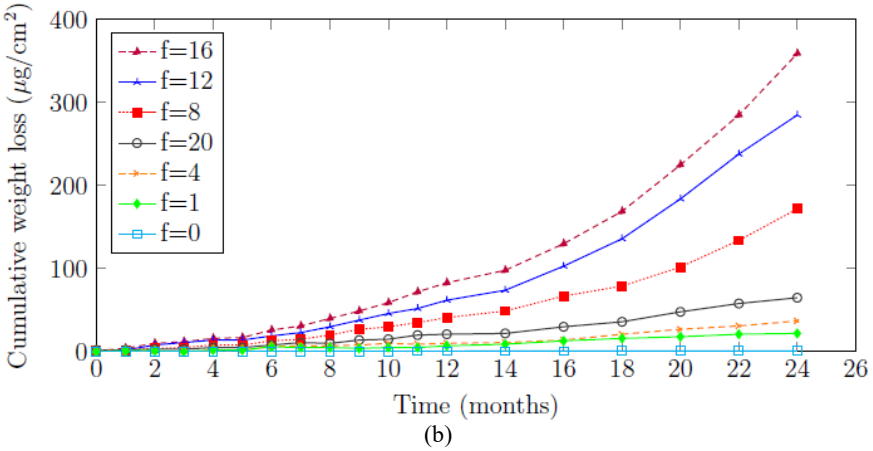

(b)

Figure 2.32: (a) Test setup of beam specimens, and (b) experimental test results illustrating the effect of crack frequency of cumulative mass loss due to chloride-induced corrosion (Arya and Ofori-Darko (1996))

2.4.2.2.3 Corrosion rate definition and pitting factor

Corrosion rate

The corrosion rate as defined by Andrade and Alonso (1996) is the amount of corrosion produced by a unit of surface area when referred to a specific period of time. The corrosion rate may be obtained through physical means by measuring the difference in the weight of the corrosion element before and after exposure to a corrosive environment, see Figure 2.33. This method for determining the corrosion rate is known as the gravimetric method. A drawback of this method is that it requires physical access to the corroding element. In RC structures the corroding element, reinforcing steel, is embedded in the concrete. Therefore, determining the corrosion rate requires the active removal of the rebar by destructive methods. This proves costly and would require active repair making it impractical.

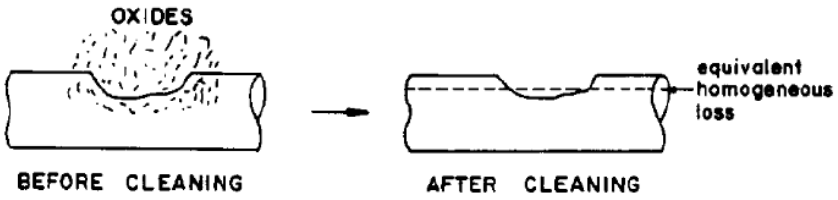

Figure 2.33: Schematic illustration of the procedure for determining the corrosion rate based on the gravimetric method (Andrade and Alonso (1996))

A practical approach to determine the corrosion rate in RC is to use non-destructive methods such as electrochemical techniques. These techniques make use of Faraday's law to convert the electrochemical parameters into gravimetric parameters as given in Equation 2.44.

$$\frac{It}{F} = \frac{\Delta W}{ZW_m} \tag{2.44}$$

where

I is the electrical current [A]

t is the time [s]

F is Faraday's constant, taken as 96 500 coulombs,

W is the weight loss [g]

Wm is the metal, taken as 55.845 g/mol for iron,

Z is the valence, +2 for iron.

In Equation 2.44 the electric current is referred to as the "corrosion intensity", denoted as I_{corr}, and has units $\mu A/cm^2$ or μm/year when uniform corrosion is assumed, represented as the equivalent homogeneous loss in Figure 2.33. See Table 2.13 for a classification of I_{corr}.

Table 2.13: Corrosion intensity classification (adapted from Andrade and Alonso (1996))

I_{corr} [μA/cm^2]	Corrosion level
< 0.1	Negligible
0.1 – 0.5	Low
0.5 – 1	Moderate
> 1.0	High

It should be noted, that I_{corr} represents an "instantaneous" value. That is to say that, it is the corrosion intensity at a particular moment in time. The corrosion rate is the representation of periodic I_{corr} readings expressed over time, I_{corr}-time domain, showing the evolution of the corrosion process. The integration of the corrosion rate, I_{corr}-time, gives the total current which has to equal the weight loss of the corroding element. For RC structures, the results of the electrochemical techniques can be verified by using the gravimetric method.

Pitting factor (α_{pit})

The consequence of corrosion in RC is the loss of load bearing capacity due to the reduction of the cross sectional area of the reinforcement. The reduction in the cross sectional area can be quantified through the loss of cross radius, shown in Figure 2.34, and is obtained through Equation 2.45.

$$P_x = 0.0115 I_{corr} t_p \tag{2.45}$$

where P_x is the loss of cross radius, and

t_p is the time from corrosion initiation.

In cracked concrete under chloride attack the corrosion may be localised to a small area and therefore the loss of cross radius may be underestimated. This type of corrosion is known as pitting corrosion. The loss of cross radius is then represented as shown in Figure 2.34 and can be obtained by applying a factor, α_{pit}, to Equation 2.45. Equation 2.46 represents the loss of cross radius as a result of pitting corrosion.

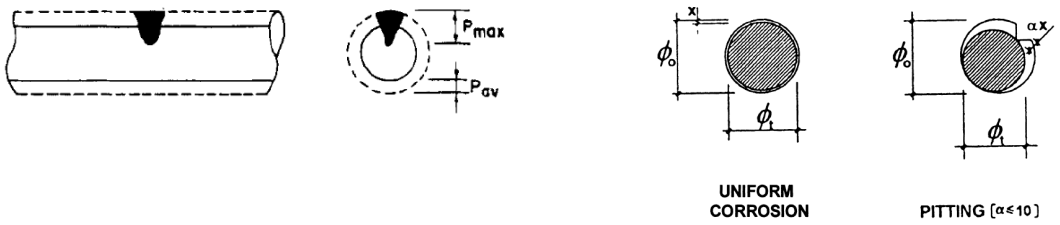

(a) (b)

Figure 2.34: Illustration of (a) pitting corrosion (Andrade and Alonso (1996)), and (b) loss of cross radius (Andrade and Alonso (2001))

$$P_{max} = \alpha_{pit} P_x \quad (2.46)$$

where

α_{pit} is known as the pitting factor, see Table 2.14 for suggested values.

Table 2.14: Suggested pitting factor, α_{pit}, for corrosion in RC

Reference	Description	α_{pit}
Carbonation	Uncracked, natural	1
Tutti (1982)	Uncracked, impressed current	4 – 10
Gonzalez et al. (1988)	Uncracked, natural	4 – 8
	Uncracked, accelerated	5 – 13
Neff et al. (2011)	Uncracked, accelerated	18
Otieno (2014)	Cracked, natural and accelerated	10

2.4.2.2.4 The influence of the mix constituents on chloride-induced corrosion

The mix constituents influence the properties of concrete and processes that occur throughout its lifespan. This section explores the effects of water binder ratio, binder type, and concrete cover on chloride-induced corrosion.

Water binder ratio (w/b), binder type, concrete cover depth

A major contributor to the properties of concrete is the water cement ratio. This aspect is normally an indicator of the strength of the concrete and porosity. Mangat et al. (1994) investigated the microstructure, chloride diffusion and corrosion in blended cement pastes and concrete. In the study Mangat et al. kept the binder content constant at 430 kg/m^3 and tested corrosion rates of 12 mm singly reinforced specimens of 100x100x370 mm made with three different water binder ratios , 0.45, 0.58, and, 0.76, respectively. The water binder ratio is the ratio of water content to that of the total cementitious content (i.e. cement and fly ash). A salt water spray chamber was used to cyclic spraying of a salt water solution for 600 days. Table 2.15 shows the result obtained from the study conducted by Mangat et al.

Table 2.15: Corrosion rate results of the different water binder ratios (adapted from Mangat et al. (1994))

Water binder ratio	i_{corr} [µA/cm^2]
0.45	0.13
0.58	0.65
0.76	2.16

The results indicate that with an increase in water binder ratio there is a corresponding increase in corrosion rate. Similar results were found in the study mentioned early by Otieno et al. (2010), see Figure 2.31.

Scott and Alexander (2007) investigated the influence of binder type, cracking and concrete cover depth on corrosion rates of steel in chloride contaminated concrete. Scott and Alexander used as four different combinations of binder (1) neat OPC as a reference, (2) OPC and Slag (SM), (3) OPC and fly ash (FA), and, (4) OPC and silica fume (SF). Other variables include the cover depth (20 mm and 40 mm) and the crack width (0.2 mm and 0.7 mm). The results of the study, shown in Figure 2.35, indicate that there is an accompanying decrease in corrosion rate due to cement replacement (blended cements). This could be as a result of the change in porosity of the concrete. Using supplementary cementitious materials increases the durability of the concrete by reducing the porosity of the concrete. Another explanation offered by other researchers (Dhir et al. (1997), Bertolini et al. (2004), Glass et al. (1997)) attributed this behaviour to the chloride binding effect. When chlorides penetrate the concrete matrix some of the chlorides react with the SCMs and form what is known as Friedal's salt. These chlorides are bound and are believed to play no part in the corrosion process. However, Glass and Buenfield (1997) have demonstrated that in the event of a drop in pH level below 12, the chlorides may become unbound and participate in the corrosion process. It should be noted that the replacement of cement with different SCMs do not always result in a decrease in free chloride content. For FA and slag a decrease in free chlorides were found by Glass and Buenfield. However, silica fume produced an increase in free chloride content. Therefore free chloride content is a function of the concrete composition and pH level (Paul (2015), Gaynor (1985), Liu (1996), and Dhir et al. (1990)).

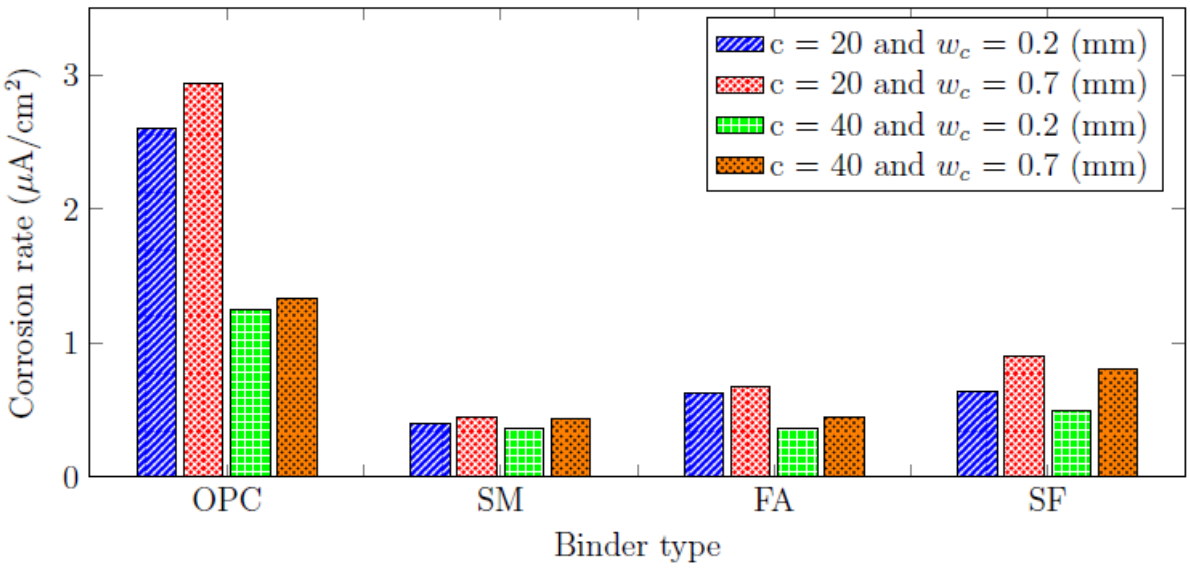

Figure 2.35: Corrosion rate versus binder type (reproduced from Scott and Alexander (2007))

The effect of concrete cover depth can also be seen from the results of Scott and Alexander (2007) shown in Figure 2.35. The results of the corrosion rates of the specimens with 40 mm concrete cover depth is consistently lower than the corresponding samples with 20 mm concrete cover depth. An explanation for this could be that the elements (H_2O, Cl^-, and, O_2) involved influencing the corrosion rate have longer distances to cover to the reinforcement level in cathodic regions. Bezuidenhout (2017) points out that doubling the concrete cover depth may result in a 75 % reduction in the oxygen diffusion flow rate and this may decrease the corrosion rate.

2.4.2.3 Chloride penetration (Time to corrosion initiation) and corrosion rate modelling

Reviewing the literature on chloride-induced corrosion in reinforced concrete it is clear that it is a complex problem with grave infrastructure and economic impact. It is also clear from the literature that chloride-induced corrosion may only initiate once chlorides reach the reinforcement level. This is echoed in the current approach to service life modelling whereby the service life of reinforced concrete structures are taken as the time to corrosion initiation. In reality the structure may survive for years even decades after corrosion initiation. This can be seen in the current research trend whereby approaches to quantify and determine the extent of corrosion damage in reinforced concrete structures is picking up steam. In this area the role of cracks and their properties in corrosion process is a hot topic of debate. In this section the current approach, time to corrosion, is presented and discussed while a model representing the propagation phase is also discussed.

2.4.2.3.1 Chloride penetration modelling (Time to corrosion)

The current approach towards modelling the time to corrosion due to chloride penetration is to use Fick's law in combination with the chloride diffusion coefficient of the concrete. The resulting equation predicting the concrete chloride profile is given as Equation 2.47.

$$C_x = C_s\left[1 - erf\left(\frac{x}{2\sqrt{tD_{app}}}\right)\right] \tag{2.47}$$

where

C_x is the percentage of chlorides at depth x (w.r.t. weight of binder),

C_s is the percentage concentration of the chlorides at the surface (w.r.t. weight of binder),

D_{app} as the apparent diffusion coefficient of chloride,

x as the depth from the surface of the concrete,

t as the time.

In order to use this model the user can make use of AASHTO T277 and NT BUILD 492 (1999) which suggest that the rapid chloride penetration test can be used to determine the apparent diffusion coefficient for the concrete. Figure 2.36a,b show an example of the influence of the apparent diffusion coefficient and time to corrosion using a chloride threshold of 1% and 5% surface chloride concentration.

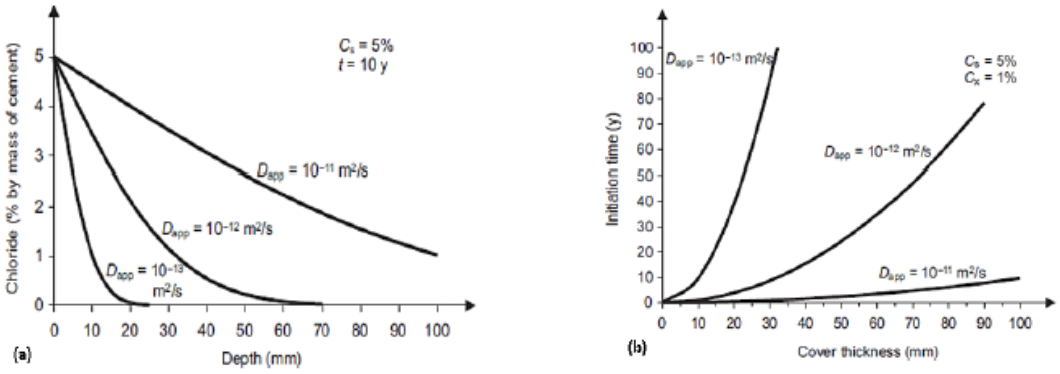

(a) (b)

Figure 2.36: Effect of D_{app} on (a) cover depth (b) time to corrosion (reproduced from Bertolini et al. (2004))

From the example shown in Figure 2.36a,b it can be seen that small values of D_{app} result in long time period to corrosion and that a large D_{app} results in a short time to corrosion period. It should be noted that the model does not take into account changes in the microstructure of the concrete and assumes that the D_{app} is constant over the service life of the concrete. This is not accurate because changes in the relative humidity would result in a change of the moisture content of the concrete which slows down diffusion. The model should account for this by introducing a relative humidity term.

2.4.2.3.2 Chloride-induced corrosion model by Otieno (2014)

As mentioned previously, currently the service life of RC structures is take as the time to corrosion. This approach is over conservative due to the fact that corrosion may take years, decades, to destroy the integrity of the RC structure. It is therefore worthwhile to develop models to predict the corrosion rate and therefore the "full" service life of the building. Reviewing the literature it seems that only a handful of these model exist (Morinaga (1988), Vu et al. (2000), Scott (2004), Otieno (2014)). In this section the empirical model derived by Otieno (2014) is presented. It should be noted that with the current approach to service life of RC structures the role of cracks in corrosion have only recently been gaining attention. As such, these empirically derived models lack terms that influence corrosion rates.

Empirical model for chloride-induced corrosion in cracked and un-cracked concrete by Otieno (2014)

Otieno (2014) tested chloride-induced corrosion in laboratory and field based specimens over a period of 28 months. Otieno used 10 mm diameter singly reinforced concrete beam specimens of dimensions 120 x 130 x 375 mm. In the investigation two water binder ratios, 0.4 and 0.55, were used and three different combinations of binder, neat OPC and two blended types (OPC/GGBS and OPC/FA), were used. Other parameters tested in the investigation is the concrete cover depth (20 and 40 mm) and crack

width (un-cracked, incipient crack (only for 20 mm concrete cover depth), 0.4 mm, and, 0.7 mm). Laboratory specimens were subjected to accelerated chloride exposure by wetting and drying cycles and field based specimens were exposed to the natural environment (maritime tidal zone). Based on the data collected Otieno regressed two empirical equations for the corrosion rate of steel in reinforced concrete, one for accelerated exposure conditions (Equation 2.48a) and one for natural exposure conditions (Equation 2.48b).

$$i_{corr} = \left(5.18e^{0.01\left(D_{90}x10^{10}\right)}\right)\left(\frac{c}{w_{cr}}\right)^{-0.96\left(D_{90}x10^{10}\right)^{-0.35}} \quad (2.48a)$$

$$i_{corr} = \left(0.64e^{0.06\left(D_{90}x10^{10}\right)}\right)\left(\frac{c}{w_{cr}}\right)^{-0.21e^{0.02\left(D_{10}x10^{10}\right)}} \quad (2.48b)$$

where i_{corr} is the corrosion rate approximately 28 months after corrosion initiation,

D_{90} is the 90 day chloride conductivity index,

c is the concrete cover depth,

w_{cr} as the surface crack width.

Figure 2.37a,b show the regressed corrosion rate values of the field based specimens, and the laboratory-based specimens, versus the average measured corrosion rates recorded in the investigation. The models show relative agreement between the predicted corrosion rate values and measured corrosion rate values.

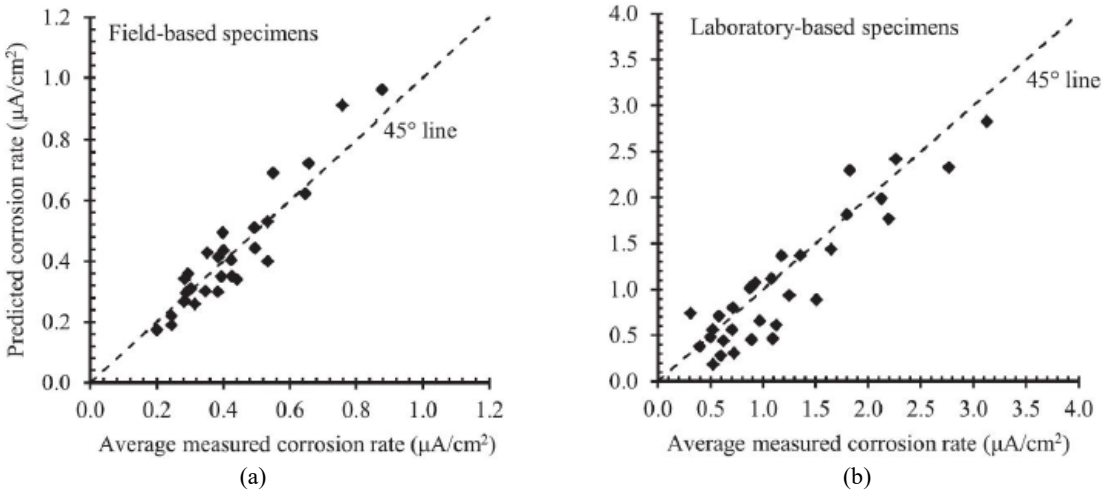

Figure 2.37: Regressed corrosion rate of (a) field-based (b) laboratory-based specimens versus average measured corrosion rate (Otieno et al. (2016))

The model proposed by Otieno (2014) does not include a time parameter and thus the evolution of the corrosion rate cannot be estimated. Also, the model only makes provision for a single crack. Thus, the influence of crack spacing is not taken into account.

2.4.3 Surface treatment agents

2.4.3.1 Introduction and classification of surface treatment agents (STA)

Surface treatment agents are chemicals that are used to alter the surface properties of the concrete. These agents can be classified into three groups, namely (1) coatings, (2) pore-liners, and (3) pore-blockers. Coatings are normally membranes that are used to cover the surface of the concrete to prevent ingress of deleterious substances. Pore-liners also known as hydrophobic or water repellents are products that gives that make the concrete hydrophobic. Pore-blockers react with the hydration products to form insoluble products that block the capillary pores of the concrete. Figure 2.38 shows the various categories of surface treatment agents.

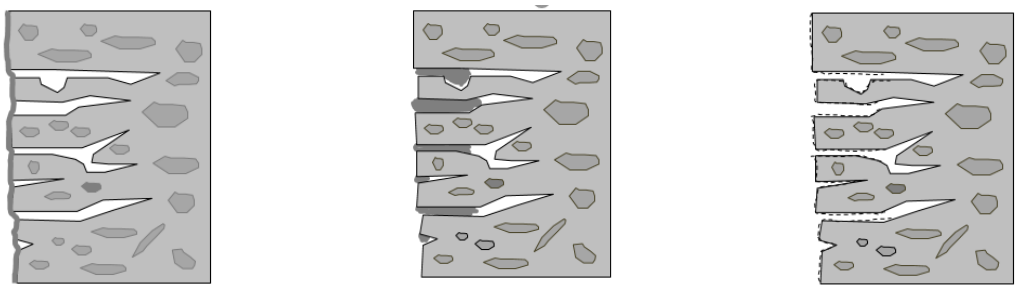

(a) (b) (c)

Figure 2.38: Classification of surface treatment agents (a) Coatings, (b) pore-blockers, and, (c) pore-liners (Medeiros and Helene (2009))

2.4.3.2 Effect of surface treatment agents on the properties of concrete

The main reason for using STA is to enhance the durability of concrete. The selection of the type of STA is dependent on the expected type of durability attack. It has been well documented that water ingress in concrete is one of the sources of durability issues in concrete. It carries deleterious substances into the concrete which initiates deterioration processes. STAs aim to prevent or delay the ingress of water by densifying the concrete matrix or imparting hydrophobicy onto the concrete. The alteration of the concrete, microstructure, may improve the overall performance of the concrete. In this section the effect of STA on the residual compressive strength and durability properties are highlighted.

Residual compressive strength

According to Pan et al. (2017) the effect of surface treatment on the compressive strength of concrete is a research area that has not gained much attention. Reason being, is that it is generally accepted that surface treatment is unable to improve the quality and porosity of the entire concrete as it does not penetrate the full depth of the concrete. However a few researchers have reported the effect of surface treatment on the residual compressive strength due to fire damage. Yuan and Li (2015) found that the use of surface coating of concrete lead to a higher residual compressive strength than untreated concrete subjected to elevated temperatures in the range of 200 to 700°C, see Figure 2.39. Li et al. (2017) reported similar findings of 3.8, 3.7, 11.0, 17.3 and 6.1% enhancement in the residual compressive strength after exposure to elevated temperatures of 150, 300, 450, 600 and 750°C.

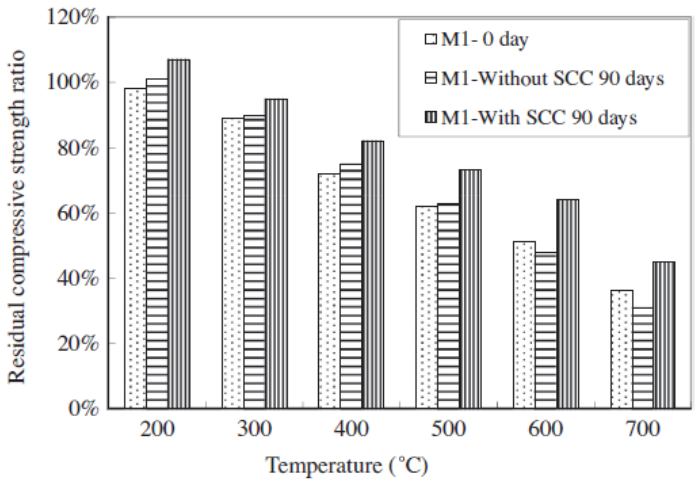

Figure 2.39: Residual compressive strength after exposure to elevated temperatures. M1 – 0 day after exposure, M1 – Without surface coating and recured for 90days after exposure, M1 – With surface coating and recured for 90 days after exposure (Lee et al.(2019)).

Durability properties

Almusallam et al. (2003) investigated the effectiveness of five generic type of surface coatings in improving the durability of concrete. Almusallam et al. performed water absorption tests on coated and uncoated specimens over a period of 56 hours and determined the chloride diffusion coefficient for the concrete and reported on the results. Almusallam et al. found that the uncoated specimens absorbed water rapidly and reported a 5% increase in weight at the end of the tests. The coated specimen had a weight gain in the range of 0.23 and 3.4%. The coefficient of chloride diffusion of the uncoated specimens was found to be 27 times greater than the minimum and 1.2 times the maximum reported for the coated specimens. The variation in results indicates that the effectiveness of the coating is dependent on its composition. Table 2.16 shows the results of the weight gain and chloride diffusion coefficients of the specimens.

Table 2.16: Weight gain of uncoated and coated specimens after 56h of testing and chloride diffusion coefficient (Almusallam et al. (2003))

Coatings	**Weight gain (%)**	**Coefficient of chloride diffusion (10^{-8} cm^2/s)**
Uncoated	4.78	0.47
Acrylic coating (AC1)	0.23	0.03
Acrylic coating (AC2)	1.46	0.23
Polymer emulsion coating (PE1)	3.42	0.40
Polymer emulsion coating (PE2)	3.32	0.45
Epoxy coating (EP1)	1.30	0.20
Epoxy coating (EP2)	0.27	0.04
Polyurethane coating (PE1)	0.21	0.03
Polyurethane coating (PE2)	1.83	0.27
Chlorinated rubber coating (CR1)	0.76	0.12
Chlorinated rubber coating (CR2)	1.04	0.17

Ibrahim et al. (1999) investigated the effect of surface treatment on carbonation and chloride-induced corrosion. Ibrahim et al. prepared untreated and treated specimens (six sealers / coatings) for carbonation depth, chloride profiling and corrosion assessment. Figure 2.40a-b show the results of the carbonation depth over exposure time and the chloride content versus depth (profiling). For carbonation, specimens were exposed to a saturated CO_2 environment. All specimens started carbonating within the first week of the investigating and the untreated specimen had the highest carbonation depth at the end of the investigation. All surface treatments resulted in a decrease in carbonation depth. The most effective coatings in this case was an acrylic coating and silane / siloxane with a topcoat. For this investigation coatings proved effective in preventing carbonation of the concrete. Figure 2.40b depicts the results of the chloride profiles of specimens exposed to 5% NaCl solution for 90 days. In this case, the untreated and silane treated specimens had the highest concentration of chlorides at the top of the specimens. The chloride concentration decreases with increasing depth. All surface treatments improved the resistance of concrete against chloride ingress.

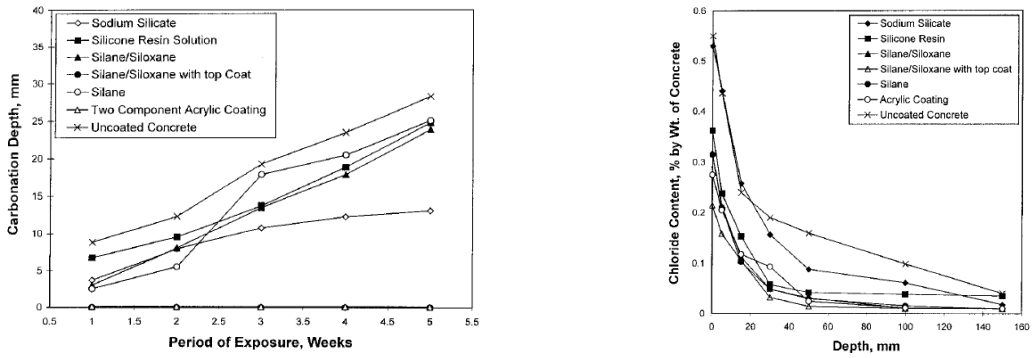

(a) (b)

Figure 2.40: (a) Carbonation depth over exposure period (b) chloride content profiling (Ibrahim et al. (1999))

Figure 2.41a,b show the results of the corrosion potential and corrosion intensity over exposure. After the initial corrosion potential reading, some specimens were treated with the various surface treatments. All treated specimens with the exception of the ones treated with sodium silicate showed an increase in the corrosion potential over the testing period. The untreated specimens had the most negative values and the silane treated specimens had the least negative values over the testing period. A similar result is seen in the corrosion intensity data. All treated specimens showed a decrease in the corrosion intensity values. The drop is attributed to the reduction in oxygen supply due to the mechanism, hydrophobic or pore-blocking, of the surface treatments.

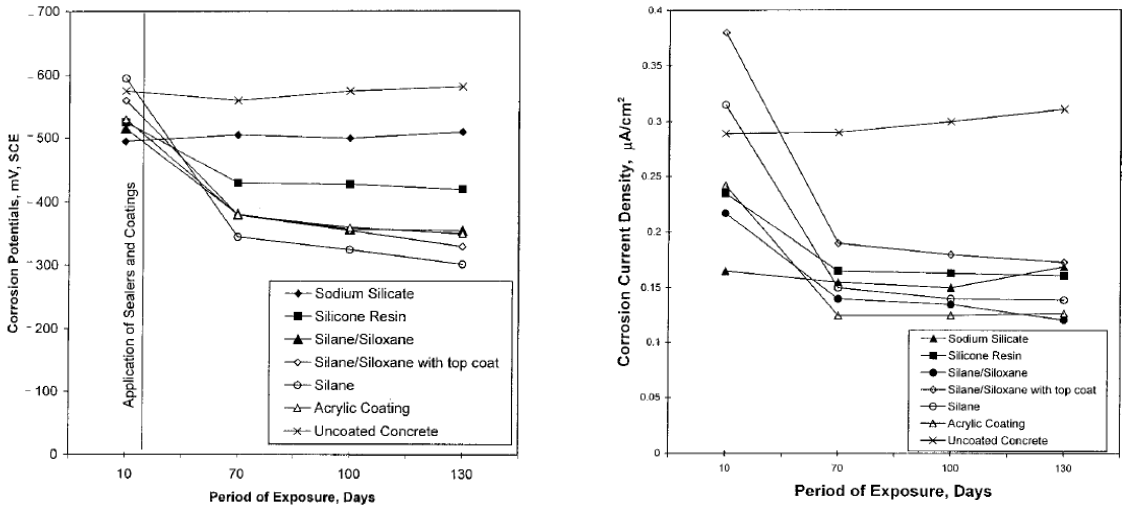

(a) (b)

Figure 2.41: Chloride-induced corrosion (a) corrosion potential, and (b) corrosion intensity, over the exposure period Ibrahim et al. (1999).

2.4.4 Corrosion Monitoring and Assessment

Carbonation and chloride-induced corrosion are deterioration processes with dire financial implications. Reduced service life, and excessive repair intervention to extend service life, are costly. The cost implications are not restricted to the repair itself, but particular economic infrastructure taken out of service, for instance highway bridges, may significantly impact economic activities. Many countries spend considerable amounts of resources on infrastructure damaged as a result of corrosion. The USA spends upwards of US$ 400 million per year, the UK £500 million, and China spends 100 million RMB as reported by Li et al. (2009). Therefore, mitigating corrosion in the design of RCS should be a primary concern. The notion that strong enough concrete, is durable, is outdated. As elaborated in preceding sections, corrosion is a complex process, with various affecting parameters.

2.4.4.1 Mechanism of corrosion in concrete

When concrete is reinforced with steel, a thin layer not more than a few nanometres thick called the passivity layer, forms around the steel and is made from different degrees of hydrated iron oxides, Fe^{2+} and Fe^{3+}. The passivity layer forms due to the high alkaline environment in the concrete and is believed to protect the reinforcing steel from corrosion. The overall process, from the destruction of the passivity layer to spalling of concrete cover, including corrosion is what is known as depassivation. In 1982 Tutti proposed an illustration of depassivation and corrosion initiation, followed by the corrosion propagation phase as seen in Figure 2.42a.The schematic has been updated and improved by various researchers to account for cracking and service life extension as shown in Figure 2.42b,c and d. As can be seen in Figure 2.42a and d, during the initiation phase, aggressive substances (chlorides or carbon dioxide) penetrate the concrete, lowering the pH significantly. It is hypothesised by Hansson et al.(2007) that the substances lowers the resistance offered by the passivity layer, which then allows anodic regions to form. In the presence of sufficient moisture and oxygen, in the cathodic region, a corrosion cell can then form thus initiating corrosion.

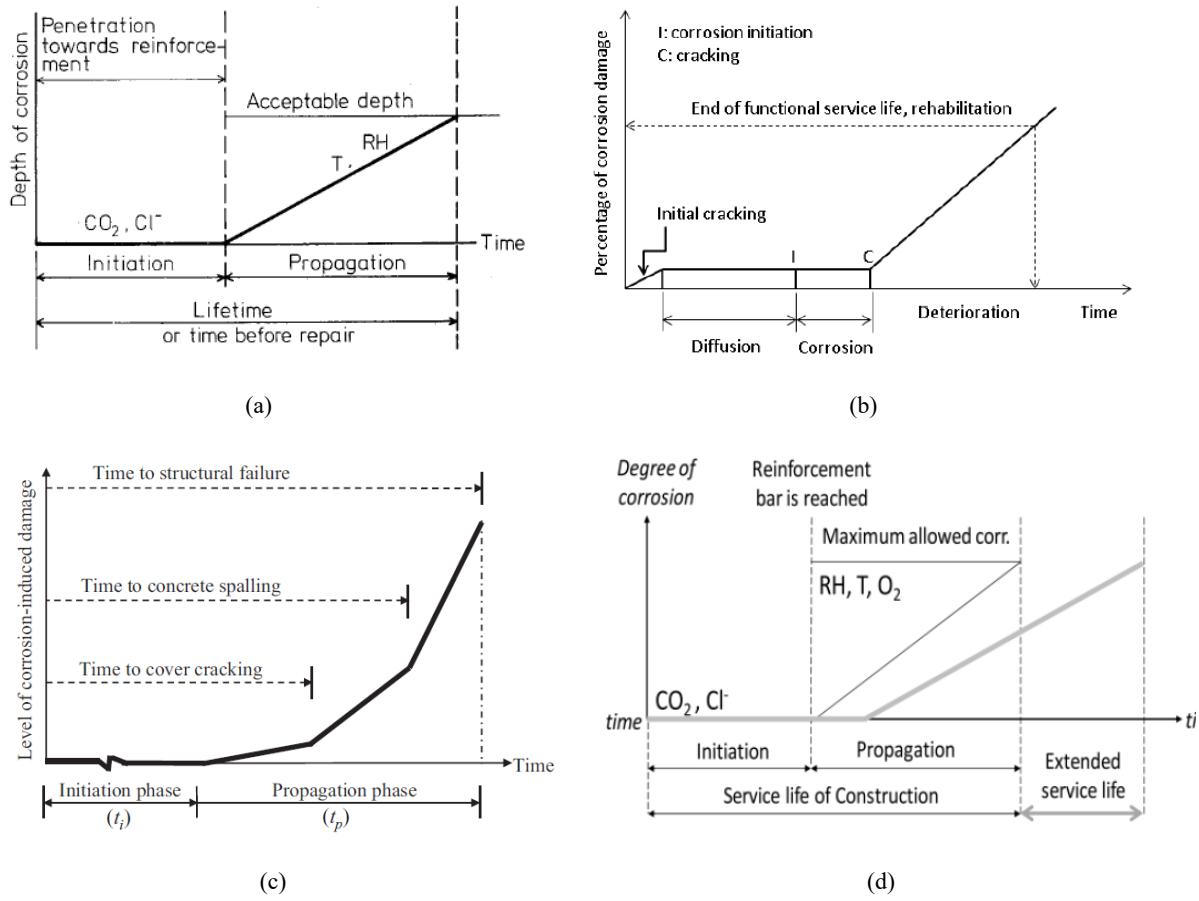

Figure 2.42: Illustration of depassivation phases (a) Tuutti (1982) (b) Lui and Weyers (1998) and (c) Otieno (2014). (d) An illustration of the effect of surface treatment on the service life of RCS (Selanders (2010)).

2.4.4.2 Depassivation model

When corrosion is initiated, expansive products form that occupy a larger volume than the original product, as seen in Figure 2.43. For steel corrosion in concrete the main products formed are ferrous hydroxide ($Fe(OH)_2$) and ferric hydroxide ($Fe(OH)_3$). These products occupy a volume 3.5 to 4.5 times larger than the original product, thus creating internal pressure in the surrounding concrete. Once the internal tensile stresses exceed the maximum tensile stress of the concrete a crack forms. The second phase, propagation phase, is a result of continued corrosion resulting in the production of more expansive products widening the cracks from the previous phase. During this phase the concrete spalls of completely resulting in unacceptable damage, see Figure 2.42c. More corrosion takes place at a faster rate due to the direct exposure of the reinforcing steel to the external environment. The diameter of the uncorroded reinforcing steel is reduced therefore compromising the load carrying capacity of the RCS. At this stage the end of service life of the structure is reached.

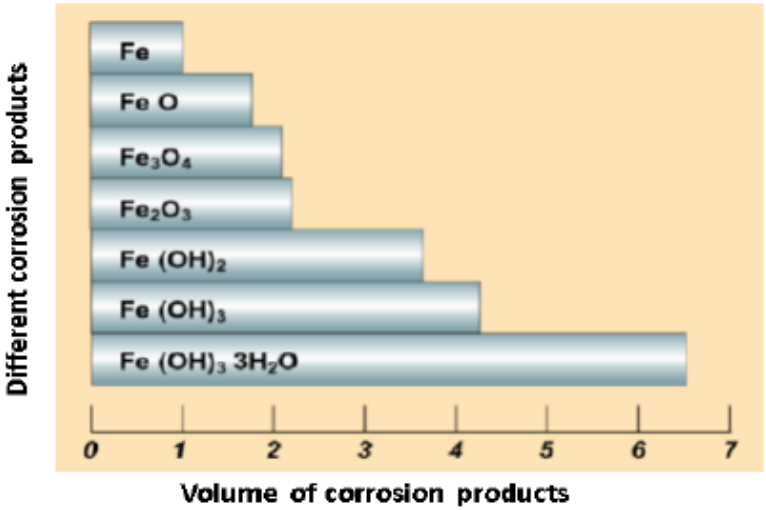

Figure 2.43: Corrosion products (reproduced from Cement Concrete and Aggregates Australia (2009))

2.4.4.3 Corrosion cell (micro- and macro-cell) and corrosion categorization

2.4.4.3.1 Corrosion cell

Corrosion of embedded steel in RC is an electrochemical process. The electrochemical cell is formed due to the difference in concentration of dissolved ions (alkalis) in the vicinity of the embedded steel. As a result the steel becomes anodic and cathodic in certain regions. The chemical changes at the anodic and cathodic regions can be given as Equations 2.49 and 2.50.

$$\text{Anode:} \quad Fe \rightarrow 2e^- + Fe^{2+} \tag{2.49}$$

$$\text{Cathode:} \quad O_2 + 2H_2O + 4e^- \rightarrow 4(OH)^- \tag{2.50}$$

Figure 2.44 graphically illustrates the electrochemical cell of the corrosion process taking place in concrete. Depending on the conditions present two types of electrochemical cells may form, a micro-cell or a macro-cell. A micro-cell forms when the anode and cathode regions are close to one another and indistinguishable from each other due to the close proximity. This may be as a result of small crack spacing. For macro-cells, the regions are spaced out and quite distinguishable from each other. The type of concrete and loading determines which type of cell forms. For instance, strain hardening cement composites (SHCC) which allows small cracks and spacing may favour micro-cell development whereas RC which is prone to macro-cell development.

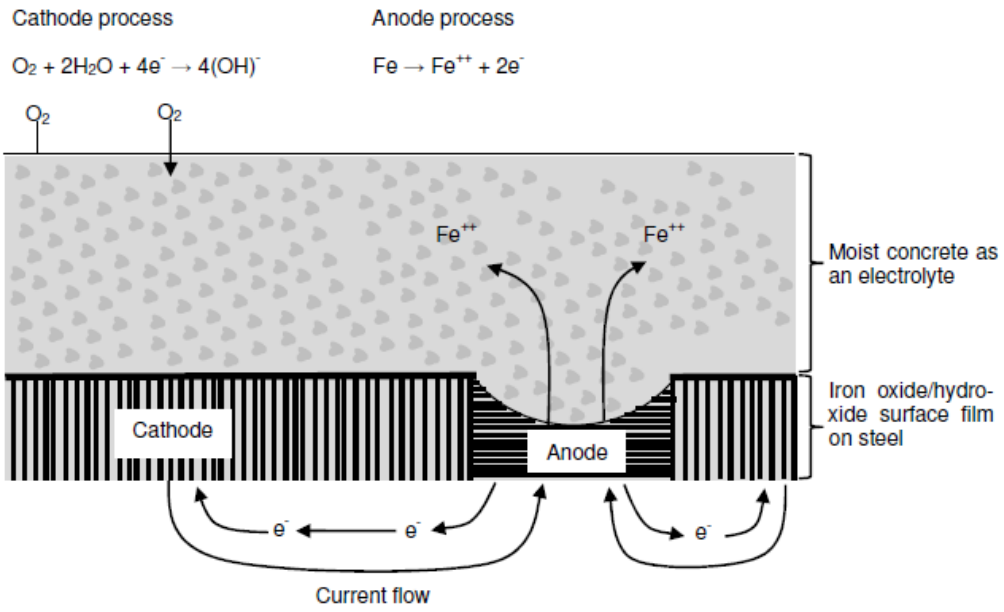

Figure 2.44: Electrochemical process of steel corrosion in moist and permeable concrete (Mehta and Monteiro (2006))

2.4.4.3.2 Corrosion categorisation

Corrosion is generally categorised in three categories (1) uniform corrosion, (2) galvanic corrosion and (3) localised corrosion. The categories are based on the corrosion mechanism and the type of damage caused by the corrosion process. For instance, uniform corrosion, is a result of the total destruction of the passivity layer surrounding the reinforcing steel over the entire or significant part of its length. This may occur as a result of the carbonation front reaching the reinforcement over the length of the RCS. Small anodic and cathodic regions thus form over the entire length of the reinforcement causing uniform corrosion to take place. However, concrete is heterogeneous and uniform corrosion may not be possible to achieve. Broomfield (2007) states that some anodic reactions can occur faster than the cathodic reactions. In this instance there would be areas with higher corrosion damage over the length of the rebar. This represents a more realistic case whereby the passivity layer has not been destroyed over the entire length of the reinforcement. This type of corrosion is called galvanic corrosion and can be simulated by the combined deterioration of chloride attack and the process of carbonation according to Song and Shayan (2008).

The last type of corrosion is localised corrosion which is often referred to as pitting. This pitting corrosion is characterised by a small anode to cathode area ratio and a high corrosion penetration rate. This type of corrosion is normally associated with chloride attacks where deficiencies or cracks have led to fast ingress of chloride. In general, the chlorides tend to cluster in the pit area causing a drastic decrease in the pH, accelerating the corrosion rate. This type of corrosion leads to high loss of reinforcement diameter in a localised area leading to a significant decrease in the load carrying capacity of RCS.

2.4.4.4 Corrosion measuring techniques (Corrosion Assessment)

For the process of corrosion it is useful to be able to determine the rate of deterioration in order to predict the remaining service life of RCS. Testing for corrosion can be categorised into destructive or non-destructive testing. Whilst destructive testing will give the actual condition or level of deterioration it is impractical and not desirable for large RCS. Alternatively, the use of non-destructive methods can give an estimation of the corrosion rate based on the potential, or give a calculated corrosion rate based on electrochemical principles. The fact that chipping open RC in places to measure pitting depth, even in a large structure, remains an option possibly to confirm non-destructive readings. This is costly and requires subsequent repair. A combination is possible, but after calibration of readings against a few actual pitting measurements, non-destructive testing will be cheaper and quicker by far. In the following sections corrosion assessment methods are presented.

2.4.4.4.1 The half-cell potential (HCP) method

The half-cell potential method for determining the probability of corrosion in RCS can be performed as set out in the ASTM C876 (2009) standard. The HCP method determines the corrosion potential, E_{corr}, by the use of either a copper-copper sulphate electrode (CSE) or a silver-silver chloride electrode (SCE) connected to a high impedance voltmeter. The high impedance voltmeter has to be in direct contact with the reinforcement and the half-cell to given corrosion potential readings. The corrosion potential values are interpreted using Table 2.17 and is only calibrated for the use of RC. It should be noted that the HCP method does not yield corrosion rate values but does provide the probability of corrosion taking place.

Table 2.17: Half-cell potential readings indicating the corrosion potential (reproduced from ASTM C876 (2009))

Corrosion potential (E_{corr} in mV)		Corrosion probability (%)
mV vs. SCE	mV vs. CSE	
$E_{corr} > -125$	$E_{corr} > -200$	10 (low risk of corrosion)
$-126 \leq E_{corr} \leq -275$	$-200 \leq E_{corr} \leq -350$	Intermediate
$E_{corr} < -276$	$E_{corr} < -350$	90 (high risk of corrosion)
$E_{corr} < -426$	$E_{corr} < -500$	Severe corrosion

Figure 2.45a shows a visual representation of the copper-copper sulphate half-cell and Figure 2.45b shows diagrammatic lay-out of the test set-up for the HCP method. As can be seen in Figure 2.45a the half-cell is constructed from an outer non-conductive material. The copper electrode is then placed in a saturated solution of copper sulphate ($CuSO_4$) with one end sticking out of the sleeve to be used as a connection to the high impedance voltmeter. The bottom end of the half-cell is porous so that an electrical connection between the concrete and the half-cell can be established.

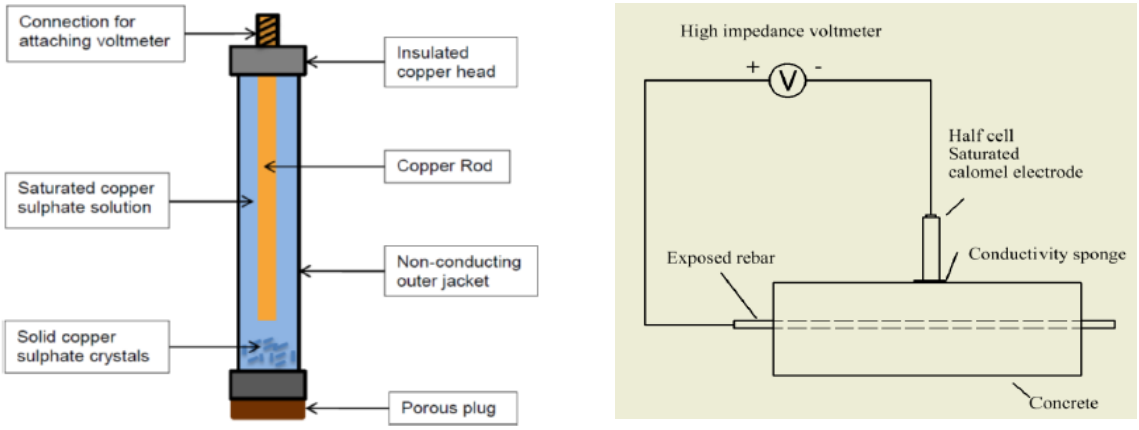

(a) (b)

Figure 2.45: (a) Diagrammatic representation of the half-cell used in the HCP method (Paul (2005)) and (b) Set-up used to conduct the HCP method (Song and Saraswathy (2007))

Factors influencing the half-cell potential (HCP) readings

The reading obtained from the HCP method can be influenced by a number of factors as summarised in Table 2.18 according to Gu and Beaudoin (1998). It should be noted that the values in Table 2.18 as published in the ASTM standard is only calibrated for plain concrete and there exist instances where values lower than -350 mV are obtained without any significant corrosion taking place. Such a condition may arise as a result of limited oxygen diffusion. Also it has been suggested by numerous researchers that the HCP method should not be used in isolation due to the various factors contributing to the readings obtained.

Table 2.18: Factor influencing the half-cell potential readings (reproduced from Gu and Beaudoin (1988))

Conditions	HCP reading	Rate of corrosion in steel bar	Applicable to ASTM C876
Lower oxygen	to negative	may not increase	no
Carbonation / lower pH	to negative	increase	yes
Higher chloride	to negative	increase	yes
Anodic corrosion inhibitor	to positive	decrease	yes
Cathodic corrosion inhibitor	to negative	decrease	no
Mixed corrosion inhibitor	to positive or negative	decrease	no
Epoxy coated rebar	to positive	not related	no
Galvanized rebar	to negative	not related	no
Dense concrete cover	to negative	not related	no
Dry concrete	to positive	not related	no
Coating and sealers	to positive	not related	no
Concrete repair patch	to positive or negative	not related	no

2.4.4.4.2 Linear Polarisation Resistance (LPR) methods

According to Ropitol (2011) the linear polarization resistance (LPR) techniques are used to characterise a material pair (e.g. concrete-steel) by scanning the current-potential (i-E) domain. In the methods, first introduced by Stern and Geary (1957), a small variation of voltage in the range of 30 mV above and below the corrosion potential is applied to the material pair. According to Stern and Geary there exist a linear relationship between corrosion potential and current response in this narrow vicinity. This linear relationship between corrosion potential and current response is graphically illustrated in Figure 2.46 and can mathematically be represented by Equation 2.51 known and the Stern-Geary equation.

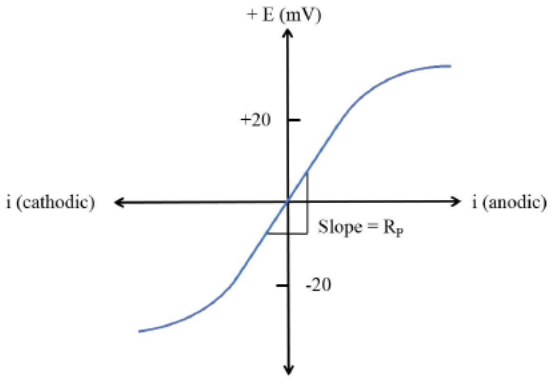

Figure 2.46: Graphic illustration of the linear relationship of corrosion potential and current response (reproduced from Poursaee (2010))

$$R_p = \left(\frac{\Delta E}{\Delta I}\right)_{\Delta E \to 0} \tag{2.51}$$

The slope of the corrosion potential and current response curve, known as the polarisation resistance (R_p), in the linear vicinity is constant under certain conditions and is inversely proportional to the instantaneous corrosion rate. Equations 2.52 and 2.53 can be used to determine the polarisation resistance.

$$I_{corr} = \frac{B}{R_p} \tag{2.52}$$

$$B = \frac{\beta_a \beta_c}{2.3(\beta_a + \beta_c)} \tag{2.53}$$

where I_{corr} is the corrosion current

$\beta_a + \beta_c$ are the Tafel coefficients

Andrade et al. (1996) reports that typically the value of the constant B is taken as 26 mV for active corrosion and 52 mV for passive corrosion. The value of the corrosion intensity can then be calculated as the ratio of the corrosion current to the polarised steel surface area represented by Equation 2.54.

$$i_{corr} = \frac{I_{corr}}{A_{pol}} \tag{2.54}$$

where i_{corr} is the corrosion current density in $\mu A/cm^2$

A_{pol} as the polarised steel surface area, in cm^2, calculated as $\pi dsLs$.

Current modulation

Corrosion assessment is a complex process due to the relative large number of factors that contribute to the corrosion rate of steel in concrete. It is essential that the latest techniques are used for accurate determination of the corrosion rate. One of the main problems that need to be address, when using any of the LPR techniques, is the accurate measurement of the polarised resistance. When the current is unconfined, as shown in Figure 2.47a and b, the area of steel polarized may be much larger area than the area below the reference electrode. This may lead to the overestimation of corrosion rates especially in the case of non-uniform and localised corrosion.

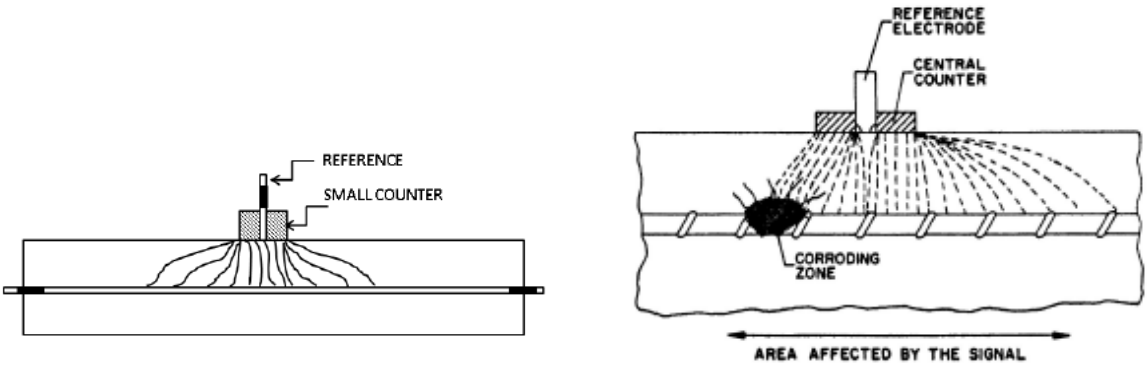

(a) (b)

Figure 2.47: (a) Polarised length as a result of unconfined current distribution due to non-uniform corrosion (reproduced from Andrade and Alonso (2004)) and (b) polarised length as a result of unconfined current distribution due to non-uniform corrosion (reproduced from Andrade et al.(1996))

A solution for the accurate determination of the polarisation resistance is found in the guard ring technique. The technique confines the polarised area to just beneath the reference electrode (RE) by adding a surrounding counter electrode (CE) and an outer guard electrode (GE). The guard ring technique is then modulated by further addition of two reference electrodes placed between the CE and the GE. The working electrode (WE), reinforcing steel, is connected to the potentiostat together with

the rest of the electrodes as depicted in the set-up of the modulated guard ring shown in Figure 2.48a. According to Paul (2015) the modification assists the polarisation of the electrodes and the concrete beneath them. Figure 2.48b,c show the effect of current modulation using the modulated guard ring technique.

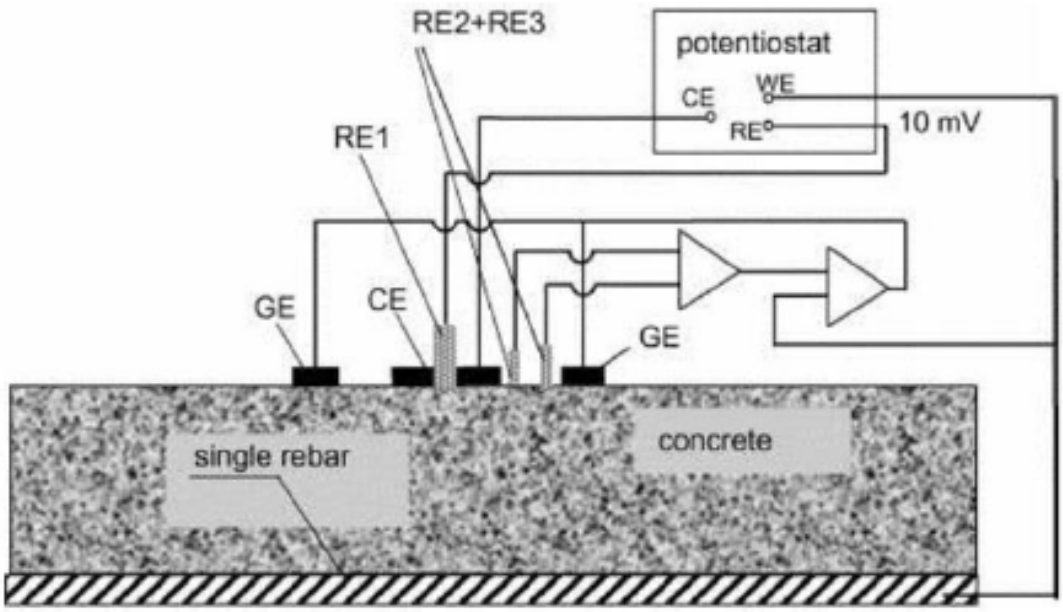

(a)

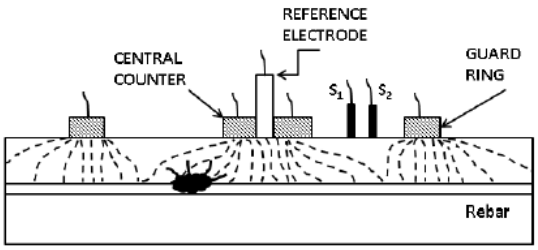

(b)

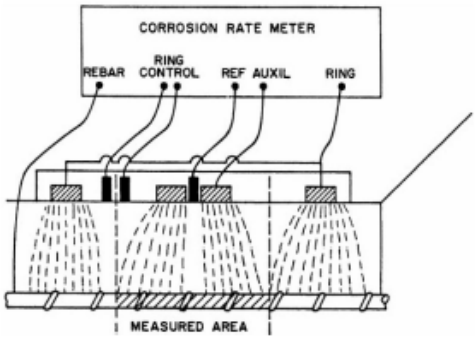

(c)

Figure 2.48: (a) Modulated guard ring set-up (reproduced from Wojtas (2004)) (b) Current distribution due to modulation, and, (c) depiction of polarised area due to modulation (reproduced from Andrade and Alonso (2001))

2.4.4.4.3 Transient techniques (Coulostatic method and Galvanostatic pulse technique)

Two of the most commonly used transient methods are the Coulostatic method and the Galvanostatic pulse technique which is also referred to as the potentiostatic method. According Montemor et al. (2003) these transient methods are preferred due to their slow concrete/steel interface reactions. A brief overview of the methods are presented in this section

Coulostatic method

The coulostatic method is performed by applying a small amount of know current, usually between 10 – 20 mA, into the reinforcing steel for a small known period of time and then observing the decay in the potential. The decay in potential as a result of corrosion can be represented as a Randles equivalent circuit as shown in Figure 2.49b. Figure 2.49a is a representation of the RC.

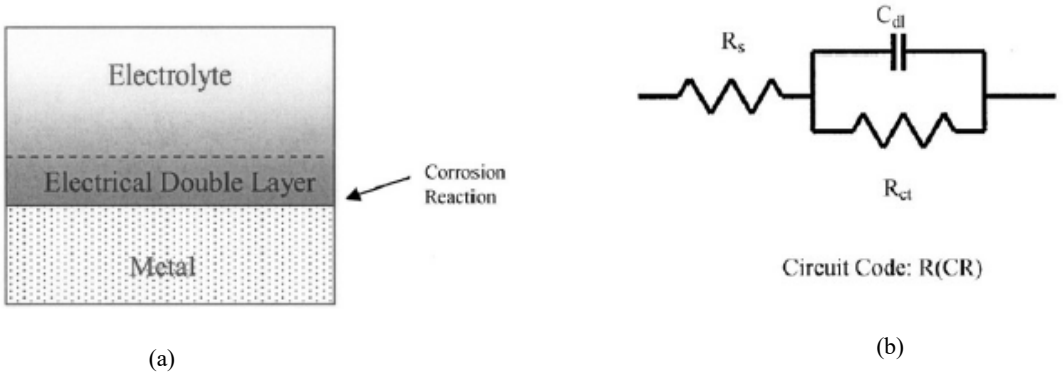

(a) (b)

Figure 2.49: (a) Representation of RC and (b) Randles equivalent circuit (reproduced from Chu et al.(2006))

In the Randles equivalent circuit, Figure 2.49b, the electrolyte resistance (R_s) is place in series with a parallel combination of impedance and double layer capacitance (C_{dl}). The polarisation resistance (R_{ct}) is then calculated using Equation 2.55.

$$\eta_T = \Delta \mathrm{IR}_s + \Delta IR_{ct}\left(e^{-\frac{t}{\tau c}}\right) \tag{2.55}$$

where η_T is the total potential change in the working electrode
ΔIR_s is the ohmic drop between the working electrode and reference
ΔIR_{ct} is the effective polarisation at charging time
τc is the coulostatic time constant

When there is a change in the current a build-up of charge in the double layer is used gradually in the corrosion reaction. As a result of the loss of the ohmic drop component and no further application of current during testing, the potential decay can be expressed using Equation 2.56.

$$\eta_t = \eta_0 e^{-\frac{t}{\tau c}} \tag{2.56}$$

where η_t is the potential shift (ΔE) at time t
η_t is the initial potential shift

$$R_p = \frac{\tau_c}{C} \tag{2.57}$$

$$C = \frac{q_s}{A\eta_0} \tag{2.58}$$

$$q_s = \Delta i \Delta t \tag{2.59}$$

$$I_{corr} = \frac{B}{R_p} \tag{2.60}$$

$$V_{corr} = 0.0116 I_{corr} \tag{2.61}$$

where q_s is the amount of charge

Δi is the current sent

Δt is the pulse duration

The values of η_0 and τ_c are obtained by fitting an exponential curve through the perturbation/potential (mV) versus time (s). A is the circumferential steel area calculated as $\pi dsLs$ and B is the Stern-Geary constant taken as 26 mV for passive corrosion or 56 mV for active corrosion. Further details on the coulostatic method can be found in Paul (2015), Otieno et al. (2010), Andrade and Alonso (2004), Gonzalez et al. (2001) and Glass (1995).

Figure 2.50a shows a diagrammatic layout of the test setup and procedure used by Paul (2015) to perform the coulostatic method. Paul (2015) made use of a laboratory manufactured pulse generator and Spider8 data logging equipment for testing. Figure 2.50b-e shows an example of the data shown by Paul (2015). In Figure 2.50b a plot of the perturbation (mV) and time (mS). The data used in the plot was collected at a frequency of 1200 Hz. The reason for this high frequency is to filter out noise. During testing, noise such as radio frequency is picked up in the data due to the unshielded concrete and steel. By collecting data at a high frequency, such as 1200 Hz, the running average can be used to smooth out the data and eliminate the vertical by subtracting the initial reading as shown in Figure 2.50b. In Figure 2.50c the complete data is shown as parts a-b, b-c, c-d, and d-e. Part c-d represents the ohmic drop. Part d-e is the only part used in the calculations and a magnified view of the data is shown in Figure 2.50d. The values of η_0 and τ_c can be determined from the equation of the exponential function (dashed line) indicated in Figure 2.50d. Figure 2.50e,f show a downward and an upward trend in the data collected. This may occur as a result of loose or poor connections between the equipment. If such results are obtained the operator is advised to check all connections (half-cell connection, working and counter electrode connection).

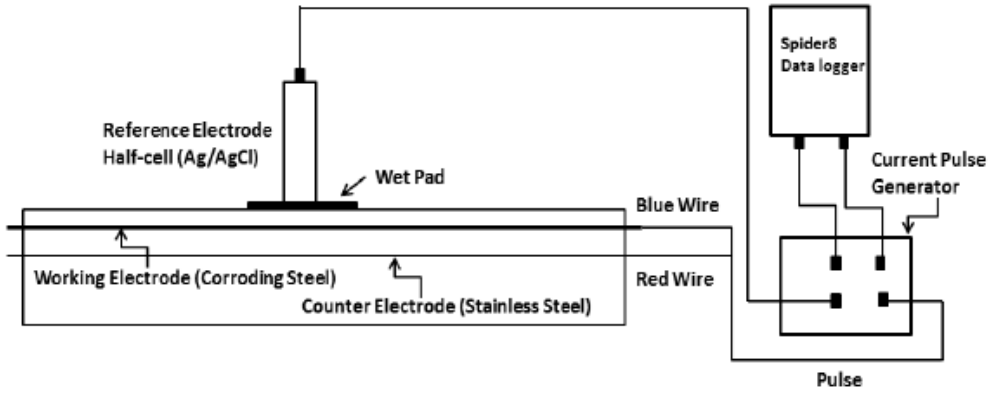

Figure 2.50: (a) Diagrammatic illustration of the setup and procedure used to perform the coulostatic method (Paul (2015))

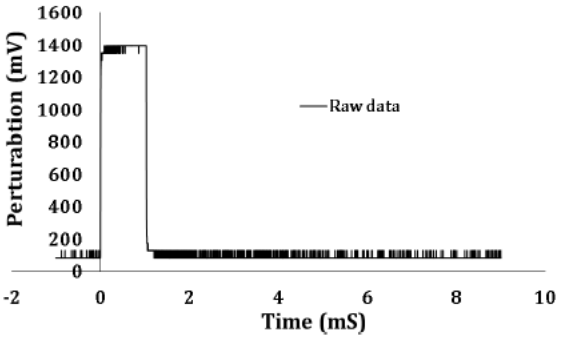

Figure 2.50: (b) Raw data obtained from the Coulostatic method (Paul (2015))

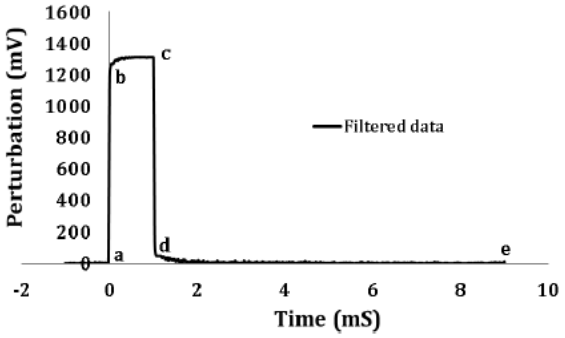

Figure 2.50: (c) Filtered data obtained from the Coulostatic method (Paul (2015))

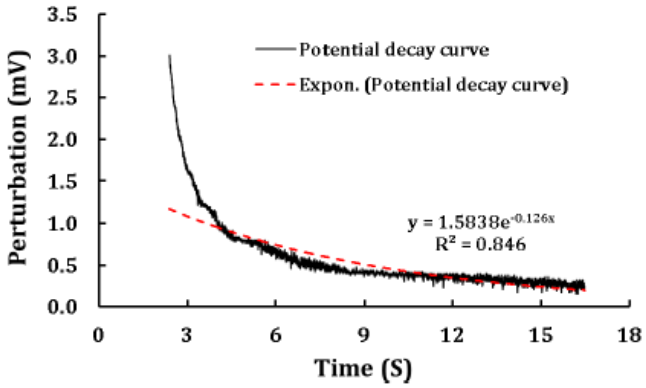

Figure 2.50: (d) Data used for determining the corrosion rate in the coulostatic method (exponential fitted curve) (Paul (2015)).

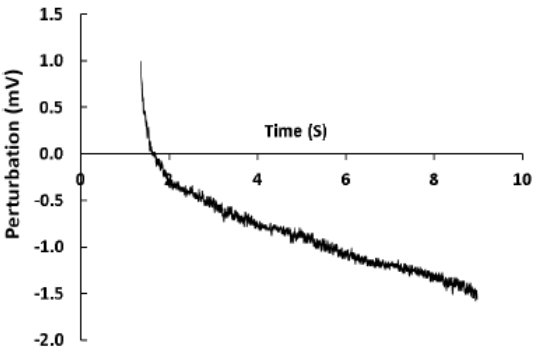

Figure 2.50: (e) Data showing downward trend from the coulostatic method (Paul (2015)).

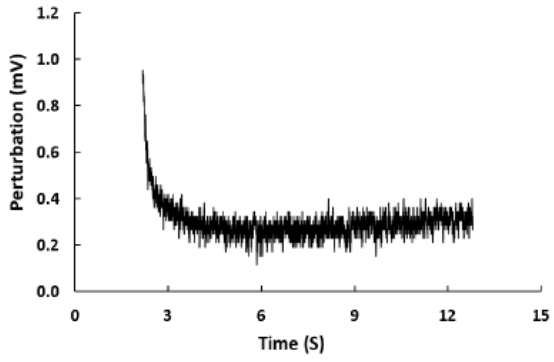

Figure 2.50: (f) Data showing upward trend from the coulostatic method (Paul (2015)).

Galvanostatic pulse technique (Potentiostatic method)

The Galvanostatic pulse technique is a polarisation technique whereby a small current, typically in the range of 10 – 100 µA, is applied galvanostatically for 5 – 30 seconds between the counter electrode and the working electrode (reinforcement). As a result of the applied current a potential develops in the working electrode which when plotted against the polarisation time yield the result shown in Figure 2.51.

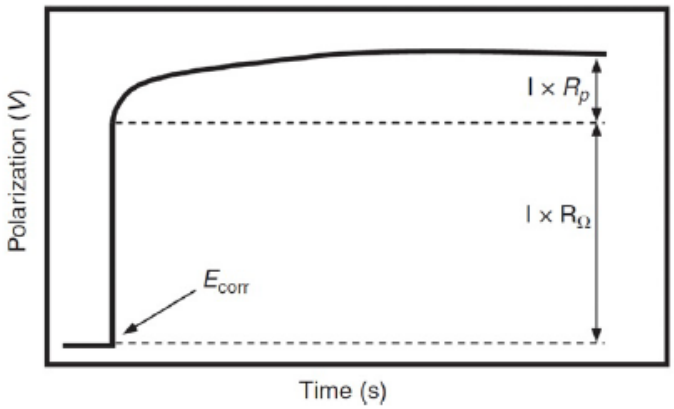

Figure 2.51: Polarised potential (V) plotted against polarised time (s) for the Galvanostatic method (reproduced from Poursaee (2010))

According to Jones et al. (1966) the total polarised potential (η_t) developed in the working electrode at a time (t) under constant applied current (I_{app}) can be described using Equation 2.62.

$$\eta_t = I_{app}\left[R_p\left(1 - e^{\frac{-t}{R_p C_{dl}}}\right) + R_o\right] \tag{2.62}$$

where η_T is the total potential (mV) in the working electrode

R_Ω is the ohmic resistance (Ω) of the concrete

C_{dl} is the double layer capacitance (C)

In order to calculate R_p and C_{dl} Equation 2.62 is transformed using the natural logarithm to yield Equation 2.63 whereby η_{max} represents the final steady state potential.

$$ln(\eta_{max} - \eta_t) - \ln(I_{app}R_p) - \frac{t}{R_p C_{dl}} \tag{2.63}$$

Plotting Equation 2.63 whereby the vertical axis represents the potential (V) and the horizontal axis time (s) yields a straight line with a slope equivalent to $\frac{1}{(R_p x C_{dl})}$ and a vertical intercept of $I_{app} x R_p$ as shown in Figure 2.52. By extrapolating the straight line graph to time equal seconds the slope and the vertical intercept can be determined. The polarisation resistance, R_p, can then be calculated due to the known applied current and subsequently the corrosion intensity, I_{corr}, using the Stern-Geary equation.

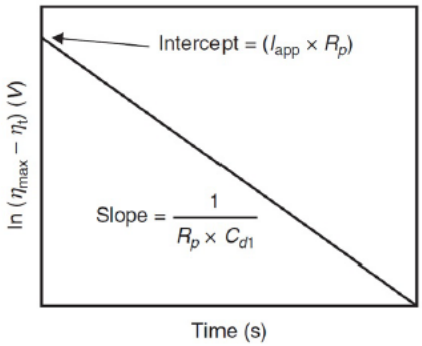

Figure 2.52: Plot of potential (V) versus time (s) as described by Equation 2.41 (reproduced from Newton et al. (1988))

2.5 Concluding summary

LWFC can experience a rise in popularity and become the material of choice for designers when certain issues plaguing its widespread usage are resolved. LWFC' vast range of applications is testimony to its versatility, which is attributed to its ability to be designed in a wide range of density, between 400 and 1600 kg/m^3. Predominantly, applications of LWFC were focused in the non-structural to semi-structural range. However, improvements over the past two decades, including the incorporation of large volumes of industrial waste into the mix design have elevated the material to be utilised structurally. The advancement of LWFC, now, as the material of choice lies not only in its "newly found" structural ability, but also in addressing durability concerns, lack of codification and key design information. A review on the body of knowledge on LWFC reveals gaps in the literature on the mechanical and durability properties of LWFC. The overall aim is to advance LWFC as a structural and durable material.

For the mechanical properties of LWFC, a vast body of literature can be found on its compressive strength and to a small degree tensile strength and elastic modulus. However, a glaring omission on the topic of bond behaviour between the reinforcing steel and LWFC is evident in the literature. This information is vital for the design of reinforcement in LWFC especially when considering anchorage and lap distances. In this chapter a comprehensive literature review is presented. Topics covered in the literature review include the mechanical properties of FC and bond between the reinforcing steel in NWC and LWAC. Based on the literature review the experimental programme described in Chapter 3, was designed and executed, of which the results are presented in Chapter 4.

For the durability properties of LWFC, only a limited number of studies have addressed the microstructure, shrinkage, transport properties, and carbonation. In this area of the literature gaps are

identified in long-term durability studies, especially those processes leading towards corrosion. There is also an absence of a strategy for preventing or delaying corrosion processes in R/LWFC. In light of these gaps in the literature a research programme into the durability properties and long-term deterioration processes in R/LWFC, carbonation- and chloride-induced corrosion, was envisioned by the author, as described in Chapter 3. A literature review on corrosion, included in this chapter, was launched and the use of surface treatment, identified by the author, showed promise as an effective tool for improving durability of LWFC. Therefore, this research programme includes the enhancement of the durability properties of LWFC with the use of surface treatment agents and evaluates its efficacy in mitigating corrosion in R/LWFC. Also, it is clear that the microstructure has an influence on the durability properties of LWFC and its influenced can be characterised using the pore parameters, as elaborated in Chapter 5.

2.6 References

ACI 224 (1994). Control of cracking in concrete structures. American Concrete Institute. Michigan.

ACI 318-11 (2011). Building Code Requirements for Structural Concrete. American Concrete Institute. Michigan.

ACI Committee 408 (1992). Abstract of: State-of-the-Art-Report: Bond under Cyclic Loads. ACI Materials Journal 88(6).

Alexander, M. and Magee, B. (1999). Durability performance of concrete containing condensed silica fume. Cement and Concrete Research. 29(6). pp. 917-922.

Alexander, M. and Beushausen, H. (2009). Deformation and volume change of hardened concrete. Fulton's Concrete Technology.

Al-Neshawy, F. and Sistonen, E. (2015). Durability of concrete.

Andrade, C. and Alonso, C. (1996). Corrosion rate monitoring in the laboratory and on-site. Construction and Building Materials. 10. pp. 315-328.

Andrade, C. and Alonso, C. and Arteaga, A. (1997). Models for predicting corrosion rates. Brussel: Brite-Euram Project.

Andrade, C. and Alonso, C. (2001). On-site measurement of corrosion rate of reinforcements. Construction and Building Materials. 15(2). pp. 141-145.

Andrade, C. and Alonso, C. (2004). Test methods for on-site corrosion rate measurements of steel reinforcement in concrete by means of the polarization resistance method. Materials and Structures. 37(9). pp. 623-643.

Andrade, C. Martinez, I. Rebolledo, N. and Castillo, A. (2017). Development of an engineering approach for modelling corrosion attack. Integral Service Life Modelling of Concrete Structures.

Arya, C. and Xu, Y. (1995). Effect of cement type on chloride binding and corrosion of steel in concrete. Cement and Concrete Research. 25(4). pp. 893-902.

Arya, C. and Ofori-Darko, F. (1996). Influence of crack frequency on reinforcement corrosion in concrete. Cement and Concrete Research. 26(3). pp. 345-353.

ASTM A944-10 (2002). Comparing Bond Strength of Steel Reinforcing Bars to Concrete Using Beam-End Specimens. ASTM International. Pennsylvania, USA.

ASTM C876 (2009). Standard test method for half-cell potentials of uncoated reinforcing steel in concrete. ASTM International. Pennsylvania, USA.

Basheer, P.A.M. et al. (1997). Surface treatments for concrete. Assessment methods and reported performance. Construction and Building Materials. 11. pp. 413-429.

Beushausen, H., Alexander, M. and Ballim, Y. (2012). Early age properties, strength development and heat of hydration of concrete containing various South African slags at different replacement ratios. Construction and Building Materials. 29. pp. 533-540.

Bezuidenhout, S.R. (2017). Corrosion propagation in cracked reinforced concrete structures. Thesis. Stellenbosch University.

Bofeldt, M. and Nyman, B. (2002). Penetration depth of hydrophobic impregnating agents for concrete. Proceedings of the International conference on Surface Technology and Water Repellent Agents. pp. 133-142.

Brady, K.C., Watts, G.R.A., and Jones, M.R. (2001). Specification for foamed concrete. Project report PR/IS/40/01.

Broomfield, J.P. (1994). Corrosion rate measurements in reinforced concrete structures by a linear polarization curve. Special Publication 151. pp. 163-182.

Broomfield, J.P. (2013). Corrosion of steel in concrete: Understanding, Investigation and Repair. 2nd Edition. CRC Press Taylor and Francis Group. ISBN 9780415334044.

Borges, P.H.R. et al. (2009). Carbonation of CH and C-S-H in composite cement pastes containing high amounts of BFS. Cement and Concrete Research. 40. pp. 284-292.

Brùhwiler, E and Wittmann, FH (1990). The wedge splitting test, a new method of performing stable fracture mechanics tests. Engineering Fracture Mechanics 35.1. pp 117-125.

BS 8110-1 (1997). Structural use of concrete. Part 1: Code of practice for design and construction. British Standard Institution. London.

BS 8110-2 (1985). Structural use of concrete. Part 2: Code of practice for special circumstances. British Standards Institution. London.

BS EN 1992-1-1 (2004). Eurocode 2: Design of concrete structures. Part 1-1: General rules and rules for buildings. British Standards Institution. London.

Byun, K.J., Song, H.W., Park, S.S., and Song, Y.C. (n.d.). Development of structural lightweight foamed concrete using polymere foam agent. Department of Civil Engineering, Yonsei University. Korea.

CEB, D.C. (1992). Design Guide, Bulletin d'information 182. pp. 18.

Cement Concrete and Aggregates Australie 2009: Chloride resistance of concrete, pp. 37.

Chen, B. and Lui, J. (2008). Experimental application of mineral admixtures in lightweight concrete with high strength and workability. Construction and Building Materials. 22(6). pp. 1108-1113.

Christodoulou, C. et al. (2013). Long-term performance of surface impregnation of reinforced concrete structures with silane. Construction and Building Materials. 48. pp. 708-716.

Chu, C.T. Fuqua, P.D. and Barrie, J.D. (2006). Corrosion characterization of durable silver coatings by electrochemical impedance spectroscopy and accelerated environment testing. Applied Optics. 45(7). pp. 1583-1593.

Dae-Jin, K., Min Sook, K., Geun Young, Y., and Young Hak, L. (2014). Bond strength of steel deformed rebards embedded in artificial lightweight aggregate concrete. Journal of Adhesion Science and Technology 27.5-6, pp. 490-507.

Desnerck, P. and De Schutter, G. (2010). Bond behaviour of reinforcing bars in self-compacting concrete: Experimental determination by using beam tests. Materials and Structures 43, pp. 53-62.

Dhir, R., El-Mohr, M. and Dyer, T. (1997). Developing chloride resisting concrete using PFA. Cement and Concrete Research. 27(11). pp. 1633-1639.

Domone., P.L.J. and Illston., J.M. (2015). Construction Materials. 4th Edition. Spon Press. London and New York.

El Zareef, M. and Schlaich, M. (2008). Bond behaviour between GFR bars and infra-lightweight concrete. Tailor Made Concrete Structures, pp. 721-727.

Elsener, B., Wojtas, H. and Böhni, H. (1994). Galvanostatic Pulse Measurements-Rapid on site corrosion monitoring. Corrosion and corrosion protection of steel in concrete. Proceeding of International conference held at the University of Sheffield, 24-28 July 1994. Volume 1.

Elsener, B. (1997). Assessment of reinforcement corrosion by means of Galvanostatic pulse technique. Proceeding of International Conference on Repair of Concrete Structures – From Theory to Practice in a Marine Environment. pp. 391-400.

Elsener, B. et al. (2003). Half-cell potential measurements - Potential mapping on reinforced concrete structures. Materials and Structures. 36. pp. 461 - 471.

Eurocode 2: Design of Concrete Structures: Part 1-1: General Rules and Rules for Buildings (2004). British Standards Institution.

Farghal Maree, A. and Hilal Riad, K. (2014). Analytical and experimental investigation for bond behaviour of newly developed polystyrene foam particles lightweight concrete. Engineering Structures 58.1, pp. 1-11.

Federation Internationale de la Precontraine (1983). FIP manual of Lightweight Aggregate Concrete. Surrey University Press. Glasgow.

Franzoni, E., Pigino, B. and Pistolesi, C. (2013). Ethyl silicate for surface protection of concrete: Performance in comparison with other inorganic surface treatments. Cement and Concrete Composites. 44. pp. 69-76.

Freitag, S.A. and Bruce, S.M. (2010). The influence of surface treatments on the service lives of concrete bridges. NZ Transport Agency Research Report 403.

Giessler, S. Standke, B. and Bùchler, M. (2005). A new silane system for corrosion reduction of steel reinforced concrete. Hydrophobe IV. Aedificatio publishers. pp. 17-26.

Glass, G.K. (1995). An assessment of the coulostatic method applied to the corrosion of steel in concrete. Corrosion Science. 37(4). pp. 597-605.

Gonzalez, J., Andrade, C., Alonso, C. and Feliu, S. (1995). Comparison of rates of general corrosion and maximum pitting penetration on concrete embedded in steel reinforcement. Cement and Concrete Research. 25(2). pp. 257-264.

Gonzalez, J. Molina, A., Escudero, M. and Andrade, C. (1985). Errors in the electrochemical evaluation of very small corrosion rates-I. Polarization resistance method applied to corrosion of steel in concrete. Corrosion Science. 25(10). pp. 917-930.

Gu, P. and Beaudoin, J.J. (1998). Obtaining effective half-cell potential measurements in reinforced concrete structures. Concrete Technology Update No. 18. pp. 1-4.

Hager, R. (1998). The revolution in concrete protection impregnation with cream. Hydrophobe II. Aedificatio publishers. pp. 295-216.

Hassanein, A.M., Glass, G.K. and Buenfeld, N.R. (1998). The use of small electrochemical perturbations to assess the corrosion of steel in concrete. NDT and E international. 31(4). pp. 265-272.

Hilal. A.A., Thom, N.H. and Dawson, A.R. (2015a). On entrained pore size distribution of foamed concrete. Construction and Building Materials. 75. pp. 227-233.

Hilal. A.A., Thom, N.H. and Dawson, A.R. (2015b). On void structure and strength of foamed concrete made with/without additives. Construction and Building Materials. 85. pp. 157-164.

Hilal. A.A., Thom, N.H. and Dawson, A.R. (2015c). The use of additives to enhance the properties of pre-formed foamed concrete. International Journal of Engineering and Technology. 7(4). pp. 286-293.

Johnson Alengara, U., Mahmud, H., and Jumaat, M.Z. (2010). Comparison of mechanical and bond properties of oil palm kernel shell concrete with normal weight concrete. International Journal of the Physical Science 5.8, pp. 1231-1239.

Ibrahim, M. et al. (1999). Use of surface treatment materials to improve concrete durability. Journal of Materials in Civil Engineering. 11(1). pp. 36-40.

Jones, D.A. and Greene, N. (1966). Electrochemical measurement of low corrosion rates. Corrosion. 22(7). pp. 198-205.

Jones, M.R. and McCarthy, A. (2005). Preliminary views on the potential of foamed concrete as a structural material. Magazine of Concrete Research 57.1, pp. 21-31.

Jumaat, M.Z., Alengaram, U.J. and Mahmud, H. (2009). Shear strength of oil palm shell foamed concrete beams. Materials and Design 30. pp. 2227-2236.

Kearsley, E.P. (1999). The effect of high volumes of ungraded fly ash on the properties of foamed concrete. PhD dissertation. University of Leeds.

Kearsley, E.P. and Wainwright, P.J. (2001a). Porosity and permeability of foamed concrete. Cement and Concrete Research 31. pp, 805-812.

Kearsley, E.P. and Wainwright, P.J. (2001b). The effect of high fly ash content on the compressive strength of foamed concrete. Cement and Concrete Research, 31(1). pp. 105-112.

Kearsley, E.P. and Wainwright, P.J. (2002). Ash content for optimum strength of foamed concrete. Cement and Concrete Research 31. pp. 241-246.

Kearsley, E.P. and Mostert, H.F. (2003). The effect of fibre reinforcing on foamed concrete behaviour. Proceedings of the International Symposium Dedicated to Professor Surendra Shah, Northwestern University, USA.

Kearsley, E.P. and Mostert, H.F. (2005). Designing mix composition of foamed concrete with high fly ash contents. Proceedings of the International Conference on the Use of Foamed Concrete in Construction. Thomas Telford, London. pp. 29-36.

Leonhardt, F. (1977). Vorlesungen ùber Massivbau: Teil 3: Grundlagen zum Bewehren im Stahlbetonbau. Vorlesungen ùber Massivbau. Springer-Verlag GmbH. ISBN: 9783540081210. URL: http://books.google.co.za/books?id=ZEf87H0i9MsC

Mangat, P. Khatib, J. and Molly, P. (1994). Microstructur, chloride diffusion and reinforcement corrosion in blended cement paste and concrete. Cement and Concrete Composites. 16(2). pp. 73-81.

Medeiros, M.H.F. and Helene, P. (2009). Surface treatment of reinforced concrete in marine environments: Influence on chloride diffusion coefficient and capillary water absorption. Construction and Building Materials. 23(3). pp. 1476-1484.

Model Code (2010). FIB. Special Activity Group 5. CEB and FIB.

Nambiar, E.K.K. and Ramamurthy, K. (2006). Air void characteristics of foam concrete. Cement and Concrete Research. 37(9). pp. 221-230.

Nambiar, E.K.K. and Ramamurthy, K. (2008). Fresh state characteristics of foam concrete. Journal of Advanced Concrete Technology. 20(2). pp. 111-117.

Neff, D. et al. (2011). Morphology of corrosion products of steel in concrete under macro-cell and self-corrosion conditions. Materials and Corrosion. 62(9). pp. 861-871.

NEN 6720. (1995). Regulations for concrete TGB 1990 – Structural requirements and calculations methods. 2.01. Standard NEN Institute, Delft.

Newton, C. and Sykes. J. (1988). A galvanostatic pulse technique for investigation of steel corrosion in concrete. Corrosion Science. 28(11). pp. 1051-1074.

Oloukun, F.A. (1991). Prediction of concrete tensile strength from compressive strength: evaluation of existing relations for normal weight concrete. ACI Materials Journal 88(3). pp. 302-309.

Orangun, C.O., Jirsa, J.O. and Breen, J.E. (1977). A re-evaluation of test data on development length and splices. ACI Journal Proceedings. Volume 74(3). American Concrete Institute.

Otieno, M.B. (2008). Corrosion propagation in cracked and uncracked concrete. Thesis. University of Cape Town.

Otieno, M.B., Alexander, M. and Beushausen. (2010). Suitability of various measurement techniques for assessing corrosion in cracked concrete. ACI Materials Journal 107(5).

Otieno, M.B. (2014). The development of empirical chloride-induced corrosion rate prediction models for cracked and uncracked steel reinforced concrete structures in the marine tidal zone. PhD thesis. University of Cape Town.

Otieno, M.B., Beushausen, H. and Alexander, M. (2016). Chloride-induced corrosion of steel in cracked concrete - Part II: Corrosion rate prediction models. Cement and Concrete Research. 79. pp. 386-394.

Owens, G. (200). Fulton's Concrete Technology. Cement and Concrete Institute.

Panesar, D.K. (2013). Cellular concrete properties and the effect of synthetic and protein foaming agents. Construction and Building Materials. 44. pp. 575-584.

Papadakis, V.G. (2000). Effect of supplementary cementing materials on concrete resistance against carbonation and chloride ingress. Cement and Concrete Research. 30(2). pp. 291-299.

Parrot, L. (1994). Design for avoiding damage due to carbonation-induced corrosion. International Congress on durability of concrete. pp. 283-298.

Park, R. and Paulay, T. (1975). Reinforced Concrete Structures. New Zealand: Wiley Interscience Publication. ISBN: 0471659177.

Paul, S.C. (2015). The Role of Cracks and Chlorides in Corrosion of Reinforced Strain Hardening Cement-Based Composite (R/SHCC). PhD dissertation. Stellenbosch University.

Pedziwiatr, J. (2008). Influence of internal cracks on bond in cracked concrete structures. Archives of Civil and Mechanical Engineering VIII.3.

Penelis, G.G. and Penelis, G.G. (2014). Concrete Buildings in Seismic Regions. CRC Press – Taylor and Francis Group.

Pettersson, K. (1992). Corrosion threshold value and corrosion rate in reinforced concrete. CBI Report 2 92.

Poursaee, A. (2010). Potentiostatic transient technique, a simple approach to estimate the corrosion current density and Stern-Geary constant of reinforcing steel in concrete. Cement and Concrete Research. 40(9). pp. 1451-1458.

Ramamurthy, K., Nambiar, E.K.K. and Indu Siva Ranjani, G. (2009). A classification of studies on properties of foam concrete. Cement and Concrete Composites. 31(6). pp. 388-396.

Robberts, J.M. and Marshall, V. (2010). Analysis and Design of Concrete Structures. Cement and Concrete Institute and Nuclear Structural Engineering.

SABS 0100-1 (2000). The structural use of concrete - Part 1: Design. The South African Bureau of Standards. Pretoria. South Africa.

SABS 5863 (2000). Concrete tests - Compressive strength of hardened concrete. The South African Bureau of Standards. Pretoria. South Africa.

SABS 6253 (2000). Concrete tests - Tensile splitting strength of concrete. The South African Bureau of Standards. Pretoria. South Africa.

SABS 920 (2011). Steel bars for concrete reinforcement. The South African Bureau of Standards. Pretoria. South Africa.

Sancak, E., Simsek, O. and Apay, A.C. (2011). A comparative study on the bond performance between rebar and structural lightweight pumice concrete with / without admixture. International Journal of the Physical Science 6(14). pp. 3437-3454.

Sandrolini,F. et al. (2012). Ethyl silicate for surface treatment of concrete - Part 1: Pozzolanic effect of ethyl silicate. Cement and Concrete Composites. 34(3). pp. 306-312.

SANS 50450-1 (2011). Fly ash for concrete - Part 1: Definition, specifications and conformity criteria. The South African Bureau of Standards. Pretoria. South Africa.

Scott, A. and Alexander, M. (2007). The influence of binder type, cracking and cover on corrosion rates of steel in chloride-contaminated concrete. Magazine of Concrete Research. 59(7). 495-505.

Selander, A. (2010). Hydrophobic impregnation of concrete structures - Effects on concrete properties. PhD thesis. KTH.

Soltani, M., An, X. and Maekawa, K. (2003). Computational model for post cracking analysis of RC membrane elements based on local stress-strain characteristics. Engineering Structures 25(8). pp. 993-1007.

Song, H. and Saraswathy, V. (2007). Corrosion Monitoring of Reinforced Concrete Structures – A Review. International Journal of Electrochemical Science. 2. pp. 1-28.

Song, Z. et al. (2016). Experimental exploration of the waterproofing mechanism of inorganic sodium silicate-based concrete sealers. Construction and Building Materials. 104. pp. 276-283.

Stern, M. and Geary, A.L. (1957). Electrochemical polarization I. A theoretical analysis of the shape of polarization curves. Journal of the Electrochemical Society. 104(1). pp. 56-63.

Taylor, H.F.W. (1997). Cement chemistry. Thomas Telford publishers.

Tutti, K. (1982). Corrosion of steel in concrete

Utgenannt, P. (2004). The influence of ageing on the salt-frost resistance of concrete. Report TVBM 1021. Division of Building Materials, Lund Institute of Technology.

van Rooyen, A.S. (2013). Structural lightweight aerated concrete. Stellenbosch, South Africa. Civil Engineering, Stellenbosch University.

Visagie, M. and Kearsley, E.P. (2002). Properties of foamed concrete as influenced by the air-void parameters. Concrete / Beton. pp. 9-14.

Wei, S. et al (2013). Characterization and simulation of microstructure and thermal properties of foamed concrete. Construction and Building Materials. 47. pp. 1278-1291.

Wittman, F.H. (2002). Crack formation and fracture energy of normal and high strength concrete. Sadhana 27(4). pp. 413-423.

Zuo, J. and Darwin, D. (2000). Splice strength of conventional and relative rib area bars in normal and high strength concrete. ACI Structural Journal 97(4).

Chapter 3 - **Experimental Programme and Research Methodology**

In this chapter the testing procedures used in the research programme to achieve the research outcomes are explained in detail. The research outcomes includes the characterisation and determination of the mechanical and durability properties of foamed concrete. The mechanical properties include the compressive and tensile strength, elastic modulus, fracture energy, and design bond. For the determination of the durability properties accelerated deterioration methods (cyclic ponding and carbonation exposure) are used to initiate corrosion.

3.1 Introduction

3.1.1 Overview of the research programme and author's contribution

In this research programme data has been obtained through co- and sole-supervision and self-experimentation. Supervised researchers are credited for the contributions as highlighted in the figures and tables. Figures and tables may be produced from data extracted, "new representation of the work" or reproduced from data available in the respective research documents. Figure 3.1 shows an overview of the research programme and highlights the role of the author.

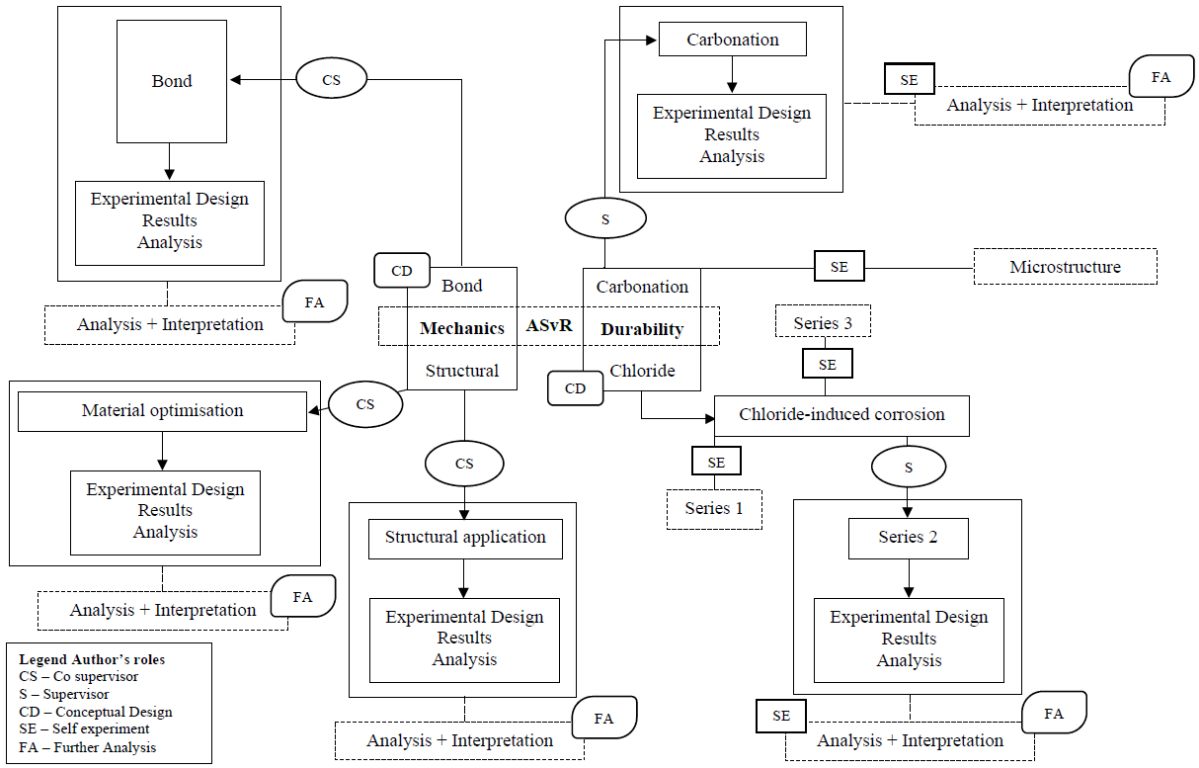

Figure 3.1: Overview of research programme and author's role

3.1.2 Overview of experimental programme

FC has mainly been utilised for non-structural application throughout its history. Thus the mechanical and durability properties were not necessarily determined. However, it is acknowledged that a fair amount of research has been published on the compressive strength of FC. Other research areas, mechanical properties (tensile strength, elastic modulus, fracture energy and bond) and durability properties (carbonation and chloride attack) lag far behind. Thus the research methodology has been designed to address this issue.

For this research programme standardised tests specimens according to the South African National Standards (SANS) and American Society for Testing Materials (ASTM) standards have been prepared to determine the tensile strength and elastic modulus. For fracture energy the wedge splitting test designed by Brühwiler and Wittmann (1990) is used. The bond behaviour of a steel bar embedded in FC is tested using the modified BE test as prescribed in the ASTM standard. These tests complete the characterisation of the mechanical properties.

Durability testing in this investigation was performed using test procedures found in literature. For carbonation-induced corrosion, a carbonation unit was constructed, the depth evolution of the carbonation front was monitored over time using standard cubes and the corrosion potential tests were performed on singly reinforced beam specimens. For chloride testing accelerated chloride exposure was used on unreinforced and singly reinforced prism samples to monitor the chloride penetration depth and chloride-induced corrosion. These carbonation- and chloride-induced corrosion tests are considered to represent the deterioration processes in reinforced LWFC.

3.2 Materials and Mix design

3.2.1 Mix constituents

3.2.1.1 Materials

The materials used in this research programme can be listed as follows:

- Sephakhu Ordinary Portland Cement (OPC) CEM I 52.5 N with relative density 3.14 and OPC CEM II 52.5 N according to SANS 50197-1:2013
- Natural dune sand (SANAS Soillab) with relative density 2.65 (Consol silica no 2)
- Ulula and AshResources (DuraPozz) Class S and Class F fly ash according to SANS 50450-1 with relative density 2.20
- Water repellent - Sikagard® 706 Thixo with relative density 0.9 and pH 8 classified in EN1504-2
- Water repellent - Sikalite® waterproofing (Sikalite (2012)) with relative density 0.9
- Water repellent - Chryso® Fuge B EN480-5
- Polypropylene fibres SAPY® Corehfil™ of 6 mm and 12 mm length (SAPY (2016)) with relative density 0.9
- High strength shrinkage compensated cementitious grout SikaGrout 212 (2016)
- Pre-formed foam made from a locally sourced natural protein based product named FoamTech

- Municipal potable water

The materials used in this research programme are based on the literature survey of Chapter 2. The use of fly ash for cement replacement and the OPC CEM II 52.5 N is to reduce cost, improve sustainability through the use of waste stream from coal burning industries, to achieve higher strength than using fine aggregate, and for long-term strength development. There is evidence of improved durability properties (Beushausen, Alexander and Ballim (2012)) and reduced heat of hydration by inclusion of fly ash.

3.2.1.2 Properties of Portland cement, fly ash and fibres

In this research programme ordinary Portland Cement (OPC) supplied from two different manufacturers, Sephakhu and Pretoria Portland Cement (PPC) was used. The cement supplied by Sephakhu and PPC conforms to SANS 50197-1:2013 and is classified as a CEM I 52.5 N and a CEM II/A-S 52.5 N. The fly ash used in this research programme is supplied by AshResources and Ulula. The fly ash supplied by AshResources and Ulula conforms to SANS 50450-1:2011 and is classified as a Class F and Class S. The chemical composition of the cement and fly ash is tabulated in Table 3.1. The polypropylene fibres used in the research programme is supplied from SAPY. Two fibre lengths, 6 and 12 mm, were used in this investigation and the properties thereof can be found in Table 3.2.

Table 3.1: Chemical composition of cement and fly ash

Chemical composition	**Cement**		**Fly ash**	
	CEM I 52.5 N*	**CEM II/A-S 52.5 N****	**Class F+**	**Class S++**
SiO_2	19.51	21.1	51	51.25
Al_2O_3	6	4.0	30	29.5
Fe_2O_3	2.8	3.1	3.5	2.5
CaO	62.4	64.8	7	7.75
MgO	3.54	1	1.75	2.25
K_2O	<1	<1	<1	<1
Na Equivalent	<1	<1	<1	<1.5
TiO_2	-		1.5	1.75

*Sephakhu OPC CEM I 52.5 N / **PPC OPC CEM II/A-S 52.5 N
+AshResources Durapozz Class F fly ash / ++Ulula Class S fly ash

Table 3.2: Properties of the fibre (SAPY (2016))

Properties	SAPY Corehfil™ Polypropylene fibres
Density	910
Melting point [°C]	160
Fibre diameter [µm]	40
Fibre length [mm]	6 / 12
Fibre colour	Natural (White)

3.2.2 Mix design and equipment

3.2.2.1 Mix design equations

A review of the mix design procedure is presented in Chapter 2. For ease of reading the FC mix design equations used in the research are relisted here as Equations 3.1 and 3.2. Figure 3.2 shows a picture of the FC mixer and foam generator used in this investigation.

$$m_{tot} = \rho_m = x + x\left(\frac{w}{c}\right) + x\left(\frac{a}{c}\right) + x\left(\frac{a}{c}\right)\left(\frac{w}{a}\right) + x\left(\frac{s}{c}\right) + x\left(\frac{s}{c}\right)\left(\frac{w}{s}\right) + x\left(\frac{f}{c}\right) + x\left(\frac{f}{c}\right)\left(\frac{w}{f}\right) + RD_f V_f \quad (3.1)$$

$$V_{tot} = 1000 = \frac{x}{RD_c} + x\left(\frac{w}{c}\right) + \frac{x\left(\frac{a}{c}\right)}{RD_a} + x\left(\frac{a}{c}\right)\left(\frac{w}{a}\right) + \frac{x\left(\frac{s}{c}\right)}{RD_s} + x\left(\frac{s}{c}\right)\left(\frac{w}{s}\right) + \frac{x\left(\frac{f}{c}\right)}{RD_f} + x\left(\frac{f}{c}\right)\left(\frac{w}{f}\right) + V_f \quad (3.2)$$

3.2.2.2 Mixing equipment and procedures

3.2.2.2.1 Foam generator

Figure 3.1 shows an annotated picture of the foam generator used in this investigation.

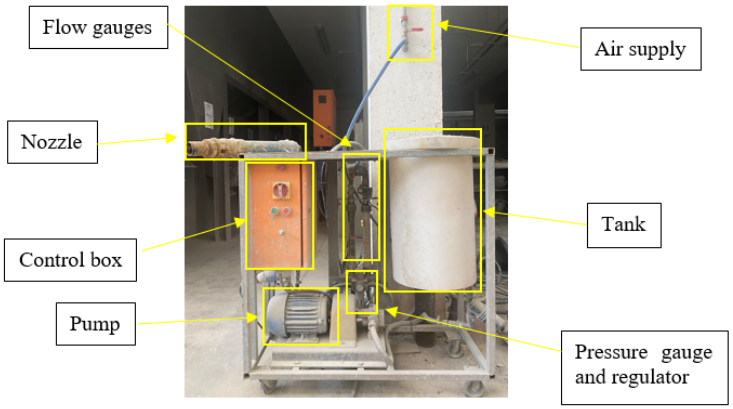

Figure 3.2: Foam generator

For stable foam generation the major components shown in Figure 3.2, highlighted in yellow, have to be working and set up accordingly. The control box of the foam generator has an on/off switch, a start button, a stop button, and a flow controller on the outside and a timer on the inside. Foam generation may be controlled from the outside with the start- and stop-buttons or can be stopped using the timer inside. The flow controller on the outside of the control box can be used to adjust the flow rate of the solution from the tank. The flow rate of the solution is shown and can be read from the solution flow gauge. The air supplied to the foam generator from the concrete lab, maximum pressure supply of 6 bar, can be controlled using the pressure regulator and the valve attached to the air flow gauge. The foaming agent used in this investigation is FoamTech and is diluted in water in a 1:40 ratio and mixed with ferrous sulphate in a ratio 1:80 ratio for stability. The solution in combination with the correct solution- and air-flow rate settings, with constant air pressure supply minimum and maximum of 5 and 6 bar operating pressure, is forced to mix together through a series of meshes in the nozzle to produce stable foam. The foam produced from the FoamTech foaming agent is only stable between density range of 70 and 80 kg/m^3 with 75 kg/m^3 being the optimum. The foam generator can produce stable foam between

flow rates of 1 to 3 litres per second. Throughout this research programme care has been taken to use stable foam with density between 70 and 80 kg/m^3 for all FC mixes. This was achieved by filling a container of known volume with the fresh foam and determining its mass for density calculations before every mix.

3.2.2.2.2 Foam mixer, mixing procedure and stability check

Figure 3.3 shows an annotated picture of the 70 litre FC mixer used throughout the investigation.

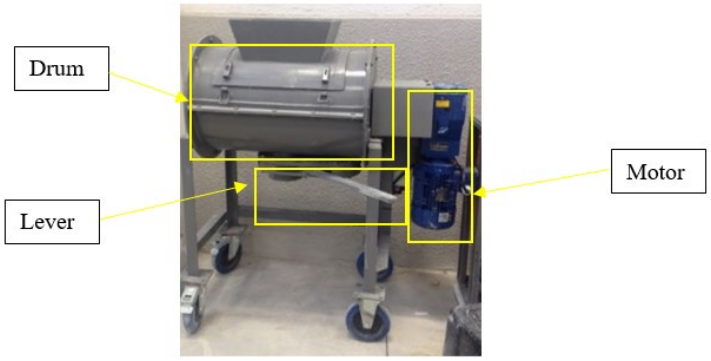

Figure 3.3: 70 L FC mixer (Ribbon type mixer)

The FC mixer shown in Figure 3.3 has a motor with on and off buttons, a drum with a 70 litre capacity, ribbon blades, a grid on the top, and a lever opening. In this research programme the base mix of FC was mixed to a homogeneous consistency before foam was added, the hydraulic turntable was used to determine the water demand and all base mixes have a spreadability between 220-250 mm. The foam is added during mixing through the grid opening at the top of the mixer. After the foam is added the mixer is allowed to continue mixing until a homogenous constancy is achieved, confirmed through visual inspection – no visible foam on the surface of the mix. Once a homogenous consistency is obtained the mixer is stopped and the fresh density of the concrete is measured by filling a 1 litre concrete cube mould, weighing it on a scale, and calculating the fresh density. The maximum allowed density deviation throughout this investigation is 50 kg/m^3. Depending on the fresh density of the concrete a mix is accepted or rejected.

3.2.3 Mix design composition, specimen preparation and stability – Mechanical testing series

3.2.3.1 Mix design composition – Mechanical testing series

The mix design composition of the concrete mixes used in the mechanical testing series are tabulated in Table 3.3. Mixes 18F, 16F, 15.5F, 15.5FN, 14F, 12F and 16FL are FC mixes designed using the methodology presented in Chapter 3.2.2. For these FC mixes, the design target wet density is calculated by multiplying the number in the description by 100. Therefore mix 16F would have an intended design target wet density of 1600 (16 x 100). Mix NWC is a normal weight concrete mix designed using the C&CI (Addis (2009)) procedure. Mixes 16F, 14F, 12F and NWC are used throughout the mechanical testing series with the exception of mix 16FL that is used for a long-term study for compressive strength development.

Table 3.3: Mix design composition for the mechanical testing series

Description	18F	16F	14F	12F	NWC	16FL[#]	15.5FN[1,2,3,4,5,6]	15.5F[1,2,3,4,5,6]
a/c	1	1	1	1		2		
s/c								1
	FD	**1600 kg/m³**	**1400 kg/m³**	**1200 kg/m³**	**FD**	**1600 kg/m³**	**1550 kg/m³**	**1550 kg/m³**
Cement[kg]	716*	606.2*	526.7*	447.2*	336.2*	404.4**	1095.71	616.7
Water [kg]	447	375.9	326.6	277.3	195	375.6	438.3	296
Fly-ash [kg]	716[+]	606.2[+]	526.7[+]	447.2[+]		808.9[++]		
Stone [kg]					1000			
Sand [kg]					835			616.7
Foam [kg]		11.7	20	28.3		9.53	16	20.7

OPC CEM II 52.5N* / OPC CEM I 52.5N**
Durapozz fly-ash[+] / Ulula class S fly-ash[++]
12 mm SAPY Corehfil™ PP fibres at 0.45% w.r.t. volume[#]
Full density (FD) - No added foam for FC mixes, base mix
12 mm SAPY Corehfil™ PP fibres at 0.2[1], 0.35[2], or 0.50[3]% w.r.t volume
24 mm SAPY Corehfil™ PP fibres at 0.2[4], 0.35[5], or 0.50[6]% w.r.t volume
Data extracted from de Villiers (2015), Grafe (2017) and Zvinokona (2018)

3.2.3.2 Specimen preparation – Mechanical testing series

3.2.3.2.1 Specimen preparation – Compressive strength (f_{cu}) and tensile splitting strength (f_t) tests

For the compressive strength testing 100 mm cube specimens were cast in moulds made from mixes 18F, 16F, 14F, 12F, NWC and 16FL and 100 mm diameter cylindrical specimens (L/D = 2) from mixes 15.5FN[1,2,3,4,5,6] and 15.5F[1,2,3,4,5,6]. For tensile splitting strength testing 100 mm cube specimen were cast from all mixes. All specimens were placed in a climate control room directly after mixing. After 24±3 hours the cubes were removed from the moulds and returned to the climate room, 22±1°C temperature and 60±5% RH, until the day of testing. A summary of the number of specimens cast for each test can be found in Table 3.4.

3.2.3.2.2 Specimen preparation – Elastic modulus test

For determining the elastic modulus cylindrical specimens, length 200 mm with L/D ratio of 2, were cast in moulds from mixes 18F, 16F, 14F, 12F, NWC, 15.5FN[1,2,3,4,5,6] and 15.5F[1,2,3,4,5,6] and place directly in a climate controlled room. After 24±3 hours the cubes were removed from the moulds and left in the climate room, 22±1°C temperature and 60±5% RH, until the day of testing. The number of specimens cast for each mix is tabulated in Table 3.4.

3.2.3.2.3 Specimen preparation – Wedge splitting test ($G_{f,\ wedge}$)

For determining the fracture energy using the wedge splitting test 100 mm cube specimens were cast in moulds with a wooden block on top to create a 20x30 mm (length x depth) cavity in the top centre of the specimens, Figure 3.8a shows an illustration of the specimens. Specimens were cast from mixes 16F, 14F, 12F, NWC, 15.5FN[1,2,3,4,5,6] and 15.5F[1,2,3,4,5,6] and place directly in a climate controlled room. After 24±3 hours the cubes were removed from the moulds and left in the climate room, 22±1°C temperature and 60±5% RH. One day prior to testing specimens were removed from the climate room and a 5x30 mm

(length x depth) saw cut was made in the length direction of the cavity, See Figure 3.8b. Specimens were returned to the climate room and tested the following day. One hour before testing, PVC blocks were glued to the specimens, 50 mm apart in the centre shown in Figure 3.8d. The number of specimens cast for each mix is tabulated in Table 3.4.

3.2.3.2.4 Specimen preparation – Three-Point Bending (TPB) ($G_{f,\ beam}$)

For determining the fracture energy using the TPB test beam specimens, 500x100x100 mm (lxbxd), were cast from mixes 15.5FN[1,2,3,4,5,6] and 15.5F[1,2,3,4,5,6] in moulds directly after mixing and stored in a climate controlled room. After 24±3 hours the specimens were removed from the moulds and returned to the climate controlled room, 22±1°C and 60±5% RH. One day prior to testing specimens were removed from the climate room and a 3x30 mm (width x depth) saw cut was made in the middle along the depth of the beam specimen. In this testing programme the target density of the mixes were kept constant while the fibre length (l_f), 12 and 24 mm, fibre content (f_c), 0.20, 0.35, and 0.50% w.r.t. volume, and sand cement ratio, 0 and 1, was varied. The number of specimens cast for each mix is tabulated in Table 3.4.

3.2.3.2.5 Specimen preparation – Beam-End test (BE test)

For determining the bond between the reinforcing steel and concrete, BE specimens were cast from mixes 16F, 14F, 12F and NWC. BE specimens, dimension 610 x 220 x 270 mm, were reinforced with stirrups (R8 bars) to prevent shear failure and an embedded steel rod for bond determination. The embedded steel rod is inserted throughout the length of the BE and is threaded at the loaded end as shown in Figure 3.4. Three distinct regions, a bonded region sandwiched between the loaded-end and free-end un-bonded regions, can be observed between the embedded steel rod and the surrounding concrete in the BE. The loaded-end un-bonded region prevents crack formation during testing and extends 50 mm into the BE from the loaded-end face. The bonded region follows directly after the loaded-end un-bonded region and represents the tested embedded length, l_e. The free-end un-bonded region extends from the end of the bonded region and penetrates the free-end face of the BE, see Figure 3.5 for BE moulds. BE specimens were demoulded and kept in the laboratory floor area. The specimens were cover with a blanket and kept wet until the day of testing. The number of specimens cast for each mix is tabulated in Table 3.4.

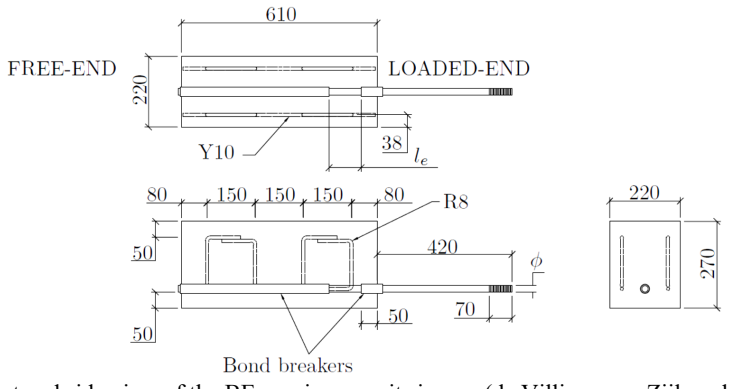

Figure 3.4: Top, front and side view of the BE specimen, units in mm (de Villiers, van Zijl, and van Rooyen (2016))

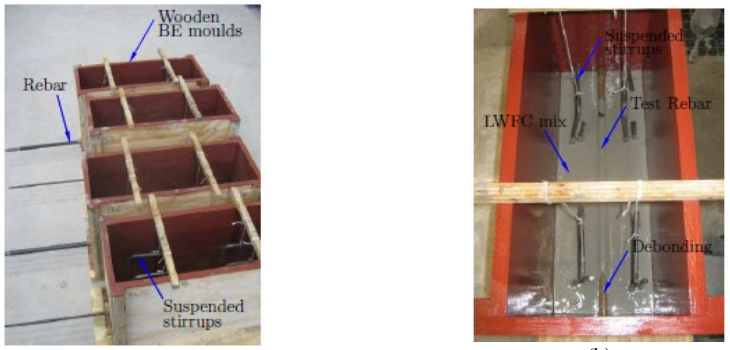

(a) (b)

Figure 3.5: BE specimen moulds indicating rebar, stirrups, LWFC mix (de Villiers (2015))

3.2.3.3 Number of specimens and stability of FC mixes – Mechanical testing Series

Table 3.4 shows the number of specimens cast for the mechanical testing series. The variation in density is a result of batching due to the volume of concrete needed to produce the required amount of specimens. A maximum variation in casting density of ±50 kg/m^3 was allowed for this series. Table 3.5 shows the density ratios of the various specimens used for testing. The data in Table 3.5 shows that all specimens conform to the mix acceptance criteria.

Table 3.4: Total number of specimens cast for each mix in mechanical testing series

Description	18F	16F	14F	12F	NWC	16FL$^{\#}$	15.5FN^{1,2,3,4,5,6}	15.5F^{1,2,3,4,5,6}
a/c	1	1	1	1		2		
s/c								1
Tests	**FD**	**1600 kg/m^3**	**1400 kg/m^3**	**1200 kg/m^3**	**FD**	**1600 kg/m^3**	**1550 kg/m^3**	**1550 kg/m^3**
C	15	21	24	9		21	18	18
T	3	3	3	3	3		18	18
E	3	3	3	3	3		18	18
W		3	3	3	3		18	18
TPB		3	3	3	3		18	18
BE		2	2	2	2			

C - Compressive strength / T - Splitting tensile / E - Elastic modulus / W - Wedge splitting cube / TPB - Three-point bending / BE - Beam-End

Table 3.5: Density ratios of the various specimens used for testing (16F, 14F, and, 12F)

Description	**1600 kg/m^3**		**1400 kg/m^3**		**1200 kg/m^3**	
	$\rho_{casting}/\rho_{target}$	α_b	$\rho_{casting}/\rho_{target}$	α_b	$\rho_{casting}/\rho_{target}$	α_b
T	1621/1600	1.013	1415/1400	1.011	1156/1200	0.963
E	1577/1600	0.986	1361/1400	0.972	1156/1200	0.963
W	1575/1600	0.984	1389/1400	0.992	1221/1200	1.018
PO	1621/1600	1.013	1415/1400	1.011	1202/1200	1.002
BE 12	1633/1600	1.021	1353/1400	0.966	1233/1200	1.028
BE 20	1610/1600	1.006	1422/1400	1.016	1160/1200	0.967

T - Splitting tensile / E - Elastic modulus / W - Wedge splitting / PO - Pull-out / BE - Beam-End
α_b = 1.008 for 16FL and a $\alpha_{b,\ average}$ = 1.003 for mixes 15.5FN^{1,2,3,4,5,6} and 15.5F^{1,2,3,4,5,6}
Data extracted from de Villiers (2015), Grafe (2017) and Zvinokona (2017)

3.2.4 Mix design composition and specimen preparation – Structural application

3.2.4.1 Mix design composition – Structural application

In this investigation six wall panels made of LWFC, with two panels comprising a wall, were prepared and tested at a concrete age of 28 days as detailed in Section 3.2.2. Table 3.6 gives the LWFC mix design

composition, 16FR, which was used to cast the wall panels and is based on the work of van Zijl, van Rooyen, Mubatapasango et al. (2017).

Table 3.6: Mix design composition of mix 16FR per 1000 L.

Description	Cement	Water	Fly ash	Foam	Fibres
Content [kg]	371.8*	479.7	743.6++	4.8	4.1[1]

PPC OPC CEM II 52.5N*
Ulula class S fly-ash++
12 mm SAPY Corehfil™ PP fibres at 0.35[1] % by volume
Data from Dunn, van Zijl, and van Rooyen (2018)

3.2.4.2 Specimen preparation – Structural application

In this investigation LWFC wall panels were cast from mix 16FR given in Table 3.6. Each LWFC wall panel, dimensions 1380x920x150 mm, was reinforced with two steel meshes *Ref*. 193 which has 5.6 mm diameter steel bars at a spacing of 200 mm in both directions, three anchor bolts, three vertical connections, and a pair of three dowel connections per horizontal interface. 40 mm drainage pipes were used for creating the dowel connections. The vertical connection and horizontal dowel connections are spaced equidistance apart at 230 mm and 345 mm, respectively. Figure 3.6 shows the mould, mesh, anchor bolts, connections and fresh LWFC during casting.

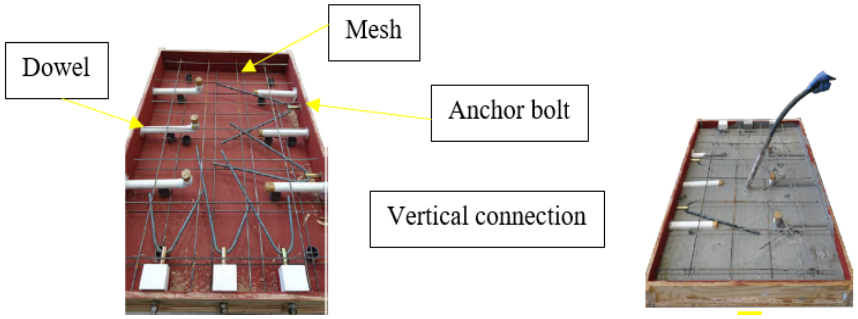

Figure 3.6: LWFC wall panel mould used showing reinforcement, vertical connection box, anchor bolts and dowel connections and during casting (Dunn, van Zijl, and van Rooyen (2018))

After casting LWFC panels were left in the laboratory floor area covered with blankets and kept wet. Prior to testing specimens were moved to the testing area and NWC panels, simulating the upper and ground floor were connected via dowel connections. Y12 rebar was used for dowel connections and was grouted at the connections with SikaGrout® 212, see Figure 3.7. LWFC wall panels were tested at an age of 28 days.

(a) (b)

Figure 3.7: (a) Y12 hand bend rebar at grouted connection (b) grout process (Dunn, van Zijl, and van Rooyen (2018))

3.3 Mechanical tests and structural application

3.3.1 Compressive strength

The compressive strength expresses the concrete strength under uniaxial compression. It is typically determined at the age of 28 days, but its evolution over time, i.e. at ages less and more than 28 days, is of interest. A procedure for determining the compressive strength is set out in SANS 5863 (2006). According to the standard a constant load rate of 0.3 ±0.1 MPa/s should be applied to the specimen, cube or cylindrical, until failure. The loading rate converts to 180 ±60 kN/min for cubes of 100 mm side lengths and 283±94 kN/min for cylindrical specimens of radius 50 mm and L/D ratio of 2. The peak load value is recorded and is divided by the corresponding loaded area to obtain the compressive strength of the specimen, given in Equation 3.3. The compressive test is conducted on a minimum of three specimens of which the average compressive stress is recorded and taken as the compressive strength of the concrete at the particular test age.

$$f_{cu} = \frac{F}{A} \tag{3.3}$$

where f_{cu} is the compressive strength,

F is the peak load,

A the loaded area.

3.3.2 Tensile splitting strength

The tensile strength is a measure of a materials' ability to carry tensile loading. For concrete an indirect method given in SANS 6253 (2000) can be used to determine the tensile strength of concrete. In this method the concrete specimen is subjected to a direct uniform compressive load which indirectly induces tension. The concrete specimen can be cylindrical, rectangular or cubical in shape. The compressive load is constantly applied at a loading rate of 0.3 ±0.1 MPa/s until failure. The peak load is then recorded and used in Equation 3.4 to determine the tensile splitting strength of the specimen. The tensile splitting strength of the concrete is taken as the average tensile splitting strength of three specimens.

$$f_t = \frac{2F}{\pi A_c} \tag{3.4}$$

where f_t is the tensile strength

A_c the crack plane area.

3.3.3 Elastic modulus

A test method to determine the elastic modulus for concrete is described in ASTM C469 (2014). The test method describes a procedure to obtain the slope (E_c) of a stress strain diagram for hardened concrete that is stressed within a customary working stress range of up to 40% of the concretes' ultimate compressive stress. During the test the cylindrical concrete specimens are loaded and unloaded, without shock at a loading rate of 200 kPa/s at least two times, to the 40 % stress limit. The loading and unloading stage provide the opportunity for the three strain gauges, spaced 120° apart, to seat properly onto the specimen and can be rectified in the event of improper seating. The testing phase consists of two additional loading and unloading cycles whereby the average of both cycles and strain, from the three strain gauges, is used to obtain the stress-strain slope. The Young's modulus of the concrete is calculated using Equation 3.5.

$$E_c = \frac{\sigma_1 - \sigma_0}{\varepsilon_1 - \varepsilon_0} \tag{3.5}$$

where E_c is the Young's modulus of the concrete,
σ_1 and σ_0 is the stress corresponding to 40 % and 33 % of the ultimate strength,
ε_1 and ε_0 is the strain corresponding to 40 % and 33 % ultimate strength.

3.3.4 Fracture Energy, G_f

3.3.4.1 Wedge splitting tests

The fracture energy of concrete can be determined using the method introduced in 1990 by Brühwiler and Wittmann. The method uses a 100 mm cubical specimen with a 20 mm deep by 30 mm wide cavity along the middle of the top surface. The specimen also has a 30 mm deep saw cut, running along the middle of the cavity, which creates a stress concentration site at its bottom tip. The test comprises of a wedge, with known angle α_w, pressing on rollers subjecting the specimen to vertical and horizontal forces. This loading configuration induces a bending moment which causes a crack to initiate and propagate vertically, from the bottom tip of the saw cut, creating a specific fracture area. In order to promote stable crack propagation after crack initiation the loading is adjusted during testing via displacement control. Two LVDTs are used to monitor the crack mouth opening displacement (COD) and its signal is used in a closed-loop actuator to maintain a pre-set COD rate. Figure 3.8 illustrates the wedge splitting test for fracture energy determination.

For sensible results a COD rate of 0.003 mm/s was used. The fracture energy, G_f, is the ratio of the area under the F_h-COD (horizontal force versus COD) and fracture area. The horizontal force, F_h, is calculated using Equation 3.6. Another useful parameter to determine is the characteristic length, l_c. The characteristic length is an indication of the brittleness of the material and is derived from the material properties using Equation 3.7.

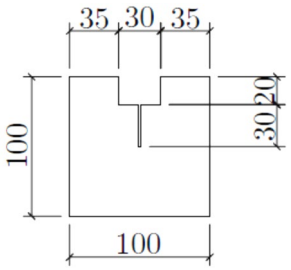

(a) Wedge splitting test specimen

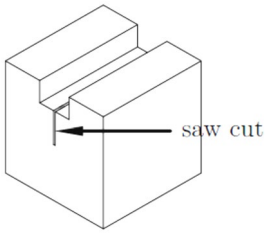

(b) Isometric view of specimen

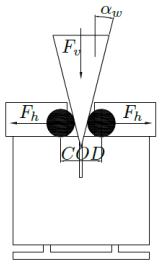

(c) Loading of wedge splitting test specimen

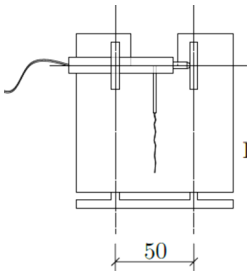

(d) LVDT configuration on specimen

Figure 3.8: Illustration of the wedge splitting test (all units in mm)

$$F_h = \frac{F_v}{2tan\alpha_w} \tag{3.6}$$

$$l_c = \frac{E_c G_f}{f_t^2} \tag{3.7}$$

where F_v is the vertical force,

E_c is the Young's modulus of the concrete,

G_f is the fracture energy.

3.3.4.2 Three-point bending (TPB) tests

A test method to determine the fracture energy for concrete is described in the Japan Concrete Institute Standard JCI-S-002-2003. The test method describes the procedure to obtain the load-displacement, force-COD, used to determine the fracture energy. The method makes use of notched rectangular beam specimens. The prescribed dimensions of the notch is 30 mm and 3 mm wide. In this investigation beam specimens of dimension 500x100x100mm were used for TPB test. The notches were saw cut into the specimens prior to testing. The COD was measured with a clip gauge, coupled to the MTM INSTRON, and complies with the prescribed minimum accuracy of 1/1000 mm stated in the standard. The clip gauge was secured over the notch between two sharp metal "knife edges" pieces glued to the beam specimens, allowing for safe and accurate measurement. Figure 3.9 shows an illustration of the beam specimens and Figure 3.10 shows a beam specimen after testing in the loading rig.

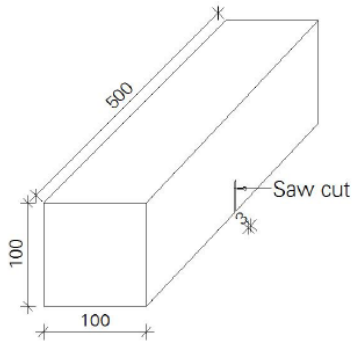

Figure 3.9: Illustration of TPB beam specimen

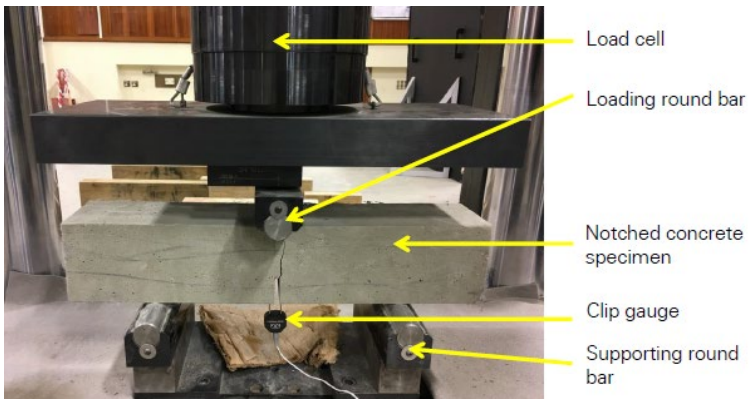

Figure 3.10: Beam specimen after testing in the loading rig (Grafe (2017))

The fracture energy of the concrete is the area under the load-COD curve divided by the projected area (cracked area). For the TPB test the fracture energy is influenced by the self-weight of the beam. Equation 3.6 gives and expression to calculate the fracture of a specimen tested in TPB taking into account the-weight of the material.

$$G_f = \frac{0.75W_0 + W_1}{A_{lig}} \tag{3.6}$$

where G_f is the fracture energy

W_0 and W_1 is the area under the load-COD up to rupture and the work done by the self-weight of the specimen and the loading rig, given as $W_1 = 0.75\left(\frac{S}{L}m_1 + 2m_2\right)COD_C$

m_1 and m_2 the mass of the specimen and jig,

S and L the length of the loading span and specimen,

g the gravitational acceleration take as 9.802 m/s^2, and

COD_C the COD at the time of rupture.

3.3.5 Bond strength (Beam-End test)

The BE test, recommended by ACI 318-11 (2011) for obtaining bond strength between steel and the surrounding concrete, is conducted through the specifications set out in ASTM A944 – 10 (2002).

Figure 3.11 shows the test set-up used for testing the BE specimen.

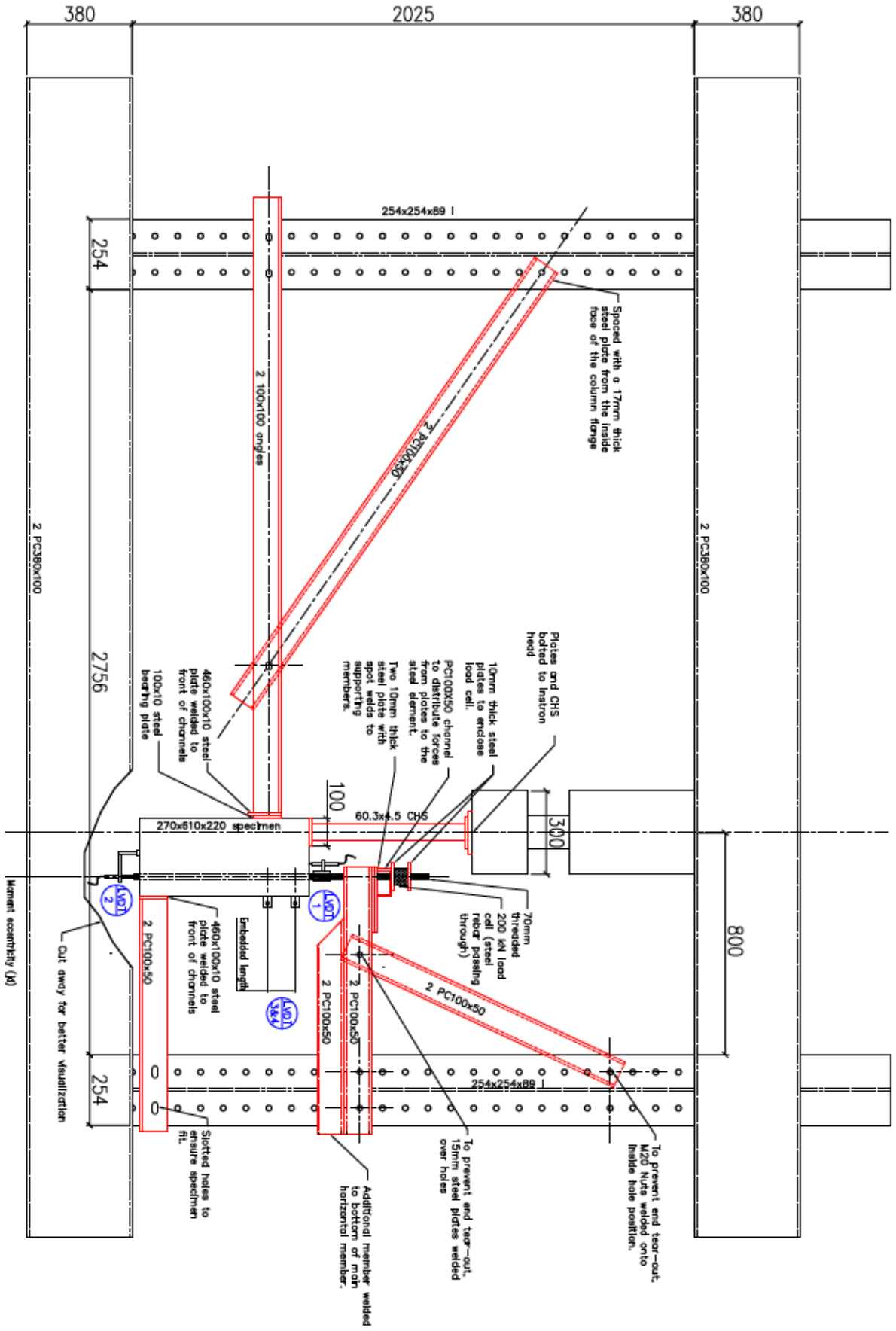

Figure 3.11: BE test setup with actuator, BE specimen, and LVDT positions, units in mm (de Villiers (2015))

In the test set-up the BE specimen is orientated upright, as shown in Figure 3.11. The threaded portion of the embedded steel rod is therefore used to secure the BE specimen to the testing rig, allowing the specimen to hang freely. Two lateral supports are also provided, one at the bottom right and the other at the top left, to the free hanging BE specimen. During testing, the force is transferred from the actuator to the BE specimen via a strut attached at the head of the actuator. Figure 3.12 depicts a schematic representation of the forces induced in the BE specimen during loading. As can be seen in Figure 3.12, compression is induced in the concrete at the application site and a tensile force is developed in the embedded steel rod. Additionally, a moment is produced over the cross-section of the loaded-end face. This moment is counteracted by the lateral supports that simulate a column support, bottom left lateral support, and an applied shear force, top left lateral support. This loading pattern and stress field generated in the BE specimen is a more realistic representation of a reinforced concrete beam behaviour in flexure and it is the reason why the BE test is recommended above the PO test. Ultimately the loading pattern cases breaks the bond and pulls the embedded steel rod from the concrete.

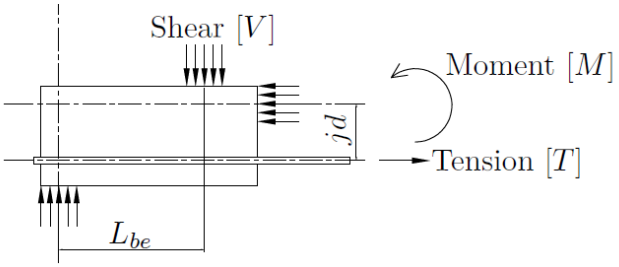

Figure 3.12: FBD Representation of the load induced in the BE specimen during testing

For bond determination three readings are required, namely, (1) tensile force in the embedded steel rod, (2) loaded-end slip, and, (3) the free-end slip. Throughout testing, the force in the embedded steel rod is recorded using a load cell placed at the connection between the protruding rod of the BE specimen and the testing rig. The loaded-end slip is recorded by seating a Linear Variating Differential Transducer (LVDT) connected to the embedded steel rod on the loaded-end face of the BE specimen. A second LVDT is then placed on the free-end face of the BE specimen and seated on the free-end of the embedded steel rod. In order to measure any surface cracks due to splitting failure two additional LVDTs are placed on the bottom surface of the BE specimen, one at the start of the bonded region and the other at the end of the bonded region. Figure 3.13 visually illustrates the placement of the load cell and locations of the LVDTs. For testing the BE specimen ASTM A944-10 (2002) does not specify a specific control system to be used during testing. However, the standard does state the specimen should only be allowed to fail after three minutes of testing.

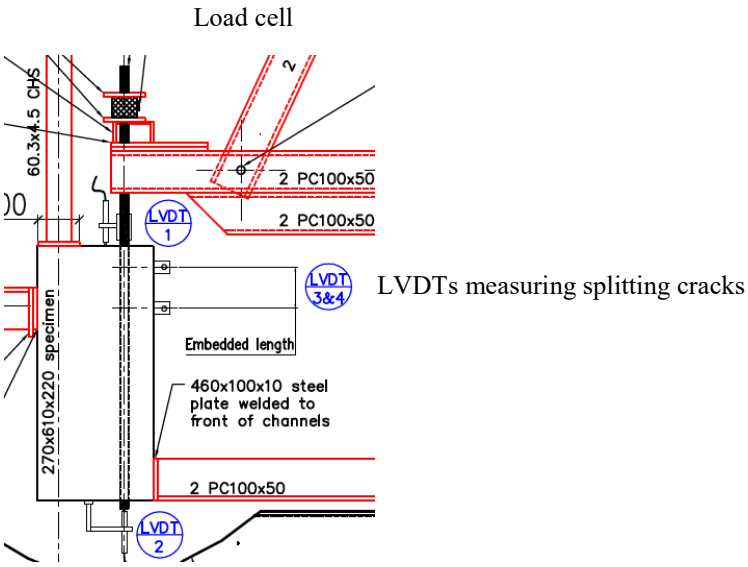

Figure 3.13: Diagrammatic illustration of the BE specimen and data measuring instruments

3.3.6 Monotonic pull over and cyclic tests

In this research programme a two panel LWFC walling system for a proposed low-rise LWFC residential building situated in low to moderate seismic zones was tested through monotonic pull-over and quasi-static "cyclic" test in accordance with the JRC scientific and policy report (Negro and Toniolo (2012)). Figure 3.14 shows the proposed LWFC building and the location of the wall, outlined in red, tested.

Figure 3.14: Proposed LWFC building (Dunn, van Zijl, and van Rooyen (2018))

The length of the highlighted wall in Figure 3.14 is 7200 mm therefore each LWFC panel has a proposed length of 3600 mm. However, due to laboratory restrictions a wall panel of 3600 mm could not be tested and a 1:3 scaled down wall panel with dimensions 1380x920x150 mm was tested. It should be noted that in order to simulate actual behaviour, stress fields, and failure mechanisms proper scaling laws should be applied. Scaling was not considered in this investigation as for seismic action it would require appropriate scaling down of reinforcement and connection elements to correctly represent strength, stiffness and mass. The purpose of the two monotonic pull-over test and quasi-static test is to show that the proposed LWFC walling system can be utilised to activate appropriate energy-dissipating failure mechanisms.

Tests set-up

Figure 3.15 shows the test set-up used to test the proposed two panel LWFC walling system.

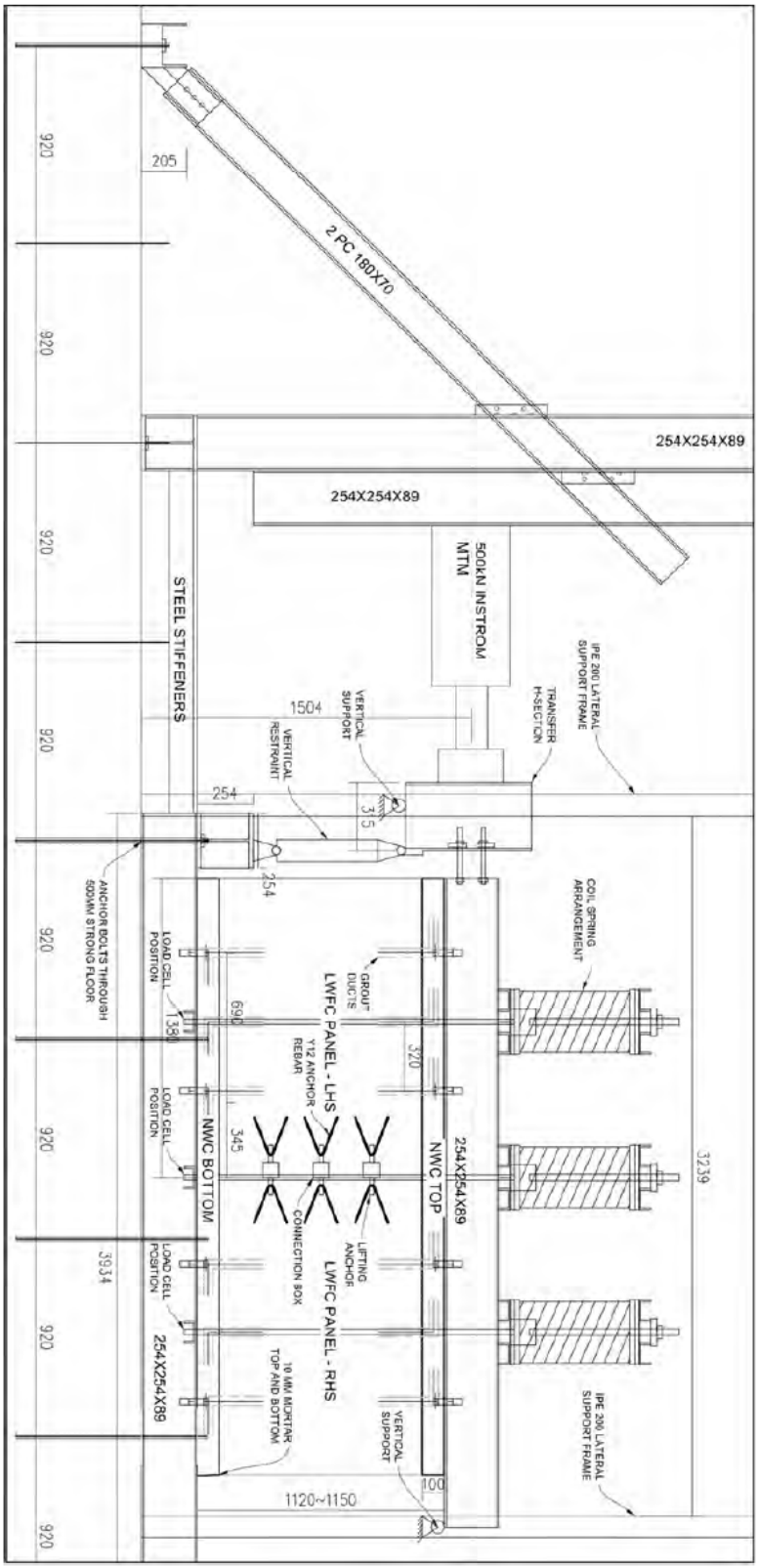

Figure 3.15: Test set-up for scaled LWFC walling system (Dunn (2017))

In Figure 3.15 the two panel LWFC walling system is sandwiched between two NWC panels. The bottom NWC panel simulates the ground floor slab and the top NWC panel simulates the hollow core floor slab and the walls above. Three pairs of springs are placed on top of the top NWC panel and are connected to the bottom NWC panel through threaded bars. A load cell, placed at the top of each spring, is used to record the pre-tensioned force and the load developed. The load induced by the three pairs of springs (six springs) represents the self-weight of the top structure and is distributed through a structural steel beam with an H-profile designated 254x254x89 in SAISC (2016). The pre-tension force, induced by tightening the threaded bars, is used to simulate the effect of the upper storey self-weight of the low-rise building. The 500 kN MTM actuator is used to apply a force (push - monotonic, push / pull - "cyclic") onto the steel beam, connected with threaded bolts, which transfers the load into the top NWC panel via shear connecting bolts. The load is transferred into the wall panels via dowel connections. The dowel connections of 12 mm diameter high yield stress (520 MPa) steel bar embedded in 40 mm diameter PVC pipe grouted with SikaGrout 212.

Figure 3.16 shows the setup for testing the LWFC walling system, the load transfer connections, and the displacement measuring point.

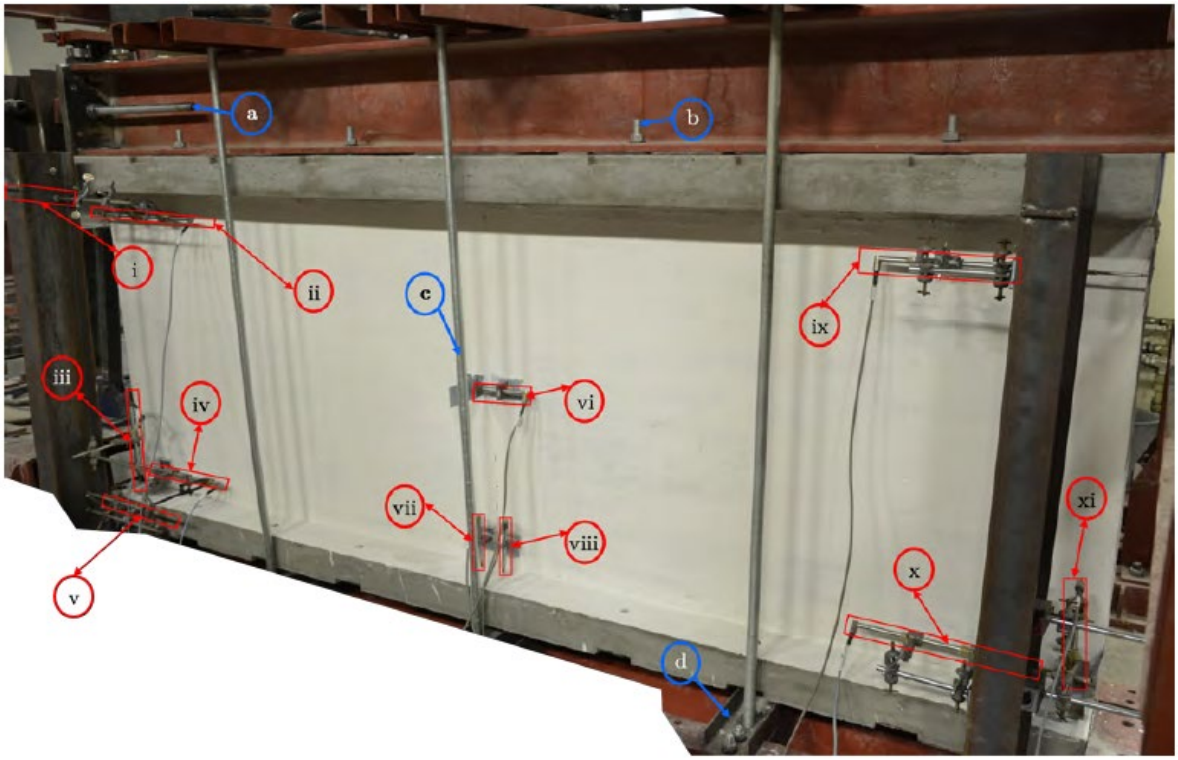

Figure 3.16: LWFC walling system in the test setup with balloons indicating loading transfer connections and displacement measurement positions. (a) Load transfer bar, (b) shear bolt, (c) 24mm threaded bar for pre-tensioning, (d) position bracket, (i) – (xi) LVDT's measuring displacement, see Table 3.7 for description. (Dunn (2017)).

Table 3.7: LVDT position for monotonic pull-over and quasi-static "cyclic" tests.

LVDT number	Position and description	Global position [a]
(i)	NWC left horizontal LVDT	A
(ii)	LWFC left panel horizontal top LVDT	B
(iii)	LWFC left panel vertical LVDT	
(iv)	LWFC left panel horizontal bottom LVDT	C
(v)	NWC left horizontal bottom LVDT	D
(vi)	LWFC vertical connection horizontal displacement LVDT	
(vii)	LWFC left panel vertical connection vertical displacement LVDT	
(viii)	LWFC right panel vertical connection vertical displacement LVDT	
(ix)	LWFC right panel horizontal top LVDT	
(x)	LWFC right panel horizontal bottom LVDT	
(xi)	LWFC right panel vertical LVDT	

a - global positions used to measure overall displacement of the walls shown in Figure 3.16

Testing

Wall 1 and Wall 2 consists of a pair of wall panels with six dowels in each connecting interface and three mechanical connections along each vertical connecting interface. Wall 3 consists of a pair of wall panels with a reduced number of four dowels per horizontal connecting interface, but retaining three mechanical connectors for the vertical interface The dashed lines in Figure 3.17a represent the horizontal connection with the highlighted in red removed for Wall 3.

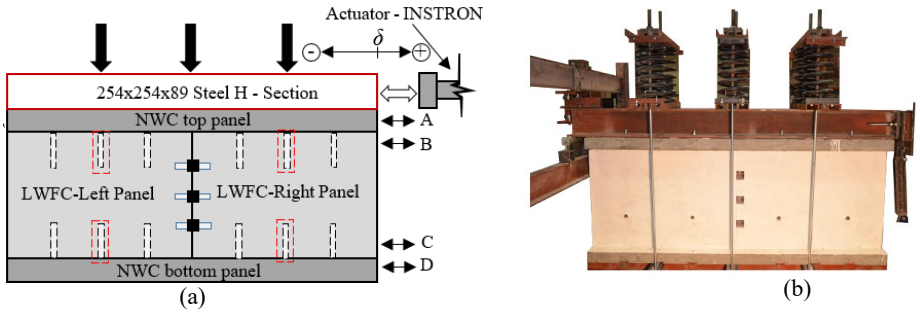

Figure 3.17: Test setup of the wall panels (a) illustration indicating loading, displacement measuring and load application site, and, (b) before testing commences (Dunn, van Zijl, and van Rooyen (2018))

Figure 3.17 shows the test setup of the two panel walling system. In Figure 3.17a the illustration shows the load application site of the actuator (INSTRON) applying a force left "push" or right "pull" direction. A positive displacement was chosen in the "pull-over" direction. The three vertical arrows represent the downward force due to the upper storeys and is induced by the threaded bar and spring system shown in Figure 3.17b. The vertical load induced by the upper storeys were calculated according to SANS 10160-1:2011 (SANS (2011a)), SANS 10160-2:2011 (SANS (2011b), and SANS 10160-4:2017 (SANS (2017)) and can be found in Dunn (2017). The vertical load was distributed evenly amongst the six springs with each inducing a force of 4.79 kN resulting in an average compression stress of 0.1 MPa in the wall panels. Positions A, B, C and D are the locations where the displacements were measured during testing. Note that more displacement measurements were taken, for instance to quantify

"rocking" uplift between each wall panel and the foundation. See Dunn, van Zijl, and van Rooyen (2018) for full details.

A monotonic pull-over test was conducted on Wall 1 and Wall 3 and a quasi-static cyclic test was performed on Wall 2. It should be noted that the walls were not tested until failure due to the limitation of the testing machine. The actuator (INSTRON) has a 50 mm stroke which gives a displacement range of -25 mm and 25 mm ($-25 < \delta$ (mm) < 25), 0 to 50 mm.

3.4 Durability properties

3.4.1 Mix design composition, specimen preparation and stability – Carbonation testing series

3.4.1.1 Mix design composition – Carbonation testing series

The mix composition of the concrete used to prepare specimens to be tested in the carbonation testing series is tabulated in Table 3.8. Mixes 14R, 14N, and 14I were designed using the methodology set out in Section 3.2.2 and have a design target density of 1400 kg/m^3. The designations R, N, and, I, stand for Reference, Non-Integral, and Integral. Surface treatment agents were employed to enhance the carbonation resistance of LWFC. For this investigation an integral surface treatment agent (I) is one that is added to the dry or fresh mix and a non-integral surface treatment agent (N) is one that is sprayed or brushed onto the concrete as per the recommendation of the manufacturer. The reference (R) is the neat LWFC without any purposeful or intended enhancement.

Table 3.8: Mix design composition of LWFC used for accelerated carbonation specimens

Description a/c	14R / 14N[#] / 14I[##] 1
	1400 kg/m^3
Cement [kg]	511.7*
Water [kg]	358.2
Fly-ash [kg]	511.7[+]
Foam [l]	18.4

Sephakhu OPC CEM I 52.5 N*
Ulula class S fly-ash[+]
Sikagard®-706 Thixo (200-300 g/m^2 after 28 days curing)[#]
Chryso® Fuge B 1.5% w.r.t. binder[##] (All mix quantities are reduced)
Data extracted from Mubatapasango (2017)

3.4.1.2 Specimen preparation – Carbonation testing series

3.4.1.2.1 Specimen preparation – Dip test, Carbonation front and X-Ray CT scanning.

In this research programme specimens were prepared for the Dip test, carbonation evolution, and x-ray CT scans using the mix design compositions for 14R, 14N, and, 14I as tabulated in Table 3.8. This was done in order to investigate the influence of surface treatment on the various properties of LWFC. After mixing, the fresh density is measured and if the mix is accepted, specimens are cast. Cubic specimens were cast with 100 mm side lengths for the dip test, monitoring the evolution of the carbonation front and x-ray CT scanning. After casting, all specimens were stored in a climate control room at a temperature of 22±2°C and RH of 65±5%. After 24±3 hours, specimens were removed from the climate room and demoulded. After demoulding, the specimens were wrapped in plastic and returned to the

climate room and stored up to the age of 28 days. After 28 days, all specimens were unwrapped (removed plastic) and specimens made from mix 14N were coated with the non-integral surface treatment agent, Sikagard®706-Thixo. Coated specimens formed the non-integral (N) test set to be tested alongside the reference (R) and integral test (I) set. The coated specimens were allowed to dry, according to the recommendation of the manufacturer, alongside the rest of the specimens. After drying specimens were placed in a carbonation tank up to the day of testing. However, for CT scanning the 100 mm cubes specimens were removed after 6 weeks of carbonation and were saw cut into smaller 30 mm cube specimens a day before testing. The saw cuts were placed parallel to the outer edges at a depth of 35 mm thereby producing a single 30 mm cube sample from each 100 mm specimen. The number of specimens produced is tabulated in Table 3.9.

3.4.1.2.2 Specimen preparation – Corrosion Assessment (HCP)

For corrosion assessment, Y12 singly reinforced rectangular specimens were cast from mixes 14R, 14N, and 14I with dimensions of 500x100x100 mm. The rebar had a total length of 540 mm and protruded 20 mm on both sides of the specimen. After casting, all specimens were stored in a climate control room at a temperature of 22±2°C and RH of 65±5%. After 24±3 hours, specimens were removed from the climate room and demoulded. After demoulding, the specimens were wrapped in plastic and returned to the climate room and stored up to the age of 28 days. After 28 days, all specimens were unwrapped (removed plastic) and specimens made from mix 14N were coated with the non-integral surface treatment agent, Sikagard®706-Thixo. Coated specimens formed the non-integral (N) test set to be tested alongside the reference (R) and integral test (I) set. The coated specimens were allowed to dry, according to the recommendation of the manufacturer, alongside the rest of the specimens. After drying specimens were placed in a carbonation tank up to the day of testing. The number of specimens produced is tabulated in Table 3.9.

3.4.1.3 Number of specimens and stability of FC mixes – Carbonation testing series

Table 3.9 shows the number of specimens cast for the durability testing series. Each time after mixing, the fresh / plastic density was measured to accept or reject the mix. A strict tolerance of ±25 kg/m^3 was imposed as the mix acceptance criterion. Table 3.10 shows the results of the measured density and target density for the various specimens prepared. The data in Table 3.10 shows that all specimens conform to the mix acceptance criteria.

Table 3.9: Total number of specimens cast for durability testing series

Description	14R	14N	14I
a / c	1	1	1
Tests	**1400 kg/m^3**	**1400 kg/m^3**	**1400 kg/m^3**
Dip test		3	
Carbonation front	25	25	25
Microstructure	1		1
Corrosion Assessment	3	3	3

Table 3.10: Fresh density of the mixes used for specimen preparation

Description	1400 kg/m^3	
	$\rho_{casting}/\rho_{target}$	α_b
Carbonation front / Dip test		
*Cubes***		
14R	1394/1400	0.996
14N	1391/1400	0.994
14I	1414/1400	1.010
CT scans – Microstructure		
*Cubes**		
14R/N	1394/1400	0.996
14I	1391/1400	0.994
Corrosion Assessment		
Rectangular Prisms		
14R/N	1386/1400	0.990
14I	1391/1400	0.994

Cubes with side-lengths 30 mm* / 100 mm**
Data extracted from Mubatapasango (2017)

3.4.2 Carbonation tests, corrosion assessment and microstructure

3.4.2.1 Dip test (Water repellent penetration)

The dip test is a test used to determine the penetration depth of water repellent agents. In this research programme the test was conducted on freshly saw cut cube specimens in line with BS EN1504-2 (2004). The freshly saw cut specimens were placed "dipped" in water. Two regions, one hydrophobic and other hydrophilic, are clearly visible once the sample is exposed to water. The hydrophobic region is greyish-white and appears completely "dry" whereas the hydrophilic region absorbs water and appears wet. The average depth from the outer edges, measured using a Vernier calliper, to the hydrophilic region is reported as the penetration depth of the water repellent agent. Figure 3.18 illustrates the specimen with measurement points and an example of the specimens tested.

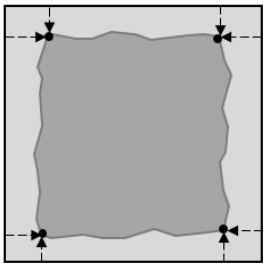

(a)

(b)

Figure 3.18: Dip test (a) illustration of measurement points, and, (b) example of specimen tested (Mubatapasango (2017))

3.4.2.2 Carbonation-induced corrosion

3.4.2.2.1 Carbonation unit – Carbonation testing series

The carbonation unit, shown in Figure 3.19, is comprised of four units, namely (1) a 31.5 kg CO_2 gas cylinder, (2) 150 litre drum, (3) a carbonation chamber, and (4) a condensing chamber. The 31.5 kg CO_2 gas cylinder, contains liquefied carbon dioxide at a concentration of 100% CO_2 and acts as a CO_2 gas reserve. A CO_2 regulator is attached to the gas cylinder and is connected to a 150 litre drum which serves as the second unit. The 150 litre drum, houses two containers of saturated ammonium nitrate solution (NH_4NO_3) which regulates the relative humidity to 65±5 %. The CO_2 gas moves from the second unit

to the third unit, the carbonation chamber, which houses all specimens and is equipped with a permanent CO_2 and temperature sensor, a fan close to the inlet for circulation and a hygrometer to monitor the relative humidity. The pressure inside the unit is regulated using an outlet pressure valve which can be opened in the event of pressure build-up. The desired concentration of CO_2 in the unit, in this case 0.13% (3-4x average atmospheric CO_2 levels), can be achieved by opening the CO_2 regulator and monitoring the readings of the CO_2 and temperature sensor. This low concentration of CO_2 was selected for the experiment as research (Shah et al. (2018)) indicates products different tend to form at concentrations well above natural conditions (>3%). Once the desired level of CO_2 concentration is reached in the unit, the CO_2 regulator can be closed shut. The concentration of CO_2 levels is monitored and in the event of any variation further adjustments can be made via opening the CO_2 regulator and outlet valve in combination. The CO_2 from the third unit moves to the fourth unit, the second 150 litre drum, via an outlet at the bottom of the third unit. The fourth unit contains a grid to allow moisture generated in the third unit to be trap and is then returned to the third unit via an outlet. A closed loop is therefore formed between the third and fourth unit.

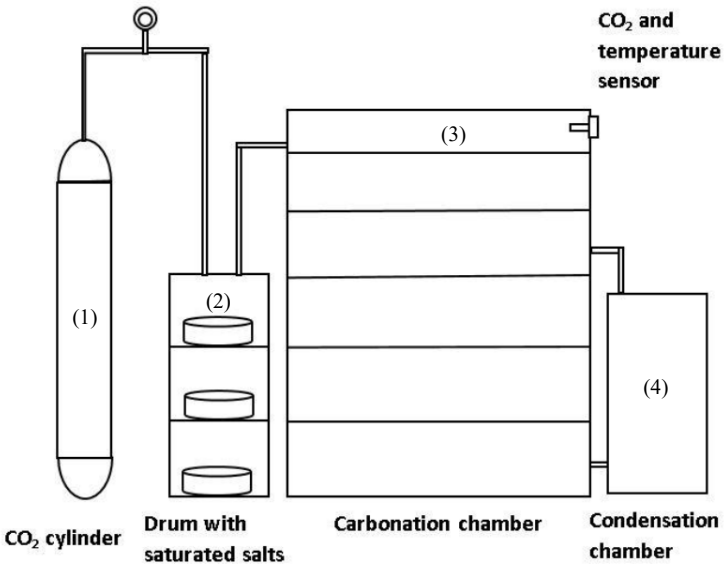

Figure 3.19: Carbonation unit setup (Mubatapasango, van Zijl, and van Rooyen (2017))

3.4.2.2.2 Carbonation depth – Carbonation testing series

The carbonation depth in concrete can be determined in accordance with the RILEM CPC-18 (1988). In this investigation concrete cubes were used to determine the carbonation depth. At the age of testing the concrete cubes were saw cut through the middle, surface cleaned using high pressure air, and sprayed with phenolphthalein. Phenolphthalein is a universal colour indicator which turns purple at pH values above 8.4-9.8 (Roy et al., (1999)). Thus the solution turned purple upon contact with the noncarbonated regions of the concrete. The depth from the surface of the concrete cube sides were measured, using a Vernier calliper, at two points along the sides to the noncarbonated region and recorded as an average carbonation penetration depth, as shown in Figure 3.20. It is acknowledged that the use of phenolphthalein is being phased out due to its carcinogenic properties.

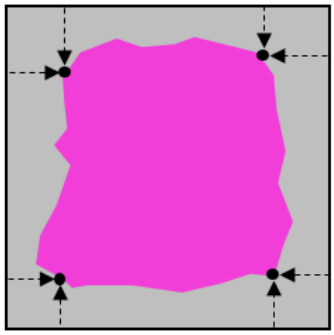

Figure 3.20: Illustration of the measuring points along the sides of the specimen

3.4.2.2.3 Half-cell potential measurements (Corrosion Assessment) – Carbonation testing series

The corrosion potential in concrete can be estimated using the half-cell potential (HCP) method put forth in ASTM C876 (2009). The method makes use of a half-cell, constructed from either a Ag/AgCl or $Cu/CuSO_4$, reference electrode and a high impedance voltmeter to determine the corrosion potential which is an indication of the probability of corrosion. For this investigation a $Cu/CuSO_4$ half-cell reference electrode was constructed using a copper rod surrounded by a saturated solution of copper sulphate encased in polycarbonate. The method requires that the solution within the half-cell comes into contact with the concrete. For this reason a small hole is drilled through the bottom of the half-cell and stopped with a porous material such as cotton wool.

Figure 3.21 shows the test set-up used to determine the corrosion potential. The $Cu/CuSO_4$ half-cell reference electrode is placed on cotton pads on the testing surface. The testing surface is smeared with an electrical contact solution, such as household detergent diluted in water, before testing to promote contact between the half-cell and the concrete as prescribed by ASTM C876 (2009).

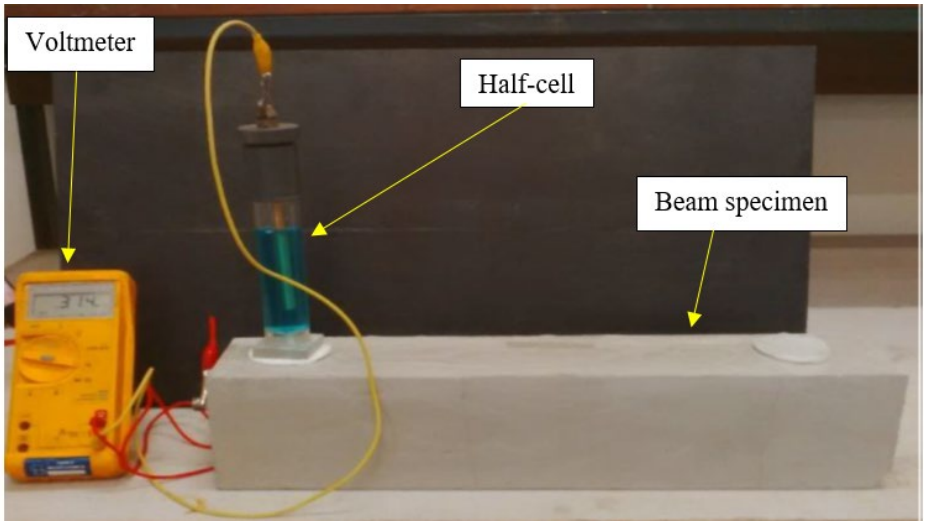

Figure 3.21: Corrosion potential setup with test specimen and equipment

3.4.2.2.4 Computed Tomography scan – Carbonation testing series

The microstructural properties of FC was investigated using micro-CT scans. Tests were conducted on cubical samples at the Central Analytical Facility (CAF) at Stellenbosch University. The micro-CT scanner of CAF an industrial GE Phoenix V | Tome |x L240, up to 240 kV and down to 5 um voxel size and can scan specimen of up to 250 mm in diameter, see Figure 3.22a. During testing the sample is placed on a rotating platform / stage located between the x-ray source and the detector. The sample attenuates the x-rays emitted from the x-ray source which is then measured by the detector. The measurements from the detector is then used in combination with specialised commercially available software, VGStudioMax, to construct a 3D image of the sample. The software allows for different analyses to be performed on the 3D image (porosity, void distribution, connectivity, etc.). An illustration of the CT scanning process is shown in Figure 3.22b.

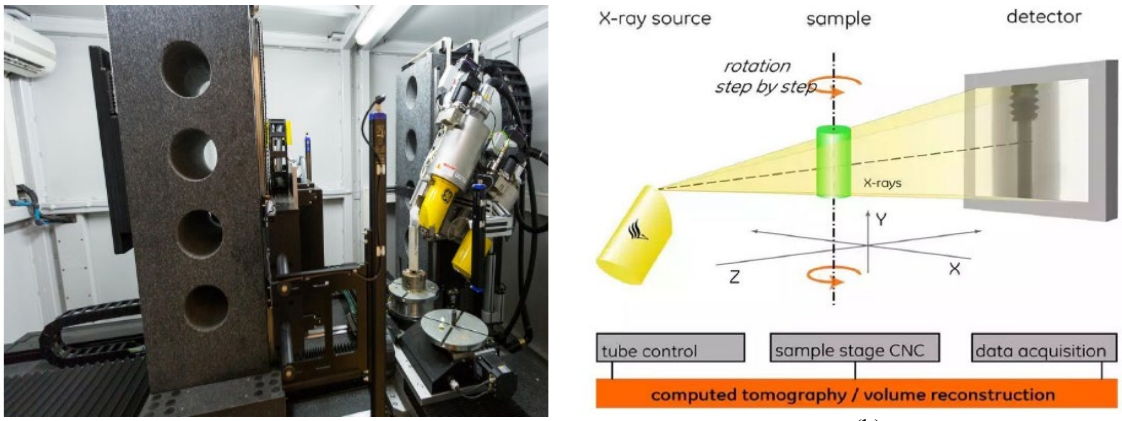

(a) (b)

Figure 3.22: Micro-CT (a) CAF Stellenbosch University (b) Illustration of the CT scanning process

3.4.3 Mix design composition, specimen preparation and stability – Chloride testing series

3.4.3.1 Mix design composition – Chloride testing series

The mix design compositions of the concrete mixes used to prepare specimens for Series 1, Series 2 and Series 3 are tabulated in Table 3.11. The mixes were prepared using the methodology set out in Section 3.2.2. The concrete mixes of Series 1 and Series 2 were all prepared using a target density of 1600 kg/m^3. For Series 3 the concrete mixes were prepared with target densities of 1200, 1400 and 1600 kg/m^3. In each series the concrete mixes were either prepared with or without the addition of a surface treatment agent (STAs) forming the sets R – Reference, N – Non-integral, and I – Integral. STAs were employed to enhance the chloride resistance of LWFC. For ease of reference and due to the large number of mixes used in the research programme, each mix design is assigned a six or eight character long designation. The first two characters represent the series (S1, S2, or S3), followed by a hyphen and three characters representing the target density and surface treatment (i.e. 16R – 1600 kg/m^3 Reference mix). The remaining set of three characters is assigned to mixes containing fly ash – underscore followed by either A1 or A2. For instance, the mix design designation S2-16N_A1 represents the mix of Series 2 with a target density of 1600 kg/m^3, non-integral surface treatment and a fly ash cement ratio of 1.

Table 3.11: Mix design composition used for Series 1, Series 2 and Series 3 (Durability - Chloride)

Description	S1-16	S2-16[1]	S2-16_A1[1]	S2-16_A2[1]	S3-12[2]	S3-14[2]	S3-16[2]
Designation	R / N[#] / I[+]	R / N* / I[+]	R / N* / I[+]	R / N* / I[+]	R / N* / I[+]	R / N* / I[+]	R / N* / I[+]
a/c	0	0	1	2	0	0	0
	1600 kg/m³	**1600 kg/m³**	**1600 kg/m³**	**1600 kg/m³**	**1200 kg/m³**	**1400 kg/m³**	**1600 kg/m³**
Cement [kg]	1145	1110	593	404	835	998	1149
Water [kg]	441	475	403	376	314	375	432
Fly-ash [kg]	0	0	593	809			0
Foam [kg]	15.1	12.5	10.4	9.5	29.8	22.8	14.9

Sephakhu OPC CEM I 52.5N
Ulula Class S fly ash
12mm SAPY Corehfil™ PP fibres at 0.45[1] or 0.50[2]% w.r.t. volume
Sikalite® 2% w.r.t. weight of binder[+]
Sikagard® - 706 Thixo (200-300 g/m² after 28 days curing)*
Chryso Fuge B 2% w.r.t. weight of binder[#]
Series 1 data from van Rooyen and van Zijl (2017) / Series 2 data from Zvinokona (2017) / Series 3

3.4.3.2 Specimen preparation and ponding test – Chloride testing series

3.4.3.2.1 Specimen preparation and ponding test – Series 1

Table 3.12 shows an overview of the number of specimens prepared for Series 1.

Table 3.12: Overview of the number of specimens for Series 1

Description	S1-16R	S1-16N	S1-16I
Corrosion assessment (Coulostatic method)			
460x100x100			
Reinforced 24 mm cover	4	4	4

For each mix four Y12 reinforced rectangular prisms with 24 mm cover depth and dimensions 460x100x100mm were cast. The Y12 rebar was 500 mm in length and protruded 20 mm from both sides of the beams, shown in Figure 3.23. All rectangular specimens were cast with a cavity (pond) of 420x70 mm on the top of the specimen for cyclic chloride exposure and a 6 mm stainless steel rod used as a counter-electrode for corrosion assessment. After casting the specimens were stored in a climate room at 65±5% RH and temperature of 23±2°C and demoulded 24 hours later. The specimens were left in the climate room up until 28 days. After 28 days the ponding face of the non-integral specimens were surface treated with Sikagard®-706 Thixo to the recommendation of the manufacturer and left for a further 7 days to cure in the climate room. After 35 days of curing all surfaces of the specimen, except the ponding surface, were sealed using bitumen and left to cure for a further 7 days in the climate room.

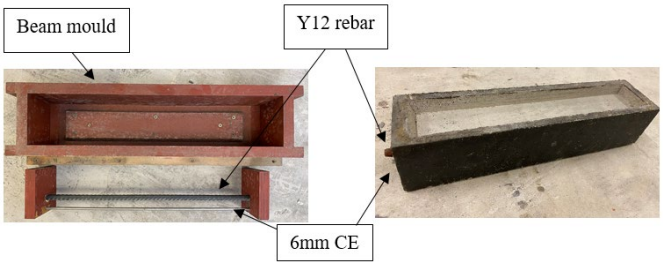

Figure 3.23: Beam mould, CE, rebar and specimens – Series 1

For Series 1 the designation of the specimens is explained with the following example. For the case of the Y12 reinforced prism specimen with 24 mm cover made from the reference mix the designation is S1-16R_24. The last two numbers in the designation represents the reinforcement cover depth, 24, in mm. After 45 days the specimens were exposed to a 0.3 M NaCl solution for four wetting-drying cycles. Each cycle consisted of a 7 days wet period and 14 days dry. Figure 3.24 shows a picture of the ponding cycle for Series 1. Crack characterisation was done using a crack ruler and the maximum on the surface was recorded as the crack width.

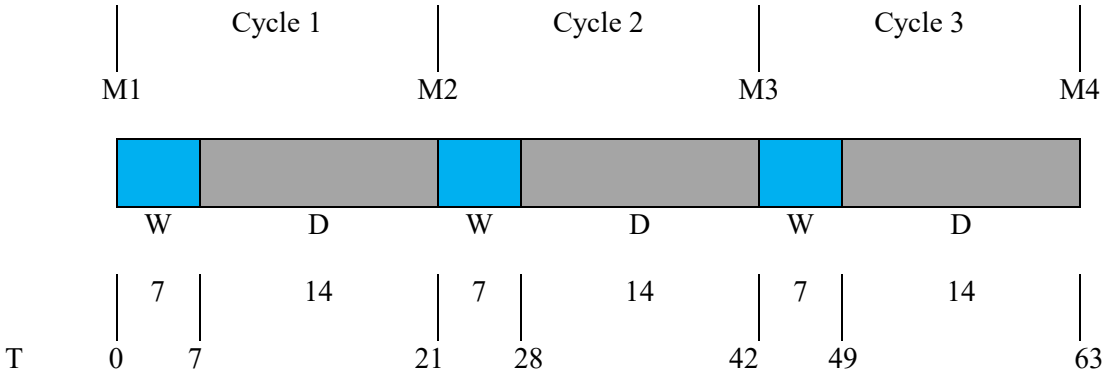

Figure 3.24: Ponding cycle and measurement data for Series 1. (M-Measurement / W-Wet / D-Drying / T-Duration [days])

3.4.3.2.2 Specimen preparation and ponding cycle – Series 2

Table 3.13 shows an overview of the number of specimens prepared for the R set of Series 2.

Table 3.13: Overview of the number of specimens for the R set of Series 2

Description a/c	S2-16R 0	S2-16R 1	S2-16R 2
Chloride penetration test			
500x100x100			
Unreinforced	3	3	3
Corrosion Assessment (Potentiostat measurements)			
460x100x100			
Reinforced 20 mm cover	3	3	3
Reinforced 35 mm cover	3	3	3

Table 3.13 shows the number of specimens prepared for the reference mix. For each reference mix three unreinforced rectangular prisms of dimensions 500x100x100mm, and eight Y12 reinforced rectangular prisms of dimensions 460x100x100mm. Four Y12 reinforced rectangular prisms had a cover depth of 20 mm and the other four had a cover depth of 35 mm. The Y12 rebar is approximately 500 mm long. The same number of specimens were casted for the non-integral (S2-16N) and integral surface treated specimens (S2-16I). All rectangular specimens were cast with a cavity (pond) of 420x70 mm on the top of the specimen for cyclic chloride exposure. After casting the specimens were stored in a climate room at 65±5% RH and temperature of 23±2°C and demoulded 24 hours later. The specimens were left in the climate room up until 28 days.

For Series 2 the designation of the specimens is adapted and explained with the following example. For the case of a Y12 reinforced prism specimen with 20 mm cover made from the reference mix with a fly ash cement ratio of two, the designation is as follows S2-16R_A2_20. The last two numbers in the designation represents the reinforcement cover depth (20 or 35) in mm.

After 28 days specimens were ponded with a 0.3 M NaCl. The cycle consisted of 7 days wet exposure and 21 days dry period, as shown in Figure 3.25. Crack characterisation was done using a crack ruler and the maximum on the surface was recorded as the crack width.

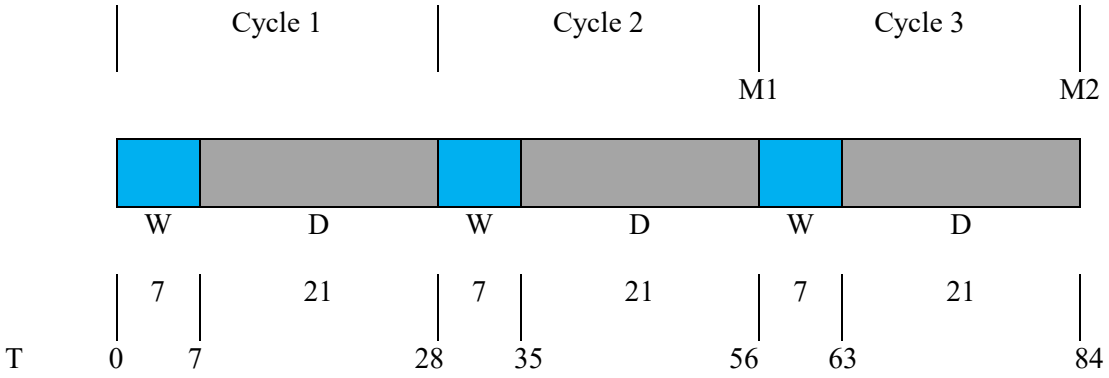

Figure 3.25: Ponding cycle and measurement data for Series 2. (M-Measurement / W-Wet / D-Drying / T-Duration [days])

3.4.3.2.3 Specimen preparation and ponding cycle – Series 3

Table 3.14 shows an overview of the number of specimens prepared for the reference mixes.

Table 3.14: Overview of the number of specimens for the reference mixes of Series 3

Description	S3-16R	S3-14R	S3-12R
Corrosion Assessment (Galvanostatic measurements)			
660x150x150			
Reinforced 69 mm cover	3	3	3

Table 3.14 shows the number of specimens prepared for the reference mix. For each reference mix, three Y12 reinforced rectangular prisms of dimensions 660x150x150mm and cover depth of 69 mm were casted. The same number of beam specimens were cast for the non-integral (N) and integral surface treated specimens (I). All rectangular specimens had a pond built of polystyrene of dimensions 200x150 mm on the top of the specimen for cyclic chloride exposure.

The Y12 reinforcement is approximately 700 mm in length and has been cleaned chemically in accordance with accordance with ASTM G1-03-2011. In the method, reinforcing steel is cleaned by placing it in an acidic solution. The solution is made from 40 g antimony trioxide, 100 g of stannous chloride and 2000 ml of hydrochloric acid. After the rebar has been cleaned it is placed in acetone. In this series the rebar has been chemically cleaned and its mass has been recorded. The rebar has an average mass of 590 g.

In this series beam specimens were ponded at a concrete age of 28 days. The ponding cycle consists of 3 days wet exposure to a 0.3 M NaCl solution and 11 days dry shown in Figure 3.26

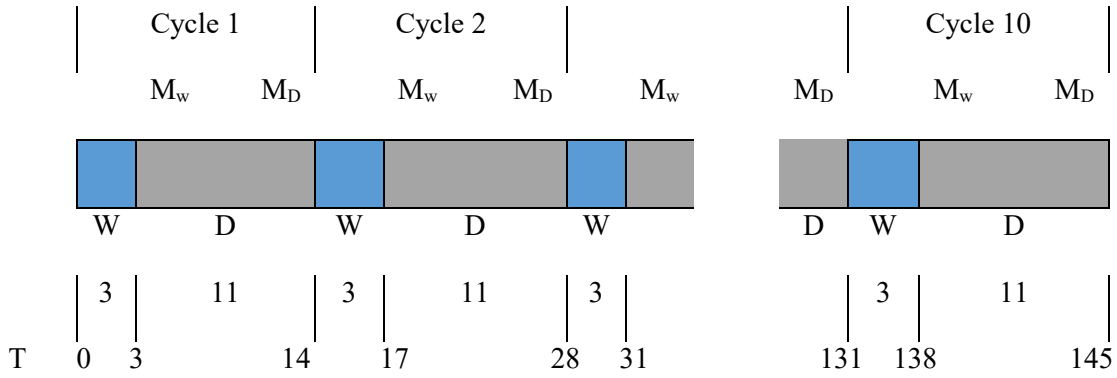

Figure 3.26: Ponding cycle and measurement data for Series 3 (M_w-wet measurement / M_D-dry measurement / W-wet / D-drying /T-Duration [days])

3.4.3.2.4 Computed Tomography scanning – Chloride testing series

The microstructural properties of FC was investigated using nano-CT scans. Tests were conducted on cylindrical samples at the Central Analytical Facility (CAF) at Stellenbosch University. The nano-CT scanner of CAF an industrial GE Nanotom S system, up to 180 kV and down to 0.5 µm voxel size and works best with samples less than 10 mm in diameter, see Figure 3.27a. The scanning process is similar to that explained in Section 3.4.2.2.4. Figure 3.27b shows a sample on the stage platform.

(a) (b)

Figure 3.27: Nano-CT (a) CAF Stellenbosch University (b) test specimen on the stage platform

Table 3.15 shows an overview of the number of specimens prepared for the x-ray CT scanning at CAF. The cylindrical specimens were cored from the beam specimens using a 10 mm coring drill bit at the end of the ponding test period. Core samples were taken between 5 and 15 mm depths, use a precision table drill, of each specimen as shown in Figure 3.24.

Table 3.15: Number of cored samples in Series 2 and Series 3

Description	S3-16R	S3-14R	S3-12R	S3-14N	S2-16R	S2-16R_A1	S2-16R_A2
CT scan – Microstructure							
Cylinders – cored							
L=9mm, D=8mm	1	1	1	1	1	1	1

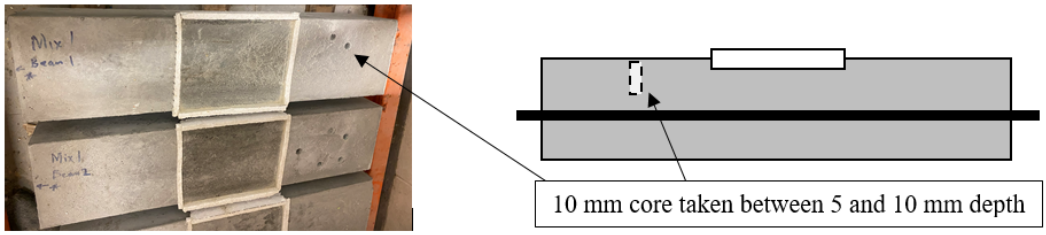

Figure 3.28: 10mm core samples used for nano-CT scanning

3.4.3.3 Number of specimens – Chloride testing series

Table 3.16 shows the total number of specimens cast for the durability testing series. Each time after mixing, the fresh / plastic density was measured to accept or reject the mix. A strict tolerance of ±25 kg/m^3 was imposed as the mix acceptance criterion. Table 3.17 shows the results of the average measured density and target density for the various mixes prepared. The data in Table 3.17 shows that all specimens conform to the mix acceptance criteria.

Table 3.16: Total number of specimens cast for durability testing series

Description	S1-16	S2-16[1]	S2-16_A1[1]	S2-16_A2[1]	S3-12[2]	S3-14[2]	S3-16[2]
Designation	R / N# / I+	R / N* / I+	R / N* / I+	R / N* / I+	R / N* / I+	R / N* / I+	R / N* / I+
a/c	0	0	1	2	0	0	0
Tests	**1600 kg/m^3**	**1600 kg/m^3**	**1600 kg/m^3**	**1600 kg/m^3**	**1200 kg/m^3**	**1400 kg/m^3**	**1600 kg/m^3**
XRF	3						
***Cl-* ingress**		3	3	3			
Corrosion							
Coulostatic	9						
Potentiostat		18	18	18			
Galvanostatic					9	9	9
Microstructure							
Nano-CT		1	1	1	2	2	2

Table 3.17: Average density ratios for the mixes used in the durability testing series

Description	S1-16	S2-16[1]	S2-16_A1[1]	S2-16_A2[1]	S3-12[2]	S3-14[2]	S3-16[2]
Designation	R / N# / I+	R / N* / I+	R / N* / I+	R / N* / I+	R / N* / I+	R / N* / I+	R / N* / I+
a/c	0	0	1	2	0	0	0
$\rho_{casting} / \rho_{target}$	1616/1600	1608/1600	1580/1600	1608/1600	1223/1200	1386/1400	1576/1600
$\alpha_{b,\ average}$	1.010	1.005	0.988	1.005	1.018	0.990	0.985

3.4.4 Chloride profiling, ponding tests and corrosion assessment

Chloride-induced corrosion was promoted by using cyclic ponding tests for accelerated chloride penetration. Three series of tests were conducted with different cyclic exposure periods of continuous wetting and drying cycles.

3.4.4.1 Chloride penetration depth measurement (Visualization and profiling)

3.4.4.1.1 Chloride penetration depth – Chloride profiling using XRF (Series 1 only)

The total chlorides present in the concrete can be determined using x-ray florescence (XRF). In this research programme, powdered samples, 5 g in total, were collected from rectangular prisms, made from

all mixes in Series 1, subjected to ponding tests. The powder was send to CAF which uses Elementar Vario EL Cube Elemental Analyzer for XRF testing. The powdered samples were collected, at week 9 of the experiment, by drilling perpendicular to the ponding surface to various depths of the rectangular prism specimens. In order to ensure enough powder was collected multiple holes were drilled in the crack and un-cracked regions of specimens using a 16 mm diameter drill bit. Powdered samples were collected at 5 mm depth interval, see Figure 3.29. Table 3.18 lists the total number of samples used for XRF testing.

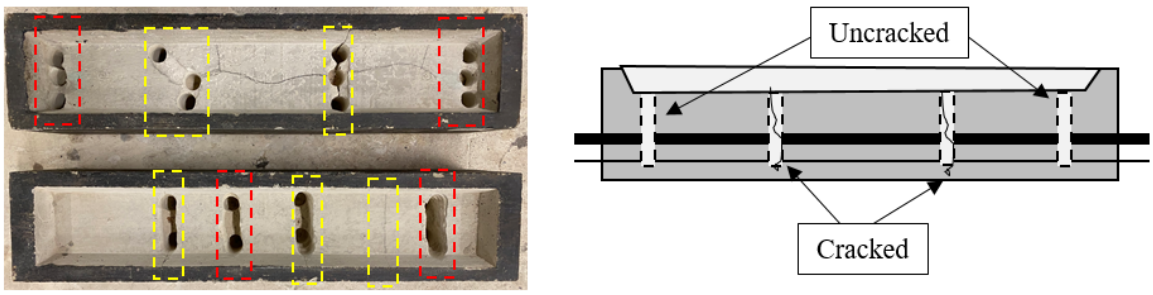

Figure 3.29: Left - Beam specimens with 16 mm diameters holes, yellow cracked region, red uncracked region. Right – schematic drawing of a beam specimen show holes drilled in cracked and uncracked region

Table 3.18: Total number of samples - XRF testing

Description	S1-16R	S1-16N	S1-16I
Chloride profiling			
Powder samples*	8	8	8

*Powder collected at 5mm depths intervals up to 40mm into the ponding surface

3.4.4.1.2 Chloride penetration depth – Visualization (Series 2 only)

Chloride penetration depth was measured using the silver nitrate colorimetric method. Silver nitrate, $AgNO_3$, turns white-grey in the presence of chlorides. In this research programme, freshly cut rectangular prism specimens were cleaned using high pressure air and then sprayed with a solution of 0.1 M $AgNO_3$. After a few minutes, a chlorinated region and an unchlorinated region can be observed. A Vernier calliper was used to record the penetration depth in the middle of the ponding surface and 20 mm each side and recording the average penetration depth was recorded.

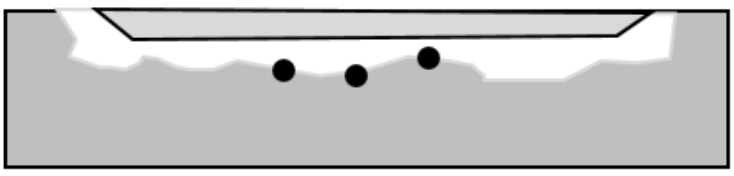

Figure 3.30: Beam illustrating measurement points for silver nitrate test - Series 2

3.4.4.2 Chloride ponding and corrosion assessment

Corrosion Assessment – Series 1

In Series 1 corrosion assessment was done on beam specimens using laboratory build pulse generator and half-cell constructed by Paul (2015), see Figure 3.31. The method used to determine the corrosion rate was the coulostatic method. A single measurement was taken at the start of each ponding cycle, as shown in Figure 3.32.

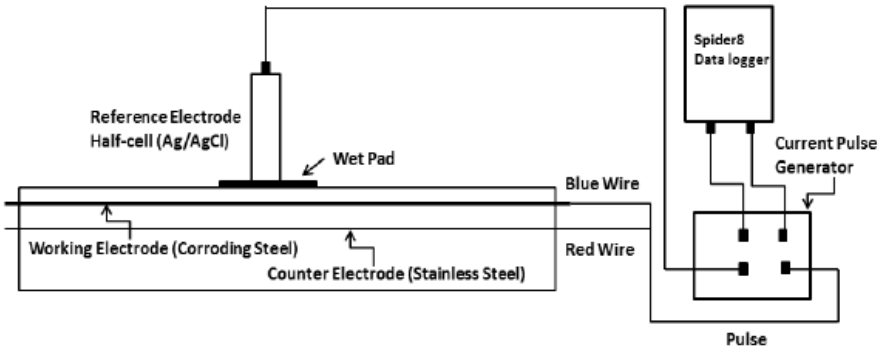

Figure 3.31: Schematic representation of implementing the coulostatic method (Paul (2015))

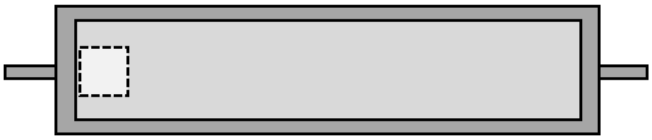

Figure 3.32: Reinforced rectangular prism (dashed lines indicating the data recording positions for Series 1).

For testing, a single measurement was recorded for each ponding cycle. The ponding area was wet using a solution of household detergent and water. The measurement was taken in the same position throughout the series as shown in Figure 3.32. The pulse generator has four connection, two for the data logger, Spider8, one for the half-cell and one for the rebar and counter-electrode, see Figure 3.33. The pulse generator was connected to the specimen via clips as shown in Figure 3.33. The pulse generator has three analogue knobs to control the current [mA], the noise zero [mA] and time [mS]. In this investigation the current and time settings were adjusted in order to achieve a small potential. Multiple measurements were taken and analysed in real-time until an appropriate response was observed, recall from Section 2.4.4.4.3 potential problems using the coulostatic method.

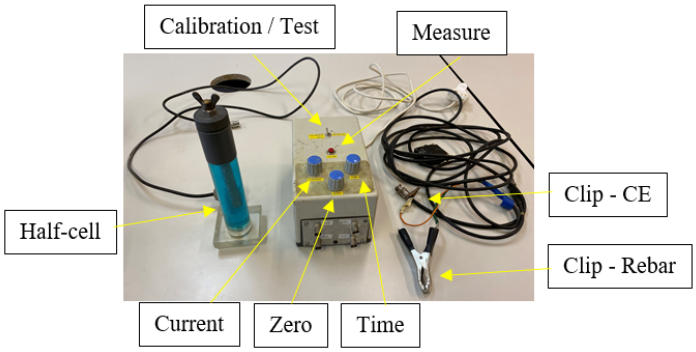

Figure 3.33: Laboratory built corrosion equipment

Corrosion Assessment – Series 2

For corrosion assessment in Series 2, the GECOR-10 was used to determine the corrosion rate. The GECOR-10 makes use of current modulation, see Section 2.4.4.4.2, and the half-cell has an internal counter electrode therefore eliminating the need for samples to be casted with a CE. The selected method for corrosion rate determination was the Potentiostat method. The connection made from the GECOR-10 to the rebar is made via a clip. The GECOR 10, does a check before implementing the selected method. The user is given feedback, either – "poor sensor contact" or "acceptable response" before proceeding. In the event of "poor sensor contact" the user can inspect the connections and restart the process to ensure an "acceptable response" outcome. The GECOR implements the selected method and requires no feedback from the user. After implementing the selected method the GECOR 10 displays the corrosion i_{corr}, E_{corr}, R_p and E_{pol}. Data recordings were taken along the length of the prism specimens on the ponding surface at intervals of 20 mm at the end of cycle 2 and cycle 3, as shown in Figure 3.25, Figure 3.34 and Figure 3.35.

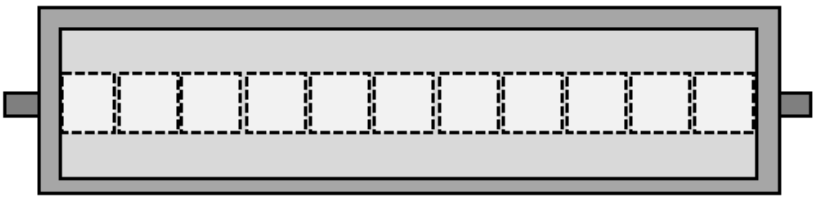

Figure 3.34: Reinforced rectangular prism (dashed lines indicating the data recording positions for Series 2).

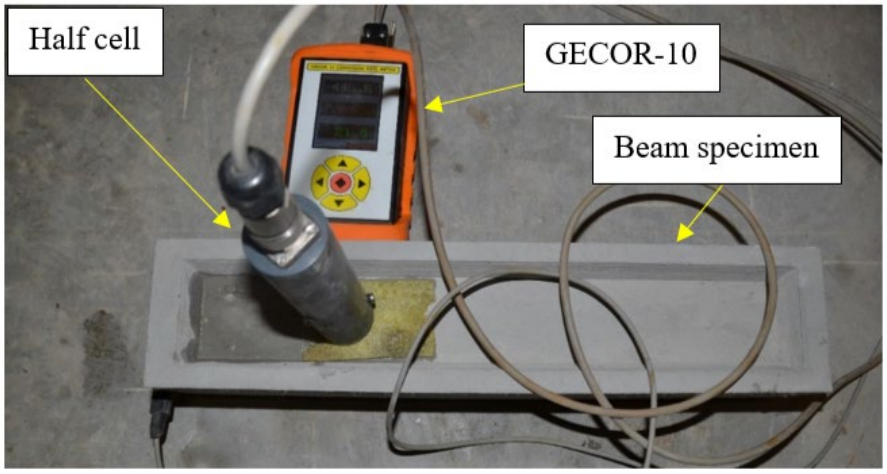

Figure 3.35: Measurement taken on a beam specimen in Series 2.

Corrosion Assessment – Series 3

For corrosion assessment in Series 3, the GECOR-10, was again used to determine the corrosion rate and corrosion potential. The selected method for corrosion rate and corrosion potential determination

was the Galvanostatic method. During a cycle three measurements were taken along the length of the pond at the end of the wetting period and the last day of the drying period, see Figure 3.26, Figure 3.36 and Figure 3.37. The "wet" measurement, M_w, was recorded within 2±1days of the wetting phase. The measurement is considered wet due to the fact that sufficient time has not yet passed for the prism specimens to be considered dry. Hence the "dry" measurement, M_D, is taken a day before the start of the wetting cycle.

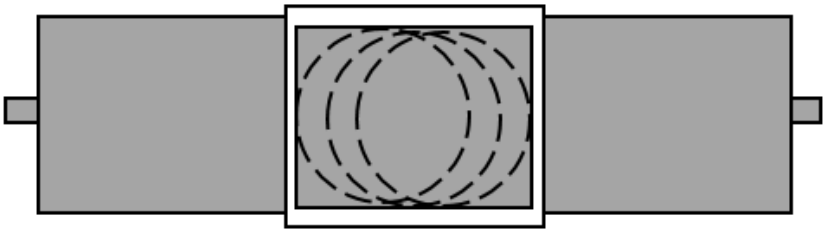

Figure 3.36: Rectangular prism specimen (dashed lines indicating the data recording positions for Series 3)

(a) (b)

Figure 3.37: Ponding cycle showings specimens of Series 3 (a) "wet" phase, and, (b) "drying" phase.

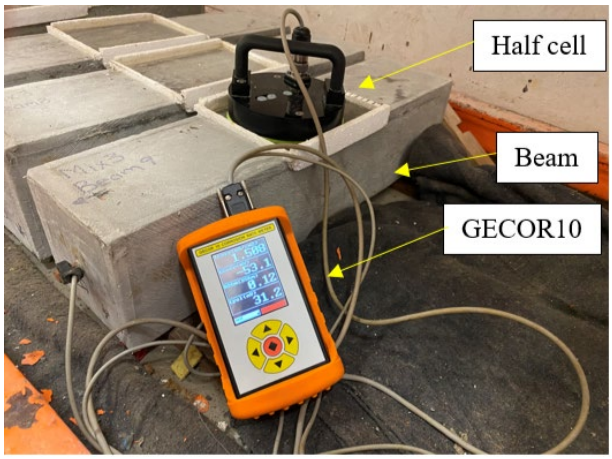

Figure 3.38: Corrosion assessment using the GECOR10 in Series 3.

3.5 Concluding summary

In this chapter details of the experimental programme and methodology followed are provided. The experimental programme designed to address the gaps in knowledge on FC highlighted in Chapter 2. The experimental programme is arranged along two themes, mechanics (Chapter 4) and durability (Chapter 5).

The mechanics theme, is focussed on characterisation of LWFC mechanical behaviour, including bod with steel reinforcement, and its structural application. Characterisation of mechanical properties consisted of an (i) initial phase and (ii) further development phase. In the initial phase LWFC with design target densities of 1200, 1400 and 1600 kg/m^3 is investigated by performing compressive strength, tensile splitting strength, elastic modulus, fracture energy and BE tests. In this section the conceptual design of the experimental programme was done by the author. The experimental design was done and performed under the co-supervision of the author and is reported in de Villiers, van Zijl, and van Rooyen (2016).

In the further development characterisation phase material improvement by the incorporation of PP fibres was envisioned by the author. The initial characterisation phase in conjunction with the parallel durability theme, discussed later, revealed further improvement was need in order to reinforce the material with steel and to decrease its cracking potential of R/LWFC. The further development phase enabled the reinforcement of R/LWFC without any cracking occurring and is reported in van Zijl, van Rooyen, Mubatapasango et al. (2017).

The mechanics theme is concluded with a demonstration of the structural application of R/LWFC. For this, a two panel walling system subjected to low to moderate seismicity made of R/LWFC was envisioned by the author. The conceptual design was done by the author and the detail experimental design and experimentation was carried out under the co-supervision of the author and is reported in Dunn, van Zijl and van Rooyen (2018). The experimental programme design includes monotonic pull-over and quasi-static tests.

The durability theme is split into two focus areas, carbonation- and chloride-induced corrosion – respectively. The conceptual and experimental design, and devising a mitigating strategy was done by the author. Carbonation testing includes the evolution of the carbonation front and corrosion potential. The detailed experimental design and experiments were carried out under the supervision of the author and is reported in Mubatapasango, van Zijl, and van Rooyen (2017) and van Zijl, van Rooyen, Mubatapasango et al. (2017).

Chloride-induced corrosion testing is split into three series. The conceptual and experimental design was done by the author for all series. Series 1 is a pilot phase and all experimental work was done by the author and is reported in van Rooyen and van Zijl (2017). In Series 2 the experimental work was done under the direct supervision of the author and reported in Zvinokona, van Zijl, and van Rooyen (2017). In Series 3 all experimental work and testing was done by the author. In the three series

FC with target densities between 1200 and 1600 kg/m^3 was subjected to accelerated chloride exposure and corrosion assessment was performed on these specimens. These tests are ongoing. Upon completion, the steel bars will be removed, cleaned and weighed to determine actual mass loss by the corrosion process.

3.6 References

ACI 318-11 (2011). Building Code Requirements for Structural Concrete. American Concrete Institute. Mitchigan.

ASTM A944-10 (2002). Comparing Bond Strength of Steel Reinforcing bars to concrete using Beam-End specimens. ASTM International. West Conshohocken, PA, 2002, www.astm.org

ASTM C469 / C469M -14 – Standard test method for Static Modulus of Elasticity and Poisson's ratio of concrete in compression, ASTM International, West Conshohocken, PA, 2014, www.astm.org

ASTM C876-09. Standard test method for corrosion potentials of uncoated reinforcing steel in concrete. ASTM International, West Conshohocken, PA, 2009, www.astm.org

Brühwiler, E. and Wittmann, F. (1990). The wedge splitting test, a new method of performing stable fracture mechanics tests. Engineering Fracture Mechanics. Vol. 35(1). pp. 117-125. ISSN 0013-7944

BS EN 480-5. (2005). Admixture for concrete, mortar and grout. Test methods. Determination of capillary absorption.

BS EN 1504-2. (2004). Products and systems for the protection and repair of concrete structures. Definitions, requirements, quality control and evaluation of conformity Surface protection systems for concrete.

Chryso (2013). Chryso® Fuge B Pore blocking water proofer description. Available online at: http://www.chryso.com

De Villiers, J.P. (2015). Bond behaviour of deformed steel reinforcement in lightweight foamed concrete. Master's thesis, Stellenbosch University. http://hdl.handle.net/10019.1/97835

Dunn, T.P.A. (2017). Precast lightweight foamed concrete walling, a structural system for low-rise residential buildings. Master's thesis, Stellenbosch University. http://hdl.handle.net/10019.1/102870

JCI (2003). Method of test for fracture energy of concrete by use of notched beam JCI-S-001-2003.

Grafe, J. (2017). Report issue s0117: Optimization of fibre content in foam concrete for improved fracture energy. Technical report, Institute of Structural Engineering, Stellenbosch University, South Africa.

RILEM CPC-18. (1988). Measurement of Hardened Concrete Carbonation Depth. Journal of Materials and Structures. Vol.21. pp. 453-455

Roy, S., Poh, K.B. and Northwood, D.O. (1999c). Durability of concrete-accelerated carbonation and weathering studies. Building and Environment. Vol.34. pp. 597-606.

SANS (2000). SANS 6253:2000 – Concrete Tests – Tensile splitting strength of concrete. The South African Bureau of Standards.

SANS (2006). SANS 5863:2006 – Concrete tests – Compressive strength of hardened concrete. The South African Bureau of Standards.

SANS (2013). SANS 50197-1:2013 - Cement- Part 1: Composition, specifications and conformity criteria for common cements. The South African Bureau of Standards.

SANS (2014). SANS 50450-1:2014 – Fly ash for concrete – Part 1: Definition, specifications and conformity criteria. The South African Bureau of Standards.

SAPY (2016). Sapy Corehfil™ polypropylene fibres. Available online at: http://sapy.com/wp-content/uploads/2016/06/SAPY-Corehfil-brochure.pdf

Sika (2016). SikaGrout® 212 High Strength shrinkage compensating cementitious grout. Available online at: http://zaf.sika.com/dms/getdocument.get/aca6b2d7-b061-352c-8e7a-c4a10d2cddc7/SikaGrout%20-212.pdf

Mubatapasango, M.S. (2017). Carbonation-induced corrosion in integral and non-integral surface treated lightweight foam concrete. Master's thesis, Stellenbosch University. http://hdl.handle.net/10019.1/102986

Mubatapasango, M.S., van Zijl, G.P.A.G., and van Rooyen, A.S. (2017). Effect of surface protection on carbonation induced corrosion in reinforced foamed concrete. Paper ID 114. 71st RILEM week and ICACMS, 3-8 September 2017, Chennai, India, Volume 4, pp. 179-188.

Negro, P. and Toniolo, G. (2012). JRC scientific and policy report: Design guidelines for connections of precast structures under seismic actions.

Ulula Ash (Pty) Ltd (2016). Ulula ash Kriel Power Station: Test certificate for class S fly-ash. Available online at: http://www.ululaflyash.com/documents/Test%20CertificateTypical%2050450%20ClassS.pdf

Zvinokona, A.R. (2018). Chloride induced corrosion of integral and non-integral surface treated lightweight foamed concrete. Master's thesis, Stellenbosch University. http://hdl.handle.net/10019.1/103360

Chapter 4 – Mechanical results and discussion

In this chapter the results of the mechanical tests (compressive strength, tensile splitting strength, elastic modulus, fracture energy) and bond tests (pull-out (PO) test and beam-end (BE) test) are presented and discussed. Furthermore, a comparison between the results of the PO and BE test is presented followed by a model predicting the bond stress in FC based on equilibrium. The low fracture energy of FC is improved through the addition of fibres - identified as the main cause of poor bond. The improved fracture energy enabled the reinforcement of FC and two panel R/LWFC walling system is presented as an application. Laboratory testing of the scale walling system showed favourable energy dissipating mechanisms and an analytical model is presented to predict the peak lateral force.

4.1 Mechanical and structural performance of LWFC

In this chapter the results of the mechanical tests (compressive strength, tensile splitting strength, elastic modulus, fracture energy) and bond tests (pull-out (PO) test and beam-end (BE) test) are presented and discussed. Furthermore, a comparison between the results of the PO and BE test is presented followed by a model predicting the bond stress in FC based on equilibrium. The low fracture energy of FC is improved through the addition of fibres - identified as the main cause of poor bond. The improved fracture energy enabled the reinforcement of FC and two panel R/LWFC walling system is presented as an application. Laboratory testing of the scale walling system showed favourable energy dissipating mechanisms and an analytical model is presented to predict the peak lateral force. Figure 4.1 shows a flow diagram of mechanical and structural testing in the research programme.

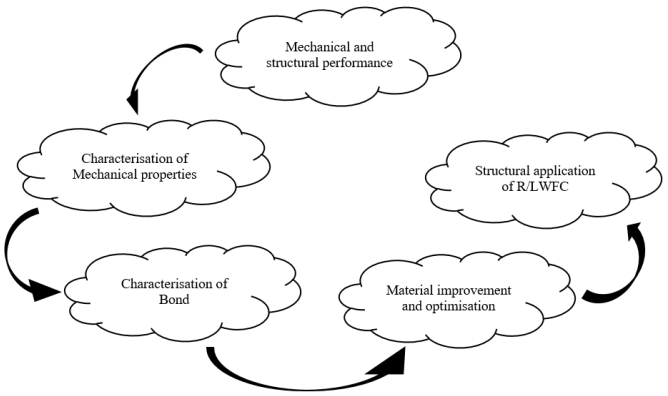

Figure 4.1: Flow diagram of results

4.2 Mechanical properties

4.2.1 Compressive strength

4.2.1.1 Variation in casting density and quality control using compressive strength as a measure

In order to produce stabile LWFC a mix designer needs (1) equipment, (2) understanding of the material, and, (3) the mix constituents. The equipment include an appropriate type of mixer (e.g. centrifugal – ribbon type) and a foam generator. The understanding of the material can be displayed by

achieving foam stability separately and when mixed with the base mix comprising of cement, sand, fly ash and water. The end result should be a LWFC mix with a density ratio, defined as the ratio of the casting density to the target density, that is close to unity (i.e. $\alpha_b = 1.0$). Interpreting the density of LWFC reveals that a mix resulting in a density ratio greater than 1 has a casting density that is greater than the design target density, see Section 2.2.1. This could be the result of foam instability or adding too little foam. A value smaller than 1 indicates too much foam has been added and a casting density lower than the target density is achieved. Reviewing the literature it is clear that the properties of LWFC is highly dependent on its density. It is therefore common to impose the density ratio as a mix design acceptance criterion on LWFC mix. Figure 4.2 shows a graph of the average 28 day cube compressive strength versus the casting density of the LWFC mixes used to prepare the specimens for the mechanical testing series. Each data point in Figure 4.2 is the average of three 100 mm cube specimens.

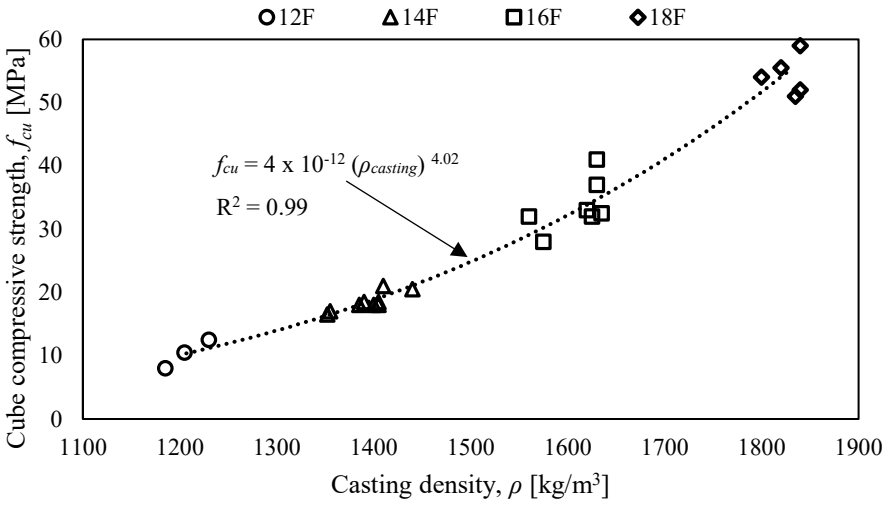

Figure 4.2: Average 28 day cube compressive strength versus the casting density of the LWFC mixes used to prepare the specimens for the mechanical testing series (produced from de Villiers (2015))

4.2.1.2 Long-term study of compressive strength in (compressive strength evolution)

The compressive strength evolution of mix 16FL was studied over a period of 56 days and is plotted in Figure 4.3 alongside an existing model proposed by Kearsley and Wainwright (2001b).

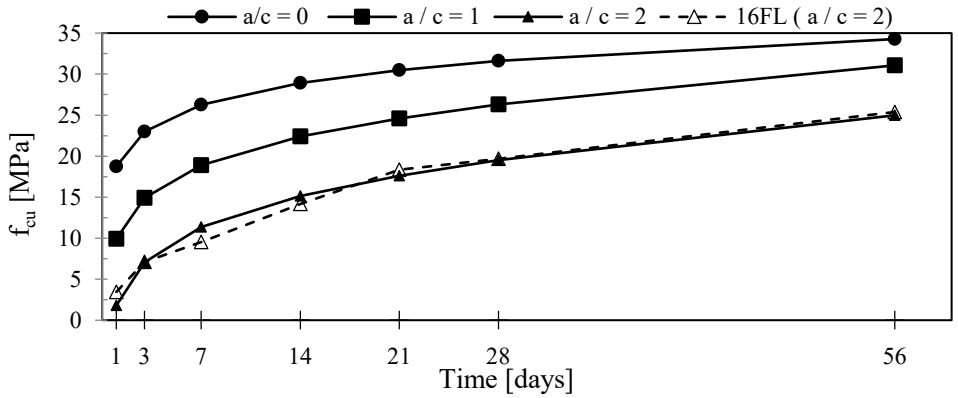

Figure 4.3: Compressive strength evolution of mix 16FL (dashed line) with strength model (solid lines), $f_{cu} = 39.6\ (\ln(t))^{1.174}(1-\rho)^{3.6}$, by Kearsley and Wainwright (2001b) (Zvinokona, van Zijl and van Rooyen (2017))

The purpose of Figure 4.3 was merely to test if a good approximation of the compressive strength for the materials used in this investigation can be found.

4.2.2 Tensile strength

The indirect tensile strength of the concrete was determined according to the splitting tests described in Chapter 3. Figure 4.4 shows a graph of the tensile splitting strength (f_t) as a function of the corresponding compressive strength (f_{cu}). Table 4.1 gives a tabulated form of the results including the COV, coefficient of variance obtained for the data.

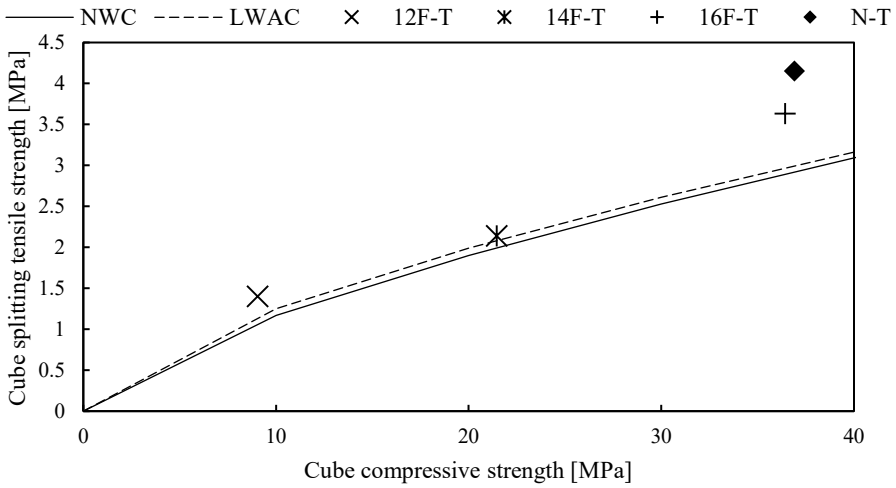

Figure 4.4: f_t as a function of f_{cu} for 12F-T, 14F-T, 16F-T, and N-T plotted alongside f_t/f_{cu}-NWC and f_t/f_{cu}-LWAC obtained from equations in BS EN 1992-1-1 (2004) (produced from de Villiers (2015))

Table 4.1: Results obtained from indirect tensile tests for LWFC and NWC mixes tested

Specimens	f_t [MPa]	f_{cu} [MPa]	f_t / f_{cu}	COV
12F-T	1.31	9.05	0.144	0.061
14F-T	2.14	21.45	0.0997	0.051
16F-T	3.63	36.43	0.099	0.042
N-T	4.15	36.91	0.112	0.015

Data extracted from de Villiers (2015)

From Figure 4.4 it can be seen that the splitting tensile strength of foamed concrete increases with density. The results of the 12F mix gives the lowest splitting strength value as shown in Table 4.1. All mixes yield tensile splitting strength values greater than those given for LWAC and NWC in BS EN 1992 – 1 - 1 (2004). The result of the 16F mix falls just short of that test for N showing that for high density LWFC mixes with the equivalent compressive strength may provide results close to that of NWC.

4.2.3 Elastic Modulus

The elastic modulus was determined according to the test method described in Chapter 3 on LWFC specimens with densities 1200 kg/m^3, 1400 kg/m^3, 1600 kg/m^3, and, 1800 kg/m^3, and NWC. The results obtained from the test are plotted in Figure 4.5 and tabulated in Table 4.2.

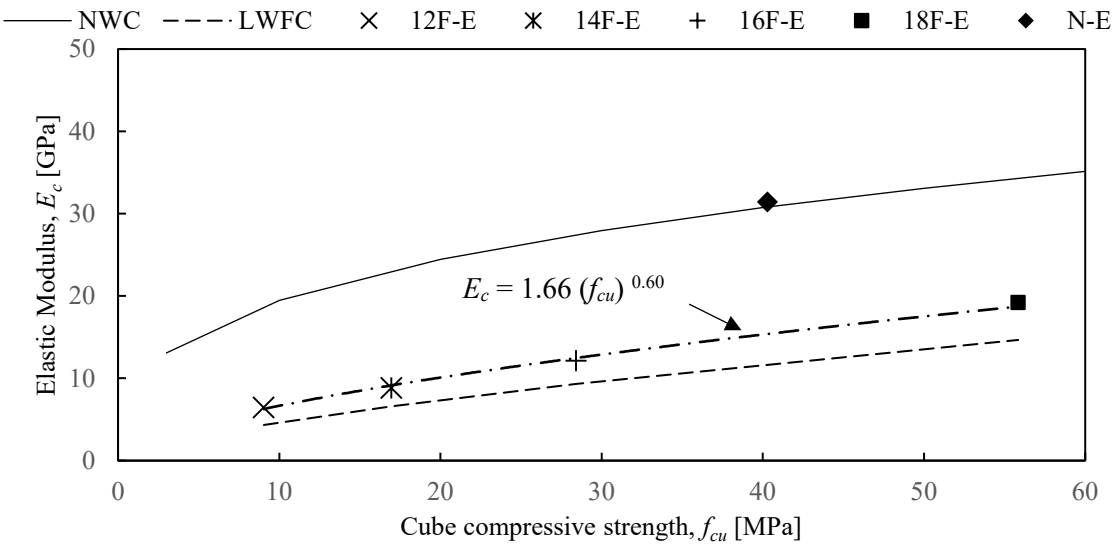

Figure 4.5: E_c (dashed-dotted-line) as a function of f_{cu} for 12F-E, 14F-E, 16F-E, 18F-E and N-E plotted alongside E_c/f_{cu}-NWC and E_c/f_{cu}-LWAC obtained from equations in BS EN 1992-1-1 (2004) (produced from de Villiers (2015))

Table 4.2: The results of the elastic modulus tests performed on LWFC and NWC specimens

Specimens	E_c [GPa]	f_{cu} [MPa]	$E_c / f_{cu} \times 10^3$	COV
12F-E	6.46	9.05	0.713	0.0298
14F-E	8.75	16.95	0.516	0.0011
16F-E	12.15	28.42	0.427	0.0216
18F-E	19.25	55.84	0.344	0.0297
N-E	31.48	40.30	0.781	0.01143

Data extracted from de Villiers (2015)

The results from Figure 4.5 show that there is an increase in the elastic modulus of LWFC concrete with an increase in density. Note that the 18F mix contains no foam (base mix) and can be viewed as the upper limit for FC mixes. The 18F recorded the highest E_c value for the mixes. It should be noted that the 18F mix obtained a higher compressive strength (55.84 MPa) than the N (40.30 MPa) mix but obtained a lower elastic modulus. The absence of coarse aggregate, stone, has a measureable impact on the elastic modulus of LWFC. The values of the elastic modulus for LWFC obtained from the test is higher than those given by BS EN 1992-1-1 (2004) for LWAC but considerably lower than those of NWC. It should be noted that the values given by BS EN 1992-1-1 (2004) for LWAC are used in design. This is a positive result for LWFC as it shows that materials with low elastic modulus are included in design codes.

4.2.4 Fracture energy

4.2.4.1 Wedge splitting test (16F, 14F, and 12F)

The wedge splitting tests were performed on LWFC wedge specimens as set out in Chapter 3. Due to the brittle nature of LWFC the control rate (crack mouth opening displacement rate (COD)) of the materials testing machine (MTM) was kept low in order to try and obtain stable fracture. Figure 4.6

shows a plot of the results obtained from the wedge splitting test. The vertical axis indicates the horizontal splitting force (F_h) and the horizontal axis shows the crack mouth opening displacement. For each density, 1200 kg/m^3, 1400 kg/m^3, and 1600 kg/m^3, three specimens were tested. However, for each sample group, only one specimen exhibited stable fracture (solid lines) and the rest failed prematurely (dashed lines). It should be noted that only the stable fracture results were used for interpretation and the rest were discarded. Possible reasons for the premature failure of the specimens include (1) LFWC inherently has a low fracture energy making it difficult to test, and, (2) specimen damage as a result of the pre-load (100 N lowest possible for the MTM used) imposed rendering the control of the COD ineffective.

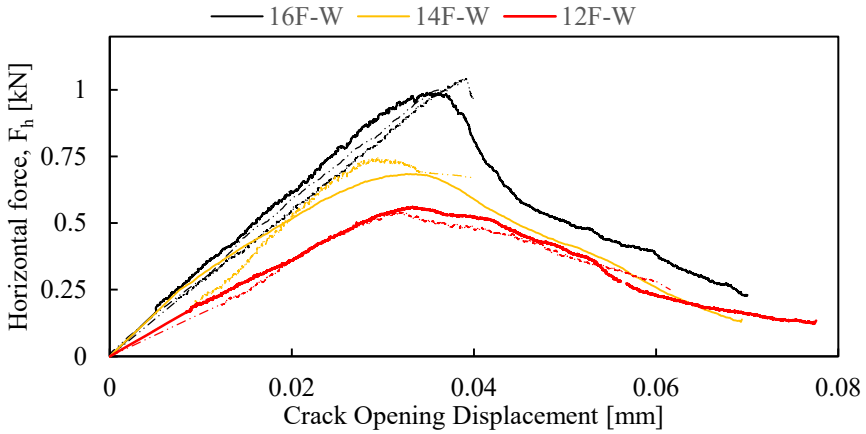

Figure 4.6: Results of the wedge splitting test on LWFC specimens 12F-W, 14F-W, and, 16F-W (reproduced from de Villiers (2015))

Table 4.3 list the values of the specific fracture energy (G*f*) calculated using the graphs in Figure 4.6 and those obtained by Wittmann (2002).

Table 4.3: Specific fracture energy (G*f*) and characteristic lengths (l_c) of LWFC tested and from Wittmann (2002)

Specimens	**G*f* [N/m]**	**l_c [mm]**
12F-W	4.67	17.58
14F-W	5.72	11.12
16F-W	7.32	6.75
Wittmann (2002)		
NC1	123.55	938
NC2	152.05	1300
HSC	158.70	538

Data extracted from de Villiers (2015)

The specific fracture energy, G_f in N/m, is obtained as the area underneath the curves, shown in Figure 4.6, normalised to the fracture area, in this case 50 x100 mm^2. The characteristic length of each specimen and those of Wittmann (2002) are also given in Table 4.3. The results show that the specific fracture energy increase and that the characteristic length with an increase in density for LWFC. The 12F-W mix obtained the lowest specific fracture energy whilst the 16F-W obtained the smallest characteristic length.

Both these results indicate the inherent brittle nature of LWFC as compared with the result of Wittmann (2002). For the samples of Wittmann (2002) HSC is the most brittle with the lowest characteristic length, however, LWFC is even more brittle (16F-W is approximate 80 times more brittle than HSC).

From the data in Table 4.3 it appears that there exist an inverse relationship between relative brittleness and the density of LWFC. Stated otherwise, the fracture energy of LWFC is (1) roughly proportional to density, air entrained, and (2) roughly inversely proportion to the air content. The characteristic length is (1) roughly inversely proportional to density, air entrained, and (2) roughly proportion to the air content. Evidence of this relationship can be confirmed by observing the data from the tests. The 16F-W, most dense tested, had the lowest characteristic length of 6.75 mm whilst the 12F-W had the highest characteristic length of 15.42 mm making it the least brittle of the samples tested. Figure 4.7a,b show the trends observed when plotting the specific fracture energy and the characteristic length as a function of the density ratio. The density ratio is an indication of the volume of air entrained into the mix calculated as the ratio of the casting density to that of the base mix density.

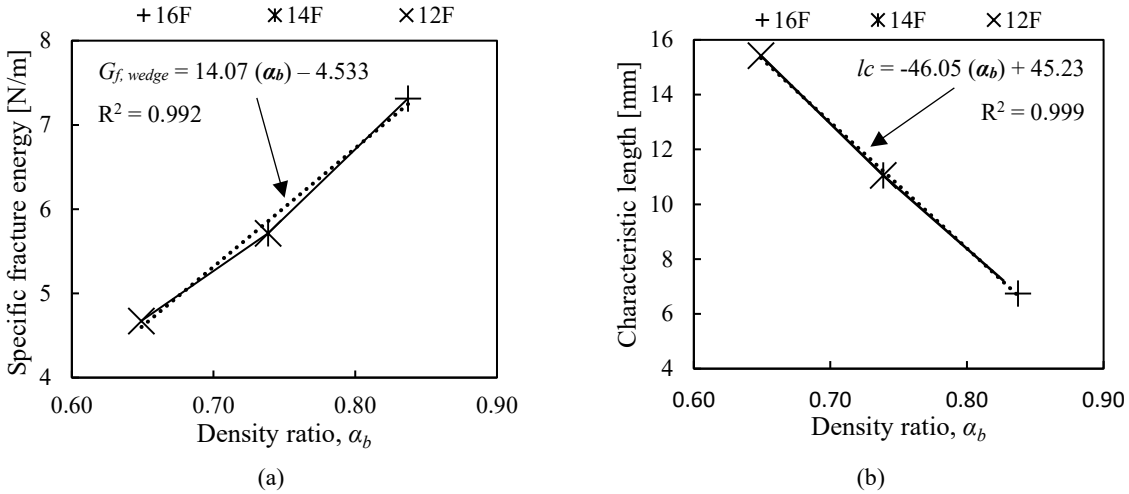

Figure 4.7: (a) Specific fracture energy, and, (b) characteristic length of LWFC as a function of density ratio (reproduced from de Villiers (2015))

4.2.4.2 Wedge splitting and three point bending (TPB) tests (15.5FN$^{1, 2, 3\ 4, 5, 6}$ and 15.5F$^{1, 2, 3, 4, 5, 6}$)

The wedge splitting and TPB tests were performed on fibre reinforced LWFC specimens with target density of 1550 kg/m^3. Mixes 15.5FN$^{1, 2, 3, 4, 5, 6}$ and 15.5F$^{1, 2, 3, 4, 5, 6}$ were used to prepare wedge splitting and TPB specimens. The fracture energy obtained from the wedge splitting and TPB tests are shown in Figure 4.8 and tabulated in Table 4.4. Additionally, Table 4.4 contains a summary of the mechanical properties (compressive- and tensile- strength and elastic modulus) of mixes 15.5FN$^{1, 2, 3, 4, 5, 6}$ and 15.5F$^{1, 2, 3, 4, 5, 6}$.

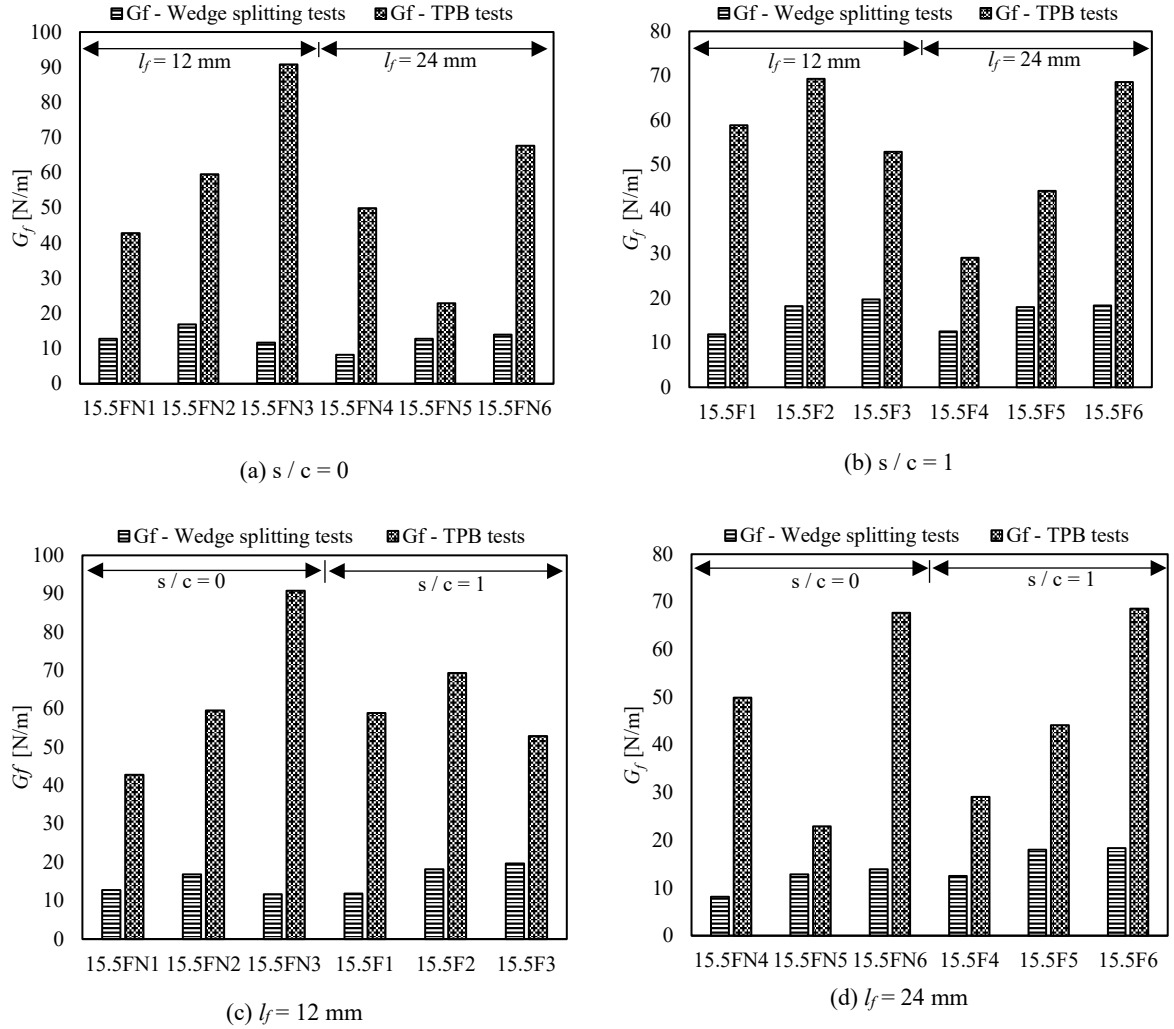

Figure 4.8: Fracture energy obtained from the wedge splitting and TPB tests influence of (a) s / c = 0, (b) s /c = 1, (c) l_f =12 mm, and, (d) l_f =24 mm (data extracted from Grafe (2017))

Table 4.4: Fracture energy results from the wedge splitting test results for mixes 15.5FN[1, 2, 3, 4, 5, 6] and 15.5F[1, 2, 3, 4, 5, 6]

Description	15.5FN 1	15.5FN 2	15.5FN 3	15.5FN 4	15.5FN 5	15.5FN 6	15.5F 1	15.5F 2	15.5F 3	15.5F 4	15.5F 5	15.5F 6
s/c	0	0	0	0	0	0	1	1	1	1	1	1
l_f	12	12	12	24	24	24	12	12	12	24	24	24
f_c	0,2	0,35	0,50	0,2	0,35	0,50	0,2	0,35	0,50	0,2	0,35	0,50
Average												
$f_{c,cu}$	23.5	28.7	28.5	25.4	23.5	23.0	15.0	12.5	14.6	14.7	12.1	12.5
f_t	2.45	2.54	2.55	1.88	2.24	1.82	1.87	1.76	1.73	1.74	1.70	1.53
E	9.8	9.9	8.1	9.0	9.0	8.4	8.9	8.2	8.7	9.1	8.0	7.8
Gf^a	12,8	16,9	11,7	8,2	12,8	13,95	11,9	18,2	19,7	12,5	18,1	18,3
Gf^b	42,8	59,6	90,8	49,9	22,9	67,7	58,9	69,3	52,9	29,1	44,1	68,6
CoV (%)												
$f_{c,cu}$	4.3	2.7	1.9	2.6	2.0	3.5	4.3	5.8	0.7	0.5	0.7	2.3
f_t	2.6	1.0	13.9	6.9	5.9	6.7	16.2	7.0	5.2	3.6	3.6	2.9
E	3.2	1.3	12.5	1.3	2.4	1.2	5.5	6.1	3.1	2.1	2.4	1.5
Gf^a	16,9	8,7	63,6	33,1	59,7	54,2	46,6	38,2	25,2	11,4	13,4	29,7
Gf^b	6,4	12,8	6,8	8,4	14,1	15,6	11,5	4,91	24,8	10,8	24,2	18,6

$f_{c,cu}$ - compressive strength [MPa] / f_t - tensile splitting strength [MPa] / E - Elastic modulus [GPa] / Gf^a - fracture energy wedge / Gf^b - fracture energy TPB [N/m]
Data extracted from Grafe (2017)

Figure 4.8a-d show the influence of fibre length, fibre dosage and sand cement ratio on the fracture energy. The fracture energy obtained for the wedge splitting test is lower than the fracture energy of the TPB test. This is due to the larger ligament length "crack area". The ligament length for the wedge splitting test is 50 mm and 70 mm for the TPB test. An increase with the increase in fibre dosage is observed for the fracture energy obtained from the wedge splitting test, Gf^a, except in the case of mix 15.5FN[3]. This is due to an outlier which is evident in the high CoV, 63.6 %, for this mix. For the same fibre dosage and fibre length the Gf^a is higher for a sand cement ratio of 1 than a neat cement mix (i.e. sand cement ratio of 0). The result of the fracture energy from the TBP, Gf^b, shows no clear trend when considering fibre dosage, fibre length, and sand cement ratio.

4.3 Design bond stress

The design bond stress was tested using the conventional pull-out (PO) test and modified beam-end (BE) tests. In this section the result of the BE tests are presented followed by the setup of a model to predict the design bond stress for PO and BE LWFC specimens.

4.3.1 General overview of the stresses at the bond interface

Figure 4.9 shows a depiction of the stresses present during the PO test. As shown in Figure 4.9, the bar is subjected to an axial tensile force, T, at the loaded end. Recall from Chapter 2 and 3 the definition of loaded-end and free-end. The stresses present during the process is the (chemical) adhesive stress, depicted as v_a, the bearing stress of the steel on the concrete, v_b, and the shear stress, v_s, respectively. The adhesive stress acts along the steel-concrete interface and is the first stress to be overcome during the PO test. The contribution of the adhesive stress is normally insignificant and can therefore be ignored as stated by Park and Paulay (1975). Model Code (2010) makes provision for a zero chemical adhesive stress in the bond-slip model, see Figure 2.18. The bearing stress acts between the steel ribs and the concrete. When this stress is large enough, crushing of the concrete occurs at which point the bar starts to slip. The shear stress is found between the ribs of the steel acting on a cylindrical part of the concrete and is active during slip. The combination of the bearing and shear stress constitutes the mechanical bond and is activated after the loss of chemical adhesion.

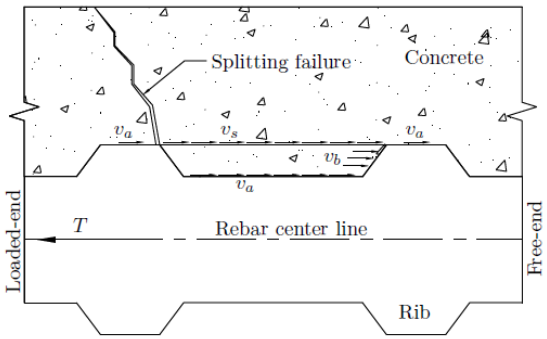

Figure 4.9: Depiction of the forces and stresses present in the PO test specimen showing the bond deterioration process (v_a, v_b, and, v_s indicating the adhesion stress, bearing stress, and, shear stress) (de Villiers, van Zijl, and van Rooyen (2016))

The two failure mechanism present can now be described in terms of the parameters depicted in Figure 4.9. For PO failure, the bearing stress and shear stress of the concrete has to be overcome. Once the bearing stress is overcome, crushing is initiated allowing slip to take place. If the shear capacity of the concrete is overcome as well, then a slip-failure surface is formed. The rebar is then free to be pulled out with only frictional forces present due to the concrete on concrete interaction.

For splitting failure, the bearing stress overcomes the concrete capacity thereby crushing it and allowing slip to take place. However, the shear capacity of the concrete is not overcome. Therefore, internal cracks arise at the steel rib-concrete interface. The steel bar is held in place because the shear capacity of the concrete is not overcome thereby resisting slip. The crack formed at the steel rib-concrete interface can however propagate toward the surface leading to the formation of secondary cracks. The formation of secondary cracks gravely compromises the integrity of the bond leading a sudden loss of bond. It is therefore evident that the formation of internal and secondary cracks impact the bond severely (Pedziwiatr (2008)).

The bond capacity and failure mode are strongly influence by the concrete properties and parameters shown in Figure 4.9. It should be noted that a type of mixed failure mode can also be achieved. This type of failure mode may be observed in the bond slip curve and is characterised by a large free-end slip followed by an abrupt splitting failure. An explanation for this behaviour is that the concrete between the ribs is crushed allowing for some degree of slip to take place. However, the shear developed is not great enough to exceed the capacity of the concrete. This resistance leads to stress gradient formation at points along the length of the bar that causes internal cracks. As the force in the bar increases the internal cracks propagate and lead to the formation of secondary cracks ending in splitting failure. Note that if during the loading stages the capacity of the concrete is overcome then PO failure would occur instead. Interpreting this behaviour leads to the conclusion that material with high shear capacity is inclined to exhibit splitting failure.

In the case of pure splitting failure the bond slip curve is characterised by a peak force at zero free-end slip. This type of behaviour may be the result of a large bearing capacity of the concrete that cannot be overcome due to the embedment length. It should be noted that zero free-end slip does not mean that no slip takes place along the embedded length of the bar. The elastic behaviour of the steel bar allows for elongation to take place and thereby slip can be initiated at the loaded-end. For this case it is therefore evident that an internal crack forms at the loaded-end and propagates to form a secondary crack ending in splitting failure before free-end slip takes place.

4.3.2 Beam-end tests (BE tests)

Bond tests were performed by de Villiers (2015) under the author's co-supervision. De Villiers investigated both PO bond and BE bond tests on LWFC of various densities and with various bar diameters. As stated in Chapter 2.4, the PO test does not represent the stress fields in a RC beam. For this reason, the PO tests are not elaborated here. The BE tests are presented here, in order to highlight the failure mechanisms and subsequent improvements by students Grafe (2017) and Dunn (2017) also

under co-supervision of the author, in order to improve fracture energy specifically to increase bond to enable the development of a steel reinforced LWFC structural wall system (Dunn (2017)).

4.3.2.1 Beam-end (BE) testing parameters

The BE tests were performed as described in Chapter 3 on LWFC and NWC specimens. The variables tested were (1) LWFC densities, ρ, (2) the nominal bar diameter, φ, and, (3) the rebar embedment length. The LWFC densities tested are 1200 kg/m^3, 1400kg/m^3, 1600 kg/m^3. Rebar made from mild steel with 12, and, 20 mm diameters were used along with an embedment length of 5φ, respectively. The reason for only testing one embedment length for the BE tests is that specimens with shorter embedment lengths may be damage during handling. Table 4.5 is a matrix of all specimens tested.

Table 4.5: Matrix of the LWFC and NWC specimens tested using the BE test

	LWFC						NWC	
ρ	12F-B		14-F-B		16F-B		N-B	
φ	12	20	12	20	12	20	12	20
l_e	5	5	5	5	5	5	5	5

4.3.2.2 Y20 LWFC bond envelopes obtained from the BE test

Figure 4.10, Figure 4.12, and Figure 4.14 show the bond-slip curves (envelopes) for the Y20 LWFC BE specimens of density 1200 kg/m^3, 1400 kg/m^3, and, 1600 kg/m^3 with a secondary vertical axis indicating the crack width as a function of the free-end slip. Figure 4.11, Figure 4.13, and Figure 4.15 show the BE specimens after testing indicating the secondary cracks formed during testing. It should be noted that the measurement of the secondary cracks are by no means be used as an indication of the onset of internal cracking. The secondary cracks can only be measured once they have reached the surface. They are progressive in nature and continue to grow throughout testing. These measurements are merely to show their development and growth during testing.

4.3.2.2.1 BE test results of 12F-B-20-5

Figure 4.10 shows the bond-slip curve of 12F-B-20-5 and crack width on the secondary axis. The bond stress as a function of the loaded-end slip and bond stress as a function of the free-end slip seems to follow and lay on top of one another. An interpretation or explanation of this behaviour is that the bar is moving “freely” and that little or no elastic deformation occurs during testing. This result is achieved when there exist a relatively weak bond between the concrete and the steel. Thus there is no resistance enabling large bond stresses to develop. Therefore it is clear that during testing the bearing and shear capacity of the concrete has been exceeded resulting in crushing of the concrete around the steel ribs.

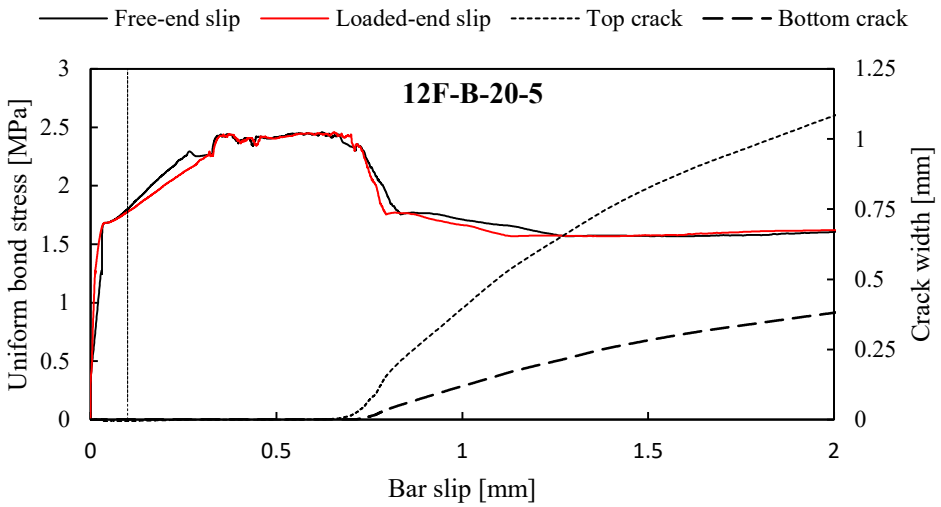

Figure 4.10: Bond-slip curves (BE) for 12F-B-20-5 with secondary axis indicating crack width (showing crack growth) (reproduced from de Villiers (2015))

Figure 4.11 shows a photograph of the specimen, 12F-B-20-5, after testing. In Figure 4.11 the secondary crack can be seen visibly on the face of the concrete (painted white for optimum visual effects). The secondary crack formed in the direction of the embedded bar and is wider at the loaded-end. Also visible in Figure 4.11 is a transverse crack, at the free-end of the embedded bar, developing at the transition point (bonded to un-bonded region). Normally, primary cracks (or flexural cracks) form at this point in structural members and immediately after the crack the tensile forces is transferred to the surrounding concrete since the un-bonded region cannot carry any tensile forces. The beam-end test therefore accurately simulates this mechanism which is confirmed by the development of cracks at this boundary.

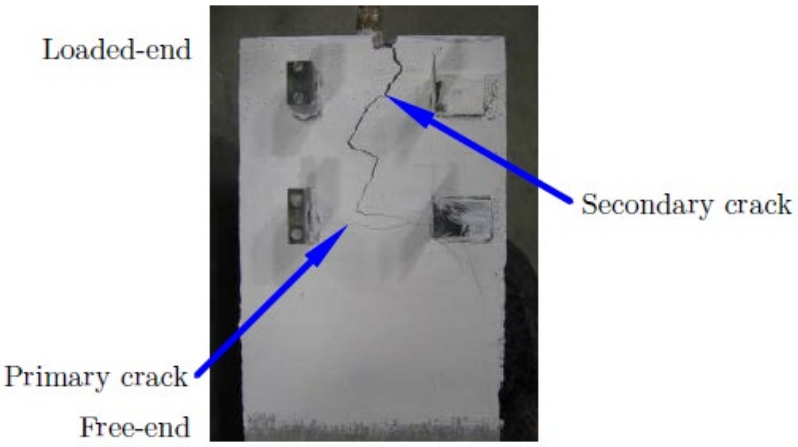

Figure 4.11: Photograph of specimen 12F-B-20-5 after testing showing the visible secondary cracks (de Villiers (2015)).

The failure mechanism in 12F-B-20-5 is splitting failure. It should be noted that most of the bond strength was retained after the formation of the secondary cracks. This this type of ductile behaviour

displayed is indicative of pull-out failure. Also, specimen 12F-P-20-5 (tested using the PO test), should similar ductile behaviour to 12F-B-20-5 but failed in pull-out fashion. The ductile behaviour here can be explain by a mix mode failure whereby the specimen experienced a combination of both pull-out and splitting failure and may result in more conservative values than the result from the PO test. This conservative value is caused by the loading experienced by the beam-end specimen, eccentric loading of the rebar.

4.3.2.2.2 BE test results of 14F-B-20-5

Figure 4.12 shows the bond-slip curve of 14F-B-20-5 and crack width on the secondary axis. The bond stress as a function of the loaded-end slip and bond stress as a function of the free-end slip have two different distinct paths. This suggest that the concrete has sufficient strength to mobilise the mechanisms that contribute to the mechanical bond. Therefore it appears that the embedded bar experienced elastic deformation, elongation, before the onset of free-end slip, this is contra to what the 1200 kg/m^3 density LWFC BE specimen, 12F-B-20-5, experienced. Comparing the results of 14F-B-20-5 with that of 12F-B-20-5 it can be seen that the 1400 kg/m^3 sample exhibited better overall bond performance. However, 14F-B-20-5, did fail in splitting failure as indicated by the sudden deterioration of bond. The equivalent PO test specimen, 14F-P-20-5, also experienced splitting failure.

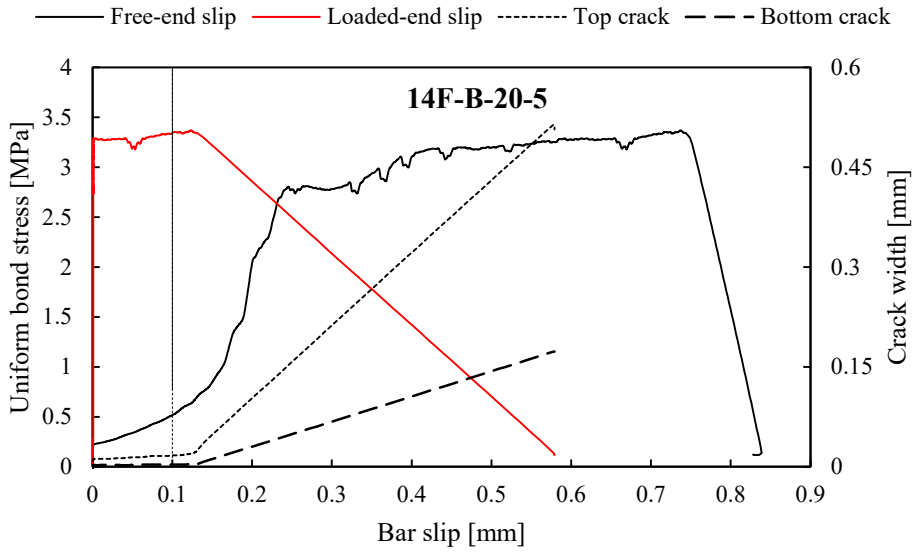

Figure 4.12: Bond-slip curves (BE) for 14F-B-20-5 with secondary axis indicating crack width (showing crack growth) (reproduced from de Villiers, van Zijl and van Rooyen (2017))

Figure 4.13 shows a photograph of specimen 14F-B-20-5 after testing. In Figure 4.13 a transverse primary crack and a longitudinal crack can be seen.

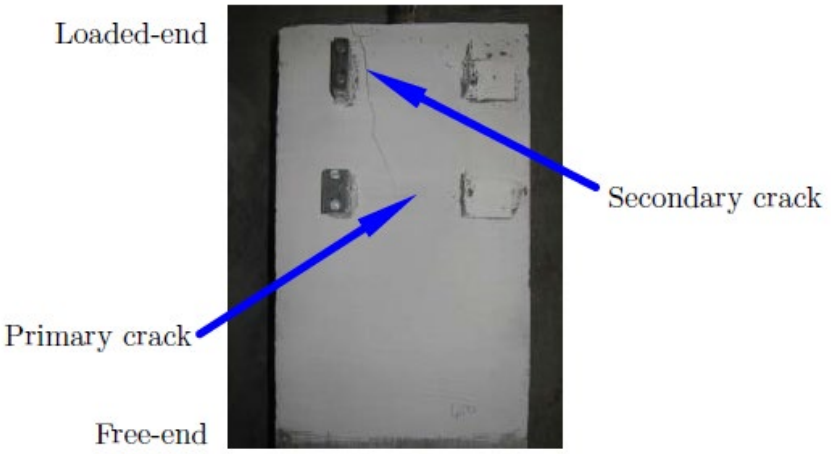

Figure 4.13: Photograph of specimen 14F-B-20-5 after testing showing the visible secondary cracks (de Villiers (2015)).

4.3.2.2.3 BE test results of 16F-B-20-5

Figure 4.14 shows the bond-slip curve of 16F-B-20-5 and crack width on the secondary axis. The bond stress as a function of the loaded-end slip and bond stress as a function of the free-end slip have two different distinct paths. This result is similar to what specimen 14F-B-20-5 experienced ending in splitting failure. Figure 4.15 confirms the failure mode with the presence of a transverse and a longitudinal secondary crack.

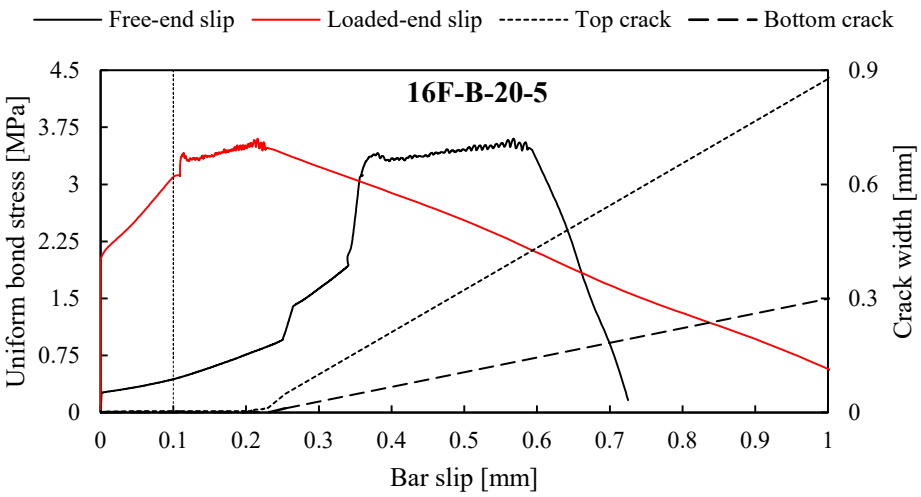

Figure 4.14: Bond-slip curves (BE) for 16F-B-20-5 with secondary axis indicating crack width (showing crack growth) (reproduced from de Villiers (2015))

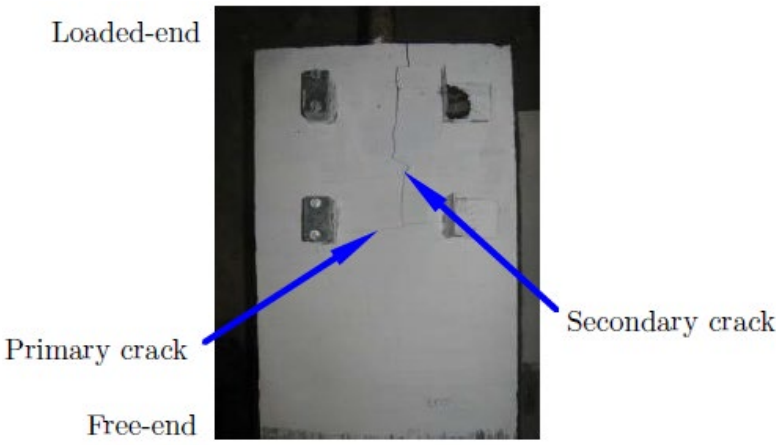

Figure 4.15: Photograph of specimen 16F-B-20-5 after testing showing the visible secondary cracks (de Villiers (2015)).

4.3.2.2.4 Comparison of the Y20 BE test results

Figure 4.16 shows the uniform bond stress, σ_b, of the BE specimens for LWFC specimens tested versus the free-end slip. From Figure 4.16 it can be seen that the largest bond stress corresponds to the highest concrete density, 1600 kg/m^3, tested. The specimen made with 1200 kg/m^3, 12F-B-20-5, has the smallest uniform bond stress. All specimens exhibited splitting failure. Specimen 12F-B-20-5 exhibited the best ductility out of all the specimens tested. Specimen 14F-B-20-5 and 16F-B-20-5 showed reduced ductility due to the increase in brittleness of the material but observed higher bond stresses due to the mobilisation of the mechanical bond mechanism.

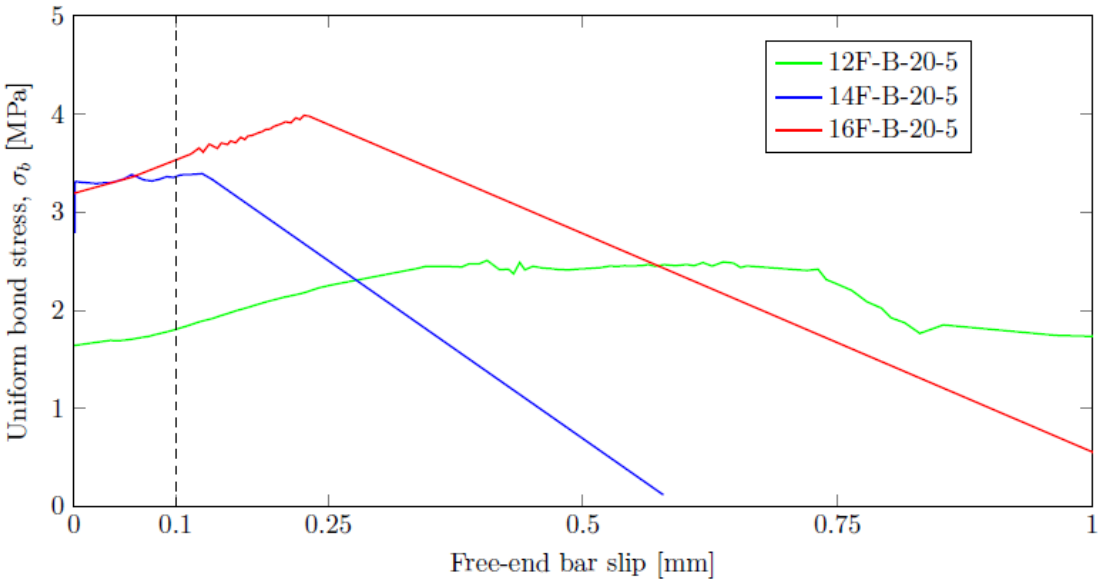

Figure 4.16: Uniform bond stress versus free-end slip (BE) for 12F-B-20-5, 14F-B-20-5 and 16F-B-20-5 (de Villiers, van Zijl and van Rooyen (2017))

4.3.2.2.5 Y12 LWFC bond envelopes obtained from the BE test

The BE test was performed on LWFC BE specimens with densities, 1200 kg/m^3, 1400 kg/m^3, and 1600 kg/m^3, reinforced with Y12 steel rebar with an embedded length of 5φ. All specimens (12F-B-12-5, 14F-B-12-5, and, 16F-B-12-5) exhibited PO failure. No visible secondary cracks formed on the surface of the concrete. Figure 4.17 shows the uniform bond stress versus the free-end slip for 12F-B-12-5, 14F-B-12-5, and, 16F-B-12-5 as calculated from the result of the BE test.

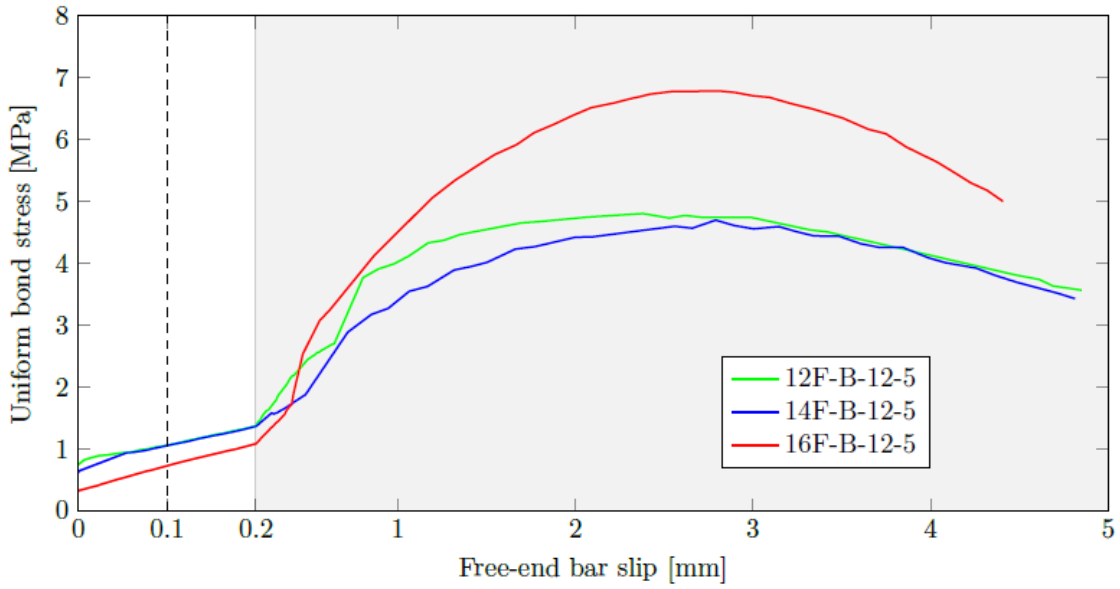

Figure 4.17: Uniform bond stress versus free-end slip (BE) for 12F-B-12-5, 14F-B-12-5 and 16F-B-12-5 (de Villiers, van Zijl and van Rooyen (2017))

From Figure 4.17 it can be seen that 16F-B-12-5 has the lowest uniform bond stress of the three specimens tested. 12F-B-12-5 and 14F-B-12 have almost exactly the same uniform bond stress. All three specimens show a positive gradient at the design point. The gradient increases after 0.2 mm slip with 16F-B-12-5 showing the most gains. No clear pattern is found for the peak bond stress as the 1600 kg/m^3 specimen corresponds to the largest peak bond stress and the lowest peak bond stress corresponding to the 1400 kg/m^3 specimen. The values of the loss of chemical adhesion stress, σ_a, are somewhat interesting, obtained from the results of the Bond Integrity discussed in the following section. It shows that the 1600 kg/m^3 specimen has the lowest loss of chemical adhesion stress. Viewing this result in combination with the result of the data (increase in gradient) it is believed that this value should be larger and that the chemical adhesion for this specimen may have been compromised early during testing as a result of the brittleness of the concrete.

The source of the compromised loss of chemical adhesion stress is due to the loading configuration of the BE test and the increased brittleness of the concrete. Recall that it has been shown, from the results of the wedge splitting test, that a direct proportionality exist between brittleness and LWFC density. The brittleness coupled with the fact that during loading the BE specimen is subject to a moment as a result

of the eccentric loading of the embedded reinforcement. This moment subjects the embedded reinforcement to flexural behaviour, whilst experiencing slip due to the axial force, causing it to exert larger stress on one side compared to the other. This type of behaviour causes the formation of cracks early on during loading of the BE specimen and is not present in the PO test.

4.3.2.3 Bond Integrity (BI) for BE tests

Structural members made from RC experiencing bending moments have what is called "flexural bond". This bond is what helps resist bending moments (Park and Paulay (1975)). An advantage offered by using the BE test to obtain design stresses over the PO test is that the BE test simulates flexural bond. A useful term that can be used to assess the condition of the bond in concrete is the bond integrity (BI). The BI can be calculated using Equation 4.1.

$$BI = \frac{dM/dt}{jd} - \frac{dT}{dt} \tag{4.1}$$

where BI as the bond integrity in Newton per second
T as the internal tension in the embedded bar
M as the external bending moment
jd as the lever arm of the external bending moment.
t as the testing time

According to Park and Paulay (1975) a bond integrity (BI) of zero means that the bond is intact. Stated differently when the rate of change of the tensile force (T) in the bar is in equilibrium with the rate of change of the external moment (M). When the BI is not in equilibrium it implies slip is taking place and possible bond deterioration. For instance, at the start of the BE test a BI value of zero is expected. Once the test commences and slip occurs there is a corresponding drop in the force of the embedded bar. In order to keep the set rate of displacement (displacement control used during testing) the rate of change in the bar force is lower and thus a positive value of BI is obtained. The materials testing machine (MTM) will continue to adjust the rate of change in the force applied in order to maintain the correct displacement set for testing. Thus the BI will cycle in and out of equilibrium. For this investigation all tests were performed using the same displacement control (rate of displacement of the loaded-end). On a final note, any positive value of BI indicates bond deterioration. However, due to the displace control used by the MTM negative values may be obtained as a result of overcorrecting.

4.3.2.3.1 Bond Integrity of Y12 LWFC BE specimens

Figure 4.18 shows the bond integrity (BI) plotted as a function of time for the Y12 LWFC BE specimens. The BI for the specimens tends to oscillate around with the spikes in the graphs indicating important points such as the loss of chemical adhesion and deterioration of the bond. Also indicated on the horizontal axis in Figure 4.18 is the time to the loss of chemical adhesion and design bond stress of the various specimens. These values are tabulated in Table 4.6.

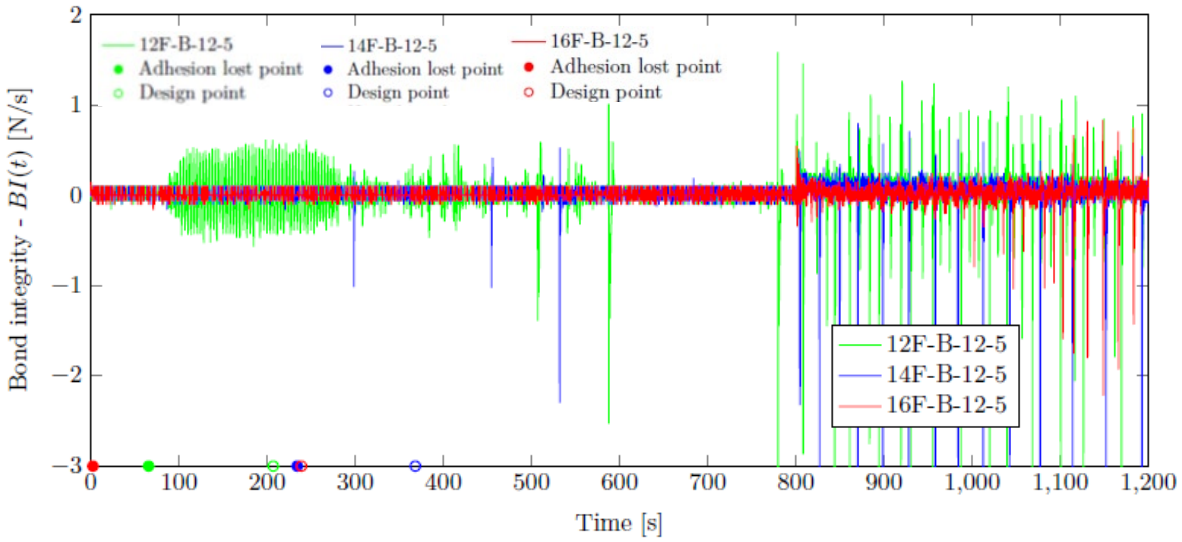

Figure 4.18: Bond integrity of the Y12 LWFC BE specimens (de Villiers (2015))

Table 4.6: Time to loss of chemical adhesion and design point for Y12 LWFC BE specimens

Description	Adhesion loss time (s)	Design point time (s)
12F-B-12-5	65.8	207.2
14F-B-12-5	234.4	368.4
16F-B-12-5	2.6	239.2

Data from de Villiers (2015)

Figure 4.19 shows the same data presented in Figure 4.18 on a shorter interval and scale. The reason for this is to show the noise boundaries that occur during testing. During testing the values of the BI tend to oscillate between -0.6 N/s and 0.1 N/s. This noise from the MTM control system when adjusting for micro-slip and internal cracking is indicated between the two dashed horizontal lines. It should therefore be noted that only values falling outside these boundaries should be used for interpretation.

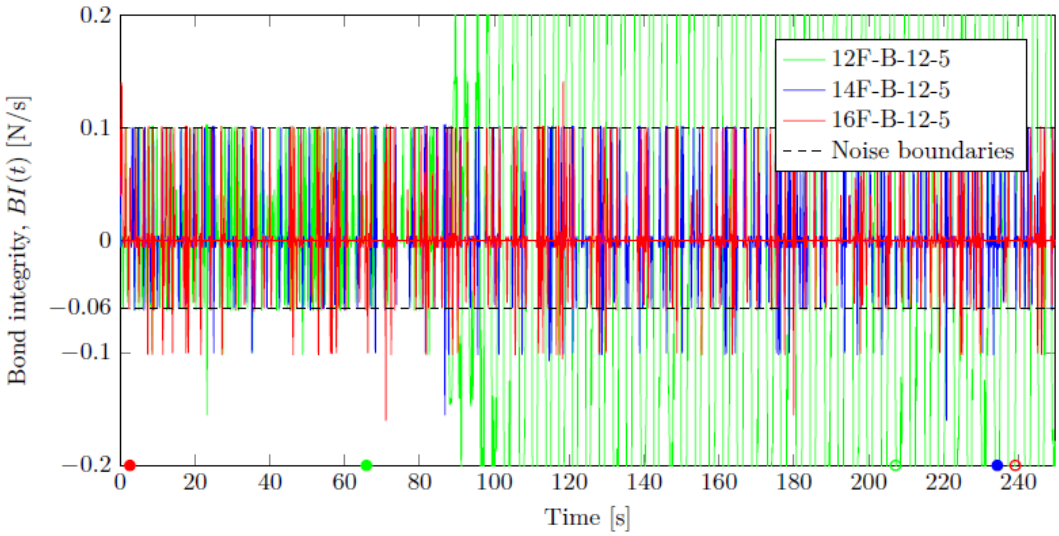

Figure 4.19: Bond integrity of the Y12 LWFC BE specimens (de Villiers (2015))

4.3.2.3.2 Bond Integrity of 12F-B-12-5 BE specimen

Figure 4.20 shows the bond integrity (BI) plotted as a function of time for the 12F-B-20-5 specimen. For specimen 12F-B-20-5 the loss of chemical bond occurred 66 seconds into the test. Prior to the loss of chemical adhesion no positive BI were measured above noise boundary. 12F-B-20-5 experienced a ductile PO failure. This is the result of crushing of the concrete between the steel ribs. The results of the BI also indicate that minimal or no cracking occurred prior to the loss of chemical adhesion. As the test progressed significant spiking can be seen in the BI up to and beyond the design point after the loss of chemical adhesion. Again, these spikes are caused by the continuous adjustment of the load by the MTM system to maintain the set rate of displacement.

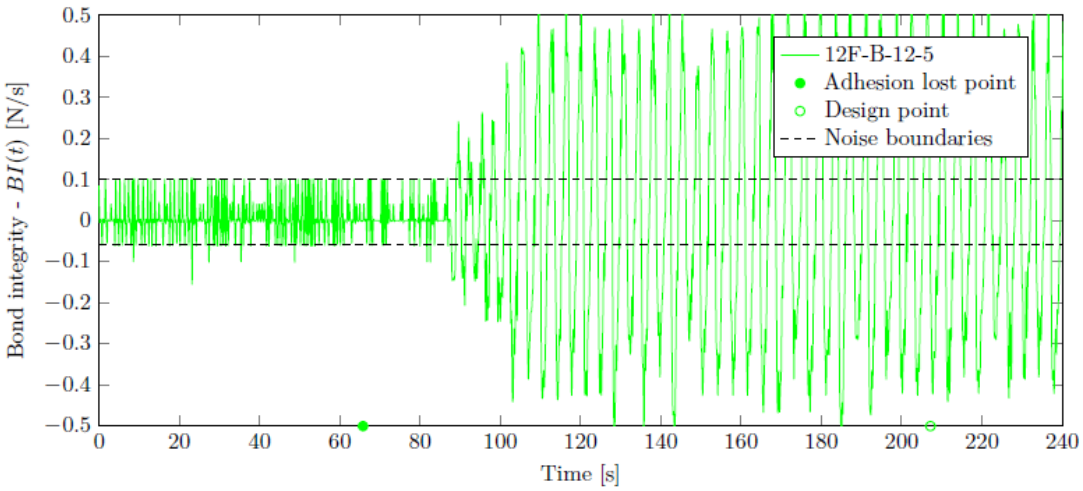

Figure 4.20: Bond integrity of the 12F-B-20-5 BE specimen (de Villiers (2015))

4.3.2.3.3 Bond Integrity of 14F-B-12-5 BE specimen

Figure 4.21 shows the bond integrity (BI) plotted as a function of time for the 14F-B-20-5 specimen. For specimen 14F-B-20-5 the loss of chemical bond and design point occurred 235 and 369 seconds into the test. Again prior to the loss of chemical adhesion no internal cracking is seen in the results.

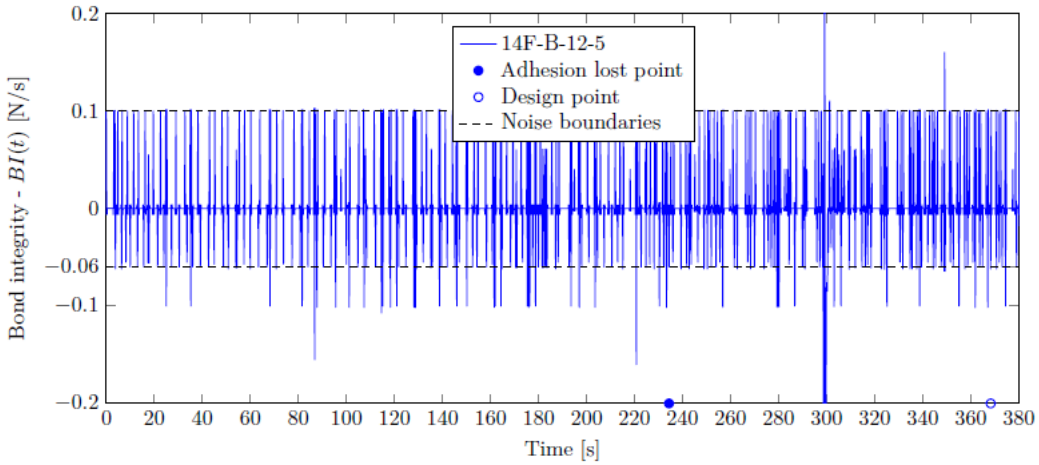

Figure 4.21: Bond integrity of the 14F-B-20-5 BE specimen (de Villiers (2015))

4.3.2.3.4 Bond Integrity of 16F-B-12-5 BE specimen

Figure 4.22 shows the bond integrity (BI) plotted as a function of time for the 16F-B-12-5 specimen. For specimen 16F-B-12-5 the loss of chemical bond and design point occurred 2.6 and 240 seconds into the test. In Figure 4.22 evidence of the early loss of chemical adhesion can be seen by the positive spike in BI just after the test commenced. This may be the result of an internal crack forming soon after loading due to the increased density and brittleness of LWFC. This result is validated by the bond-slip curve of this specimen.

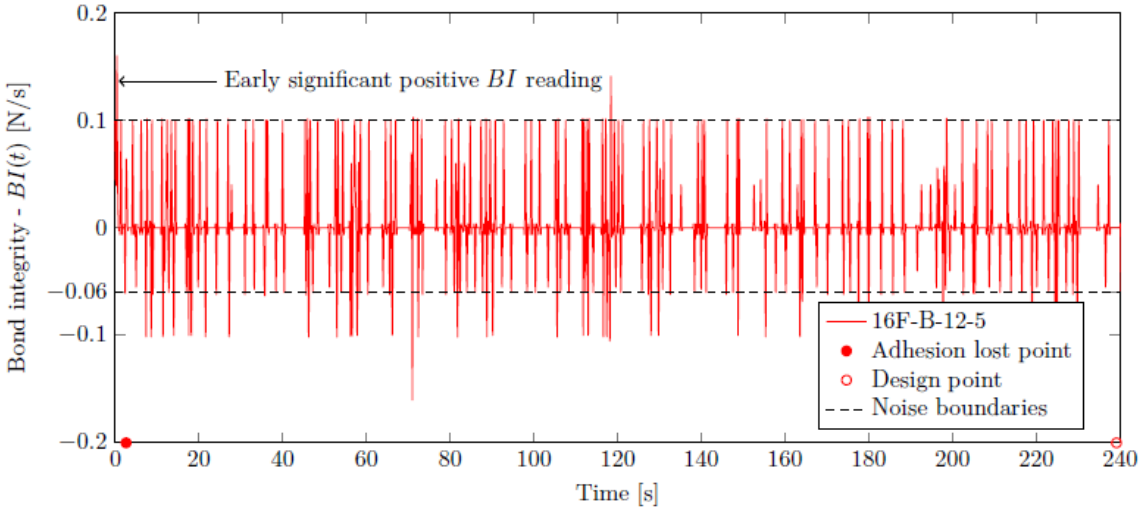

Figure 4.22: Bond integrity of the 16F-B-20-5 BE specimen (de Villiers (2015))

4.3.2.4 Comparison and conclusion of the BE test results for LWFC and NWC

Table 4.7 lists the values of the design bond stress obtained for the LWFC and NWC specimens using the results of the BE tests. The values obtained for NWC far surpass that of LWFC specimens. No clear trend is seen in the design bond stress values for LWFC densities.

Table 4.7: Design bond stress values obtained from the BE tests

Specimen	Design bond stress (MPa)
N-B-12-5	6.43
12F-B-12-5	1.06
14F-B-12-5	1.05
16F-B-12-5	0.72
N-B-20-5	12.65
12F-B-20-5	1.81
14F-B-20-5	3.36
16F-B-20-5	3.53

Data from de Villiers (2015)

4.3.2.5 Comparison of the PO and BE test results for LWFC and NWC

As stated in Section 4.2.2, PO tests were also performed on LWFC by de Villiers (2015) under the author's co-supervision. Although the PO tests do not represent actual bond in RC beams, it is insightful to compare the PO and BE results, whereby in fact significant differences are illuminated. In this section a comparison of the results obtained from the PO and BE tests is presented. A brief discussion of bond specification for design is given.

4.3.2.5.1 Comparison of the PO and BE test results

Figure 4.23 show the results of the design bond stress values for the 12F, 14F, 16F and NWC obtained from the PO and BE tests conducted on specimens with Y12 and Y20. The values obtained for the PO test is shown alongside the BE test values with the difference indicated with the hatched area.

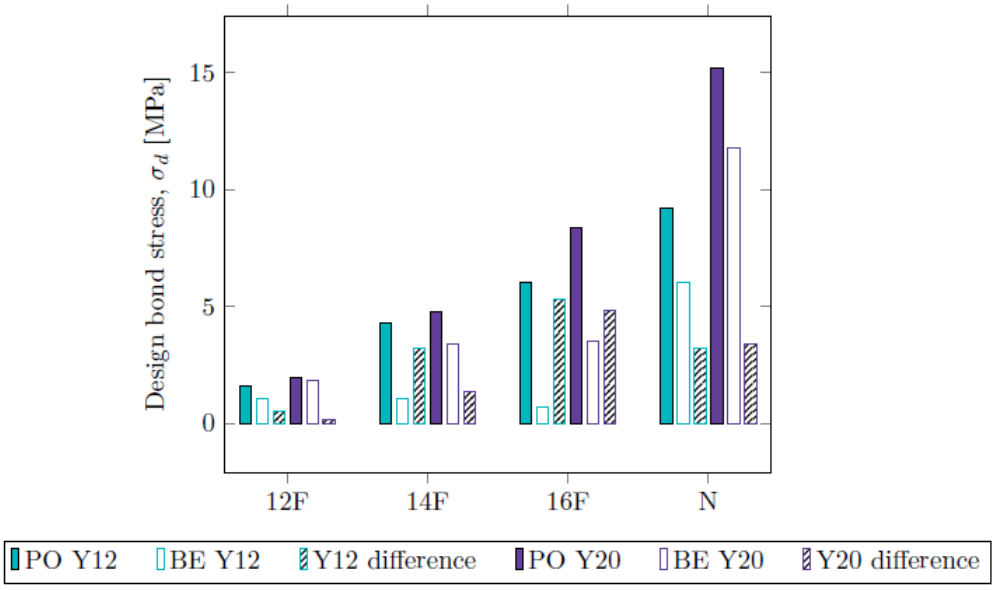

Figure 4.23: Design bond stress of 12F, 14F, 16F and NWC for PO and BE test results (de Villiers, van Zijl and van Rooyen (2017))

From Figure 4.23 it can be seen that the design bond values obtained for the BE test specimens were lower than the corresponding values obtained from the PO test in all cases. This could be due to the fact that the BE test simulates more realistic behaviour (accounting for flexure). The difference in the results between the BE and PO test seems to increase with an increase in density for LWFC specimens. Overall larger differences are found when comparing the values of the PO test than those obtained from the BE tests.

Table 4.8 lists the results of the design bond stress values for the 12F, 14F, 16F and NWC obtained from the PO and BE tests conducted on specimens with Y12 and Y20. The highest design bond stress obtained for LWFC specimens is that of 16F-B-20 and 16F-P-20, 8.34 and 3.53 MPa, respectively. Comparing these values to the corresponding NWC counterpart it is calculated that 16F-B-20 and 16F-P-20 developed about 30% and 55% of the design bond stress of developed in NWC with the same reinforcement.

Table 4.8: Design bond stress of 12F, 14F, 16F and NWC for PO and BE test results

Description	φ	σ_d [MPa]		
		PO	BE	Δ
N	10	1.76	-	-
	12	9.21	6.00	3.21
	20	15.18	11.81	3.38
16F	10	1.20	-	-
	12	6.01	0.72	5.28
	20	8.34	3.53	4.81
14F	10	0.94	-	-
	12	4.27	1.05	3.23
	20	4.74	3.36	1.38
12F	10	1.89	-	-
	12	1.59	1.06	0.54
	20	1.94	1.80	0.14

Data from de Villiers, van Zijl and van Rooyen (2017)

4.3.2.5.2 Bond stress for design considerations

Figure 4.24 shows the design bond stress of 12F, 14F, 16F and NWC obtained from the PO and BE test as a function of compressive strength. Also included in Figure 4.24 are values for NWC given in SANS 0100-1 (2000) and BS EN 1992-1-1 (2004). It should be noted that the method for obtaining the design bond stress given in SANS 0100-1 (2000) and BS EN 1992-1-1 (2004) are not listed in the standards. Recall that the method used in this study is that found in Leonhardt (1977) (design bond corresponding to 0.1 mm slip). Therefore a comparison cannot be made between the results obtained in this study and that given in the codes. They are merely shown here in Figure 4.24 as what may be deemed acceptable design bond stress value by the various codes.

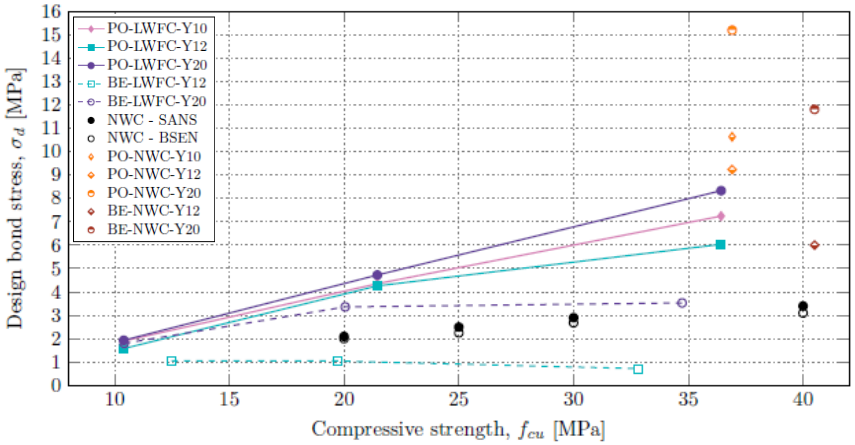

Figure 4.24: Design bond stress of 12F, 14F, 16F and NWC obtained from the PO and BE test as a function of compressive strength. (Values for NWC from SANS 0100-1 (2000) and BS EN 1992-1-1 (2004) also included) (de Villiers, van Zijl, and van Rooyen (2017))

The following observations and conclusions can be drawn from the results of the PO and BE test;

- There seems to exist a direct proportionality between σ_d and f_{cu} for LWFC from the PO tests
- No correlation is found between σ_d and f_{cu} for LWFC from the BE tests
- More conservative values for σ_d are obtained when using the BE test than the PO test

- Higher values of σ_d are obtained for NWC specimens than those in the design standards suggesting the method used in the study (design point at 0.1 mm slip) is not the method used in the design standards. Note, however that the standardised bond values represent characteristic values, while average experimental bond strengths are shown have been determined experimentally

4.3.3 Comparison of mechanical performance and bond improvement

The normalised values of the mechanical properties and bond stress (PO and BE) values are shown in Figure 4.25 and Figure 4.26. Each property has been normalised against its respective density. Figure 4.25 and Figure 4.26 show that there is a relationship between the compressive strength and the tensile splitting strength of the concrete. Evidence of the relationship between compressive strength and tensile splitting strength can be seen in the way both graphs behaves. Both graphs tend to show a similar pattern. A similar observation can be made for the fracture energy and the characteristic length. An increase in the characteristic length would signal an improved bond between the reinforcing steel and the surrounding concrete matrix. This is due to the fact that a material with larger characteristic length requires a smaller embedment / anchorage length for the reinforcement. Therefore the bond behaviour of a material may be brought about with an increase in fracture energy. In this research the improvement of the fracture energy, hence bond behaviour of R/LWFC, was investigated by the addition of synthetic fibres. Figure 4.27 shows the normalised mechanical properties and includes the results of a selected optimised mix ($15.5F^2$) for fracture energy. The selected optimised mix has a fracture energy 2.5x greater than the 1600 kg/m^3 mix and 11x larger characteristic length.

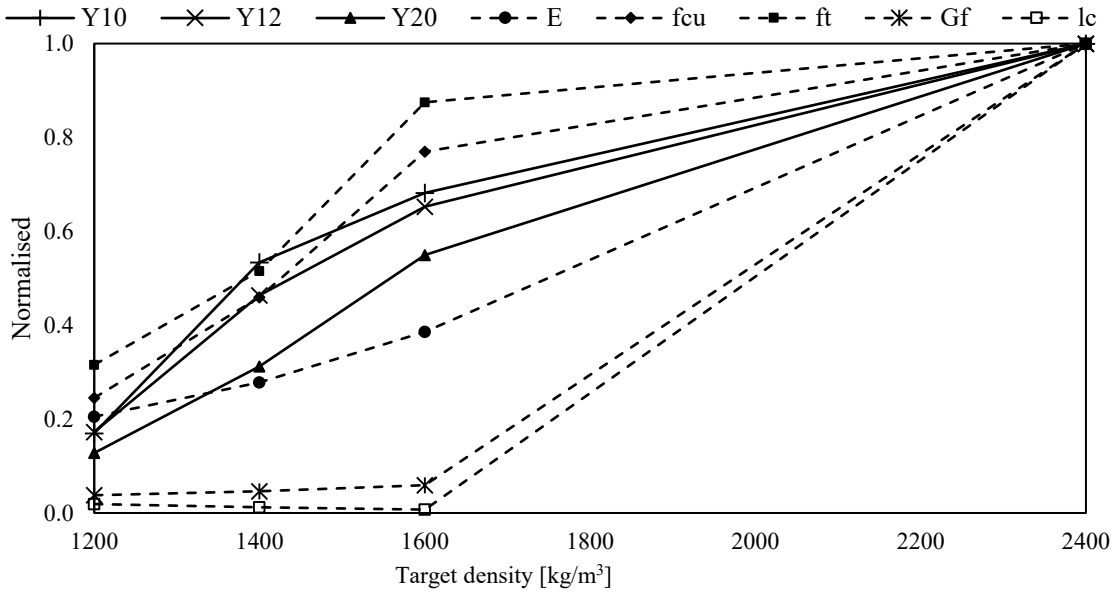

Figure 4.25: Normalised values of the mechanical properties and bond values (PO test) (de Villiers, van Zijl and van Rooyen (2017))

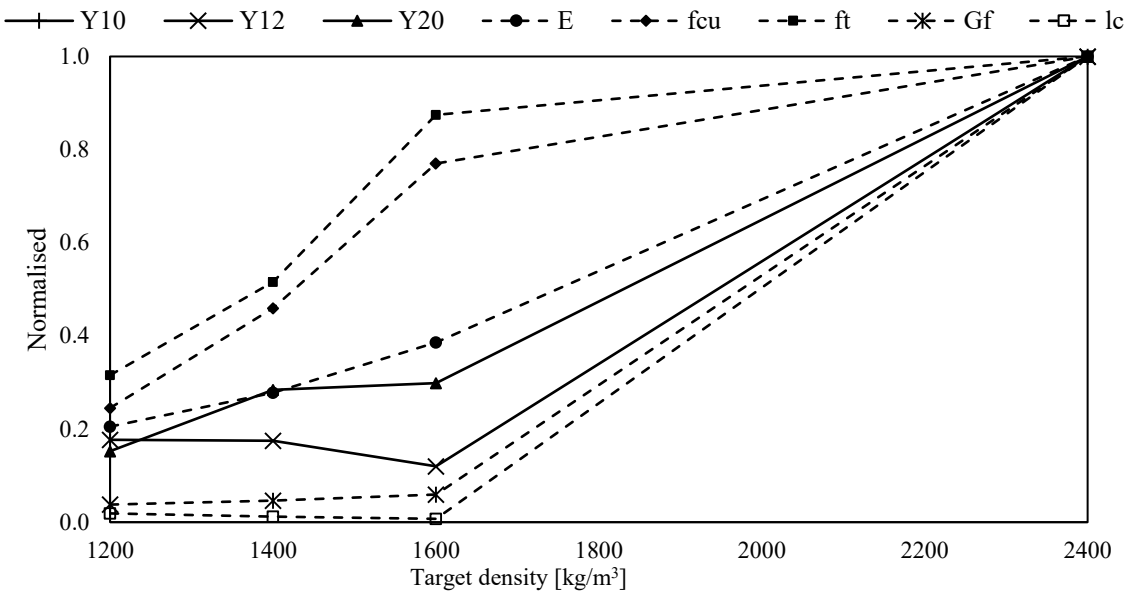

Figure 4.26: Normalised values of the mechanical properties and bond values (BE test) (de Villiers, van Zijl, and van Rooyen (2017))

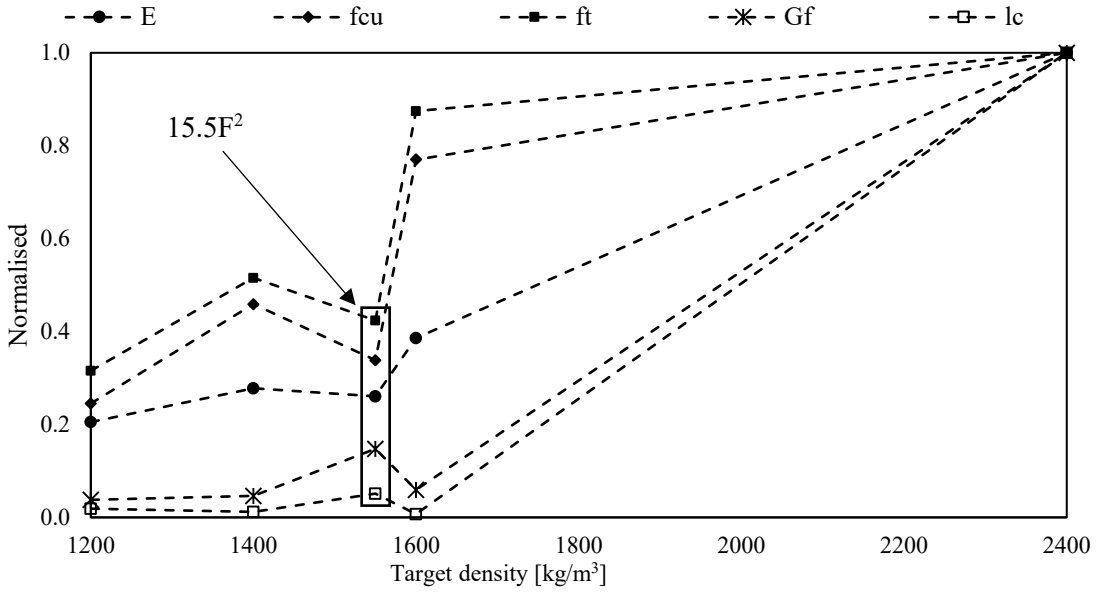

Figure 4.27: Normalised values of the mechanical properties and selected optimized mix ($15.5F^2$) (van Zijl, van Rooyen, Mubatapasango et al. (2017))

The addition of fibres in concrete causes a decrease in fcu, E, and ft due to the loss of cross-sectional area but increase ductility through bridging of micro-cracks. Recall, that the characteristic length is directly proportional to the fracture energy and stiffness and inversely proportional to the square of the tensile strength – Equation 3.7. Therefore an increase in the fracture energy and decrease in the tensile strength of LWFC through the addition of fibres is greatly improves the characteristic length of the material

4.3.3.1 Model for determining design bond stress in Reinforced Lightweight Foamed (R/LWFC)

4.3.3.1.1 Model for predicting design bond stress in LWFC

It is often quite convenient to be able to predict the value of certain properties of concrete without conducting physically test. The amount of time saved for design considerations by using prediction models often saves revenue on large scale projects. LWFC is a relatively new material for which no bond stress prediction model exist. Although a few models do exist for predicting bond in lightweight concrete (Dae-Jin et al. (2014), Zuo and Darwin (2000), these models are not applicable to LWFC and should not be used. In this section a model is development for predicting the design bond stress, at 0.1 mm free-end slip, for LWFC by means of a mathematical formula derived from equilibrium conditions. The equation is valid for predicting bond stress values of PO tests and with the use of additional factors can predict the equivalent values as obtained by the BE tests.

Figure 4.28 shows a depiction of the stresses that contribute towards the bond between the steel reinforcement and concrete. In Figure 4.28, T_d is the force in the bar at the design point, v_b and v_s represent the bearing stress and shear stress, respectively. The embedded length is represented by l_e, whilst the rib spacing, rib height, rib width, and inner bar diameter are represented by c, h, a, and e, respectively. These variable have been defined before and are re-listed here for convenience. Note that the chemical adhesion stress is left out from Figure 4.28 because this stress has already been overcome at the onset of free-end slip.

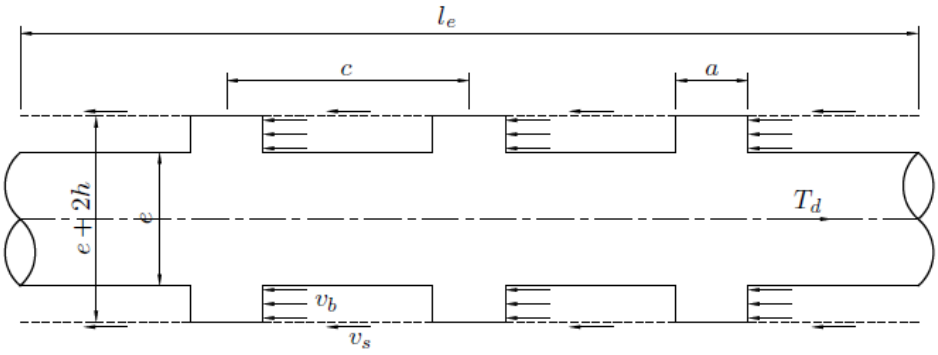

Figure 4.28: A depiction of the stresses that contribute towards the bond between the reinforcement and concrete

For equilibrium purposes, the force in the bar T_d must be equal to the opposing forces represented by the product of the stress (v_b and v_s) and the corresponding area (A_b and A_s).

$$T_d = v_b A_b + v_s A_s \tag{4.2}$$

Given T_d as the force in the bar when the design point is reached, in N,

v_b as the bearing stress, in MPa,

v_s as the shear stress, in MPa,

A_b as the area on which v_b acts (representative rib area), in mm^2, and

A_s as the area on which v_s acts (representative shear area), in mm^2.

Equation 4.2 describes pure PO failure and does not account for splitting failure. Equation 4.3 is a modification of Equation 4.2 and incorporates dimensionless weighting factors to make provision for splitting failure.

$$T_d = w_p(v_b A_b + v_s A_s) + w_s(v_b A_b + v_s A_s) \tag{4.3}$$

Given w_p and w_s as the dimensionless PO failure and splitting failure weighting factors.

The weighting factors w_p and w_s are introduced to account for the contribution of each terms towards the bond. For instance, during PO failure both v_b and v_s contribute towards the bond. However, during splitting failure v_b is the dominant term contributing to the bond. The reason for this is that the concrete between the ribs do not shear off during splitting failure. Therefore the contribution of the shear term is negligible. Before a crack develops, both terms contribute towards the bond development. However, after the onset of crack formation (leading to splitting failure) the bearing stress is the only contributor to the bond and is the source of energy for crack generation. Therefore the bearing force, v_b A_b, can be used to account for the loss of bond as a result of internal crack formation. Also, the weighting factors, w_p and w_s, are used to account for the susceptibility of LWFC to fail in one of the two failure modes expected. The terms in Equation 4.3 can be calculated from Equations 4.4 to 4.9.

$$v_b = f_{cu} \tag{4.4}$$

$$A_b = 2h\, e\left(\frac{l_e}{c}\right) \tag{4.5}$$

$$*v_s = (f_{cu})^{1/3} \tag{4.6}$$

$$A_s = \left(l_e - \frac{l_e}{c}a\right)\pi(e + 2h) \tag{4.7}$$

$$**w_p = \left(\frac{\rho}{1200}\right)^2 \tag{4.8}$$

$$**w_s = -\left(\frac{\rho}{1200}\right)^{0.25} \tag{4.9}$$

*Note the shear capacity of LWFC was not investigated in this study and therefore the relationship in Chapter 6 of BS EN 1992-1-1 (2004) was used to derive a formula for v_s

**Calibrated weighting factors based on the results of the BE tests accounting for the density of LWFC and contribution towards the bond (based on the mechanism involved)

Substituting Equations 4.4 to 4.9 yields Equation 4.10.

$$\Psi = T_d = \left(\frac{\rho}{1200}\right)^2 \left[2h\, e\left(\frac{l_e}{c}\right) + (f_{cu})^{1/3}\left(l_e - \frac{l_e}{c}a\right)\pi(e+2h)\right] - \left(\frac{\rho}{1200}\right)^{0.25}\left[2h\, e\left(\frac{l_e}{c}\right)\right] \quad (4.10)$$

Figure 4.29 shows the measured PO test results of LWFC plotted against the mathematical prediction model. Also indicated is the 45 degree line and the error (difference) in the measured versus predicted results. It should be noted that model was set-up and weighting factors were calibrated using testing data from experiments conducted on LWFC PO specimens with densities between 1200 and 1600 kg/m^3. The model is therefore only valid for a density range of 1200 and 1600 kg/m^3 and extrapolation is ill-advised.

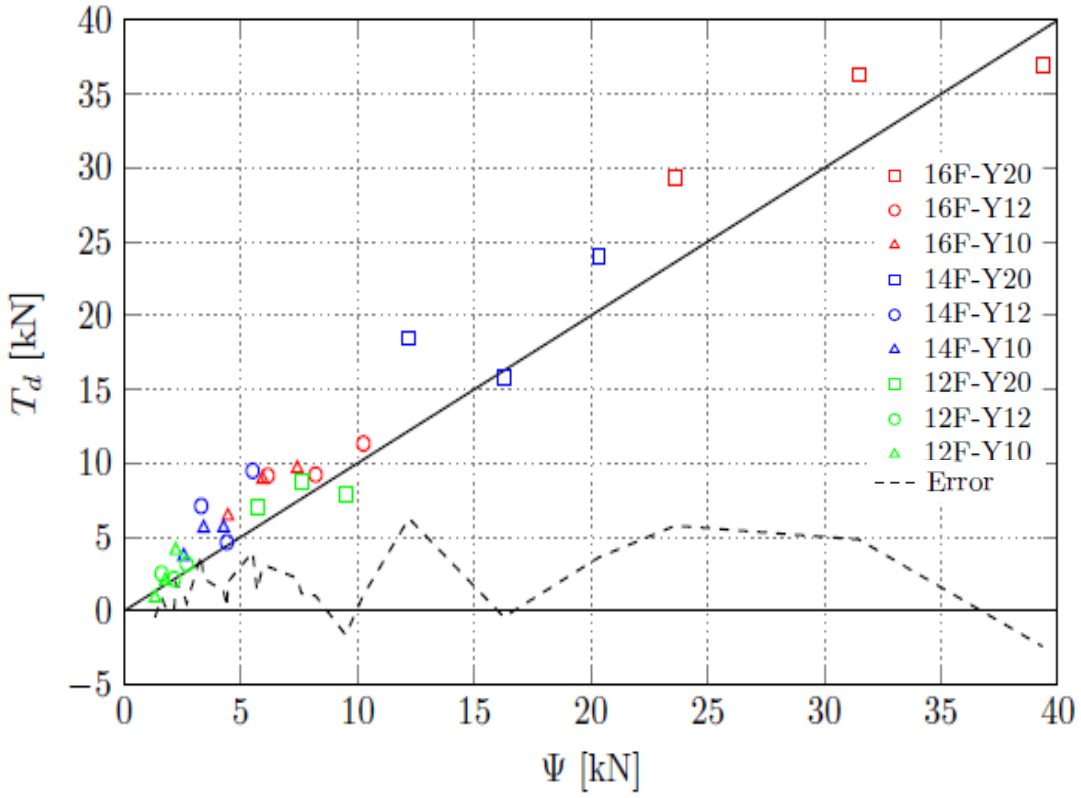

Figure 4.29: Measured pull-out test results of LWFC plotted against the mathematical prediction model. Also indicated is the 45 degree line and the error (difference) in the measured versus predicted results (de Villiers, van Zijl, and van Rooyen (2017))

From Figure 4.29 it can be seen that most of the measured data falls above the 45 degree line meaning that the model underestimates the actual results. However, there are instances whereby the model overestimated the measured results. The largest discrepancy, negative 47% error, is recorded for the 12F-P-10-3 specimen which has the lowest bond stress, smallest embedded length, and smallest bar diameter size. On the other side of the spectrum a negative 6% error is recorded for specimen 16F-P-

20-5 which is the specimen with the highest density, highest bond, largest embedded length and largest bar diameter size tested.

4.3.3.1.2 BE test prediction

The mathematical model derived for predicting the design bond stress values of LWFC as determined by the PO test can be modified to predict the design bond stress values of LWFC as determined by the BE test. Firstly, it should be noted that the mix design acceptance criteria for LWFC mixes varies throughout the literature. It is therefore common to accept a measured density that is within 50 kg/m^3 of the target design density. This criteria was also adopted in this part of the research programme and as such density variations do exist between specimens. For instance, the PO test for the 1200 kg/m^3 target density had a measured density of 1202 kg/m^3, however, the BE specimens had a measured density of 1233 kg/m^3. Such variations may result in a skewed interpretation / representation of the results. Therefore in order to account for this a correction, μ, can be introduced. This was achieved by normalising the results of the design bond strength to the density thereby representing it as the bond stress per kg/m^3 as seen in Figure 4.30.

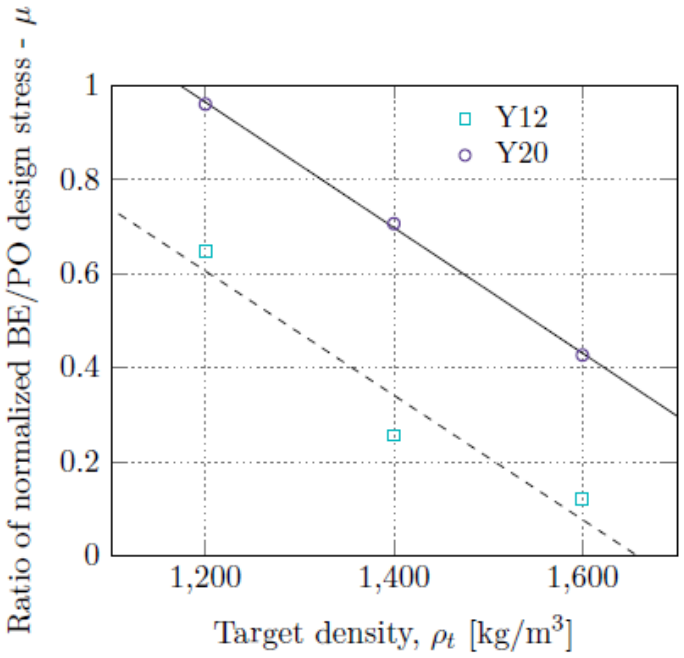

Figure 4.30: Normalised bond stress for PO and BE tests as a function of target density, ρ_t. (de Villiers, van Zijl, and van Rooyen (2017))

A regression analysis was performed on the data represented in Figure 4.30 to obtained the correction factors for the Y12 and Y20 specimens and is given as Equation 4.11 and Equation 4.12.

$$\mu_{12} = -0.00132\rho_t + 2.1894 \quad (4.11)$$

$$\mu_{20} = -0.00133\rho_t + 2.5629 \quad (4.12)$$

The correction factors can then be applied to Equation 4.10, see Equation 4.13 and Equation 4.14, to yield two prediction models for the Y12 and Y20 embedded reinforcement.

$$T_d = \mu_{12} \Psi \tag{4.13}$$

$$T_d = \mu_{20} \Psi \tag{4.14}$$

Figure 4.31 shows the measured BE test results of LWFC plotted against the mathematical prediction model.

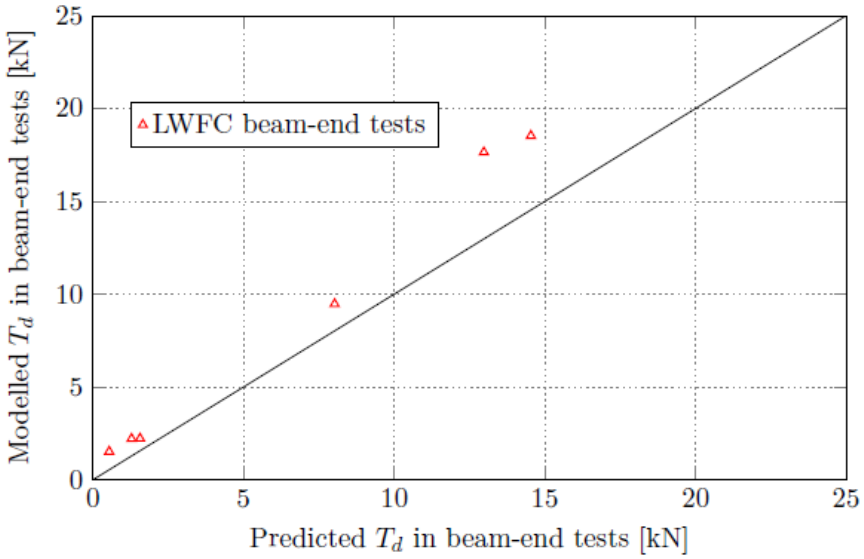

Figure 4.31: Measured BE test results of LWFC plotted against the mathematical prediction model (de Villiers, van Zijl, and van Rooyen (2017)).

Bond of reinforcing steel with concrete is an ongoing research topic, as reflected by the recent publication of fib Bulletin 72 on bond and anchorage of reinforcement (fib 2014), following an earlier version on bond of reinforcement in concrete (fib 2000). Despite a significant experimental program reported here and by de Villiers, van Rooyen and van Zijl (2017), the pool of data on bond in FC cannot be considered to be sufficient. As a direct example, BE bond tests have not been performed on FC with improved fracture energy by inclusion of fibre reinforcement as reported in this dissertation.

4.4 Two panel walling system testing

4.4.1 Background and motivation

LWFC can be considered as the ideal construction material based on its low self-weight coupled with good thermal performance and fire resistance. A drawback of LWFC is its mechanical properties.

However, a few researchers (Kearsley and Wainwright (2001a), Jones and McCarthy (2005), Nambiar and Ramamurthy (2006)) have shown that there is a range of LWFC densities that can produce compressive strengths sufficient for structural use, say 25 MPa. However Jones and McCarthy have advised against the direct substitution of LWFC for NWC based on compressive strength. The research on the characterisation of the mechanical properties and bond behaviour of R/LWFC carried out by de Villiers (2015) under the co-supervision of the author established that it is indeed possible to achieve high compressive strengths, in excess of 25 MPa, but the low tensile strength and fracture energy of LWFC results in brittle behaviour and causes poor reinforcement bond. These results resonate with the advice of Jones and McCarthy. Furthermore de Villiers, van Zijl, and van Rooyen (2016) postulated that the addition of polypropylene fibres could be used to improve the fracture energy of LWFC through bridging of micro-cracks at the concrete-reinforcement interface which would subsequently lead to improved bond behaviour. This postulation was confirmed through research done by Grafe (2017), also under co-supervision of the author, focused on the optimisation of fibre content in FC for the improvement of bond behaviour. The research findings by Grafe indicated that the addition of 0.35 % polypropylene fibres by volume could result in an increase of approximately 250 % in the fracture energy and 1100% in the characteristic length of LWFC.

As part of this research programme the mechanical and bond properties of FC have been characterised. It has been shown that the fracture energy of FC can be improved which de Villiers, van Zijl, and van Rooyen (2017) classify as the main cause of poor bond. Bearing this in mind a suitable structural application exploiting the properties of R/LWFC was identified. Figure 4.32 shows a proposed low rise residential unit made of LWFC. This residential unit is envisioned to be erected in the Western Cape Province of South Africa. This area is situated in a seismic zone and experiences low to moderate seismic events. A two panel walling system made of LWFC, representing the wall highlighted in red, was tested in order to demonstrate activation of appropriate energy dissipation mechanisms. An extract of the experimental work, carried out by Dunn (2017) and reported in Dunn, van Zijl, and van Rooyen (2018) under the co-supervision of the author, is reported in this section.

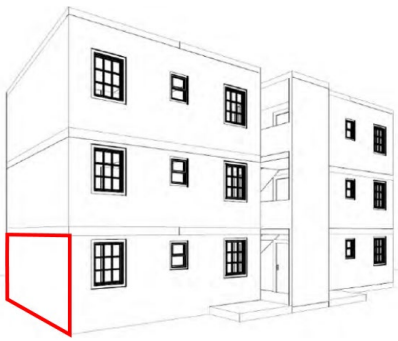

Figure 4.32: Proposed LWFC building (Dunn, van Zijl, and van Rooyen (2018))

4.4.2 Mechanical properties, results and discussion

Mechanical properties

Table 4.9 presents a summary of the results found for the mechanical properties of mix 16FR used for casting walls 1 to 3.

Table 4.9: Mechanical properties of Mix 16FR

Description	*f_{cu} [MPa]	**f_{cu} [MPa]	E_c [GPa]	f_t [MPa]	Gf^a [N/m]	Gf^b [N/m]	l_c^a [mm]	l_c^b [mm]
Mix 16FR	20	24	9.5	1.41	18.21	69.3	87.8	334.5

*cube / **cylinder

Pull-over tests

Figure 4.33a and b show the results of the lateral force versus the overall wall displacement of Wall 1 and Wall 3.

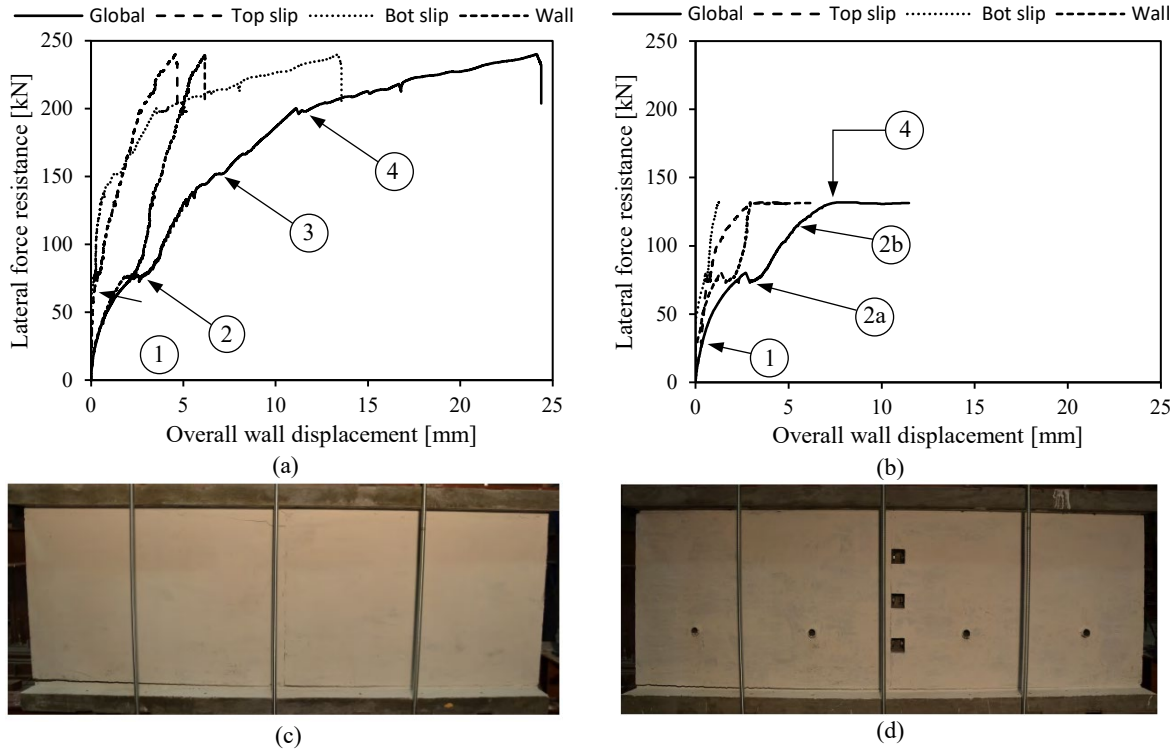

Figure 4.33: Pull-over test (a) Wall 1 six horizontal connections, and, (b) Wall 3 four horizontal connections, and showing (c) individual panel rotation of Wall 1, and (d) two panel rotation as a unit Wall 3 (Dunn, van Zijl, and van Rooyen (2018))

During testing four causes of nonlinear displacement were observed as indicated (1) cracking – along the bottom and top horizontal interfacial connection, (2) initial lifting and rotation of panels, (3) individual panel movement and rotation, and, (4) slip and lifting – along the top and bottom horizontal interfaces. Wall 1 exhibited all four failure mechanisms. However Wall 3 only experienced slight vertical movement by individual panel rotation (mechanism (3)) and instead rotated as a unit. The individual rotation of Wall 1 allows extra local deformation and energy dissipation without causing global failure and can be viewed as a positive design feature. The rotations and deformations of Wall 1 and Wall 3 are shown in Figure 4.33c and d.

The overall displacement of Wall 3 and Wall 1 before the onset of slip failure (mechanism / stage (4)) is 7 mm and 10 mm respectively. The peak resistance of Wall 3 is 132 kN and 240 kN for Wall 1. The reduction in overall displacement and peak lateral force resistance is due to the reduced number of horizontal connections (dowels). Comparing the behaviour of Wall 1 with that of Wall 3 it is observed that Wall 1 allows for more energy dissipation and exhibits more ductile behaviour than Wall 3. The number of horizontal connections as applied here, appears to have a significant influence on the peak resistance, displacement behaviour, and dissipation capacity of the walling system. Wall uplift is seen in Figure 4.33, but full uplift and overturning was prevented in the test setup. Full details are given in Dunn, van Zijl and van Rooyen (2018). The restraining forces to prevent further uplift were recorded during the experiments, and taken into consideration in the evaluation of results. However, these forces do confine the wall between the floor beams, contributing to frictional resistance against pull-over, and contribute to the resistance seen in Figure 4.33a, b.

Quasi-static cyclic test

Figure 4.34a-c show the results obtained from the quasi-static cyclic test performed on Wall 2.

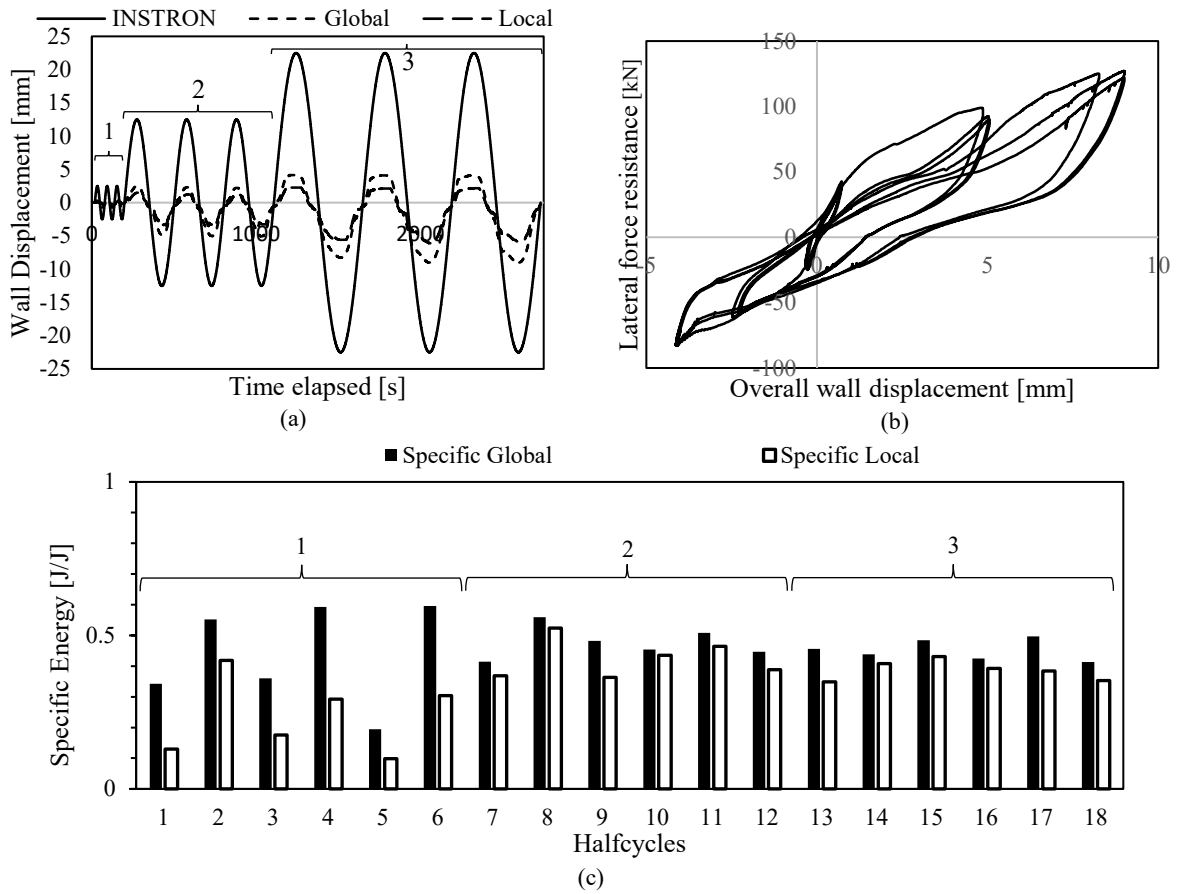

Figure 4.34: Wall 2 results (a) INSTRON, global, and local displacement during testing, (b) hysteresis loop, and, (c) specific energy (Dunn, van Zijl, and van Rooyen (2018))

In Figure 4.34a a significant difference between the INSTRON crosshead displacement, used as control during testing, and global- and local-displacement can be observed. It is acknowledged that the

difference between the INSTRON and the wall response may be caused by flexibility and gaps in the total loading chain. However, reasonable results for the total wall and slip displacements were obtained.

The hysteresis loop for Wall 2 is displayed in Figure 4.34b and the area under each loop for the pull and push cycles "half-cycles" is given in Figure 4.34c and is expressed as the specific energy. In this case the specific energy, J/J, is the energy of each half-cycle normalised by the elastic-plastic half-cycle area – peak cycle force multiplied by the ultimate displacement of the cycle (Negro and Toniolo (2012)). The results of the specific energy for each pull half-cycle is greater than the push half-cycle. This is due to the unforeseen slip during testing. The global- and local- specific energy is fairly constant for each cycle within a group and increases from one group to another. The local specific energy dissipated within the wall is lower than that of the global specific energy dissipated by the wall and the panels. The additional global specific energy dissipated is due to "failure" slip between the wall panels and the NWC simulating the upper storeys. The lower specific energy in the wall panels is due to the shear deformation caused by the cracking of the wall panels. The failure mechanism present in the wall and at the interfaces contribute to the global specific energy.

4.4.3 Design Analytical Model for Peak Lateral Force

There are three mechanisms, namely (1) chemical adhesion and mechanical interlock, (2) friction and (3) dowel action; that contribute to the peak lateral force resistance of a wall. An analytic expression used to determine the shear stress design limit, T_{Rdl}, for an interface intersected by dowels can be found in the fib Model Code (2010) and is represented here as Equation 4.15. This expression can be used to determine the peak lateral resistance force of the LWFC walls.

$$T_{Rdl} = \mu\sigma_n + \kappa_1\rho f_{yd}(\mu\sigma_n \sin\alpha + \cos\alpha) + \kappa_2\rho\sqrt{f_{yd}f_{cd}} \leq \beta_c v f_{cd} \tag{4.15}$$

where κ_1 is the interaction ("effectiveness") factor

κ_2 is the interaction coefficient for flexural resistance ≤ 1.6

σ_n is the lowest compressive stress, resulting from the normal force on the interface.

ρ is the degree of reinforcement across the interface $\rho = A_s / A_c$

f_y is the reinforcement steel yield strength

f_{ck} characteristic value of compressive strength of concrete

f_{yd} design yield strength of reinforcing steel in tension

f_{cd} design value of the cylinder compressive strength of concrete, and

α is the inclination of the reinforcement crossing the interface.

β_c is the coefficient for the strength of the compression strut

$\kappa_1 = (\sigma_n / f_y) \leq 1.0$ and $v = 0.55\ (30 / f_{ck})^{1/3} \leq 0.55$

The input parameters of the walls for the analytical model with the model output for Wall 1 and Wall 3 is given in Table 4.9. The predicted peak lateral resistance force for Wall 2 is 20 % lower than the

experimental value, 202 kN and 240 kN respectively. In contrast, the predicted value of Wall 3 is 6 % higher than the experiment result, 140 kN and 132 kN respectively. The difference between the results of Wall 1 and Wall 3 is attributed to the degree of reinforcement across the two interfaces of the walls $\rho_{Wall\ 1}$ = 0.16 % and $\rho_{Wall\ 3}$ = 0.11 %.

Table 4.10: Model input parameters and predicted values (output)

ν	μ	κ_1	κ_2	f_{ck} MPa	f_{yd} MPa	f_{cd} MPa	α deg.	σ_n MPa	$\rho_{Wall\ 1}$ %	$\rho_{Wall\ 3}$ %	β_c MPa
0.55	0.6	0.5	1.1	20	520	22	90	0.065	0.16	0.11	0.4
Peak Lateral Force [kN]											
			Wall 1	Wall 3							
Experimental result			240	132							
Analytical result			202	140							

Data extracted from Dunn, van Zijl, and van Rooyen (2018)

4.5 Concluding summary

In this chapter the results of the mechanical characterisation tests and of a structural application of LWFC, with design densities in the range of 1200 to 1600 kg/m^3, are presented. The mechanical characterisation tests were conducted to confirm research trends and fill the knowledge gap on key information needed for the design of R/LWFC. The integration of the results from the mechanical characterisation tests performed by de Villiers (2015) and Grafe (2017), and Zvinokona (2017), under co- and direct supervision of the author, confirms the ability of LWFC to achieve strengths sufficient for structural use and the beneficial gain in the long-term compression strength of LWFC made with high volumes of fly ash. The applicability of the model proposed by Kearsley and Wainwright (2001) for long-term compressive strength is confirmed to give results within reasonable accuracy (within 2 MPa) for the materials used in the testing programme.

The gap in knowledge of the bond between reinforcing steel and LWFC, identified in the literature as key design information, is addressed by performing PO and BE tests. The results of PO and BE tests, reported in the completed work of de Villiers (2015) show that LWFC has low design bond stress values compared to NWC and LWAC. An analysis of the normalised mechanical properties of LWFC, performed by the author, revealed a direct relationship between the fracture energy and characteristic length. The relatively low bond stress of LWFC is attributed to its low fracture energy as reported in de Villiers, van Zijl, and van Rooyen (2016). A solution for the increase in fracture energy of LWFC is found by the inclusion of low volume polypropylene fibres. An optimum amount of 0.35% by volume is reported in van Zijl, van Rooyen, Mubatapasango et al. (2017).

For a demonstration of the application of the work done on the mechanical characterisation of LWFC, a structural application in the form of a walling system was envisioned. A proposed two-panel walling system for low-rise residential units subjected to low to moderate seismicity was designed and tested to scale. The testing programme comprised of two monotonic pull-over tests and a quasi-static test and is

also reported on in Dunn, van Zijl, and van Rooyen (2018). The results of the tests demonstrate that the LWFC walling system can be designed to activate sufficient energy dissipation mechanism for seismic resistance.

It should be noted that throughout the research programme the author was responsible for the fundamental, conceptual solutions, as well as the mix design and mix design adaptions thereof. All mix design and adaptions, such as the incorporation of fibres, was either done first by the author or in consultation. Two main conceptual interventions were developed by the author. The first comprises fibre reinforcement to improve fracture energy and thereby bond (de Villiers, van Zijl and van Rooyen 2016). The second also entailed fibre reinforcement, but here to control LWFC cracking when restrained by steel bar reinforcement. The restrained cracking is elaborated in greater detail Chapter 5, as it influenced the durability assessment through accelerated corrosion of steel bar reinforced LWFC (R/LWFC) beams specimens. In Chapter 4 the relevance is that the structural walling test required that the R/SHCC walls were constructed without formation of cracks prior to the actual mechanical test loading despite a significant reinforcement ratio of 0.16% represented by two steel meshes in the 150 mm thick walls. This was indeed successful as reported by Dunn, van Zijl and van Rooyen (2018).

4.6 References

Addis, B. (2009). Fundamentals of concrete. Cement and Concrete Institute. Jack Brilliard Printing Services. Midrand, South Africa.

Brùhwiler, E. and Wittmann, F. (1990). The wedge splitting test, a new method of performing stable fracture mechanics test. Engineering Fracture Mechanics. 35(1). pp. 117-125.

BS EN 1992-1-1. (2004). Eurocode 2: Design of concrete structures – Part 1-1: General rules and rules for buildings. British Standards Institutions. London.

Dae-Jin, K., Min Sook, K., Geun Young, Y., and Young Hak, K. (2014). Bond strength of steel deformed rebars embedded in artificial lightweight aggregate concrete. Journal of Adhesion Science and Technology. 27.5-6. pp. 490-507.

De Villiers, J.P. (2015). Bond behaviour of deformed steel reinforcement in lightweight foamed concrete. Master's thesis, Stellenbosch University. http://hdl.handle.net/10019.1/97835

De Villiers, J.P., van Zijl, G.P.A.G., and van Rooyen, A.S. (2016). Fracture of lightweight foamed concrete in evaluation of bond behaviour of steel reinforcement embedded in lightweight foamed concrete. Proceeding of the 9th International Conference on Fracture Mechanics of Concrete and Concrete Structures (FraMCoS-09). Available at: http://framcos.org/FraMCoS-9/Full-Papers/289.pdf

De Villiers, J.P., van Zijl, G.P.A.G., and van Rooyen, A.S. (2017). Bond of deformed steel reinforcement in lightweight foamed concrete. Structural Concrete, International Journal of fib, June 2017, 18(3). pp. 496-506.

Dunn, T.P.A. (2017). Precast lightweight foamed concrete walling, a structural system for low-rise residential buildings. Master's thesis, Stellenbosch University. http://hdl.handle.net/10019.1/102870

Dunn, T.P.A., van Zijl, G.P.A.G., and van Rooyen, A.S. (2018). Investigating a reinforced lightweight foamed concrete walling system for low-rise residential buildings in moderated seismic regions. Journal of Building Engineering. 20. pp. 663-670.

Grafe, J. (2017). Report issue s0117: Optimization of fibre content in foam concrete for improved fracture energy. Technical report, Institute of Structural Engineering, Stellenbosch University, South Africa.

Jones, M.R. and McCarthy, A. (2005). Preliminary views on the potential of foamed concrete as a structural material. Magazine of Concrete Research. 57(1). pp. 21-32.

Kearsley, E.P. and Wainwright, P.J. (2001a). Porosity and permeability of foamed concrete. Cement and Concrete Research. 31. pp. 805-812.

Kearsley, E.P. and Wainwright, P.J. (2001b). The effect of high fly ash content on the compressive strength of foamed concrete. Cement and Concrete Research. 31(1). pp. 105-112.

Kearsley, E.P. and Wainwright, P.J. (2002). Ash content for optimum strength of foamed concrete. Cement and Concrete Research. 32(2). pp. 241-246.

Leonhardt, F. (1977). Vorlesungen über Massivbau: Teil 3: Grundlagen zum Bewehren im Stahlbetonbau. Vorlesungen über Massivbau. Springer-Verlag GmbH. ISBN: 9783540081219. URL: http://books.google.co.za/books?id=ZEf87H0i9MsC.

Model Code. (2010). Special activity group 5, fib Bulletin, no. 55.

Nambiar, E.K.K. and Ramamurthy, K. (2006). Air void characteristics of foam concrete. Cement and Concrete Research. 37(9). pp. 221-230.

Negro, P. and Toniolo, G. (2012). JRC scientific and policy report: design guidelines for connections of precast structures under seismic actions. Joint Research Centre European Commission, Luxembourg, Publications Office of the European Union.

Park, R. and Paulay, T. (1975). Reinforced Concrete Structures. New Zealand: Wiley-Interscience Publication. ISBN: 0471659177.

Pedziwiatr, J. (2008). Influence of internal cracks on bond in cracked concrete structures. In: Archives of Civil and Mechanical Engineering VIII.3

SAISC. (2016). South African Steel Construction Handbook. 8th Edition. Institute of Steel Construction. South Africa.

SANS. (2000). SANS 0100-1:2000 - The structural use of concrete – Part: Design. The South African Bureau of Standards, Pretoria.

SANS. (2011a). SANS 10160-1:2011 – Basis of structural design and actions for buildings and industrial structures – Part 1: Basis of structural design. The South African Bureau of Standards, Pretoria.

SANS. (2011b). SANS 10160-2:2011 – Basis of structural design and actions for buildings and industrial structures – Part 2: Self-weight and imposed loads. The South African Bureau of Standards, Pretoria.

SANS (2017). SANS 10160-4:2017. Basis of Structural Design and Actions for Building and Industrial Structures – Part 4: Seismic Actions and General Requirements for Buildings, South African Bureau of Standards, Pretoria.

Sika. (2016). SikaGrout® 212 High Strength shrinkage compensating cementitious grout. Available at: http://zaf.sika.com/dms/getdocument.get/aca6b2d7-b061-352c-8e7a-c4a10d2cddc7/SikaGrout%20-212.pdf

Ulula Ash (PTY) Ltd. (2016). Ulula ash Kriel Power Station: Test certificate for class S fly-ash. Available at: http://www.ululaflyash.com/documents/Test%20CertificateTypical%2050450%20ClassS.pdf

Van Zijl, G.P.A.G., van Rooyen, A. S., Mubatapasango, M.M., Dunn, T.P.A., and Grafe, J. (2017). Durability and bond of reinforced lightweight foamed concrete. High Technology Concrete: Where Technology and Engineering Meet, Springer, pp. 2185-2193.

Wittmann, F.H. (2002). Crack formation and fracture energy of normal and high strength concrete. Sad Hana. 27(4). 413-423.

Zuo, J. and Darwin, D. (2000). Splice strength of conventional and high relative rib area bars in normal and high strength concrete. ACI Structural Journal. 97(4).

Zvinokona, A.R. (2018). Chloride induced corrosion of integral and non-integral surface treated lightweight foamed concrete. Master's thesis, Stellenbosch University. http://hdl.handle.net/10019.1/103360

Chapter 5 – **Durability results and discussion**

This chapter presents the results of the durability test performed on LWFC. For durability associated with carbonation LWFC specimens were exposed to an accelerated carbonation environment (0.13% CO_2 concentration) for a duration of 13 weeks. The evolution of the carbonation front was monitored on freshly cut cube specimens sprayed with phenolphthalein indicator. For corrosion assessment the half-cell potential test was performed on singly reinforced rectangular prisms. The enhancement of the durability properties of LWFC specimens was explored using two types of surface treatments. Chloride-induced corrosion was promoted on R/LWFC by cyclic ponding test. The penetration of chlorides was tested on freshly cut beams and corrosion rate assessment was done using the Coulostatic, Potentiostat and Galvanostatic method.

5.1. Introduction

Concrete throughout its lifetime will experience multiple degradation processes. These processes may be the result of mechanical influences, short- and long-term deformations, or the interaction with the external environment. For RCS one of the main degradation processes that designers try to delay or avoid is corrosion due to carbonation and chloride penetration. These processes tend to shorten the lifespan of the concrete and is expensive to fix or repair once the processes have advanced. The outcome of both processes is the corrosion of steel which eventually compromises the structural integrity of any RCS. In this section, the results of accelerated carbonation testing and accelerated chloride penetration, obtained through direct supervision and experimentation by the author, are presented and discussed, and can be found in Mubatapasango, van Zijl and van Rooyen (2017), Mubatapasango (2017), van Zijl, van Rooyen, Mubatapasango et al. (2018), van Rooyen and van Zijl (2017), Zvinokona (2018) and Zvinokona, van Rooyen, and van Zijl (2017). Figure 5.1 shows the flow (black arrows) of the chapter with the central durability theme connect connected by black lines.

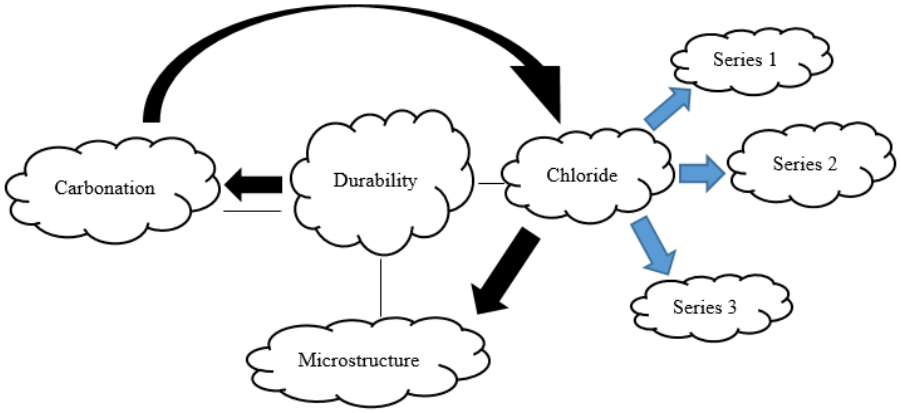

Figure 5.1: Chapter layout

5.2. Carbonation in R/LWFC

5.2.1 Dip test – STA penetration in LWFC specimens

Table 5.1 contains the results of the dip test conducted on specimens coated with Sikagard®706-Thixo. Eight measurements, two on each side of the cube specimens, were taken on three specimens and a summary of the results are presented in Table 5.1.

Table 5.1: Result of the dip test (penetration depth Sikagard®706-Thixo)

Description	Sample 1	Sample 2	Sample 3
Mean (mm)	4.53	4.42	4.48
Median (mm)	4.53	4.40	4.49
Minimum (mm)	4.31	4.14	4.35
Maximum (mm)	4.74	4.90	4.69
COV (%)	3.42	5.49	2.50

Data extracted from Mubatapasango (2017)

The overall mean penetration depth of Sikagard®706-Thixo in LWFC is 4.48 mm. It should be noted that Sikagard®706-Thixo is listed by the manufacturer as a class 2 pore-liner (BS EN 1504-2 (2004)). For this classification an average penetration depth in excess of 10 mm is expected. Granted, the test on which the penetration results are based on is a standard NWC mix with a water / cement ratio of 0.7. The LWFC used in this investigation has an equivalent effective water / cement ratio of 0.7. However, the mechanism which drives the penetration of (solids) fluids in LWFC differs from that of NWC. It is believed that the lowered sorptivity of LWFC lead to a decrease in the penetration depth of surface treatment agent. This idea is based on the work done by Nambiar and Ramamurthy (2008) on the sorption characteristics of foamed concrete. Nambiar and Ramamurthy found a decrease in sorptivity with an increase in foam content (decrease in density).

5.2.2 Computed Tomography (CT) scanning – Microstructural

In this part of the research programme the influence of STAs on the microstructure of FC was investigated using CT scans of two 30 mm cube samples. The samples were made from mixes 14R and 14I, respectively. The omission of a sample from mix 14N is firstly due to the fact that the mix does not differ from that of 14R, effectively 14R and 14N are the same in regions away from the surface treatment influence. Secondly, the carbonation front had not sufficiently penetrated the cubes, 100 mm cubes used to prepare the 30 mm cubes, to influence the microstructure. The two samples were scanned for one hour each with the tube voltage set at 120 kV and tube current of 100 µA. The tube setting and sample size resulted in a resolution of 100 µm. Figure 5.2a,b shows high resolution cross-sectional images of the CT samples with the air voids present as represented by the processing software VGStudio Max 2.2.

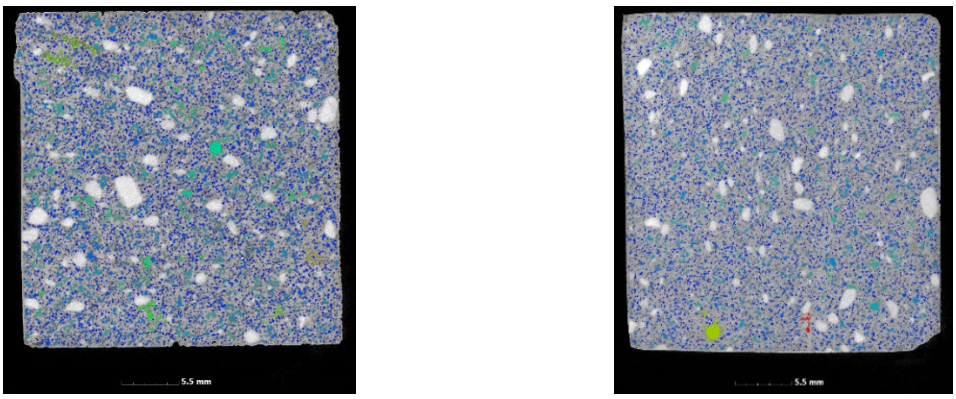

(a) (b)

Figure 5.2: Cross-section of the CT scanning specimens showing the air-void distribution in mix (a) 14R/N, and, (b) 14I as represented by processing software VGStudio Max 2.2 (Foam Structure Analysis)

5.2.2.1 Porosity of FC and influence of STA

Table 5.2 is a tabulation of the material volume, air volume and porosity of mix 14R/N and 14I. The material- and air volumes were determined through CT scans and indicate that the air volume present in mix 14R/N is higher than that of 14I for the range of interconnected pore diameter size considered. The porosity based on the results of the CT scans show that mix 14R/N has a higher porosity than 14I, 19.14 and 14.82 % respectively. Also, a large discrepancy is found between the results of the porosity based on the results of the CT scans and that based on mix volume proportions. For clarity it should be noted that the calculated porosity of FC based on the mix volume proportion (ratio of foam- and mix volume) of FC is expected to be lower than the total porosity which includes the porosity of the paste. It should be noted that the total porosity cannot be determined by x-ray CT due to the limited resolution. For instance, capillary pores are not detected. The value in the CT results presented here, lies in the comparison of void size distribution in the microstructure through inclusion scale (micrometer to millimetre). Based on the results of Kearsley and Wainwright (2001) and Hilal et al. (2015) the total porosity of mixes 14R, 14N and 14I is expected to be in the range of 40 and 50%.

Table 5.2: Porosity of FC calculated using CT results and mix composition

Description	Volume [mm^3]	Air [mm^3]	Porosity* [%]	Porosity** [%]
14R/N	26860	5142	19.14	24.53
14I	27720	4110	14.82	24.28

*Calculated on CT scan results / **Calculated using the mix composition
Data extracted from Mubatapasango (2017)

5.2.2.2 Pore size distribution and air void size parameters

Figure 5.3 shows the pore diameter size distribution and the cumulative oversize graph as a function of pore size for mixes 14R/N and 14I, respectively. The air void parameters, D_{50} and D_{10}, for mixes 14R/N and 14I are tabulated in Table 5.3.

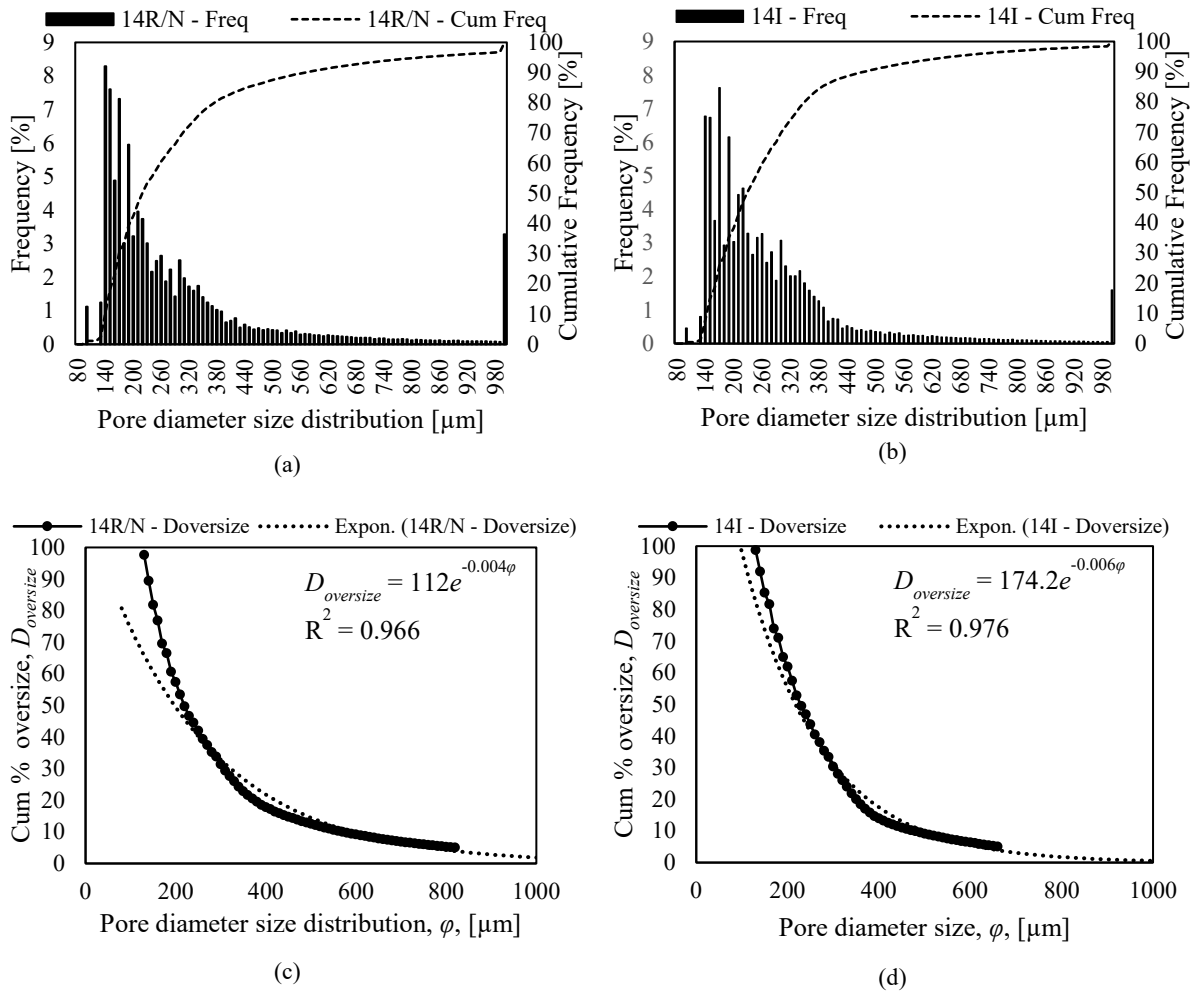

Figure 5.3: Pore diameter size distribution (a) 14R/N and (b) 14I and Cumulative % oversize (c) 14R/N and (d) 14I (data used from Mubatapasango (2017))

Table 5.3: Air void parameters for mixes 14R/N and 14I

Description	D_{10} [µm]	D_{50} [µm]	φ_{ave} [µm]
14R/N	604	201.6	311.45
14I	476.3	208	287.02

Foam Structure Analysis

The results in Table 5.3 show that the use of STAs causes a decrease in in the D_{10} air void parameter, only a slight increase is observed for the D_{50} air void parameter and a decrease in the average pore diameter.

5.2.3 Carbonation depth (Evolution of the carbonation front)

The results of the carbonation depth obtained from the phenolphthalein test as described in Chapter 3 tracked over the duration of the investigation is shown in Figure 5.4a,b and tabulated in Table 5.4. The results indicate small penetration depths for all samples, 14R, 14N, and, 14I, for the first two weeks. This is due to the fact that high levels of relative humidity were present in the climate chamber during

the first two weeks of carbonation. After two weeks the relative humidity was controlled at 65±5% in the climate chamber and samples began to carbonate at a higher rate. As discussed in Chapter 2.3 there is a relationship between relative humidity and CO_2 diffusion coefficient. The carbonation coefficients obtained from the regression shown in Figure 5.4b is given in Table 5.4.

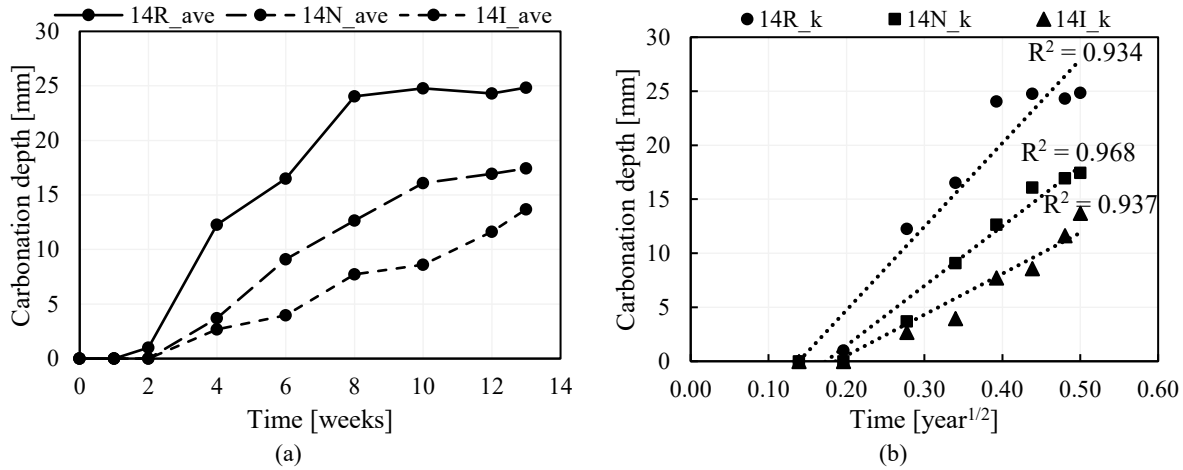

Figure 5.4: Carbonation penetration depth as a function of time weeks and after 0.13% CO_2 concentration exposure at RH 65% (produced from data extracted from Mubatapasango (2017))

Table 5.4: Average carbonation penetration results in mm and variation

Description									
Time[weeks]	**0**	**1**	**2**	**4**	**6**	**8**	**10**	**12**	**13**
Carbonation penetration depth [mm]									
Average									
14R	0	0	1	12.27	16.51	24.06	24.77	24.32	24.84
14N	0	0	0	3.70	9.09	12.65	16.09	16.95	17.43
14I	0	0	0	2.68	3.96	7.72	8.60	11.62	13.70
CoV (%)									
14R				21.6	13.4	16.5	12.9	10.5	11.8
14N				38.6	19.5	21.5	9.70	9.40	10.1
14I				36.5	19.0	23.8	19.7	16.1	12.2

Data compiled from Mubatapasango (2017)

Table 5.5: Carbonation coefficient, k, of the various beam sets in Series 1

Description	**k [mm/year$^{1/2}$]**	**R^2**
14R	77.3	0.934
14N	55.2	0.968
14I	37.9	0.937

*regression analysis excluded the reading of week 0 in Table 5.4

The results of the phenolphthalein test in Table 5.4 show high variability in the results of week 4 with CoV values of 21.6, 38.6 and 36.5% for the 14R, 14N and 14I sets. The rate of carbonation penetration of the specimens in increasing order is the integral surface treated specimens (14I), non-integral surface treated specimens (14N), and the reference specimens (14R). At the end of the experiment the reference specimens had achieved the highest carbonation depth of 24.84 mm. The non-integral and integral specimens achieved a carbonation penetration depth of 17.43 and 13.70 mm. The results of the

carbonation penetration depth over time and carbonation coefficients indicate that surface treatment can be used to retard the rate of carbonation in LWFC.

5.2.4 Corrosion potential of singly reinforced LWFC prism specimens

The corrosion potential measurements done on Y12 singly reinforced specimens from mixes 14R, 14N, and 14I using the HCP method as described in Chapter 3.4 are tabulated in Table 5.6. Figure 5.5 displays the average HCP values for each mix.

Table 5.6: Corrosion Potentials (HCP method) of 14R, 14N and 14I

Description								
Time [weeks]	1	2	4	6	8	10	12	13
HCP (mV)								
Average								
14R	-354	-428	-365	-326	-255	-209	-143	-139
14N	-400	-463	-417	-372	-360	-207	-130	-130
14I	-478	-525	-508	-472	-292	-227	-106	-108
CoV (%)								
14R	1.19	4.12	6.98	5.03	12.5	11.6	9.16	9.88
14N	7.97	3.56	9.61	13.7	8.18	23.5	35.7	32.8
14I	8.55	2.06	3.25	4.77	18.2	15.1	36.8	26.7

Compiled from data extracted from Mubatapasango (2018)

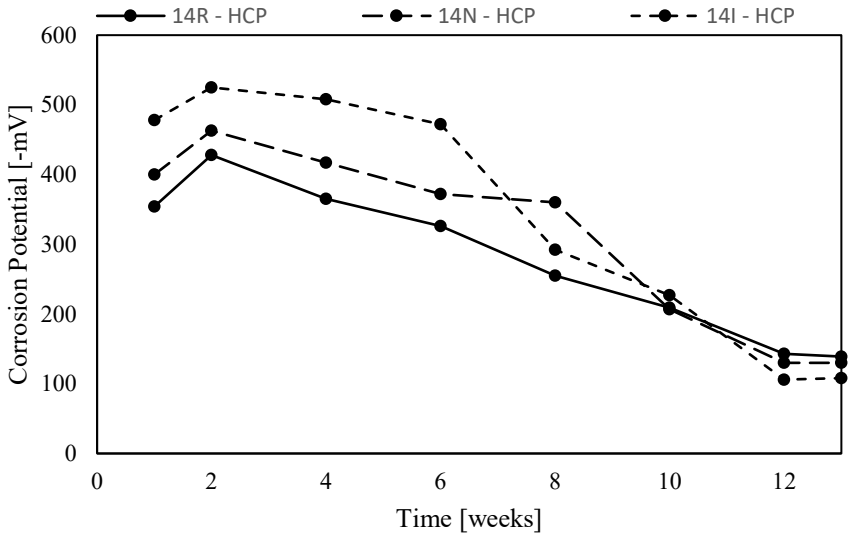

Figure 5.5: Corrosion Potential, HCP method, of reinforced 14R, 14N and 14I LWFC specimens (produced from data extracted from Mubatapasango (2017))

HCP values for the 14R set show good correlations with high CoVs only recorded in week 8 and 10, 12.5 and 11.6%, respectively. Mix 14N and 14I show more variability in the results with readings recording CoVs well over 15%. Mix 14N and 14I have a maximum CoV of 35.7 and 36.8%, respectively. The values of the HCP should be explained in conjunction with the observations made during the experiments. For the first two weeks high relative humidity values were recorded in the climate chamber which cause high negative values to be obtained for the HCP with a peak experienced in week 2. According to Table 2.10 in Section 2.3.4.4.1 severe corrosion is expected to take place. However, the high level of humidity leads to low concentrations of oxygen at the rebar which resulted

in such extremely negative values. After week two the HCP values increases and becomes less negative as the experiment progresses. The values of the HCP at week 12 and 13 are close to each other and indicate that the HCP readings have started to stabilise. Interpreting the results of week 12 and 13 using Table 2.10 in Chapter 2 a low risk of corrosion, less than 10%, is expected. This is in line with the results of the carbonation penetration which indicate that the carbonation front has not yet reached the level of the reinforcement and therefore no corrosion should be taking place. It is acknowledged that longer exposure periods are required to investigate where the carbonation front reaches the steel and corrosion potential increases. No corrosion occurred in the reinforcement bars after 13 weeks of exposure, as confirmed by removal of bars from these specimens and visual inspection.

5.3 Chloride penetration in LWFC

5.3.1 Overview of durability (chloride) testing series

In this research programme, the durability of R/LWFC against chloride ingress and chloride-induced corrosion was investigated in three series. In all three series, the penetration of chloride was promoted using cyclic ponding tests consisting of a wet and a dry cycle. In the wet cycle the specimens were exposed to a 0.3 M NaCl solution and in the dry cycle the specimens were left to dry. In all three specimens corrosion assessment was performed using an LRP method.

Series 1 consists of three ponding cycles with a 7 day wet and 14 day dry period. Custom made laboratory equipment, a pulse generator and a half-cell built and first used by Paul (2015) at Stellenbosch University, was used to implement the coulostatic method. Due to the sensitivity of the equipment and labour intensity, only a single reading was recorded on each specimen. At the end of ponding cycle 3 XRF tests for chloride were conducted on powdered samples collected from the beam specimens. Series 2 consists of three ponding cycles with a 7 day wet and 21 day dry period. For corrosion assessment commercially available equipment known as GECOR-10 implementing the Potentiostat method. Using this technique corrosion profiles were obtained in beam specimens at the end of cycle 2 and cycle 3.Series 3 consists of 10 ponding cycles with a 3 day wet and 11 day dry period. Corrosion assessment was done using the GECOR-10 implementing the Galvanostatic method and two readings were taken during each ponding cycle. The difference in the ponding cycles for each series is to allow sufficient drying for oxygen penetration at the cathodic regions through FC cover, longer drying periods to investigate whether more aggressive corrosion would occur, as it is well known that reaching equilibrium in the climate chambers may take several days or weeks.

In this chapter an overview of Series 1 reported in van Rooyen and van Zijl (2017), Series 2 obtained through direct supervision and reported in Zvinokona (2018) and Series 3, designed and performed by the author, is given.

5.3.2 Computed Tomography (CT) scanning – Microstructural investigation

In this part of the research programme, the influence of density, STAs and fly ash on the microstructure of FC was investigated using CT scans of eight cored cylindrical samples. The samples were cored from

specimens prepared for chloride penetration and corrosion testing, similar to those described in Section 5.2.3 on specimens for carbonation. The influence of density and STAs on the microstructure of FC was evaluated using three samples with different densities obtained from Series 3 namely S3-12R, S3-14R and S3-16R. The influence of STAs were evaluated on samples with different surface treatment from Series 3, S3-14R and S3-14I. The influence of fly ash on the microstructure of FC was evaluated on samples with different ash cement ratios from Series 2, namely, S2-16R, S2-16R_A1 and S2-16R_A2. Each of the samples used in this investigation were scanned for one hour with the tube voltage set at 140 kV and tube current of 130 µA. The tube setting and sample size resulted in a resolution of 10 µm. Table 5.7 shows a summary of the samples used in the investigation. Figure 5.6 shows cross-sectional images of the CT samples, from the porosity / inclusion (PIA) and foam structure analysis (FSA), as represented by the processing software VGStudio Max 3.3.

Table 5.7: CT samples use to investigate the microstructure of FC

Description			
Density	S3-12R	S3-14R	S3-16R
STAs	S3-14I	S3-14R	
Fly ash	S2-16R	S2-16R_A1	S2-16R_A2

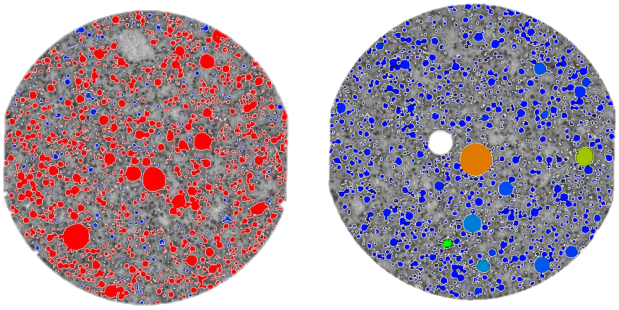

Figure 5.6: Cross-sectional image of specimen S12-R (a) PIA (interconnected pores) and (b) FSA (individual pores) represented by processing software VGStudio Max 3.3.

5.3.2.1 Porosity of FC and influence of density, STAs, and fly ash

Table 5.8 is a summary of the parameters obtained from the CT scans and the porosity of FC specimens.

Table 5.8: Summary of the volume, air and porosity of FC

Description	**Volume [mm^3]**	**Air [mm^3]**	**Porosity***	**Porosity****
Density				
S3-12R	422	176	29.4	40.8
S3-14R	482	118	19.7	30.4
S3-16R	515	85	14.2	19.9
STA				
S3-14R	482	118	19.7	30.4
S3-14I	461	142	23.5	29.1
S3-14N	482	116	19.4	30.4
Fly-ash				
S2-16R	530	73	12.1	16.7
S2-16R_A1	524	79	13.2	13.9
S2-16R_A2	504	100	16.6	12.7

*Calculated on CT scan results / **Calculated using the mix composition

The results of S3-12R, S3-14R and S3-16R in Table 5.8 can be used to evaluate the influence of density on the porosity of FC. The results confirm that there is an increase in porosity with a decrease in density. Similarly, an evaluation of the results of S2-16R, S2-16R_A1 and S2-16R_A2 shows that there is an increase in porosity with the addition of fly ash. Examining the results of S3-14R and S3-14I shows that there is an increase in the porosity with the use the integral surface treatment. From the results for S3-14R and S3-14N it is clear that the pore characteristics are unaltered in the case of non-integral treatment. Note that the S3-14N core was taken deeper into the specimen, where no influence of surface applied STA is present.

5.3.2.2 Pore size distribution and air void size parameters

Table 5.9 is a summary of the air void parameters obtained through CT scans. The equations listed as $D_{oversize}$ in Table 5.9 were obtained from using the cumulative oversize distribution for each mix and can be found in Appendix A1-2.

Table 5.9: Air void parameters obtained from CT scanning – Porosity / Inclusion and foam structure analysis

Description	D_{10} [µm]	D_{50} [µm]	φ_{ave} [µm]	$D_{oversize}$ [µm]	R^2
Porosity / Intrusion Analysis (PIA)*					
Density					
S3-12R	178	77.4	98.9	$172.6e^{-0.016\varphi}$	0.981
S3-14R	243.8	82.9	132	$114.6e^{-0.01\varphi}$	0.970
S3-16R	374.5	106.3	171.5	$94.6e^{-0.006\varphi}$	0.970
STA					
S3-14R	243.8	82.9	132	$114.6e^{-0.01\varphi}$	0.970
S3-14I	215.7	81.6	113.2	$133.1e^{-0.012\varphi}$	0.976
S3-14N	209.4	75.3	116.3	$123.4e^{-0.012\varphi}$	0.970
Fly ash					
S2-16R	349.3	119.4	186.1	$115.3e^{-0.007\varphi}$	0.989
S2-16R_A1	336	106.1	162.9	$105.1e^{-0.007\varphi}$	0.974
S2-16R_A2	314.5	84.6	155.7	$90.4e^{-0.007\varphi}$	0.979
Foam Structure Analysis (FSA)**					
Density					
S3-12R	197.4	96.9	116.8	$235.5e^{-0.016\varphi}$	0.979
S3-14R	166.1	85.6	104.0	$277e^{-0.02\varphi}$	0.971
S3-16R	187.6	92.9	113.0	$242.6e^{-0.017\varphi}$	0.971
STA					
S3-14R	166.1	85.6	104.0	$277e^{-0.02\varphi}$	0.971
S3-14I	180.1	90.6	110.9	$255.6e^{-0.018\varphi}$	0.978
S3-14N	151.0	81.1	94.0	$322.3\ e^{-0.023\varphi}$	0.976
Fly ash					
S2-16R	256.4	110.1	135.4	$167.8e^{-0.011\varphi}$	0.996
S2-16R_A1	248.6	102.3	128.7	$154.1e^{-0.011\varphi}$	0.998
S2-16R_A2	187.98	87.4	109.0	$202.4e^{-0.016\varphi}$	0.996

Porosity / Intrusion Analysis (PIA) shows the interconnected pores and is thus an indication of interconnectivity*
Foam Structure Analysis shows individual pores and therefore does not show interconnectivity**

The results of S3-12R, S3-14R and S3-16R in Table 5.9 indicate that there is an increase in the air void parameters obtained from the PI analysis with an increase in density. No trend regarding density is found for the FSA. For fly ash addition, the results of S2-16R, S2-16R_A1 and S2-16R_A2 show that there is a decrease in all air void parameters in the PIA results. Similarly, this decrease is seen in the results of

the FSA. The use of an integral surface treatment also shows a decrease for the air void parameters in the PIA and FSA, similar to the results in Table 5.3. The decrease in interconnectivity of integral surface treatment therefore explains lower depth of carbonation observed in these specimens compared to the reference specimens. See Appendix A1-2 for the air void distribution and $D_{oversize}$ graphs for CT samples.

5.3.3 Chloride penetration in LWFC – Series 1

Cracks in RC are not uncommon. In fact, one of the reason for reinforcement is to aid in controlling cracks widths to fine widths. Here the cracks were caused by drying shrinkage restrained by the reinforcement. As discussed in Section 2.3.2, the approach for predicting the service life of RCS has been to take the time to corrosion initiation as the lifespan of the concrete. This conservative approach in used because there is little information available on corrosion rates or corrosion rate models for predicting the propagation phase for RCS service life modelling. The influence of cracks and crack spacing on corrosion rates has only recently been investigated (Bezuidenhoud (2017), Paul (2015), Otieno (2014)). In the following sections, the cracks in the RC beams used for testing corrosion rates are characterised in terms of orientation, width, and spacing.

5.3.3.1 Crack characterisation – Series 1

Table 5.10 gives the crack distribution for the beam sets used in Series 1. The 16R set contains crack widths of 0.05 mm only. The integral surface treated beam set 16N does not contain cracks of 0.15 mm widths and has 14 cracks. The crack distribution in the 16I group is almost uniform with eight cracks.

Table 5.10: Total number of cracks per beam set for Series 1

Description	Crack width [mm]			
	0.05	0.1	0.15	0.2
$16R_{tot}$	11			
$16N_{tot}$	7	6		1
$16I_{tot}$	2	3	2	1

Extracted from van Rooyen and van Zijl (2017)

5.3.3.2 Chloride-induced corrosion (Coulostatic method)

The results of the average corrosion rate obtained for beam set 16R, 16N and 16I in Series 1 using the coulostatic method is presented in Figure 5.7 and tabulated in Table 5.11. All readings were taken before the start of a new ponding cycle. The reading of week 0 corresponds to a baseline reading before ponding commenced.

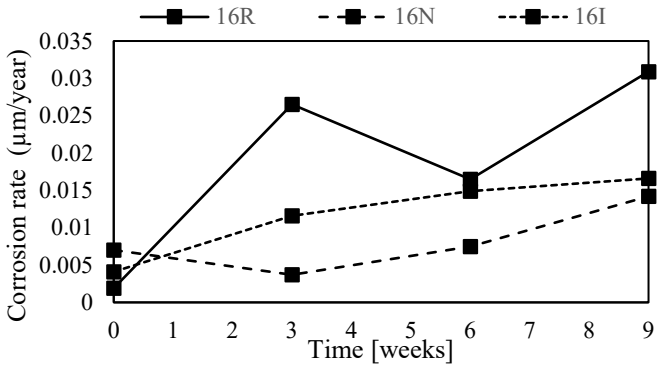

Figure 5.7: Average corrosion rate for Series 1 - Coulostatic method (reproduced from van Rooyen and van Zijl (2017))

Table 5.11: Average corrosion rate in Series 1 - Coulostatic method

Description	Time [weeks]			
	0	3	6	9
Corrosion rate (µm/year) – Coulostatic method				
$16R_{ave}$	0.0019	0.0255	0.0165	0.0309
$16N_{ave}$	0.0070	0.0037	0.0075	0.0142
$16I_{ave}$	0.0041	0.0116	0.0149	0.0166

Data extracted from van Rooyen and van Zijl (2017)

The results in Figure 5.7 show that prior to ponding, the 16R beam set had the lowest corrosion rate and thereafter consistently had the highest corrosion rate. Beam set 16I had the second lowest initial corrosion rate and maintained this pattern for the duration of testing. The highest initial corrosion rate was achieved by the 16N group set and subsequently achieved the lowest corrosion rates out the entire group sets thereafter.

5.3.3.3 Chloride profiling – XRF

After three ponding cycles chloride profiling was done on one specimen from each beam set (16R, 16N, 16I). As detailed in Chapter 3 powder was collected at 5 mm depths (up to a depth of 40 mm) in the uncracked- (NC) and cracked (C) region of the ponding surface. XRF testing was conducted at the Central Analytical Facilities (CAF) at Stellenbosch University. The XRF and crack distribution per beam set of the specimens used are shown in Figure 5.8a-b. A tabulated form of the XRF results is given in Table 5.12.

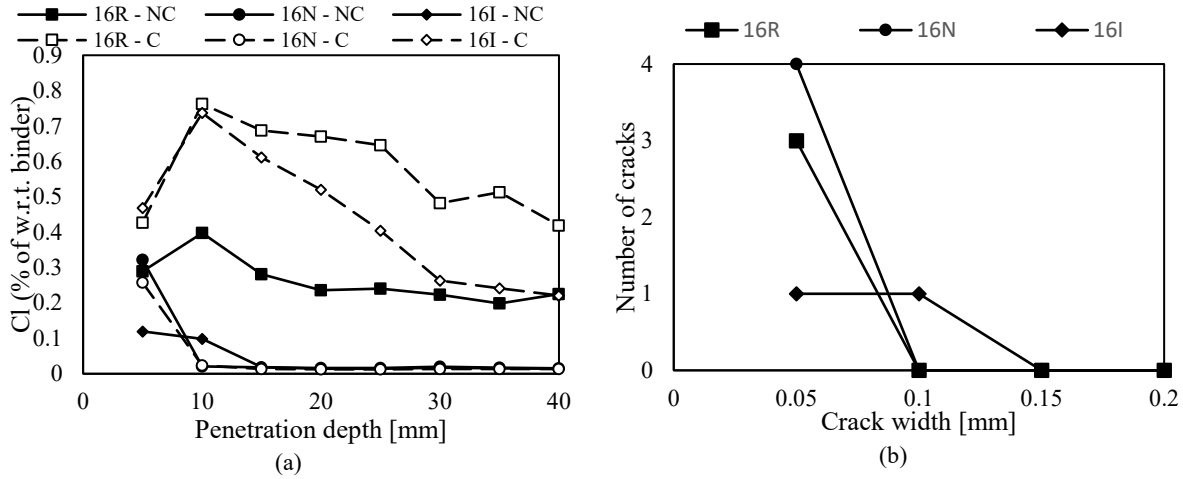

Figure 5.8: Series 1 (a) chloride content profile of beam specimens after 3 ponding cycles (NC – no crack, C – crack), and, (b) crack distribution of XRF tested specimens (reproduced from van Rooyen and van Zijl (2017))

Table 5.12: Chloride content profile of Series 1 (uncracked and cracked regions)

Description	Profile depth [mm]							
	5	10	15	20	25	30	35	40
XRF – Chloride profiling – uncracked region (Cl % of w.r.t. binder)								
16R	0.2890	0.3980	0.2820	0.236	0.2410	0.2240	0.1986	0.2260
16N	0.3220	0.0206	0.0176	0.0162	0.0160	0.0202	0.017	0.0154
16I	0.1196	0.0989	0.019	0.0141	0.0141	0.017	0.0154	0.0141
XRF – Chloride profiling – cracked region (Cl % of w.r.t. binder)								
16R	0.427	0.7630	0.6880	0.6700	0.6460	0.4830	0.5130	0.4190
16N	0.2570	0.0236	0.0139	0.0127	0.0124	0.0136	0.0135	0.0133
16I	0.4680	0.7370	0.6120	0.5210	0.4040	0.2630	0.2410	0.2210

Data compiled from van Rooyen and van Zijl (2017)

The results in Figure 5.8a show that there is a high concentration of chlorides close to the surface in all specimens. For the 16R-NC and 16R-C beam specimens the high concentration of chlorides is at the 10 mm depth, 0.398 and 0.763 % w.r.t. binder. The concentration of chlorides at the reinforcement level, 24 mm, for the 16R-NC group is higher than the threshold chloride content (0.3% w.r.t. binder). For the integral surface treatment, a large difference is found in the chloride profile for the cracked and uncracked regions, 16I-C and 16I-NC. The maximum concentration of chlorides for 16I-NC is at 10 mm and the concentration at the reinforcement level is over the chloride threshold. For the uncracked regions, 16I-NC negligible concentrations of chlorides is found at depths in excess of 15mm. For the non-integral surface treatment, the highest concentration of chlorides in the uncracked- and cracked region (16N-NC and 16N-C) is found close to the surface at a 5mm depth. Insignificant amounts of chloride concentrations is found at depths exceeding 5 mm in the 16I-NC and 16I-C.

5.3.4 Chloride penetration in LWFC – Series 2

The chloride penetration of Series 2 LWFC specimens was determined at the end of cycle 1, 2 and 3. Figure 5.9 shows the pictures of the specimens used in cycle 2 after application of the 0.1 M concentration of silver nitrate and Table 5.13 lists the test results after cycle 1, 2, and, 3 of cyclic wetting and drying periods by ponding of aqueous solution.

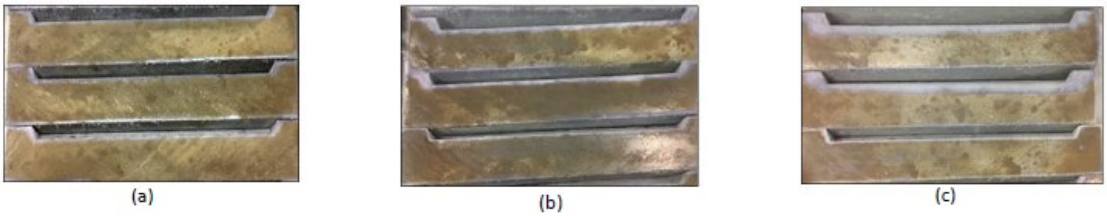

Figure 5.9: Photographs of the specimens after testing used in cycle 2 (a) a/c = 0, (b) a/c = 1, and, (c) a/c = 2. From top to bottom 16R, 16I, and, 16N.

Table 5.13: Chloride penetration depth in mm at the end of cycle 1, 2, and 3.

Description	**16R**			**16I**			**16N**		
a / c	0	1	2	0	1	2	0	1	2
Ponding cycle									
#1 [28d]	7	9	22	5	8	13	3	3	5
#2 [56d]	10	11	27	8	10	15	5	5	5
#3 [90d]	11	12	34	9	12	19	5	5	6

Data compiled from Zvinokona (2018)

From the data presented in Figure 5.9 and Table 5.13 it can be seen that there is an increase in chloride penetration depth with an increase in fly-ash to cement ratio. Also evident in the data from Table 5.13 is that there is an increase in chloride penetration with time and that the addition of surface treatment, both non-integral and integral, leads to a decrease in chloride penetration. The non-integral surface treatment agent is more effective than the integral STA. This is due to the difference in the method of action and the concentration of the STA. The integral STA's primary mechanism is the blocking of capillary pores by reacting with CaOH to produce insoluble products thereby causing blockages. This process is distributed throughout the concrete and may be somewhat less effective than the non-integral

STA that is concentrated at the surface of the concrete. Evidence of the pore size reduction is can be found in Table 5.9. The non-integral surface treatment agent is a silane product. These silane based products react with the surface of the concrete to make it hydrophobic. The hydrophobic nature of the surface treated layer prevents the penetration of fluids thereby preventing aggressive substances from penetrating into the concrete matrix.

5.3.5 Chloride-induced corrosion (Potentiostat measurements) – Series 2

5.3.5.1 Crack Characterisation – Series 2

Figure 5.10 shows the typical distribution of cracks in the reinforced concrete prisms used in this investigation. As discussed in Section 2.3 the causes of crack formation may be mechanical, thermal, hygral or chemical related. Normally a type of loading is associated with the formation of certain cracks. In this investigation, two types of cracks are present (1) drying shrinkage cracks due to restraint of drying shrinkage by a single bar reinforcement, and (2) plastic settlement cracks over the same reinforcing bar. The cracks that form in the transverse direction are caused by restrained drying shrinkage and the cracks that form in the longitudinal direction are caused by plastic settlement. Table 5.14 lists the orientation of the crack and its properties for the reinforced beam specimens with fly ash cement = 0.

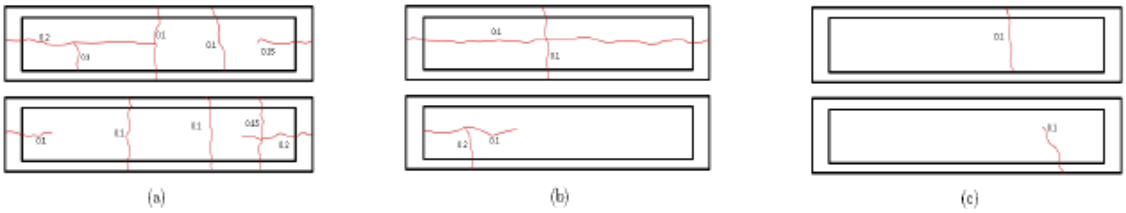

Figure 5.10: Typical crack distribution (a) a / c = 0, (b) a / c = 1, and, (c) a / c = 2 (Zvinokona, van Zijl, van Rooyen(2017))

Table 5.14: Crack distribution of reinforced prism specimens made with a / c = 0 and cover depth 35 mm

Description	Specimen	Transverse crack width [location(s)]*	Longitudinal crack size
a / c = 0 cover 35 mm			
16R	1 2 3	0.2 mm [19.6 cm] 0.2 mm [18 cm] 0.2 mm [20 cm]	0.1 mm^{RE}
16N	1 2 3	0.1 mm [15cm / 22 cm] 0.2 mm [15cm] / 0.1 mm [25 cm] 0.1 mm [14 cm / 30 cm] / 0.2 mm [22 cm]	
16I	1 2 3	0.2 mm [19.5 cm] 0.2 mm [22 cm] 0.2 mm [15cm] / 0.1 mm [25 cm]	

*All locations of transverse cracks measured from the left end of the beam specimens
RE – Right End
LE – Left End
Extracted from Zvinokona (2018)

More details on crack distribution for Series 2 are provided in Appendix B. The cracks found in the beam specimens of Series 2 range in size, width and length. No discernible trend in terms of location and crack width is found. However, it is noted that the frequency and crack widths decrease with an increase in fly ash content. Specimens made with higher ash cement ratio were less prone to cracking and have fewer cracks.

5.3.5.2 Chloride-induced corrosion rate profile (Potentiostat measurements) – Series 2

Figure 5.11a-f show the results of the corrosion profiles at week 12 for mix 16R, 16N, and, 16I.

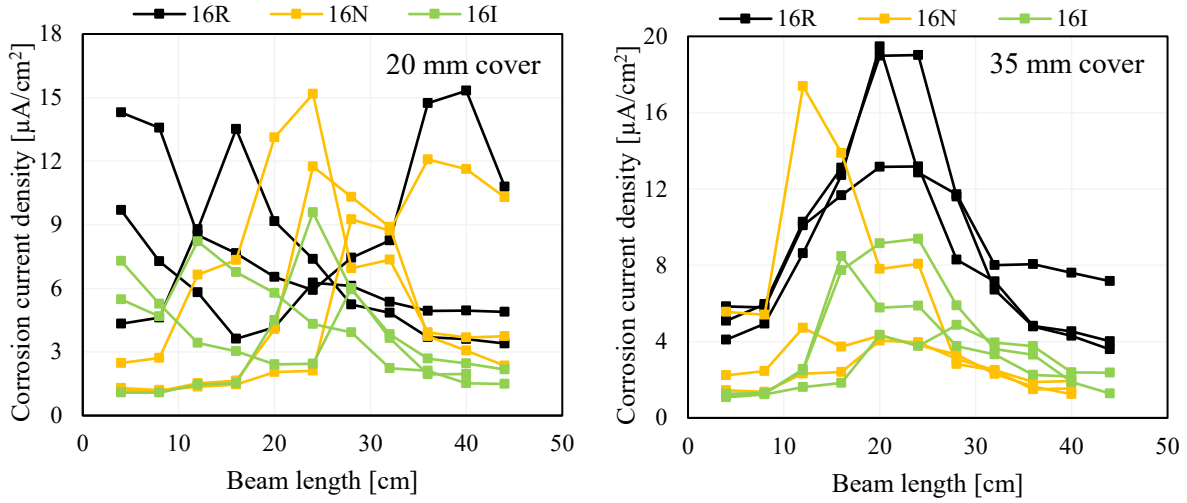

Figure 5.11: Corrosion profile of 16R, 16N, and 16I beams with (a) 20 mm, and, (b) 35 mm and a / c = 0

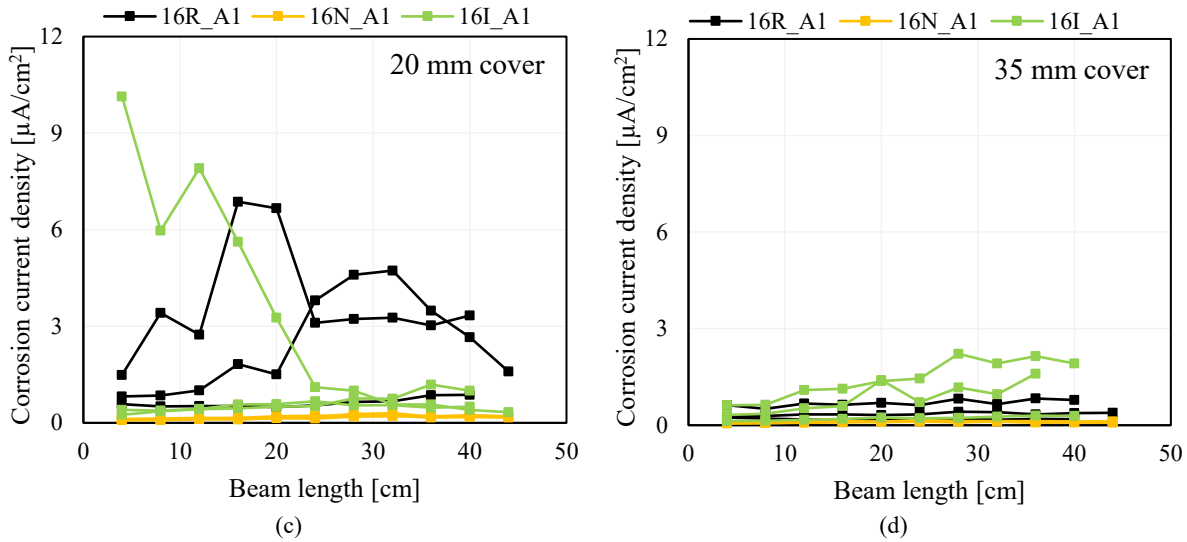

Figure 5.11: Corrosion profile of 16R, 16N, and 16I beams with (c) 20 mm, and, (d) 35 mm and a / c = 1

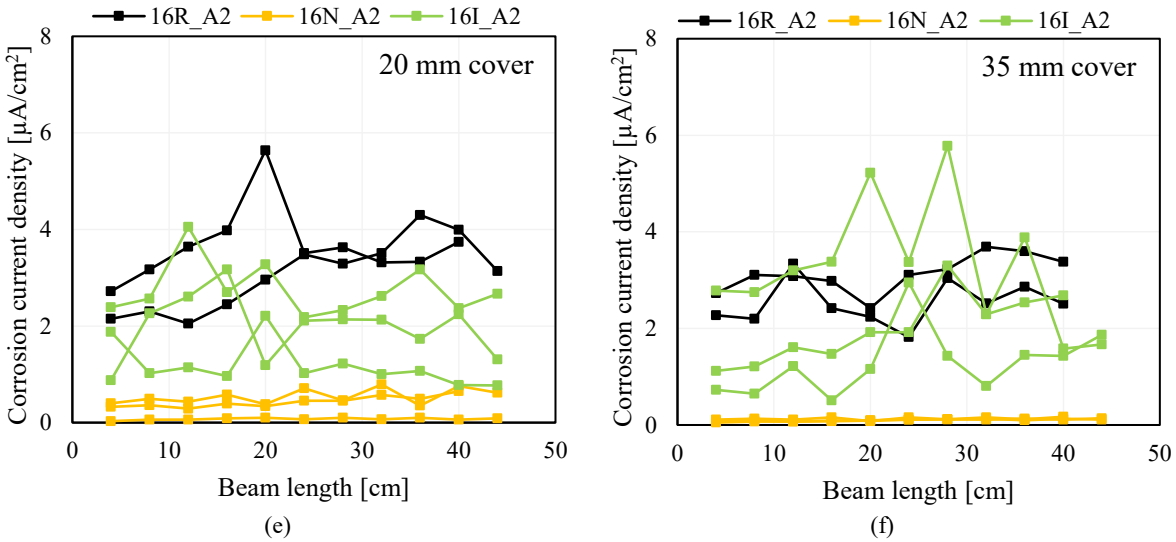

Figure 5.11: Corrosion profile of 16R, 16N, and 16I beams with (c) 20 mm, and, (d) 35 mm and a / c = 2

The corrosion profiles in Figure 5.11 must be interpreted keeping in mind the cracks on the specimens given in Table 5.14. Firstly, it is worthwhile mentioning that the purpose of the study of chloride-induced corrosion in LWFC was to assess the durability properties of steel reinforced LWFC under conditions of chloride exposure. The study includes the use of surface treatment to enhance resistance to chloride ingress, and thereby the R/LWFC durability properties against chloride-induced corrosion. However, comparison of the data of the 16R, 16N and 16I is complicated by the unique crack patterns displayed by each specimen. Nevertheless, a general trend is seen in Figure 5.10 that the highest corrosion rates occurs in the reference (R), untreated beams, and the lowest corrosion rates in the non-integral (pore liner) surface treated specimens. Also, a general trend of high corrosion rates is found in the vicinity of the crack area.

5.3.6 Chloride-induced corrosion (Galvanostatic measurements) – Series 3

In this section the results of the corrosion rate measurements obtained from the 1200, 1400 and 1600 kg/m^3 specimens are presented. The discussion is kicked off with the presentation of the results of the 1200 kg/m^3 (12R, 12N, 12I) specimens which is followed by a comparison of the corrosion rate and corrosion potential for the different densities reported. The rest of the results (14 and 16 set) follow a similar trend and can be found in Appendix C. The effect of surface treatment on corrosion rate is also elaborated on.

5.3.6.1 Corrosion rate and corrosion potential for 1200 kg/m^3 (12R, 12N, 12I)

Figure 5.12 shows the average corrosion rate measurements obtained on the 12R, 12N, and, 12I specimens using the Galvanostatic method over a period of 21 weeks. All three sets have an initial reading that is higher than the rest of the readings. This reading was taken immediately at the end of the 3 day wetting ponding period which is known to cause an increase in the corrosion rate results due to the moisture content in concrete, as pointed out by Bezuidenhout (2017). The initial high reading is followed by a lower second reading which is at the end of the 11 day dry cycle whereby moisture levels in the concrete have dropped. The third reading (wet) obtained in the series is higher than the second reading but lower than the initial reading. This alternating, zig-zag pattern is seen in most of the data over the recording period whereby a high corrosion rate value is obtained after the wet cycle followed by a lower corrosion rate value corresponding to the reading after the dry period. From week 0 to week 5 the data follows a slightly downward trend, reaching a minimum at week 5. The results from week 6 to week 21 appear to have entered a stabilised phase. For prolonged periods of time the highest corrosion rate values are found in the reference set, 12R, followed by the integral set, 12I, and lowest in the non-integral set, 12N. This seems to indicate that the non-integral surface treatment is performing the best against chloride-induced corrosion.

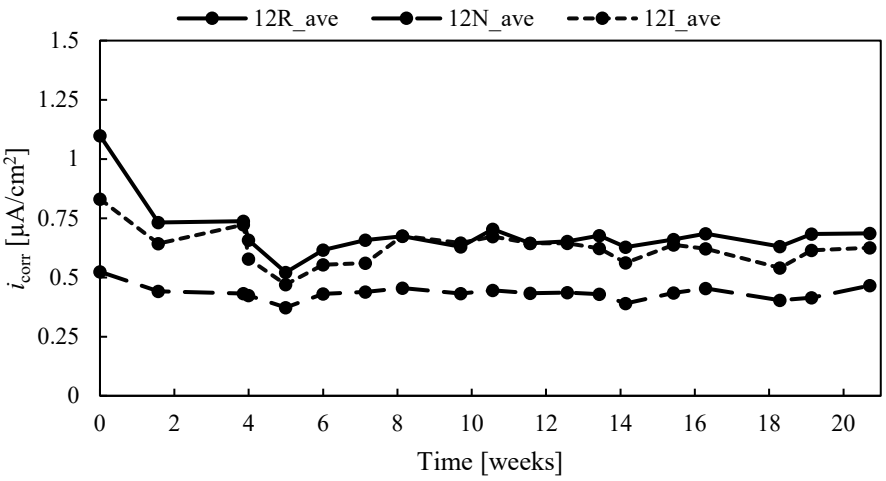

Figure 5.12: Average corrosion rate measurements obtained on the 12R, 12N, and, 12I specimens using the Galvanostatic method over a period of 21 weeks

Figure 5.13 shows the average corrosion potential measurements obtained on the 12R, 12N, and, 12I specimens using the Galvanostatic method over a period of 21 weeks. An initial relatively high corrosion potential value is obtained for all three sets, after which the corrosion potentials follow a downward albeit oscillating trend. The downward trend continues until it reaches a minimum at week 5 for set 12R and 12N. Thereafter a reasonably uniform trend is observed with the corrosion rate oscillating between higher (wet) and lower (dry) rates. After week 11 set 12I follows a slight upward trend. For the corrosion potential results the 12N set gives the lowest corrosion potential results which reinforces the notion that the non-integral surface treated specimen set (12N) has a better chloride-induced corrosion resistance than the other sample sets. Low corrosion potential values have been linked to low corrosion rate values throughout literature (Paul (2015), Bezuidenhout (2017), Song and Caraway (2007)).

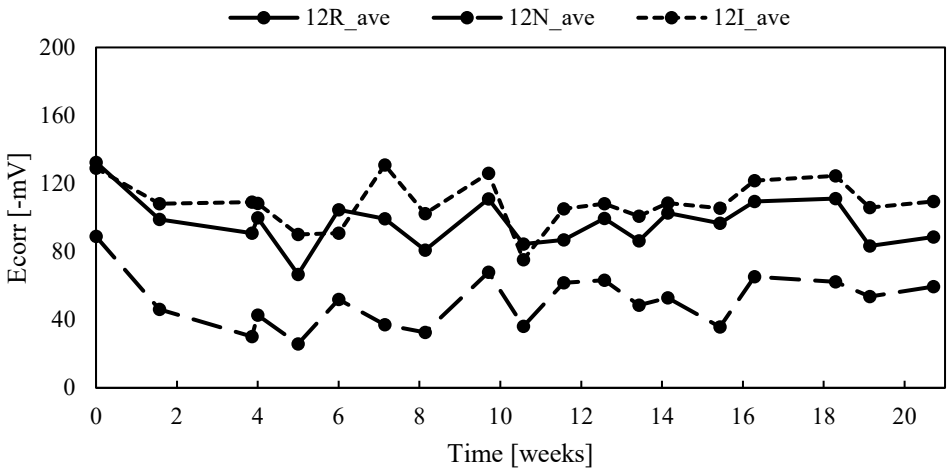

Figure 5.13: Average corrosion potential measurements obtained on the 12R, 12N, and, 12I specimens using the Galvanostatic method over a period of 21 weeks. Note the negative y-axis values

It must be kept in mind that high corrosion potential, i.e. highly negative half-cell potentiostat measurements, indicate high probability of corrosion, but cannot present information on actual corrosion

current or corrosion rate. In practice, a sharp increase in corrosion potential points at corrosion initiation. To monitor corrosion propagation, i.e. the second phase of corrosion process, corrosion rate must be measured, for instance by the GECOR10 apparatus.

Figure 5.14a-d show the results of the average corrosion rate versus the corrosion potential for 12R, 12N, 12I, and the combination of all the data. A regression analysis was performed on the data and the R-squared values are indicated in each of the figure showing poor correlation. These results are contrary to what other researchers have found. Bezuidenhout (2017) found R-squared values ranging from 0.67 to 0.76 using the same corrosion rate measuring technique.

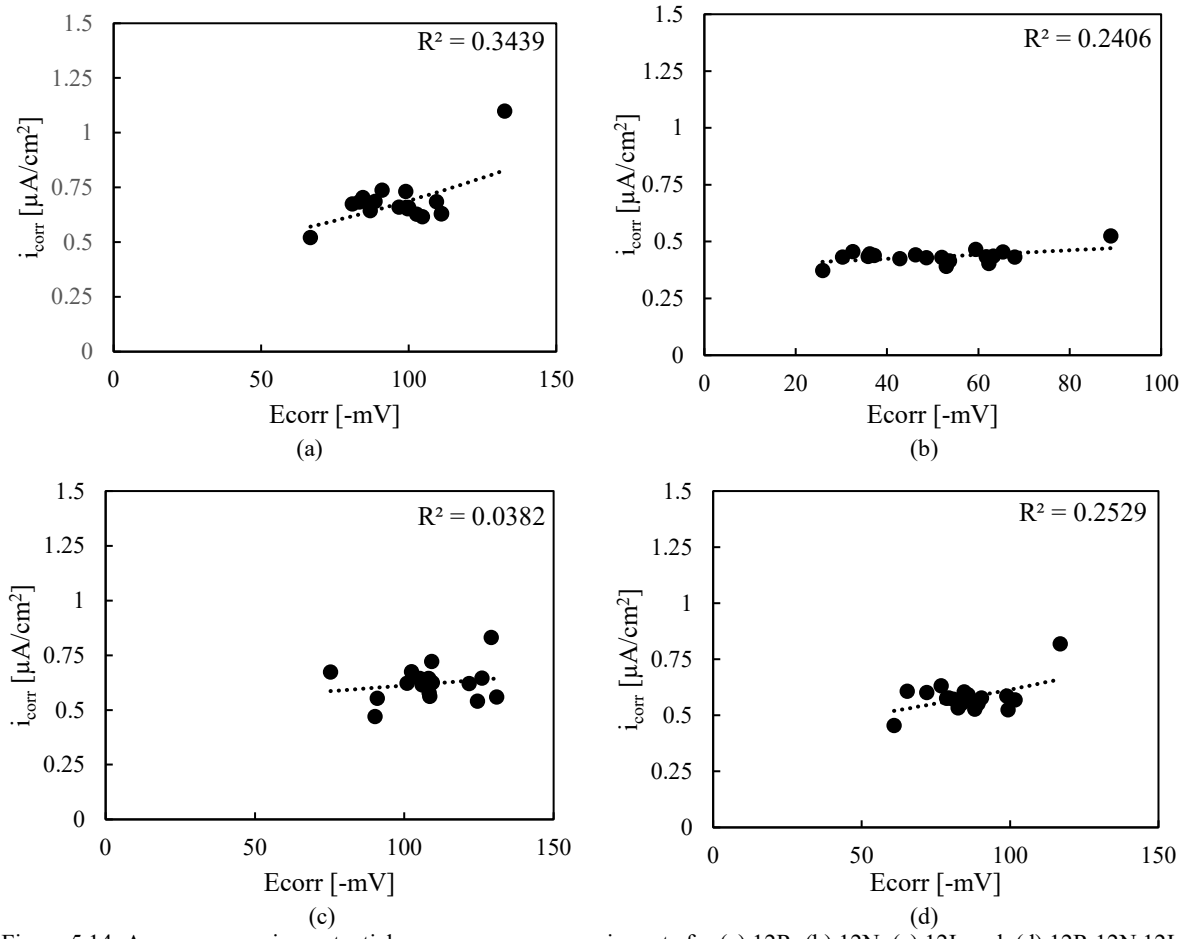

Figure 5.14: Average corrosion potential versus average corrosion rate for (a) 12R, (b) 12N, (c) 12I, and, (d) 12R 12N 12I.

5.3.6.2 The influence of density on corrosion rate and corrosion potential (16N, 14N, 12N)

Figure 5.15 and Figure 5.16 show the average corrosion rate measurements obtained on 1600, 1400, and, 1200 kg/m^3 specimens of all three types (R, N, I) and 16N, 14N, and, 12N and using the Galvanostatic method over a period of 21 weeks. The results in Figure 5.15 and Figure 5.16 follow the same general trend observed for 12R, 12N and 12I samples. That is to say that the same trend is seen of an initial high reading followed by a low reading and subsequent slightly oscillating wet-dry readings. In this case the lower the density the lower the corrosion rate. For the non-integral set, the highest density mix, 16N, consistently achieved the highest corrosion rate values except for the first reading where the

14N mix has slightly higher reading. The other sets show inconsistencies whereby different densities have the highest corrosion rate at different time intervals. For instance, in the case of the reference set, the 12R (lowest density) has the highest corrosion rate values for the first 7 weeks. For the integral set, the 12I (lowest density) has the lowest corrosion rate values after week 7.

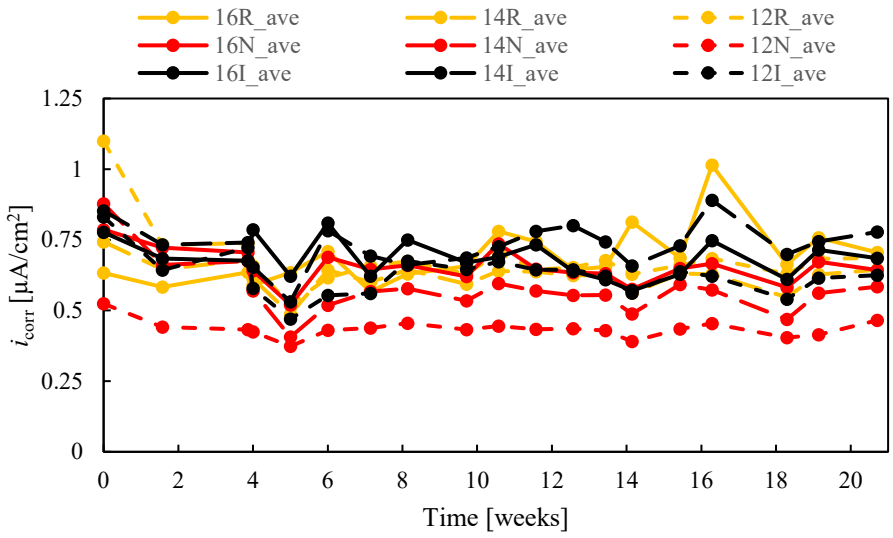

Figure 5.15: Average corrosion rate measurements obtained on the 1600, 1400, and, 1200 kg/m^3 specimens using the Galvanostatic method over a period of 21 weeks

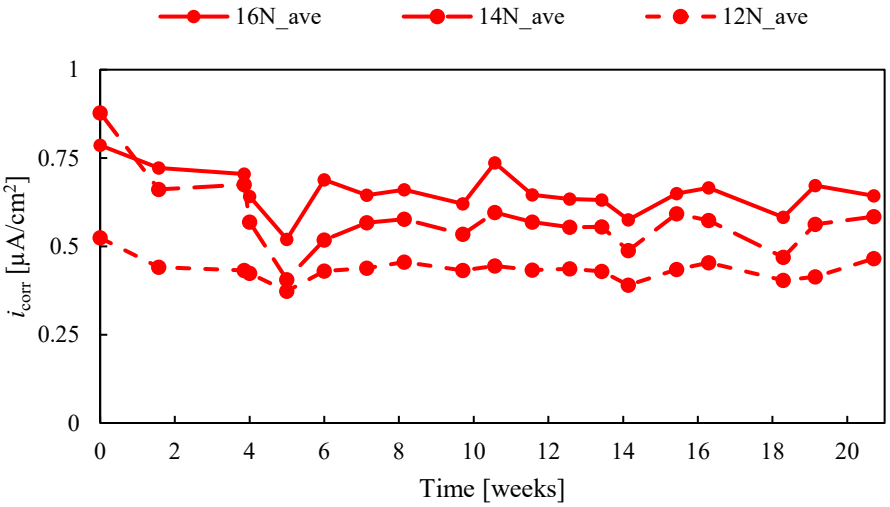

Figure 5.16: Average corrosion rate measurements obtained on the 16N, 14N, and, 12N specimens using the Galvanostatic method over a period of 21 weeks

Figure 5.17 and Figure 5.18 show the corrosion potential measurements obtained on the 1600, 1400, and, 1200 kg/m^3 of all three types (R, N, I) and 16N, 14N, and, 12N and specimens using the Galvanostatic method over a period of 21 weeks. No clear pattern with regard to density can be observed the in the results of the corrosion potential. For instance, from week 0 to week 8 the 14N mix had the least negative corrosion potential values whilst the 16N had the largest negative corrosion potential

values. After week 8 the largest negative corrosion potential alternates between 12N and 16N. Generally mix 14N had the least corrosion potential values for the duration of testing.

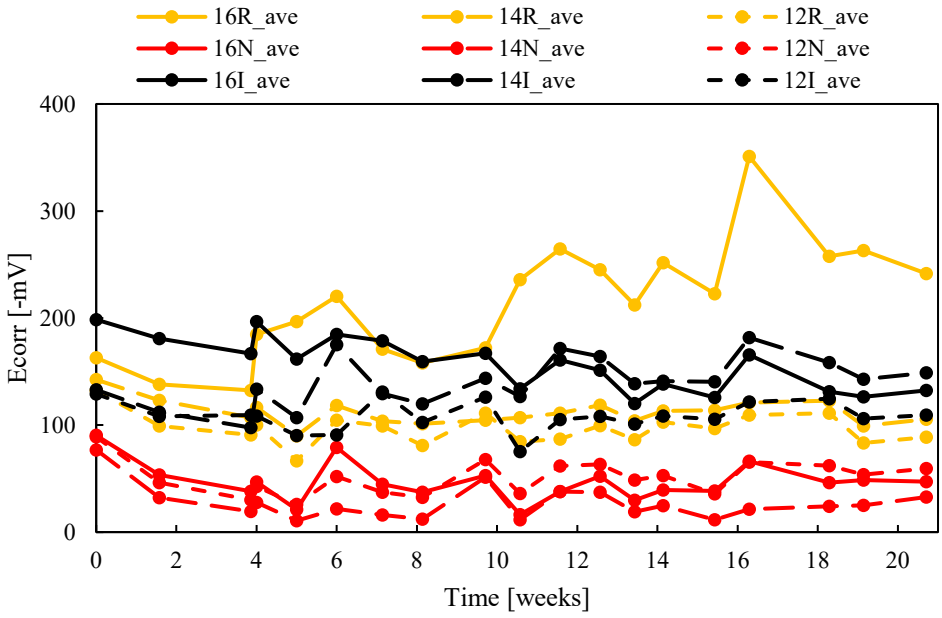

Figure 5.17: Average corrosion potential measurements obtained on the 1600, 1400, and, 1200 kg/m^3 specimens using the Galvanostatic method over a period of 21 weeks.

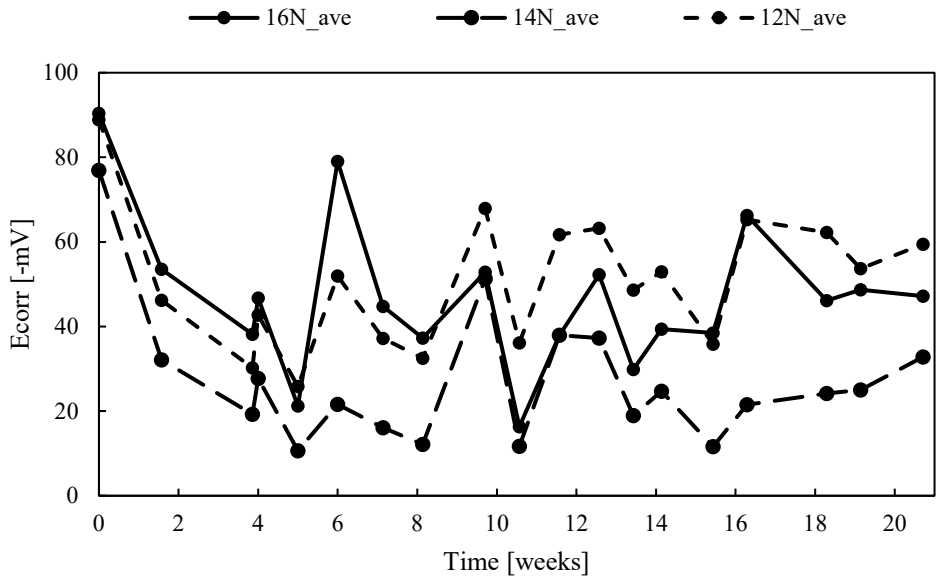

Figure 5.18: Average corrosion potential measurements obtained on the 16N, 14N, and, 12N specimens using the Galvanostatic method over a period of 21 weeks.

5.4 Corrosion rate and potential per cycle

Table 5.15 presents a tabulated summary of the average corrosion rate and corrosion potential measurements over 21 weeks and per cycle for all specimens in Series 3.

Table 5.15: Average corrosion rate and corrosion potential over 21 weeks and per ponding cycle (all specimens)

Description	Weeks	Cycle [1:1 wet:dry reading]									
	[1-21]	1	2	3	4	5	6	7	8	9	10
Average											
i_{corr} [µA/cm^2]											
16R	0.689	0.608	0.613	0.672	0.599	0.719	0.694	0.734	0.850	0.711	0.705
16N	0.654	0.754	0.673	0.604	0.653	0.678	0.640	0.603	0.658	0.627	0.643
16I	0.685	0.731	0.731	0.715	0.685	0.679	0.686	0.590	0.688	0.662	0.685
14R	0.650	0.694	0.646	0.565	0.622	0.617	0.631	0.594	0.630	0.587	0.644
14N	0.513	0.769	0.622	0.462	0.572	0.565	0.562	0.522	0.582	0.516	0.584
14I	0.754	0.793	0.697	0.657	0.677	0.706	0.790	0.701	0.809	0.721	0.778
12R	0.683	0.916	0.698	0.568	0.666	0.667	0.648	0.652	0.672	0.657	0.686
12N	0.435	0.483	0.428	0.402	0.447	0.439	0.435	0.409	0.445	0.409	0.465
12I	0.624	0.737	0.650	0.512	0.618	0.659	0.644	0.592	0.629	0.578	0.625
E_{corr} [-mV]											
16R	215	150	159	208	165	204	255	232	287	260	241
16N	47	72	42	50	41	35	45	35	52	47	47
16I	157	190	182	173	169	151	156	129	146	129	132
14R	109.1	132.7	111.8	104.1	102.4	105.8	114.9	108.7	117.4	111.1	105.4
14N	33.8	54.5	23.5	16.1	14.1	31.5	37.6	21.8	16.6	24.6	32.8
14I	140.6	122.5	115.6	141.1	124.6	135.2	167.9	139.8	161.1	150.7	148.9
12R	96.5	115.8	95.5	85.7	90.1	97.8	93.3	94.5	103.1	97.3	88.6
12N	50.7	67.6	36.5	38.9	34.8	52.0	62.5	50.8	50.6	58.0	59.4
12I	108.5	118.7	108.8	90.6	116.7	100.6	106.7	104.7	113.6	115.2	109.4
CoV (%)											
i_{corr}											
16R	9.37	13.3	18.3	37.5	15.0	6.51	10.6	23.9	13.7	7.27	4.25
16N	8.88	9.10	11.2	3.81	9.50	9.52	8.26	9.47	9.38	12.8	12.3
16I	38.3	30.7	41.9	47.0	38.8	38.4	38.5	32.6	39.6	39.0	34.8
14R	5.47	7.61	6.65	10.3	4.73	6.46	3.87	5.50	5.11	5.66	5.53
14N	6.76	17.6	16.6	10.4	9.13	13.0	12.0	13.7	12.1	14.1	16.3
14I	29.7	19.2	26.4	37.6	29.4	31.0	35.3	31.1	42.5	42.3	40.7
12R	15.6	13.3	18.8	13.5	16.6	17.1	13.2	14.9	16.5	16.9	15.4
12N	7.04	2.93	4.42	9.34	6.87	12.0	10.9	8.03	7.50	9.29	7.71
12I	13.3	18.9	15.5	13.8	14.6	11.9	9.44	13.0	12.4	10.7	12.1
E_{corr}											
16R	15.3	8.0	10.5	39.9	8.8	26.7	29.4	31.5	27.9	28.1	24.1
16N	62.3	23.9	49.5	74.3	72.9	68.6	64.5	87.6	66.1	76.7	78.5
16I	83.8	48.8	71.7	87.7	85.0	87.0	83.0	94.9	93.7	111.5	102.7
14R	5.59	10.72	6.76	10.9	11.4	16.0	6.98	6.06	4.30	8.41	7.80
14N	23.8	7.5	38.5	65.2	46.8	35.4	43.5	68.7	18.8	41.4	35.3
14I	48.4	6.2	24.9	49.0	46.9	47.1	51.1	63.2	60.2	65.6	71.6
12R	9.61	9.99	10.2	17.1	6.80	10.1	11.5	9.39	6.68	10.7	8.65
12N	2.16	4.20	7.53	5.28	9.04	1.95	6.24	3.21	7.21	3.49	3.15
12I	7.48	9.32	15.9	9.64	17.0	9.77	12.1	10.7	8.06	6.76	7.11

See Appendix D for data on individual specimens

The results in Table 5.15 for the reference mixes (16R, 14R, and 12R) show that the lowest and highest average corrosion rate is recorded in the 12R set, 0.57 and 0.92 µA/cm^2, respectively. No clear trend in

the average corrosion rate with respect to density is observed in the reference set as the second highest corrosion rates are found in the 16R set. However, a trend of decreasing average corrosion potential is found with a decrease in density. Similarly, the results of the integral surface treated mixes (16I, 14I, and 12I) reveal no clear trend in average corrosion rates with density; highest average corrosion rate is found in the 14I set and lowest in the 12I set, but follows the same trend of decreasing average corrosion potential with decreasing density. For the non-integral surface treated mixes (16N, 14N, and 12N), no clear trend is observed in the average corrosion rates and average corrosion potentials with respect to density.

Figure 5.19a-d shows the influence of density and surface treatment on the average corrosion rate and average corrosion potentials in all specimens over a 21 week period. The error bars in Figure 5.19c,d indicate the maximum and minimum values.

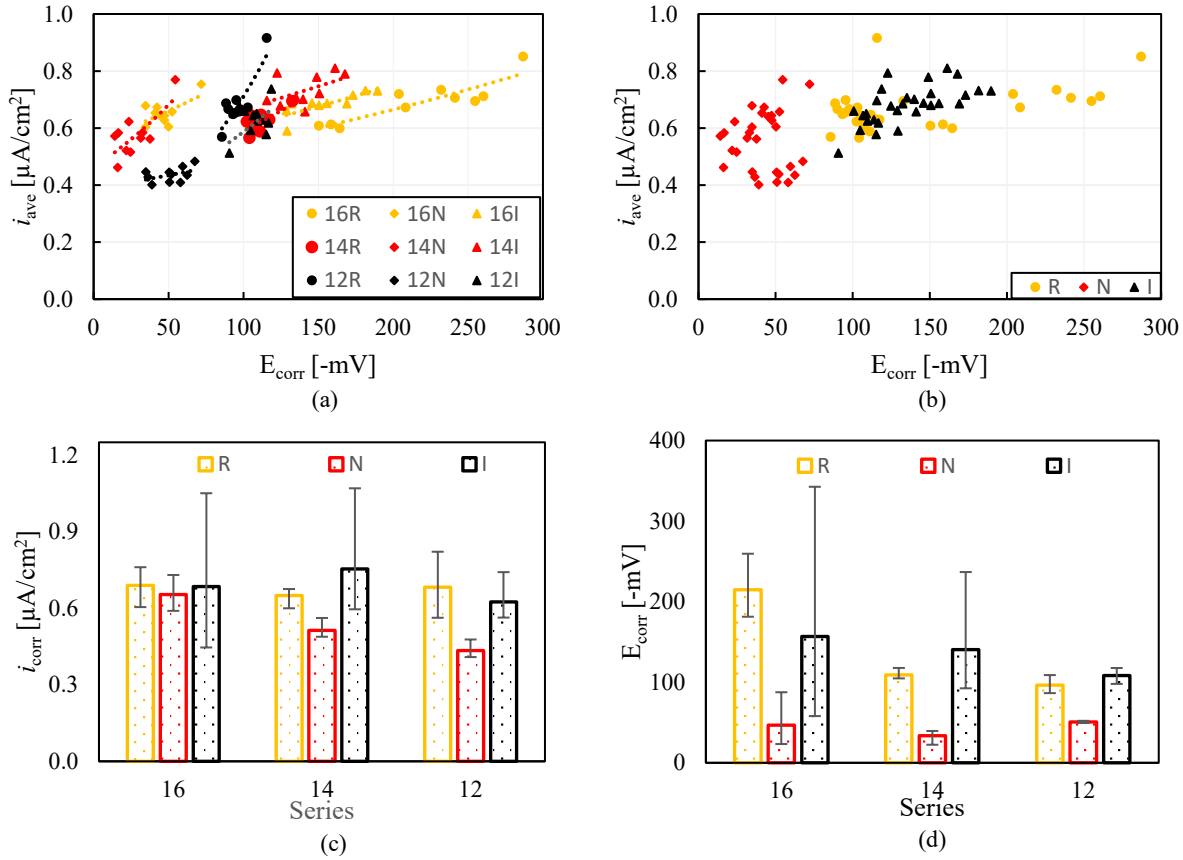

Figure 5.19: Average corrosion rate versus average corrosion potential indicating the effect of (a) density, and, (b) STA for all specimens. The average (c) corrosion rate, and, (d) corrosion potential over 21 weeks for respective specimen groups

The effect of density and STAs on the average corrosion rate and average corrosion potential can be evaluated by comparing the results in Figure 1a-d of the 16, 14, and 12 series and the reference (R) to the non-integral (N) and integral (I) surface treated sets. Analysing the results displayed in Figure 1a-d confirms the trends observed in the results found in Table 5.15. That is to say (1) no clear trend is observed for corrosion rate versus density in the R and I sets, (2) a decrease in corrosion rate with a

decrease in density is found in the N set ,(3) a decrease in corrosion potential with a decrease in density is found for the R and I sets, and, (4) no clear trend in corrosion potential versus density for the N set.

Recall from Section 2.4.4.4.1 that high corrosion rates are expected to be found in conjunction with high negative corrosion potentials, Table 2.17. This relationship stems from the theory that there are two co-existing electrochemical reactions for a corroding metal, namely, dissolution-deposition of the metal (steel in this case, see Equation (2.49)) and the reduction-oxidation of the species in the electrolyte. According to Zhang (1996) these reactions have their own exchange current and Tafel slopes (see Equation (2.53)) and therefore the corrosion of the metal occurs a certain potential, corrosion potential, whereby the total rate of oxidation is in equilibrium with the total rate of reduction. The Tafel slopes (anodic- and cathodic coefficients) are an indication of the rate of the anodic- and cathodic reactions. The cathodic reaction, see Equation (2.50), is the governing reaction at the onset of corrosion in concrete. This cathodic reaction is influenced by the availability of oxygen and water at the concrete-steel interface which is directly influenced by the transport properties and the microstructure of the concrete. Note that the work done by Kearsley and Wainwright (2001), Nambiar and Ramamurthy (2007) and Hilal et al. (2014) on the porosity, water absorption and water vapour permeability, see Section 2.2.3.3.2, revealed an increase in porosity, water absorption, and water vapour permeability with a decrease in density of FC. The increase in the water absorption and water vapour permeability is only marginal. Based on these results, it is expected that untreated FC with low densities would have marginally higher moisture and oxygen contents at the steel-concrete interface and subsequently may have slightly higher corrosion rates and more negative corrosion potentials than untreated FC with higher densities. Analysing the average corrosion rates at week 21 for the 16R, 14R and 12R shows that there is a negligible difference between the values 0.689, 0.650 and 0.683 obtained for the sets. Analysing the average corrosion potentials at week 21 for the 16R, 14R and 12R shows that there is a decrease in the corrosion potential which is attributed to increase in the air content.

For integral and non-integral surface treated FC average corrosion rates and average corrosion potentials lower than the reference mixes are expected. Recall from Section 2.4.3.1 the different mechanisms for surface treatment (1) pore-blocking (integral-I) and (2) pore-liners – hydrophobic impregnation (non-integral-N). The integral surface treatment in this research was added and mixed homogenously with the FC therefore ensuring uniform properties. A clear trend of a reduced average interconnected pore size is found with the addition of the integral surface treatment concluded from the results of the PIA performed in this research, see Table 5.9. The reduction in the average interconnected pore size increases the resistance of FC to fluid ingress. The non-integral treatment was applied to the surface of the concrete based on the manufacturers' recommendation. Both STAs method of action is to impede water penetration into FC. Based on the chloride profiling results the non-integral surface treatment outperformed the integral surface treatment. Based on the mechanism for improved durability, impediment of water, the cathodic reaction is expected to be lower in the treated FC and therefore the average corrosion rate and average corrosion potential can be expected to be lower than the untreated

FC. Analysing the average corrosion rates at week 21 for the R, N and I sets shows that the non-integral surface treatment has the lowest corrosion rates. The corrosion rate of the integral surface treated FC is lower than the reference FC for the 16 and 12 series, however, it is higher in the 14 series than the reference. Analysing the average corrosion potentials at week 21 for the R, N and I shows that the corrosion potential is lower in the treated FC with the lowest values found in the non-integral treated FC. As stated in Table 2.18, tabulated in Section 2.4.4.4.1, coatings and sealers may influence corrosion potential readings which might explain the consistently low E_{corr} readings in the non-integral, or surface treated specimens.

5.5 Concluding summary

In this chapter the results of accelerated carbonation and chloride durability tests, known to lead to corrosion in reinforced concrete, and characterisation of the microstructure of LWFC using X-ray CT are reported. As identified in Chapter 2, there is a gap in knowledge on carbonation- and chloride-induced corrosion of R/LWFC and on a strategy to mitigate corrosion and enhance the durability of R/LWFC. Therefore a research programme and mitigation strategy were devised by the author.

For carbonation-induced corrosion, a carbonation chamber was built for accelerated carbonation testing. A carbonation chamber was conceptualised and designed by the author along with a testing programme. The experimental work was carried out and reported by Mubatapasango (2017) under the guidance of the author. The results, after 13 weeks of accelerated carbonation, of the evolution of the carbonation front showed that LWFC carbonates at a high rate and the use of surface treatment agents as a mitigating strategy proved successful by achieving an overall 45% reduction. A regression analysis of the carbonation penetration results, performed by the author, revealed a reduced carbonation coefficient for surface treated LWFC confirming the efficacy of the mitigating strategy. The results of the corrosion potential showed higher corrosion potential from week 1 to week 11 for treated specimens, but lower corrosion potential thereafter. It is acknowledged that a longer period of assessment is needed, to allow corrosion initiation and propagation, to establish the full benefit of the proposed surface treatment.

For chloride-induced corrosion, an experimental programme comprising of three test series, implementing the same corrosion mitigating strategy as in the carbonation test, was devised by the author. Series 1 served as a pilot study and the 12 week experimental programme was performed and the test results were analysed by the author. Corrosion rates obtained through the coulostatic method, using customary lab built equipment, and XRF testing of powdered samples in the cracked and uncracked regions of LWFC specimens showed that surface treatment was effective in reducing corrosion rates and chloride ingress as reported in van Rooyen and van Zijl (2017). Corrosion rates are lower for treated specimens than for untreated specimens. Through XRF chloride profiling performed by the author, non-integral surface treatment was found to be most effective in limiting chloride ingress.

For Series 2, the experimental work was carried out and reported in Zvinokona (2018) under the guidance of the author. For this series the incorporation of polypropylene fibre for crack control, and fly

ash as cement replacement was proposed and designed by the author. From silver nitrate tests on exposed specimens, it was found that chloride penetrates deeper into LWFC specimens containing high fly ash to cement ratio for untreated and integral surface treated specimens. A slight increase in the chloride penetration depth is observed in the non-integral surface treated samples reported in Zvinokona, van Zijl, and van Rooyen (2018). These results are in line with that of Series 1 confirming that non-integral surface treatment is effective at reducing chloride ingress. The addition of fly ash reduces the restrained shrinkage cracking. Analysis of the corrosion rate profiles obtained using the GECOR-10 is complicated by the unique crack pattern of each beam set. However, when comparing less complicated samples, with minimal cracks, the lowest corrosion rates are obtained for the non-integral LWFC specimens.

For Series 3, all experimental work was conducted by the author. In this series corrosion rate and corrosion potential was measured over a period of 21 weeks using the GECOR-10, Galvanostatic method, on LWFC with densities between 1200 and 1600 kg/m^3. For the 1200 kg/m^3 density specimens the lowest corrosion rates and corrosion potentials are found in the non-integral surface treated specimens followed by integral surface treated and untreated specimen. This result reinforces the idea that non-integral surface treatment fairs the best for chloride-induced corrosion. However, in the other density sets, no clear trend is observed for surface treatment except in the case of the 1600 kg/m^3 whereby the highest corrosion rate was found in the non-integral mix. No clear trend in corrosion rate values is observed in density variation.

In order to support some of the findings in the durability results an experimental programme on the characterisation of the microstructure of LWFC was devised and executed by the author. The author sough to find a link between the microstructural pore parameters, obtained through CT scans, and the decrease in carbonation penetration due to integral surface treatment, decrease in chloride penetration due to surface treatment, and increase in chloride penetration due to fly ash inclusion. The results of the PIA and FSA show that there is a decrease in the interconnected pore sizes and average pore size in integral surface treated specimens, interpreted as smaller and less connected voids. For the addition of fly ash a reduction is observed in the pore parameters obtained through both PIA and FSA. The increase in chloride ingress due to fly ash addition is therefore attributed to the increase in capillary suction. It is hypothesised that fly ash addition increases the number of capillary pores.

5.5 References

Bezuidenhout, S.R. (2017). Corrosion propagation in cracked reinforced concrete structures. Master's thesis, Stellenbosch University. http://hdl.handle.net/10019.1/102853

BS EN 1540-2. (2004). Products and systems for protection and repair of concrete structures. British Standards Institutions. London.

Hilal. A.A., Thom, N.H. and Dawson, A.R. (2015). On entrained pore size distribution of foamed concrete. Construction and Building Materials. 75. pp. 227-233.

Kearsley, E.P. and Wainwright, P.J. (2001). Porosity and permeability of foamed concrete. Cement and Concrete Research. 31. pp. 805-812.

Mubatapasango, M.S., van Zijl, G.P.A.G., and van Rooyen, A.S. (2017). Effect of surface protection on carbonation induced corrosion in reinforced foamed concrete. Paper ID 114. 71st RILEM week and ICACMS, 3-8 September 2017, Chennai, India, Volume 4, pp. 179-188.

Mubatapasango, M.S. (2017). Carbonation-induced corrosion in integral and non-integral surface treated lightweight foam concrete. Master's thesis, Stellenbosch University. http://hdl.handle.net/10019.1/102986

Nambiar, E.K.K. and Ramamurthy, K. (2006). Air void characteristics of foam concrete. Cement and Concrete Research. 37(9). pp. 221-230.

Otieno, M.B. (2014). The development of empirical chloride-induced corrosion rate prediction models for cracked and uncracked steel reinforced concrete structures in the marine tidal zone. PhD thesis. University of Cape Town.

Paul, S.C. (2015). The Role of Cracks and Chlorides in Corrosion of Reinforced Strain Hardening Cement-Based Composite (R/SHCC). PhD dissertation. Stellenbosch University.

Song, H. and Saraswathy, V. (2007). Corrosion Monitoring of Reinforced Concrete Structures – A Review. International Journal of Electrochemical Science. 2. pp. 1-28.

Van Rooyen, A.S., and van Zijl, G.P.A.G. (2017). Chloride profiling of integral and non-integral surface treated foamed concrete. Paper ID 120. 71st RILEM week and ICACMS, 3-8 September 2017, Chennai, India, Volume 4, pp. 11-16.

Van Zijl, G.P.A.G., van Rooyen, A. S., Mubatapasango, M.M., Dunn, T.P.A., and Grafe, J. (2017). Durability and bond of reinforced lightweight foamed concrete. High Technology Concrete: Where Technology and Engineering Meet, Springer, pp. 2185-2193.

Zhang, X.G. (1996). Corrosion and Electrochemistry of Zinc. Springer, Boston. MA.

Zvinokona, A.R., van Rooyen, A.S., and van Zijl, G.P.A.G. (2017). Chloride induced corrosion in structural lightweight foam concrete. 9th International Symposium on Cement and Concrete (ISCC 2017). 1-3 November 2017, Wuhan, China.

Zvinokona, A.R. (2018). Chloride induced corrosion of integral and non-integral surface treated lightweight foamed concrete. Master's thesis, Stellenbosch University. http://hdl.handle.net/10019.1/103360

Chapter 6 – **Conclusions and Recommendations**

In this investigation the mechanics and durability properties of LWFC have been investigated. The conclusions based on the results of the tests performed are presented and recommendations for future studies are given.

6.1. Summary

LWFC in its current form has been around for over 50 years and its predecessors under a century (i.e. cellular concrete (McCormick (1967)), gas concrete, aerated concrete (Valore(1954))). These types of concrete with high amounts of entrained air have mostly throughout their histories been limited to non- and semi-structural applications. However, in the last 25 years improved technology and the availability of manufacturing equipment have led to improved concrete properties. For LWFC improved foaming agents, foaming technology and utilisation of waste (i.e. fly-ash (Kearsley and Wainwright (2002), palm oil fuel ash Liem et al (2013)), have led to improved mechanical properties which have opened up several avenues of investigation and leading to the potential for structural application. Despite this demonstration FC has not enjoyed widespread structural utilisation. A general unfamiliarity and lack of standards for the material could be a reason. In addition key information on LWFC such as bond between the reinforcing steel and durability against chloride ingress and carbonation is limited. This research programme aimed to address the gaps in information on LWFC hindering its advancement as the structural material of choice in industry. Particularly it addresses bond behaviour of R/LWFC and durability associated with chloride penetration and carbonation (i.e. chloride- and carbonation-induced corrosion).

In this research programme the mechanical and bond behaviour was determined through mechanical characterisation tests and the modified beam-end test of LWFC with densities in the range of 1200 to 1600 kg/m^3. The results of the mechanical characterisation tests and BE test show evidence that LWFC with densities equal to or greater than 1400 kg/m^3 can be designed and reinforced appropriately for structural application. A demonstration of this is shown through the design and testing of a 2 panel LWFC concrete walling system for use in moderate seismic areas. The walling system demonstrated suitable energy dissipating through activation of various energy dissipating mechanisms such as “rocking” and diagonal cracking.

The research programme addressing LWFC durability against carbonation and chloride attack was performed through accelerated tests. For this research series the durability of LWFC was enhance through the utilisation of surface treatment agents (STAs) (integral – hydrophobic impregnation, and, non-integral – silane treatment). Results of the accelerated carbonation testing showed that the rate and depth of carbonation can be reduced significantly through the use of STAs. Similar results are found for accelerated chloride attack though ponding tests. The results of the corrosion assessment conducted on

accelerated chloride testing specimens revealed on average higher corrosion rates for untreated concrete specimens than surface treated specimens.

6.2 Conclusions

6.2.1 Mechanical properties

The following conclusions are based on the results of the mechanical tests:

- LWFC with wet target densities equal to and greater than 1400 kg/m^3 can produce mean compressive strengths sufficient for structural application (above 20 MPa).
- LWFC has an elastic modulus that is significantly lower than NWC (less than 50%) but has comparable values to that of LWAC (in literature and design codes). It is therefore possible to utilise LWFC with such low elastic modulus although careful consideration should be given to stiffness in the design process.
- A similar proportionality 0.1 to compressive strength is found for the tensile splitting strength of LWFC.
- The specific fracture energy of LWFC is considerably lower than NWC. The specific energy of LWFC with 1400 kg/m^3 density is found to be more than 26 times lower than typical NWC values.
- The specific fracture energy of LWFC can significantly be improved with low fibre volume addition.
- A direct proportional relationship is found between the brittleness and casting density, and, specific fracture energy and casting density.
- The average design bond stresses obtained from the BE test are lower than that obtained by the PO test. This is due to the fact that the BE test simulates flexural behaviour.
- The average bond stresses obtained from the BE and PO tests are found to be higher than the average bond stress values found in design codes BS EN 1992-1-1:2004, SABS 0100-1:2000.
- LWFC with a density of 1400 kg/m^3 achieved average bond stress sufficient for structural use. The use of LWFC with densities lower than 1400 kg/m^3 may therefore not suitable.
- A laboratory experiment validated the viable use of steel reinforcement LWFC in a structural wall system subjected to in-plane shear action. No shrinkage cracks occurred due to restraint by the steel reinforcement to LWFC drying shrinkage, while various energy-dissipating mechanisms were mobilised, including diagonal cracking in the LWFC and shear slip along the foundation and the upper floor interfaces.

6.2.2 Durability properties

The following conclusions are based on the durability test results:

- LWFC exhibits high rates of carbonation at low levels of CO_2 concentration (0.13%).
- Surface treatment can be utilised effectively to reduce the high rate carbonation exhibited by LWFC.

- The resistance of LWFC to chloride penetration can significantly be enhance by utilising surface treatment (integral and non-integral surface treatment). In uncracked LWFC, both integral and non-integral water repellent treatment significantly reduces chloride ingress into LWFC.
- No trend is found in the air void parameters with density variation (FSA results). While total porosity is larger for lower density LWFC as tested here, foam structure of X-ray CT 3D images indicate that the average, as well as oversize (D_{10} and D_{50}) void diameter is unaffected by density. This indicates foam stability, and to which the success in producing structural strength in LWFC is attributed, by controlling the entrained void size and dispersion.
- The addition of an integral STA reduces the interconnected pore space length (PIA results), but does not clearly affect the pore size (FSA). In addition to the hydrophobic nature of STA, the blocking of inter-connective throats between pores explains lower chloride penetration in STA treated specimens.
- Fly ash addition increases the penetration depth of chloride in LWFC and is attributed to the reduced pore diameter size (higher capillary suction due to reduced pore diameter).
- Reinforced LWFC is highly susceptible to cracking due the large drying shrinkage strains. The restrained cracking as a result of large drying shrinkage strains eliminates the time to corrosion period and therefore shortens the lifespan of any potential R/LWFC structure.
- Non-integral STA treated R/LWFC consistently showed the lowest corrosion rates, which is in agreement with the lower chloride penetration depth in uncracked and cracked parts of LWFC specimens.
- Corrosion rate measured on R/LWFC specimens have poor correlation with the corrosion potential.
- On average high corrosion rates are recorded for untreated LWFC specimens.

No visual inspection of the reinforcement was performed in these tests. It is acknowledged that this is the final verification of actual deterioration by the corrosion process. Visual inspection of rebar will be done after continuation of the corrosion process, which is currently continued. Monitoring of the corrosion rates and visual inspection of signs of significant corrosion will be used to determine, at which point, the tests will be stopped and rebars will be extracted destructively from the specimens for inspection and weighing to determine corrosion mass loss These results will be written up for publication by the author

6.3 Practical implications of the research

In this research programme tests were done to characterise the mechanical and durability properties of structural FC. The results of the compressive strength tests confirm that the compressive strength is strongly influenced by the density, yet can be designed to achieve structural strength levels. Since the properties of FC are highly dependent on its density it is important that strict tolerances be imposed on the mix acceptance criteria. A deviation of ±50 kg/m^3 may result in a ±10% change in compressive strength. The tensile strength of FC holds a similar relationship to that of normal concrete, of

approximately 10% of the compressive strength. The elastic modulus of FC is low compared to NWC. This has to be taken into account during design. For instance, R/LWFC structural elements will have higher deflections compared to RC. These deflections may exceed serviceability limit state requirements. The design of structural elements made of R/LWFC may indeed be govern by serviceability limit states. Research can be done to improve the elastic modulus of FC with nano-materials.

LWFC is highly susceptible to drying shrinkage. Although shrinkage is not characterised by this dissertation, it is a general observation. This should be taking into account during the design of R/LWFC. LWFC should be reinforced appropriately to prevent cracking due to shrinkage restraint. The formation of cracks leads to the reduction in service life and should be avoided.

The results of the carbonation testing reveal that FC carbonates at a high rate for a low concentration of CO_2. STAs are a practical way of retarding the rate of carbonation and could be added to all FC mix for improved durability. Non-integral STA proved to be the most effect at reducing chloride ingress. A combination of the two, integral and non-integral STAs, may prove to be the most effective.

6.4 Recommendations

6.4.1 Mechanical properties

Based on the results obtained in this research for the mechanical properties of LWFC the following recommendations are made for future studies:

- Investigate the effect of fibres on the bond properties of LWFC. The addition of fibres will result in an increase of the specific fracture energy of LWFC, therefore decreasing the brittleness, which will result in higher bond stress due to bridging of micro-cracks at the bond interface.
- Incorporation of nano-materials to improve the overall mechanical properties of LWFC. The addition of nano-materials will lead to an increase in the strength to density ratio. The increase in the compressive strength of LWFC will enhance the overall bond performance by providing an increase in the bearing stress resistance at the bond interface. The addition of nano-materials may improve the elastic modulus of LWFC.
- Investigate the effect of confinement on the bond stress ratio in foamed concrete. The provision of secondary reinforcement, shear stirrups, introduces a confinement effect in concrete which may result in additional bond capacity. The addition of secondary reinforcement may minimise the tendency of splitting failure for high density (greater than 1400 kg/m^3) thus providing additional bond capacity.

6.4.2 Durability properties

Based on the results obtained in this research for the durability properties of LWFC the following recommendations are made for future studies:

- LWFC is susceptible to high drying shrinkage strains which leads to cracking due to the addition of reinforcement (restrained shrinkage cracks). It is recommended that future studies address shrinkage directly by the incorporation of chemical additives and low shrinkage cement.
- LWFC experiences high rates of carbonation. It is recommended to investigate the incorporation of zeolites to improve the resistance to carbonation. Similarly, the addition of zeolites can be utilised to delay the ingress of aggressive substance (i.e. chloride ions).

6.5 References

Kearsley, E.P. and Wainwright, P.J. (2002). Ash content for optimum strength of foamed concrete. Cement and Concrete Research. 32(2). pp. 241-246.

Lim, S.K., Tan, C.S., Lim, O.Y. and Lee, Y.K. (2013). Fresh and hardened properties of lightweight foamed concrete with palm oil fuel ash as fill. Construction and Building Materials. 46. pp. 39-47.

McCormick, F.C. (1967). Rational proportioning of preformed foam cellular concrete. American Concrete Institution Journal. 64(2). pp. 104-110.

Valore, R.C. (1954). “Cellular concretes – Part 2. Physical Properties. Journal of American Concrete Institution. 25(9). pp. 817-836

Appendix A - Frequency and $D_{oversize}$ (Porosity / Intrusion Analysis)

Density

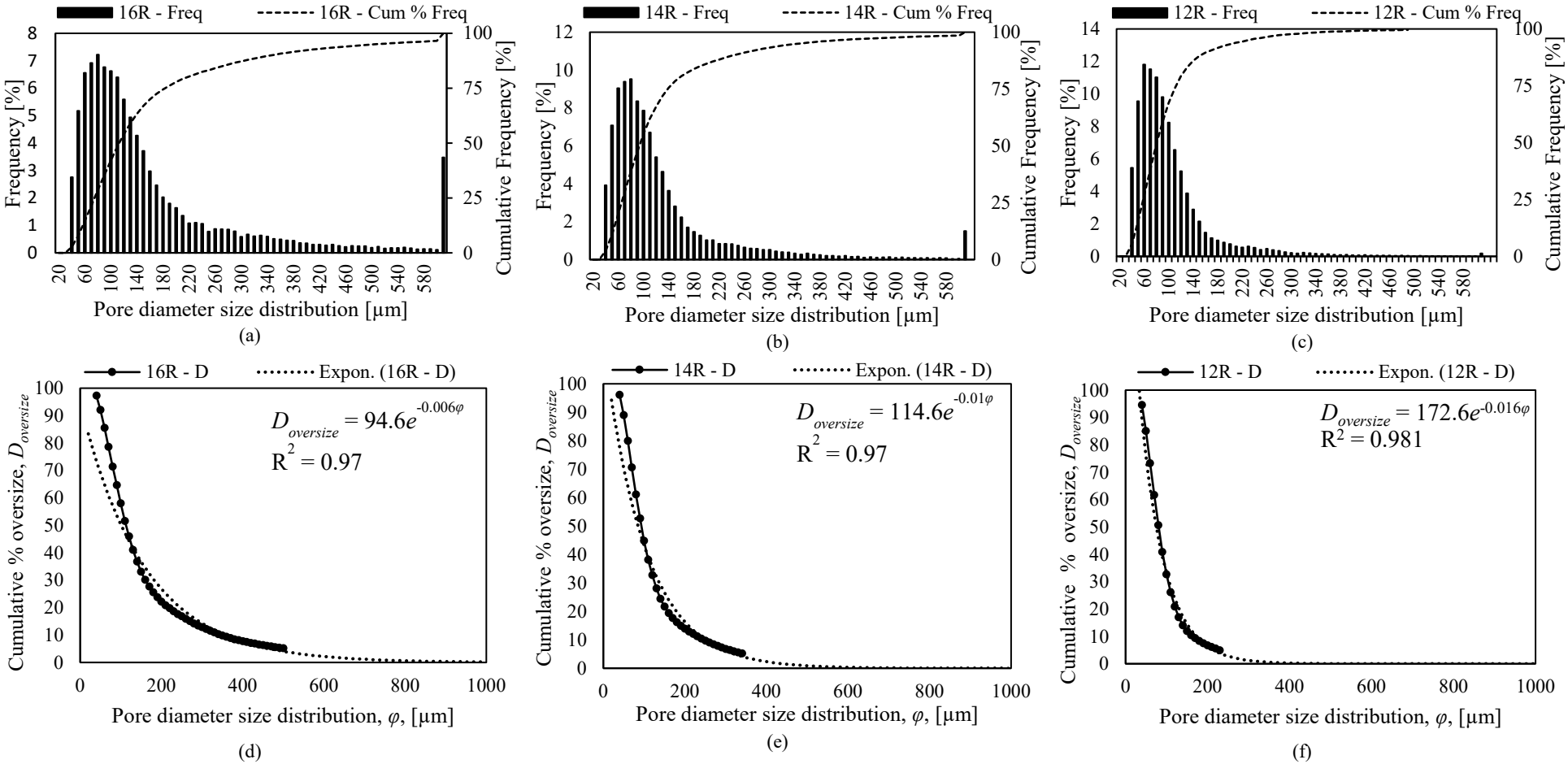

Figure A.1: Frequency distribution Doversize distributions used to illustrate the effect of density on the microstructure

STA

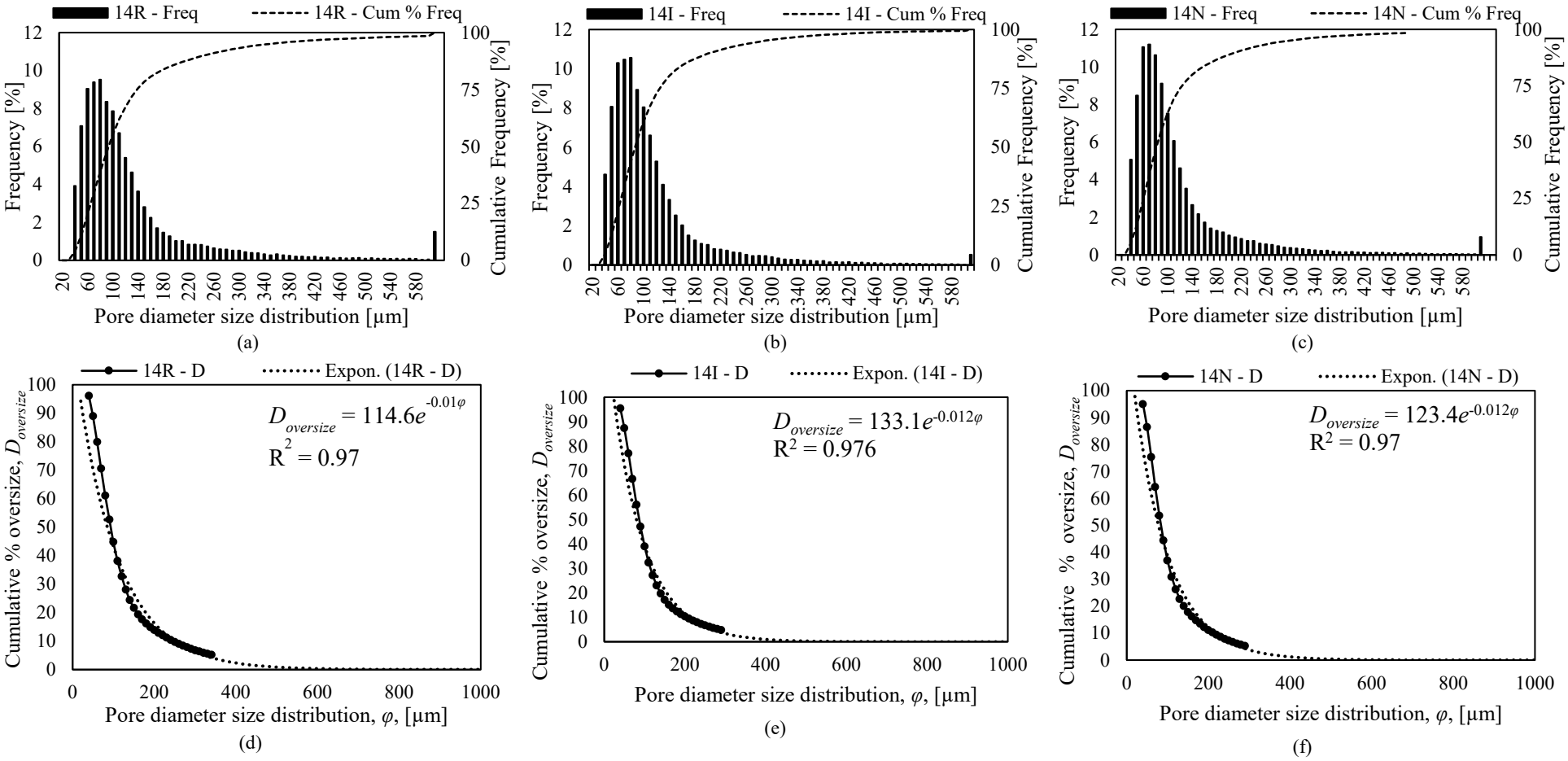

Figure A.2: Frequency distribution Doversize distributions used to illustrate the effect of STAs on the microstructure

Fly ash

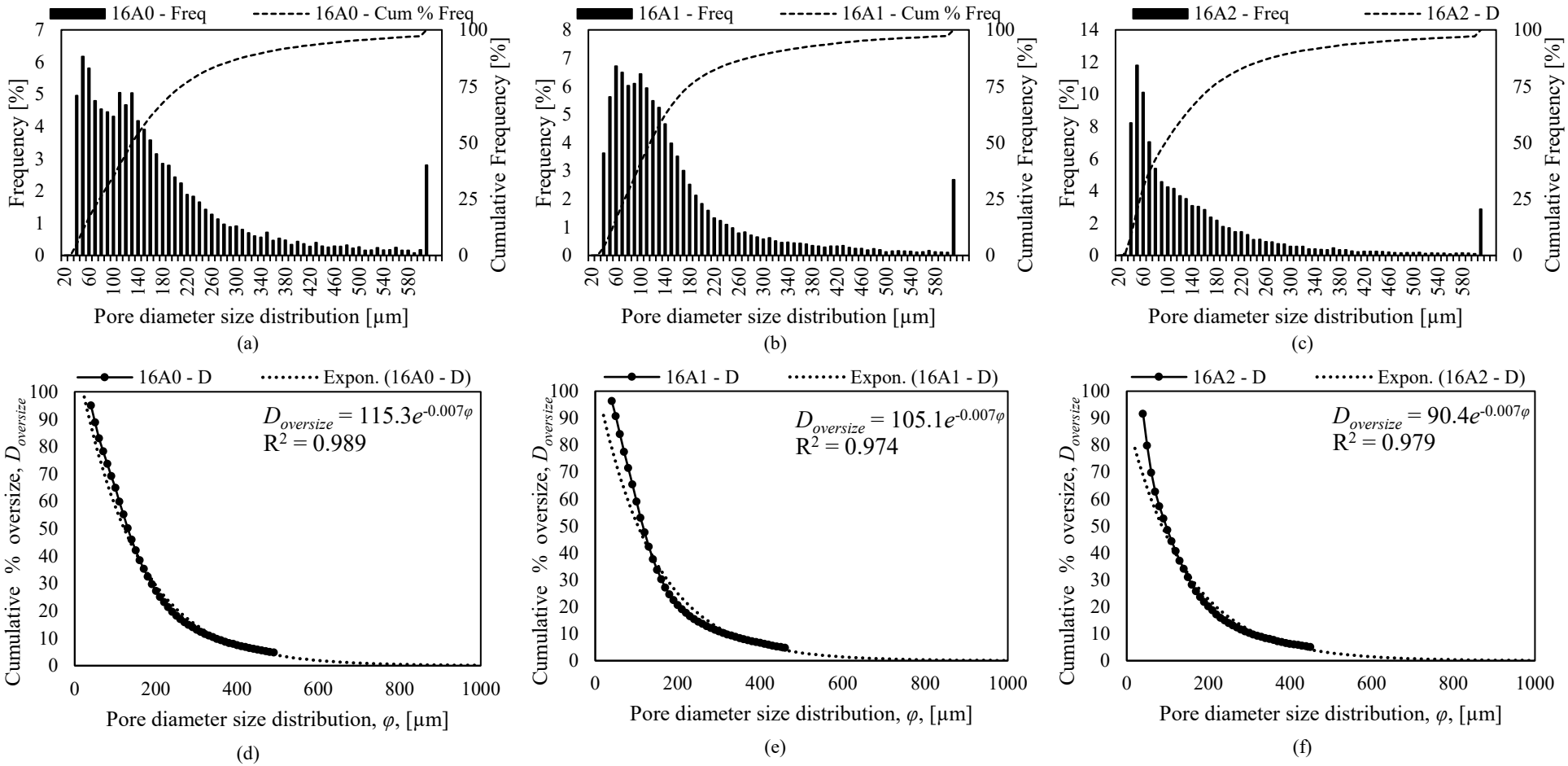

Figure A.3: Frequency distribution Doversize distributions used to illustrate the effect of fly-ash on the microstructure

Appendix A – Frequency and $D_{oversize}$ (Foam Structure Analysis)

Density

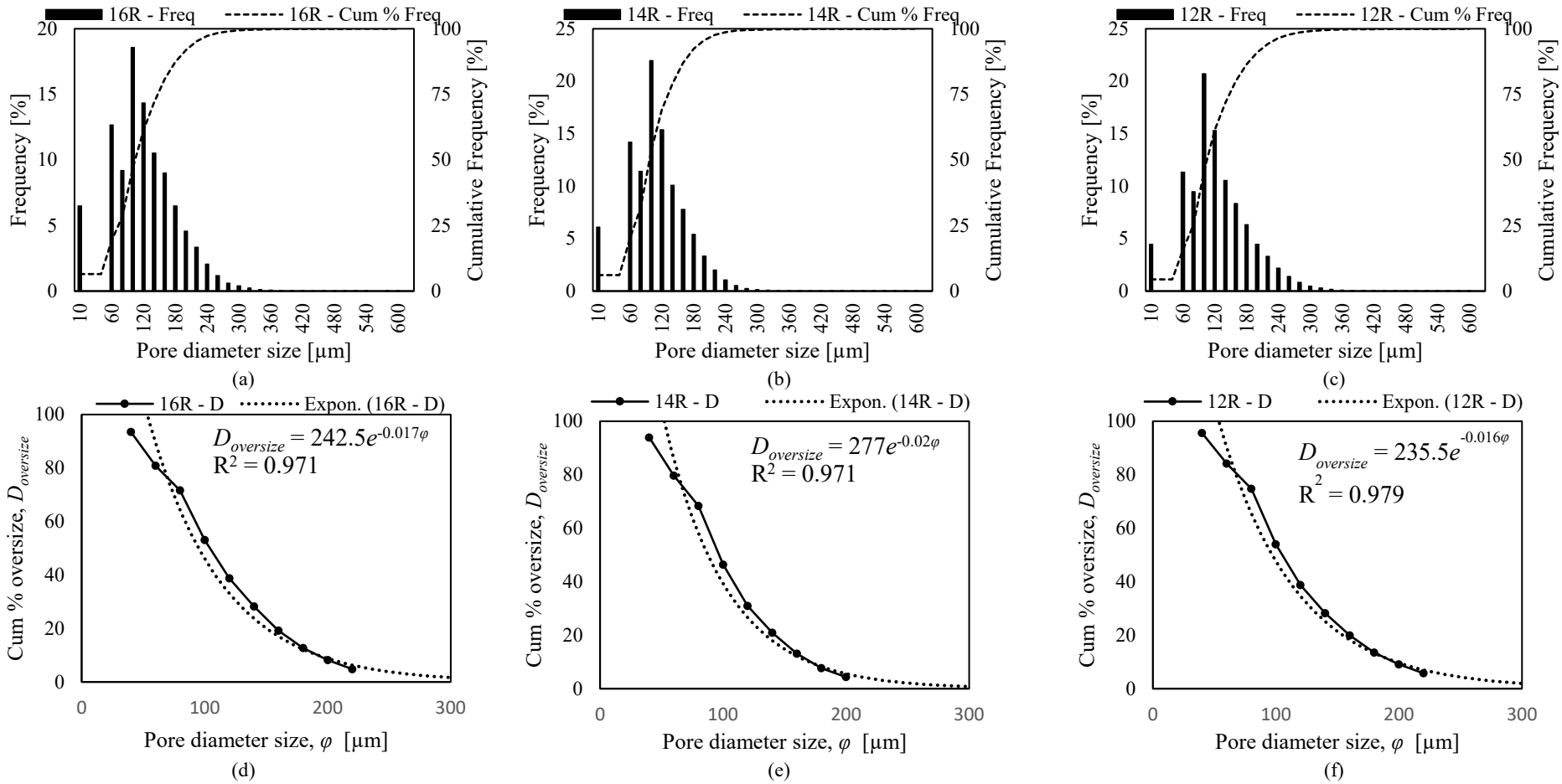

Figure A.4: Frequency distribution Doversize distributions used to illustrate the effect of density on the microstructure

STA

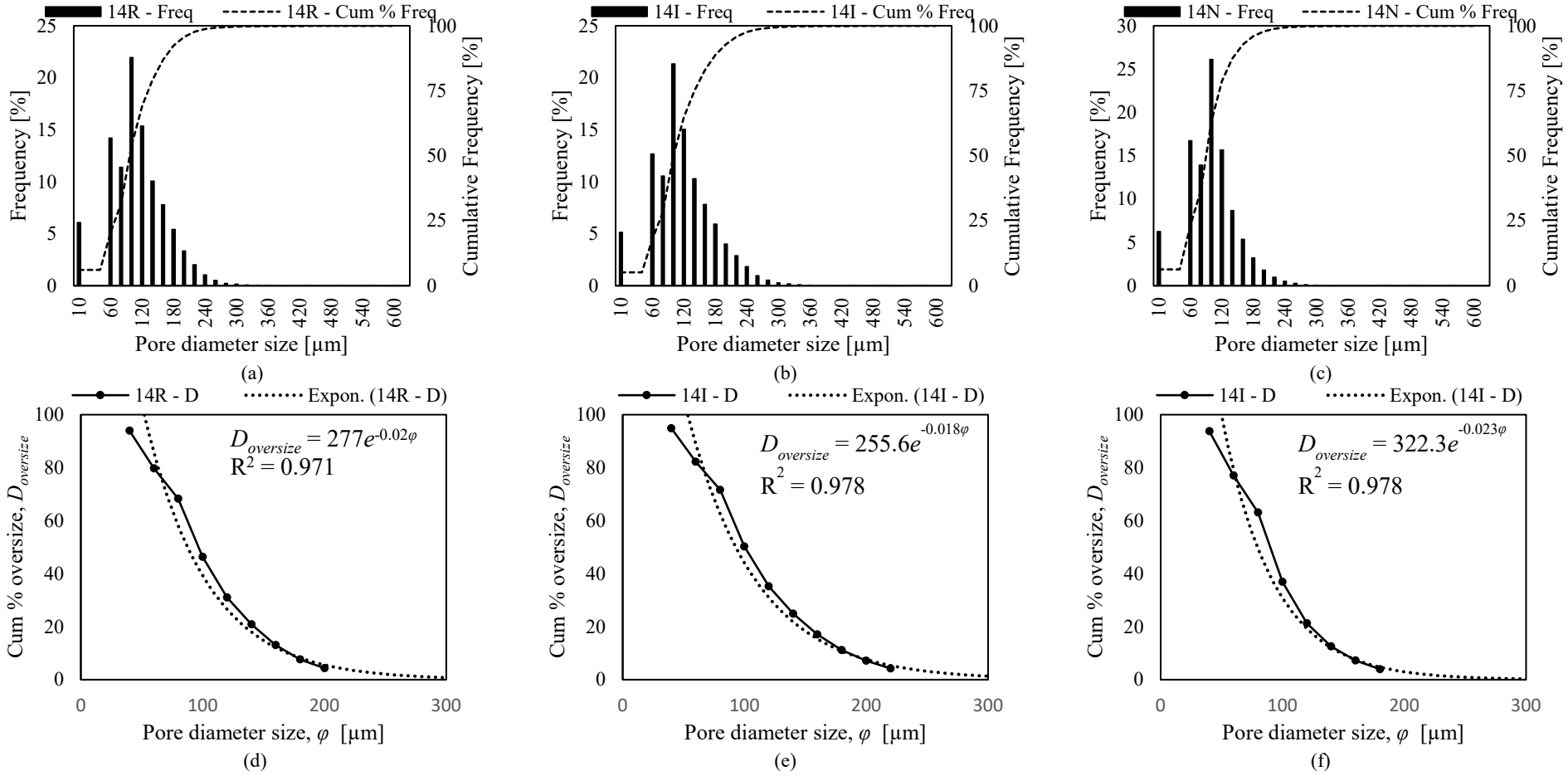

Figure A.5: Frequency distribution Doversize distributions used to illustrate the effect of STAs on the microstructure

Fly ash

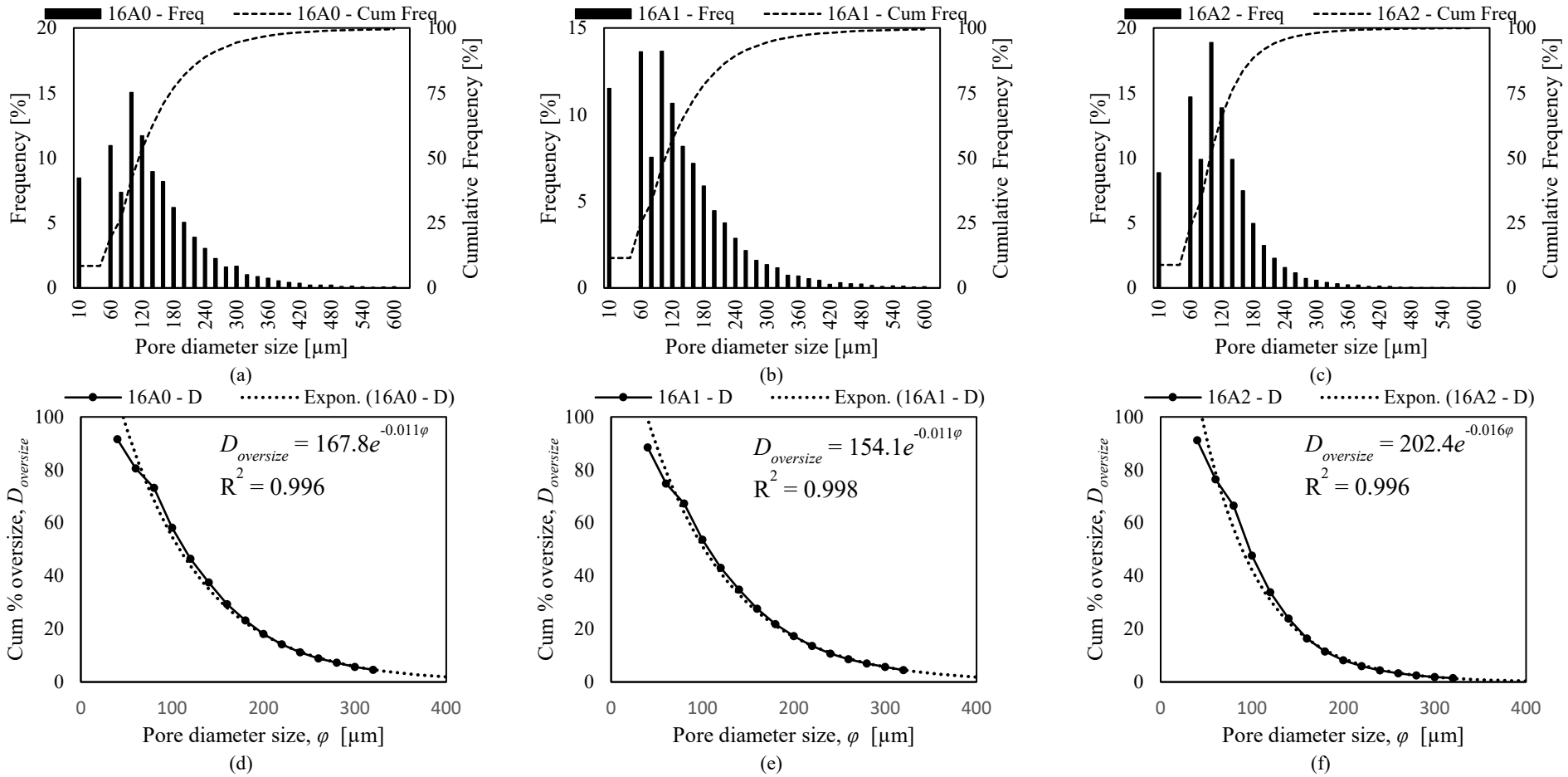

Figure A.6: Frequency distribution Doversize distributions used to illustrate the effect of fly-ash on the microstructure

Appendix B - Crack characterisation (Series 2)

S2–16

Table B.1: Crack width, orientation and location in beam specimens S2-16_20

Description	Specimen	Transverse crack width [location(s)]*	Longitudinal crack size
a / c = 0 cover 20 mm			
16R	1	0.15-0.2 mm [21.6 cm]	0.4mm
	2	0.15 mm [25 cm]	0.1 mm^{RE}
	3	0.1 mm [6cm] / 0.2 mm [20 cm / 27 cm]	
16N	1	0.2 mm [20 cm]	0.1 mm^{RE}
	2	0.1 mm [7.5 cm / 16.5 cm] / 0.2 mm [25 cm]	0.1 mm^{RE}
	3	0.1 mm [9.5 cm / 32 cm] / 0.2 mm [20.5 cm]	
16I	1	0.2 mm [23 cm]	0.1 mm^{RE}
	2	0.15 mm [23 cm]	0.2 mm^{LE} / 0.1 mm^{RE}
	3	0.2 mm [15.6 cm]	0.2 mm^{LE} / 0.1 mm^{RE}

*All locations of transverse cracks measured from the left end of the beam specimens
RE – Right End
LE – Left End
Extracted from Zvinokona (2018)

Table B.2: Crack width, orientation and location in beam specimens S2-16R_35

Description	Specimen	Transverse crack width [location(s)]*	Longitudinal crack size
a / c = 0 cover 35 mm			
16R	1	0.2 mm [19.6 cm]	
	2	0.2 mm [18 cm]	
	3	0.2 mm [20 cm]	0.1 mm^{RE}
16N	1	0.1 mm [15cm / 22 cm]	
	2	0.2 mm [15cm] / 0.1 mm [25 cm]	
	3	0.1 mm [14 cm / 30 cm] / 0.2 mm [22 cm]	
16I	1	0.2 mm [19.5 cm]	
	2	0.2 mm [22 cm]	
	3	0.2 mm [15cm] / 0.1 mm [25 cm]	

*All locations of transverse cracks measured from the left end of the beam specimens
RE – Right End
LE – Left End
Extracted from Zvinokona (2018)

S2-16_A1

Table B.3: Crack width, orientation and location in beam specimens S2-16_A1_20

Description	Specimen	Transverse crack width [location(s)]*	Longitudinal crack size
a / c = 0 cover 20 mm			
16R	1	0.1 mm [24 cm / 36 cm]	
	2	0.1 mm [12.5 cm] / 0.15 mm [32.5 cm]	0.1 mm^{RE}
	3	0.1 mm [18 cm]	0.1 mm^{RE}
16N	1	0.2 mm [20 cm]	0.1 mm^{RE}
	2	0.1 mm [7.5 cm / 16.5 cm / 25 cm]	0.2 mm^{RE}
	3	0.1 mm [9.5 cm / 32 cm] / 0.2 mm [20.5 cm]	0.1 mm^{LE}
16I	1	0.1 mm [18.5 cm]	0.1 mm^{RE}
	2	0.1 mm [30 cm]	0.1 mm^{LE+RE}
	3	0.2 mm [18.6 cm]	0.1 mm^{RE}

*All locations of transverse cracks measured from the left end of the beam specimens
RE – Right End
LE – Left End
Extracted from Zvinokona (2018)

Table B.4: Crack width, orientation and location in beam specimens S2-16_A1_35

Description	Specimen	Transverse crack width [location(s)]*	Longitudinal crack size
a / c = 0 cover 35 mm			
16R	1		
	2	0.2 mm [18 cm]	
	3	0.1 mm [28 cm]	
16N	1	0.1 mm [15cm / 22 cm]	
	2	0.2 mm [12cm] / 0.1 mm [25 cm]	
	3	0.1 mm [14 cm / 30 cm] / 0.2 mm [22 cm]	0.1 mm^{LE}
16I	1	0.2 mm [19.5 cm]	0.1 mm^{LE+RE}
	2	0.1 mm [35 cm]	0.1 mm^{LE}
	3		0.1 mm^{LE+RE}

*All locations of transverse cracks measured from the left end of the beam specimens
RE – Right End
LE – Left End
Extracted from Zvinokona (2018)

S2-16_A2

Table B.5: Crack width, orientation and location in beam specimens S2-16_A2_20

Description	Specimen	Transverse crack width [location(s)]*	Longitudinal crack size
a / c = 0 cover 20 mm			
16R	1	0.1 mm [18 cm]	
	2		
	3		
16N	1		0.1 mm
	2		
	3		
16I	1	0.1 mm [16 cm]	
	2	0.1 mm [20 cm / 32 cm]	
	3	0.1 mm [15.6 cm]	0.1 mm

*All locations of transverse cracks measured from the left end of the beam specimens
RE – Right End
LE – Left End
Extracted from Zvinokona (2018)

Table B.6: Crack width, orientation and location in beam specimens S2-16_A2_35

Description	Specimen	Transverse crack width [location(s)]*	Longitudinal crack size
a / c = 0 cover 35 mm			
16R	1	0.1 mm [26 cm]	
	2		
	3		
16N	1	0.1 mm [14 cm / 22 cm]	0.1 mm
	2	0.1 mm [11 cm]	
	3		
16I	1		0.1 mm
	2	0.1 mm [22 cm]	
	3	0.2 mm [15.6 cm]	

*All locations of transverse cracks measured from the left end of the beam specimens
RE – Right End
LE – Left End
Extracted from Zvinokona (2018)

Appendix C – Corrosion rate and potentials (Series 3)

1600 kg/m³ set – Corrosion rate and potentials

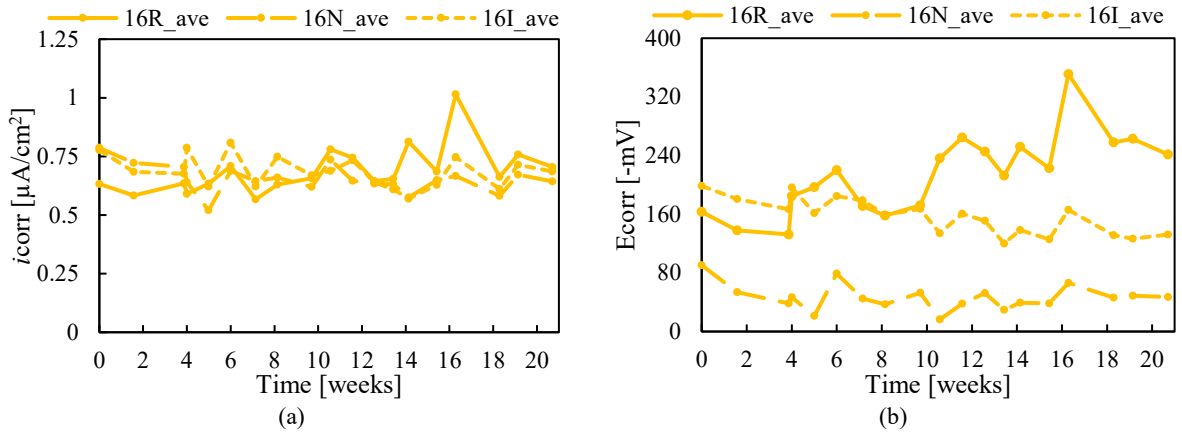

Figure C.1: Corrosion (a) rate and (b) potential

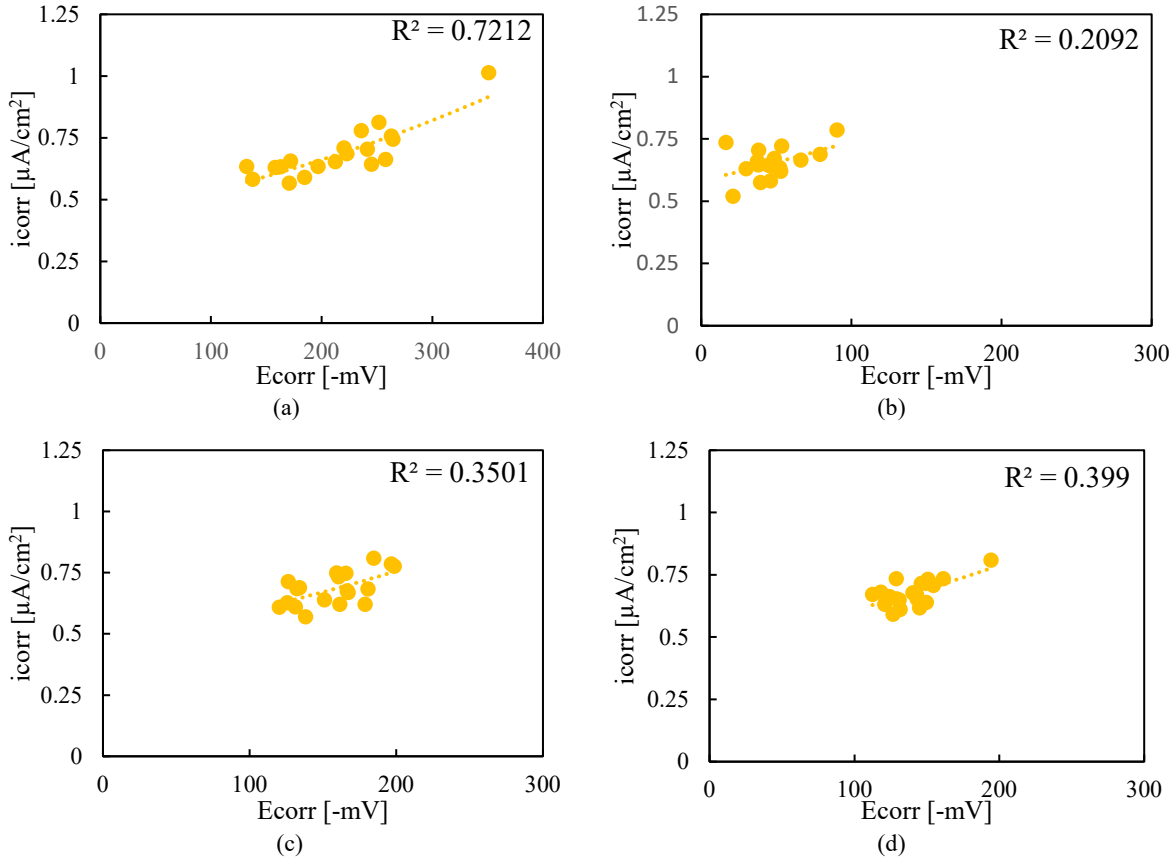

Figure C.2: Average corrosion potential versus average corrosion rates (a)16R, (b) 16N, (c) 16I, and, (d) 16R 16N 16I

1400 kg/m³ set – Corrosion rate and potentials

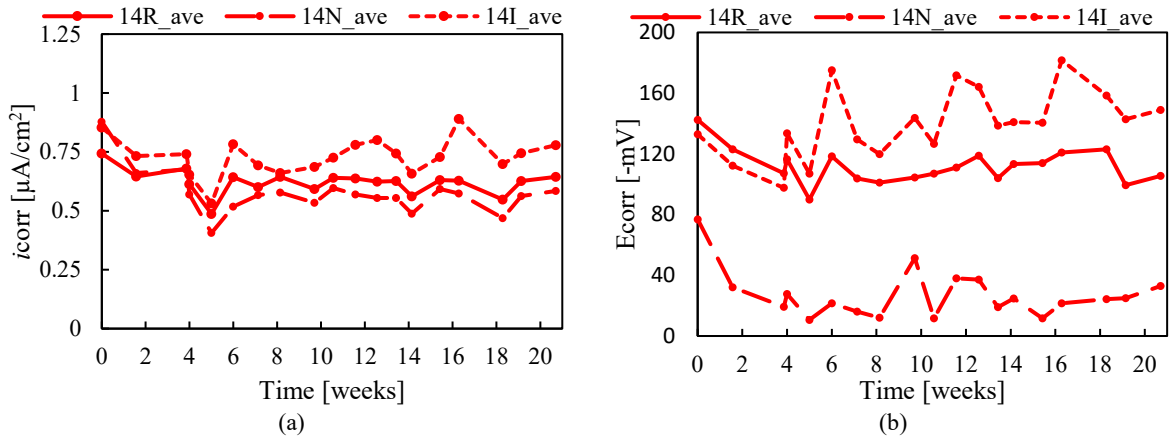

Figure C.3: Corrosion (a) rate and (b) potential

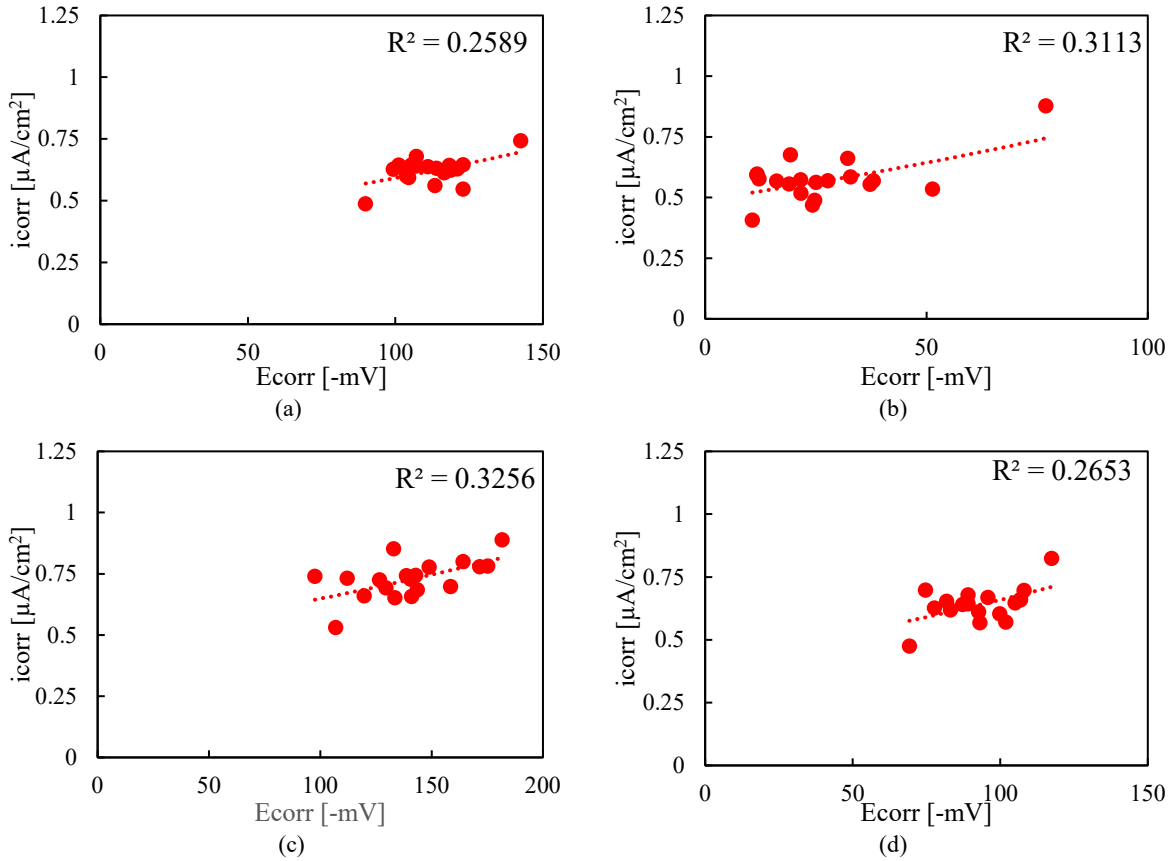

Figure C.4: Average corrosion potential versus average corrosion rates (a)14R, (b) 14N, (c) 14I, and, (d) 14R 14N 14I

1200 kg/m³ set – Corrosion rate and potentials

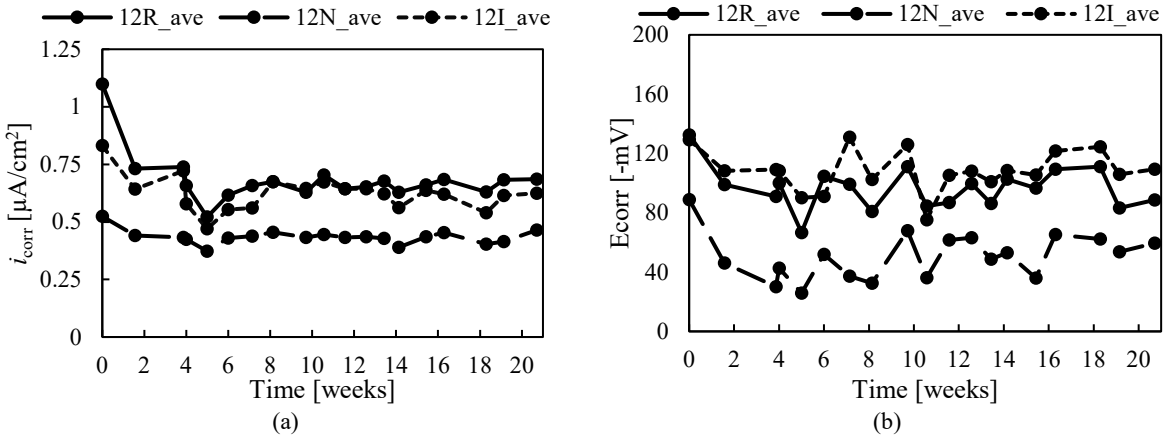

Figure C.5: Corrosion (a) rate and (b) potential

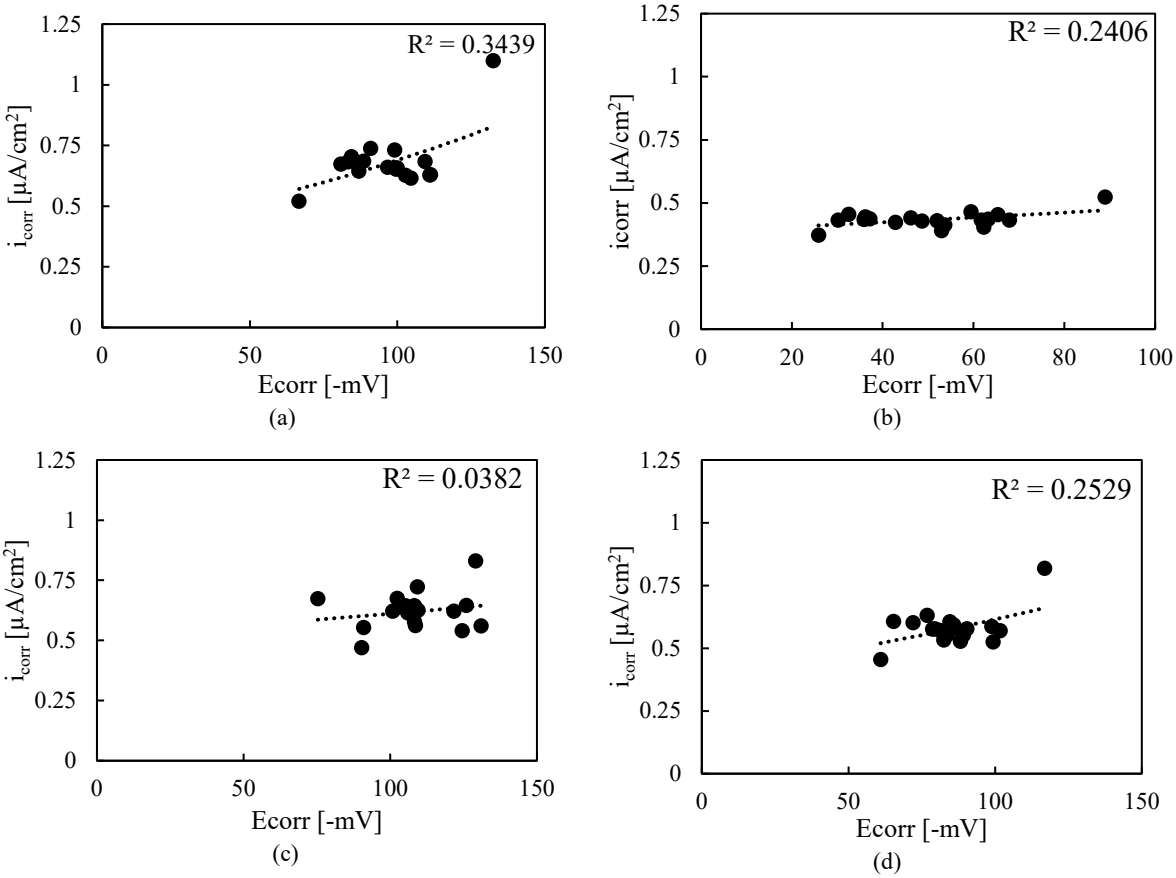

Figure C.6: Average corrosion potential versus average corrosion rates (a)12R, (b) 12N, (c) 12I, and, (d) 12R 12N 12I

Appendix D – I_{corr} versus E_{corr}

1600 kg/m³ set – Corrosion rate and potentials

Table D.1: I_{corr} and E_{corr} values for the 16 Series

Description	Weeks	Cycle [1:1 wet:dry reading]									
	[1-21]	1	2	3	4	5	6	7	8	9	10
i_{corr} [µA/cm²]											
16R											
	0.604	0.582	0.568	0.490	0.563	0.663	0.593	0.534	0.777	0.641	0.663
	0.703	0.525	0.504	0.497	0.511	0.777	0.768	0.961	1.015	0.764	0.728
	0.761	0.718	0.767	1.028	0.722	0.716	0.721	0.706	0.759	0.728	0.725
16N											
	0.730	0.838	0.773	0.630	0.740	0.768	0.691	0.678	0.737	0.722	0.723
	0.590	0.670	0.591	0.608	0.599	0.648	0.567	0.540	0.586	0.525	0.536
	0.641	0.754	0.655	0.574	0.620	0.618	0.662	0.592	0.651	0.634	0.671
16I											
	1.050	1.038	1.157	1.190	1.053	1.039	1.053	0.854	1.067	1.021	1.018
	0.446	0.506	0.452	0.467	0.434	0.430	0.444	0.405	0.439	0.426	0.476
	0.559	0.649	0.584	0.489	0.570	0.570	0.562	0.509	0.558	0.540	0.560
E_{corr} [-mV]											
16R											
	181	161	148	153	149	154	164	149	264	261	238
	260	157	145	146	160	280	348	327	395	350	315
	204	134	182	326	184	178	253	220	202	170	172
16N											
	29	71	33	28	25	21	27	14	26	21	21
	23	52	23	20	15	15	22	13	30	22	21
	88	94	72	103	83	68	86	77	101	99	100
16I											
	343	320	366	388	372	336	339	302	339	332	325
	58	129	87	59	51	52	57	36	41	20	39
	70	120	92	73	84	64	71	50	58	34	34
Average											
i_{corr} [µA/cm²]											
16R	0.689	0.608	0.613	0.672	0.599	0.719	0.694	0.734	0.850	0.711	0.705
16N	0.654	0.754	0.673	0.604	0.653	0.678	0.640	0.603	0.658	0.627	0.643
16I	0.685	0.731	0.731	0.715	0.685	0.679	0.686	0.590	0.688	0.662	0.685
E_{corr} [-mV]											
16R	215	150	159	208	165	204	255	232	287	260	241
16N	47	72	42	50	41	35	45	35	52	47	47
16I	157	190	182	173	169	151	156	129	146	129	132
CoV [%]											
i_{corr}											
16R	9.37	13.32	18.27	37.54	15.02	6.51	10.62	23.89	13.70	7.27	4.25
16N	8.88	9.10	11.21	3.81	9.50	9.52	8.26	9.47	9.38	12.8	12.3
16I	38.3	30.7	41.9	47.0	38.8	38.4	38.5	32.6	39.6	39.0	34.8
E_{corr}											
16R	15.3	8.0	10.5	39.9	8.8	26.7	29.4	31.5	27.9	28.1	24.1
16N	62.3	23.9	49.5	74.3	72.9	68.6	64.5	87.6	66.1	76.7	78.5
16I	83.8	48.8	71.7	87.7	85.0	87.0	83.0	94.9	93.7	112	103

1400 kg/m³ set – Corrosion rate and potentials

Table D.2: I_{corr} and E_{corr} values for the 14 Series

Description	**Weeks**	**Cycle [1:1 wet:dry reading]**									
	[1-21]	**1**	**2**	**3**	**4**	**5**	**6**	**7**	**8**	**9**	**10**
***i*corr** [µA/cm²]											
14R											
	0.600	0.664	0.618	0.552	0.608	0.590	0.613	0.567	0.611	0.568	0.618
	0.675	0.768	0.707	0.642	0.663	0.673	0.665	0.640	0.675	0.634	0.694
	0.590	0.650	0.614	0.502	0.596	0.588	0.614	0.574	0.604	0.560	0.619
14N											
	0.562	0.754	0.609	0.426	0.584	0.573	0.564	0.502	0.554	0.489	0.566
	0.488	0.612	0.502	0.430	0.503	0.471	0.479	0.446	0.514	0.443	0.477
	0.675	0.943	0.754	0.530	0.629	0.651	0.643	0.618	0.680	0.615	0.708
14I											
	1.070	0.998	0.952	1.006	0.956	1.014	1.175	1.006	1.295	1.152	1.224
	0.596	0.748	0.612	0.478	0.575	0.584	0.671	0.583	0.596	0.518	0.593
	0.526	0.634	0.527	0.487	0.502	0.521	0.524	0.513	0.537	0.4925	0.517
E_{corr} [-mV]											
14R											
	118	153	122	120	119	83	123	113	124	110	106
	105	125	106	99	91	111	104	99	112	100	95
	113	120	107	93	98	123	118	114	117	123	115
14N											
	22	52	23	10	14	26	29	14	21	14	21
	40	60	35	31	22	47	61	43	14	38	49
	19	52	13	9	6	22	23	9	14	21	29
14I											
	237	132	155	239	207	225	287	265	298	291	300
	923	114	89	88	81	92	127	73	94	83	76
	92	121	102	97	86	89	89	82	91	78	71
Average											
***i*corr** [µA/cm²]											
14R	0.650	0.694	0.646	0.565	0.622	0.617	0.631	0.594	0.630	0.587	0.644
14N	0.575	0.769	0.622	0.462	0.572	0.565	0.562	0.522	0.582	0.516	0.584
14I	0.730	0.793	0.697	0.657	0.677	0.706	0.790	0.701	0.809	0.721	0.778
E_{corr} [-mV]											
14R	109	133	112	104	102	106	115	109	117	111	105
14N	27	55	24	16	14	32	38	22	17	24	33
14I	140	123	116	141	125	135	168	140	161	151	145
CoV [%]											
***i*corr**											
14R	6.10	7.61	6.65	10.3	4.73	6.46	3.87	5.50	5.11	5.66	5.53
14N	13.4	17.6	16.6	10.4	9.13	13.0	12.0	13.7	12.1	14.1	16.3
14I	33.1	19.2	26.4	37.6	29.4	31.0	35.3	31.1	42.5	42.3	40.7
E_{corr}											
14R	4.77	10.7	6.76	10.9	11.4	16.0	6.98	6.06	4.30	8.41	7.80
14N	33.0	7.5	38.5	65.2	46.8	35.4	43.5	68.7	18.8	41.4	35.3
14I	48.6	6.2	24.9	49.0	46.9	47.1	51.1	63.2	60.2	65.6	71.6

1200 kg/m³ set – Corrosion rate and potentials

Table D.3: I_{corr} and E_{corr} values for the 12 Series

Description	**Weeks**	**Cycle [1:1 wet:dry reading]**									
	[1-21]	**1**	**2**	**3**	**4**	**5**	**6**	**7**	**8**	**9**	**10**
***i*corr** [µA/cm²]											
12R											
	0.665	0.888	0.674	0.556	0.638	0.654	0.652	0.632	0.653	0.635	0.672
	0.821	1.077	0.87	0.668	0.814	0.813	0.752	0.781	0.817	0.802	0.822
	0.562	0.782	0.551	0.482	0.548	0.534	0.542	0.545	0.547	0.533	0.564
12N											
	0.418	0.503	0.419	0.377	0.435	0.415	0.415	0.382	0.423	0.395	0.414
	0.408	0.473	0.411	0.373	0.416	0.390	0.390	0.391	0.420	0.372	0.49
	0.477	0.473	0.455	0.455	0.489	0.512	0.500	0.456	0.492	0.462	0.49
12I											
	0.741	0.934	0.792	0.610	0.740	0.770	0.728	0.701	0.739	0.664	0.731
	0.563	0.631	0.587	0.446	0.525	0.605	0.618	0.539	0.586	0.524	0.583
	0.568	0.646	0.572	0.480	0.589	0.603	0.586	0.537	0.562	0.546	0.561
E_{corr} [-mV]											
12R											
	94	105	92	88	84	101	92	91	101	97	90
	109	132	109	102	99	108	107	107	113	110	97
	87	110	86	67	88	84	81	86	96	85	79
12N											
	50	64	34	39	34	54	65	51	46	56	57
	50	69	35	36	39	51	57	49	54	57	60
	52	69	40	41	31	51	65	53	52	61	60
12I											
	98	108	94	93	89	96	98	93	103	107	101
	110	115	100	100	136	114	97	102	112	114	108
	118	134	133	79	125	92	125	120	126	125	120
Average											
***i*corr** [µA/cm²]											
12R	0.683	0.916	0.698	0.568	0.666	0.667	0.648	0.652	0.672	0.657	0.686
12N	0.435	0.483	0.428	0.402	0.447	0.439	0.435	0.409	0.445	0.409	0.465
12I	0.624	0.737	0.650	0.512	0.618	0.659	0.644	0.592	0.629	0.578	0.625
E_{corr} [-mV]											
12R	97	116	96	86	90	98	93	95	103	97	89
12N	51	68	37	39	35	52	63	51	51	58	59
12I	109	119	109	91	117	101	107	105	114	115	109
CoV [%]											
***i*corr**											
12R	15.6	13.3	18.8	13.5	16.6	17.1	13.2	14.9	16.5	16.9	15.4
12N	7.04	2.93	4.42	9.34	6.87	12.0	10.9	8.03	7.50	9.29	7.71
12I	13.3	18.9	15.5	13.8	14.6	11.9	9.44	13.0	12.4	10.7	12.1
E_{corr}											
12R	9.61	9.99	10.2	17.1	6.80	10.1	11.5	9.39	6.68	10.7	8.65
12N	2.16	4.20	7.53	5.28	9.04	1.95	6.24	3.21	7.21	3.49	3.15
12I	7.48	9.32	15.9	9.64	17.0	9.77	12.1	10.7	8.06	6.76	7.11